

Modelling and measurement of 3D fields in stellarators and tokamaks

Shaun Robert Haskey

A thesis submitted for the degree of
Doctor of Philosophy of
The Australian National University.

September 2014

Declaration

This thesis, to the best of my knowledge and belief, does not contain any results previously published by another person or submitted for a degree or diploma at any university except where due reference is made in the text. This thesis consists of several publications. The extent to which each publication is my own work is described in the synopsis, as well as the foreword to each chapter.

Shaun Haskey

30 September 2014

Acknowledgements

First and foremost I would like to thank my fiancé, Heather, for travelling around the world with me to a small town in the middle of the bush. She has been there for the highs and lows, put up with my hectic work schedule and absent mindedness, and proof read parts of this thesis. I'm not sure how I could have done it without her.

I am greatly indebted to my supervisor, Boyd Blackwell, for his knowledge of all things H-1NF, electronics, and plasma physics. He has taught me a huge amount over the past few years and has always found time to answer and discuss my constant stream of questions. The other members of my supervisory panel have also contributed greatly. John Howard provided many suggestions and much insight with the synchronous imaging and tomographic inversion work and Matthew Hole has improved my understanding of the theoretical side of this project. David Pretty also deserves a special mention for providing the pyfusion module and getting me started with Linux, Python and Emacs - I'm not sure how I got anything done without them.

For the work that was conducted at DIII-D, I would like to thank Matthew Lanctot for getting me started, helping out with MARS-F, always finding time to chat, and improving some of my first poorly written draft papers. Raffi Nazikian was also instrumental in organising my trip to DIII-D and making sure it was highly productive and fun.

This project has also received an extensive amount of technical support. John Wach deserves a huge thanks for helping with the design of the helical Mirnov array, performing the complicated installation, and always going the extra mile to get the job done properly. Steven Marshall provided a large portion of the HMA amplifier design. Michael Blacksell provided plenty of advice and has been a great sounding board for all things electronics. David Anderson and the electronics unit have also been great and always willing to help me out when I was stuck or trying to find some obscure component.

A large number of codes were used in this work, and the authors of these codes, Yue-qiang Liu, Carolin Nührenberg, and Axel Könies, have been extremely kind by providing them, spending time to include new functionality, and helping with the interpretation of the results.

AINSE and ANSTO have been very generous by funding one of my scholarships along

with the extensions and contributing towards this work on H-1NF. The Australian tax payers also deserve a huge thanks for paying for this research and my scholarships.

I am also very thankful for the friendship from all those already mentioned, my friends outside of work in Canberra and in Perth, as well as many other people at RSPE including: Cameron, Jason, Cormac, Horst, Alex, Romana, Sam, Juan, Clive, Bernhard, Greg, Mark, Fenton, Lei, James, Trevor, Wes, Chris, and Ben.

Last and far from least, I would like to thank my family. Mum, Dad, and Carolyn - I could not have got to this point without your constant encouragement, support, and interest in my work.

Publications

The research presented in this thesis has resulted in the following papers:

- **S. R. Haskey**, B. D. Blackwell, B. Seiwald, M. J. Hole, D. G. Pretty, J. Howard, and J. Wach. *A multichannel magnetic probe system for analysing magnetic fluctuations in helical axis plasmas*. Review of Scientific Instruments, 84(9):093501, 2013
- **S. R. Haskey**, N. Thapar, B. D. Blackwell, and J. Howard. *Synchronous imaging of coherent plasma fluctuations*. Review of Scientific Instruments, 85(3):033505, 2014
- **S. R. Haskey**, B. D. Blackwell, and D. G. Pretty. *Clustering of periodic multi-channel timeseries data with application to plasma fluctuations*. Computer Physics Communications, 185(6):1669–1680, 2014
- **S. R. Haskey**, M. J. Lanctot, Y. Q. Liu, J. M. Hanson, B. D. Blackwell, and R. Nazikian. *Linear ideal MHD predictions for $n = 2$ non-axisymmetric magnetic perturbations on DIII-D*. Plasma Physics and Controlled Fusion, 56(3):035005, 2014
- **S. R. Haskey**, B. D Blackwell, B. Seiwald, and J. Howard. *Visible light tomography of MHD eigenmodes on the H-1NF stellarator using magnetic coordinates*. Nuclear Fusion, 54(8):083031, 2014
- M. J. Lanctot, R. J. Buttery, J. S. de Grassie, T. E. Evans, N. M. Ferraro, J. M. Hanson, **S. R. Haskey**, R. A. Moyer, R. Nazikian, T. H. Osborne, D. M. Orlov, P. B. Snyder, M. R. Wade and the DIII-D team. *Sustained suppression of type-I edge-localized modes with dominantly $n= 2$ magnetic fields in DIII-D*. Nuclear Fusion, 53(8):083019, 2013
- J. D. King, E. J. Strait, R. L. Boivin, D. Taussig, M. G. Watkins, J. M. Hanson, N. C. Logan, C. Paz-Soldan, D. C. Pace, D. Shiraki, M. J. Lanctot, R. J. LaHaye, L. L. Lao, D. J. Battaglia, A. C. Sontag, **S. R. Haskey**, and J. G. Bak. *An upgrade of the magnetic diagnostic system of the DIII-D tokamak for non-axisymmetric measurements*. Review of Scientific Instruments, 85(8):083503, 2014

- **S. R. Haskey**, M. J. Lanctot, Y. Q. Liu, C. Paz-Soldan, J. D. King, B. D. Blackwell, and O. Schmitz. *Effects of resistivity and rotation on the linear plasma response to non-axisymmetric perturbations on DIII-D*. Plasma Physics and Controlled Fusion, 57(2):025015, 2015
- **S. R. Haskey**, B. D. Blackwell, J. Howard, C. Nührenberg, A. Könies, et al. *Experiment-theory comparison for low frequency modes on the H-1NF stellarator*. Submitted to plasma physics and controlled fusion, November 2014
- **S. R. Haskey**. *Clustering techniques for plasma imaging diagnostics*. In preparation, September 2014
- C. Paz-Soldan, R. Nazikian, **S. R. Haskey**, N. C. Logan, E. J. Strait, N. Ferraro, J. M. Hanson, J. D. King, M. J. Lanctot, R. Moyer, M. Okabayashi, J-K. Park, and M. Shafer. *Observation of multi-component plasma response and its relationship to density pumpout and edge-localized mode suppression*. Physical Review Letters. Accepted for publication in February, 2015
- R. Nazikian, C. Paz-Soldan, J. D. Calle, J. S. deGrassie, D. Eldon, T. E. Evans, N. M. Ferraro, B. A. Grierson, R. J. Groebner, **S. R. Haskey**, C. C. Hegna, J. D. King, N. C. Logan, G. R. McKee, R. A. Moyer, M. Okabayashi, D. M. Orlov, T. H. Osborne, J-K. Park, T. L. Rhodes, M. W. Shafer, P. B. Snyder, W. M. Solomon, E. J. Strait, M. R. Wade. *Pedestal bifurcation and resonant field penetration at the threshold of Edge-Localised-Mode suppression in the DIII-D tokamak*. Physical Review Letters. Accepted for publication in February, 2015
- J. D. King, E. J. Strait, N. M. Ferraro, J. M. Hanson, **S. R. Haskey**, M. J. Lanctot, Y. Q. Liu, N. Logan, C. Paz-Soldan, D. Shiraki, and A. D. Turnbull. *Multiple kink mode contributions to three-dimensional tokamak equilibria due to kinetic resonances*. Submitted to Physical Review Letters, December 2014
- J. D. King, E. J. Strait, S. A. Lazerson, N. M. Ferraro, N. C. Logan, **S. R. Haskey**, J. M. Hanson, M. J. Lanctot, Y. Q. Liu, R. Nazikian, M. Okabayashi, C. Paz-Soldan, D. Shirakil, and A. D. Turnbull. *Experimental tests of linear and nonlinear 3D equilibrium models in DIII-D*. Submitted to Plasma Physics, December 2014

Abstract

This thesis presents advances in the modelling, analysis, and measurement of 3D fields, which have significantly improved the diagnosis and understanding of Alfvén waves in the H-1NF stellarator and the role of non-axisymmetric magnetic perturbations (MPs) in edge localised mode (ELM) suppression on the DIII-D tokamak. Alfvén waves and MPs impact on the performance of stellarators and tokamaks; consequently, improved measurement and understanding of these effects is critical to optimising the operation of these devices and the success of magnetic confinement fusion.

To further understand the plasma fluctuations in H-1NF, a sixteen former, tri-axis helical Mirnov array (HMA) was designed and installed. The new array complements two existing poloidal Mirnov arrays by providing polarisation information, higher frequency response, and much improved toroidal resolution for spontaneously excited H-1NF fluctuations. The quantity and complexity of the data obtained from this new array led to the development of a periodic datamining algorithm which has been used to extract distinct plasma fluctuations in multi-channel oscillatory timeseries data.

A state of the art synchronous imaging technique which overcomes frame rate and readout noise limitations of cameras is described and demonstrated on longer-lived H-1NF fluctuations. This technique can be used to image modes in the kHz - MHz range, opening up the possibility of high resolution imaging of high frequency MHD instabilities, which play an important role in stability and particle transport on both tokamaks and stellarators. In order to make the most of the data from the synchronous imaging technique, a 3D tomographic reconstruction technique which uses magnetic coordinates was developed for inversion of a set of high-resolution 2D visible light emission projections. This tomographic inversion technique was used to obtain the detailed radial structure of global MHD eigenmodes in H-1NF without assumptions about the radial functional form.

Information about the modes, which was obtained using these diagnostic systems and analysis techniques is compared with calculations of the H-1NF continuum gap structure and several discrete normal modes within the framework of linearised ideal compressible MHD, using the CONTI and CAS3D codes. The observations have good agreement with modes where compressibility (beta induced Alfvén eigenmodes) or interaction with sound

modes is important (beta-induced Alfvén-acoustic eigenmodes), in terms of their dominant mode numbers, radial structure, and polarisation. The frequency dependence on H-1NF configurations (rotational transform profile), could be recovered for these modes if the plasma temperature decreases near rational rotation transform values. Tests of this hypothesis await completion of an upgraded helium line ratio temperature diagnostic.

In tokamaks, an outstanding issue is the plasma response to externally applied 3D magnetic field perturbations and how the response leads to ELM suppression. Extensive modelling using the single fluid linear MHD code, MARS-F, shows the ability to tailor the plasma response through careful control of the applied MP field. Metrics are described, which allow the identification of regions of parameter space where the MP directly couples to the pitch-resonant harmonics or the kink mode. Several important parameteric dependencies such as q_{95} , toroidal rotation, resistivity, and β_N are also discussed. Finally, recent experiments on DIII-D using the modelling presented here show the importance of coupling to the kink mode in order to maximise the residual pitch-resonant harmonics and achieve ELM suppression. This finding critically influences the way that MPs are optimised to achieve the vital goal of ELM suppression on tokamaks.

Synopsis

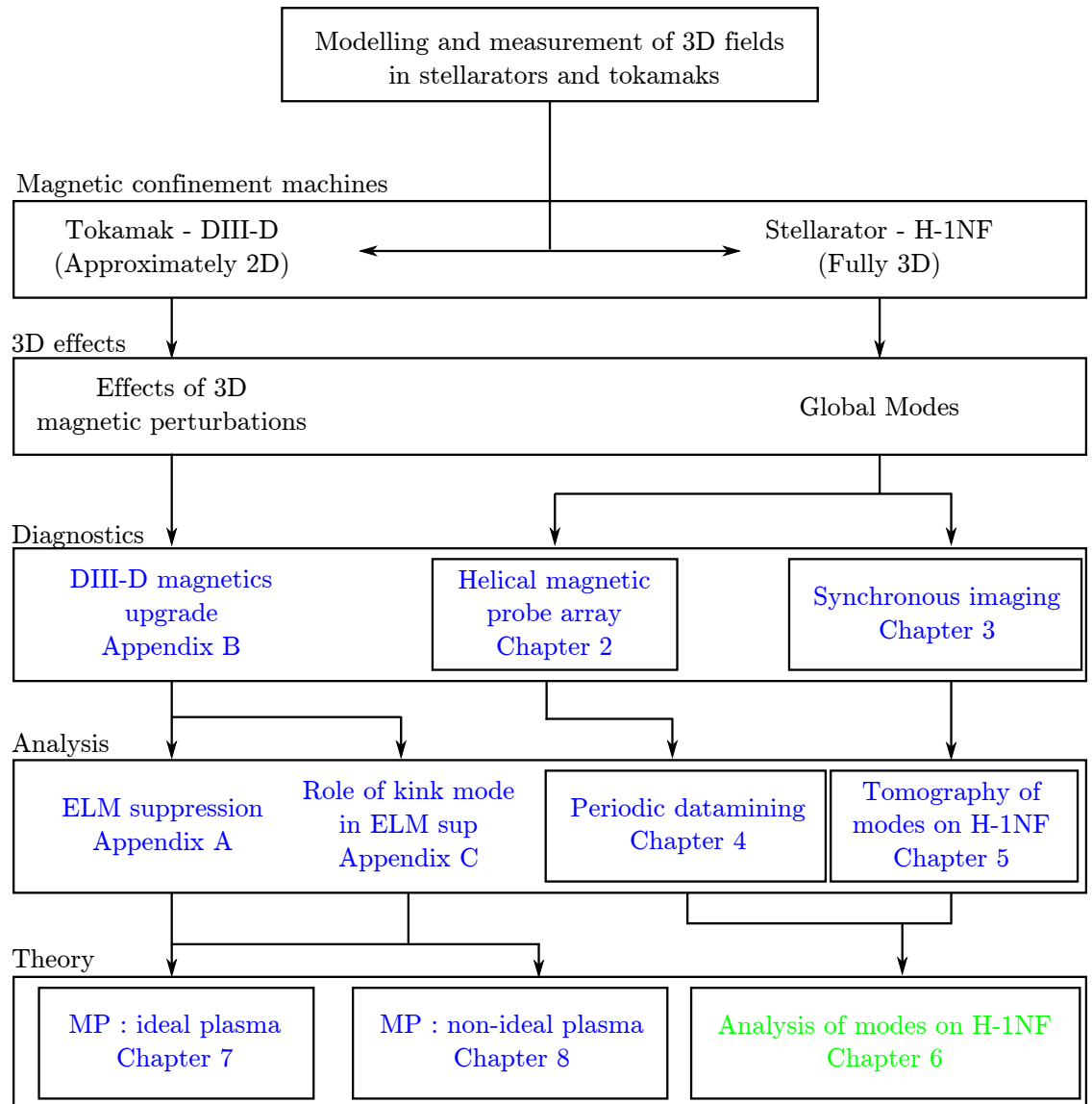


Figure 1: Relationship between the various publication chapters in this thesis. Chapters marked in blue and green are published and under review respectively. Publications where I performed the majority of the research and writing are included in the main body of the thesis and have individual boxes around them in this diagram. Papers where I am a co-author are included as a single page in the appendices.

The research presented in this thesis introduces solutions to some of the challenges faced in diagnosing and analysing plasma configurations where all three spatial dimensions

Table 1: The status of the publications and extent to which the research and writing of the publications that form the chapters of this thesis are my own work. The journals (Review of Scientific Instruments, Computer Physics Communications, Nuclear Fusion, Physics of Plasmas, Physical Review Letters, and Plasma Physics and Controlled Fusion) and impact factors are also shown. I am responsible for 100% of the writing of the first drafts of the papers in chapters 2, 3, 4, 5, 6, 7, 8, the 80%-85% values given recognise contributions by co-authors to improvements before submission and during the refereeing process.

Chapter	Journal	Status	Research	Writing	IF
Chapter 2	RSI	Published	80%	85%	1.7
Chapter 3	RSI	Published	80%	80%	1.7
Chapter 4	CPC	Published	90%	85%	3.2
Chapter 5	NF	Published	90%	85%	2.7
Chapter 6	PPCF	Under Review	75%	85%	2.4
Chapter 7	PPCF	Published	80%	80%	2.4
Chapter 8	PPCF	Published	90%	85%	2.4
Appendix A	NF	Published	15%	5%	2.7
Appendix B	RSI	Published	5%	0%	1.7
Appendix C	PRL	Accepted	20%	10%	7.7

of the plasma must be considered. This research has focused on the two most advanced types of magnetic confinement fusion devices, the tokamak and stellarator. Specifically, research relating to the DIII-D tokamak, which in many cases can be approximated as 2D but where the application of 3D fields has been found to be exceptionally useful, and the H-1NF heliac, which produces strongly shaped plasmas where the full 3D case must be considered, has been undertaken.

The difficulties in dealing with all three spatial dimensions has led to the development of several unique diagnostics (chapters 2, 3, and appendix B), innovative data analysis techniques and experimental observations (chapters 4, 5, and appendices A and C), and theoretical modelling and comparisons of experimental data with theory (chapters 6, 7, and 8). The solutions to these challenges have resulted in several publications, which are presented as chapters in this thesis. Each chapter contains a publication and a foreword, which provides the context for the publication in the thesis. All publications where I am the primary researcher and author are included in the main thesis, while publications where I am only a contributing author are included as a single page in the appendices. Additionally, derivations and information which may be useful for future research on similar topics are included as appendices D, E, F, G, H, I, and J. The status and extent to which these publications are my own work is summarised in table 1.

The general structure of this thesis is illustrated in figure 1. The research is split between the stellarator (H-1NF) and tokamak (DIII-D), in particular, global modes and

the effects of 3D magnetic perturbations on these machines respectively. From this point, the general flow of the research is from diagnostic development to data analysis techniques, to modelling and comparison with theory, with three main intertwined threads:

- Thread 1 : The design and installation of the helical Mirnov array (chapter 2) led to the development of the periodic datamining technique (chapters 4), which helped with the analysis of modes on H-1NF (chapter 6) by producing mode polarisation information and mode structure in the toroidal and poloidal directions.
- Thread 2 : The development of the synchronous imaging technique (chapter 3) required the development of a novel tomographic inversion technique (chapter 5), which in turn provided crucial information about radial mode structure for analysis of modes in H-1NF (chapter 6).
- Thread 3 : Observations of edge localised mode (ELM) suppression on DIII-D using 3D magnetic perturbations (appendix A) motivated the installation of a new set of magnetic diagnostic probes (appendix B) and prompted significant modelling efforts aimed at untangling the effects 3D magnetic perturbations have on DIII-D plasmas in the ideal MHD case (chapter 7) and the case where plasma rotation and resistivity are considered (chapter 8). These modelling efforts in turn have motivated some of the experiments shown in appendix C.

A natural progression to threads 1 and 2 is the external excitation of modes in H-1NF. Some effort was put into preliminary experiments which were marginally successful. Appendix I describes these efforts and provides a basis for future work. Each of these threads is described in greater detail in the following subsections.

Thread 1 : The magnetic component of modes on H-1NF

To better understand the magnetic component of plasma fluctuations in H-1NF, a 48 probe helical Mirnov array (HMA) was designed and installed as part of this PhD research. The probes were designed to complement two existing poloidal Mirnov arrays by providing higher frequency response and information on the toroidal and poloidal mode numbers and mode polarisation. The HMA is a unique type of Mirnov array that has been designed to deal with the difficulties of the fully 3D geometry of H-1NF. A tightly spaced toroidal array which is commonly installed on tokamaks, is often impossible to install on stellarators such

as H-1NF due to access issues caused by the 3D nature of these machines. Details of the design, installation, calibration, and initial results from this unique magnetic probe array are described in the paper in chapter 2.

The large number of magnetic probes, high digitisation rate (2MHz in the case of the HMA), and the fact that magnetic probe arrays are among the “always on” diagnostics on major experiments means that large databases of multidimensional data are generated as part of every experimental campaign. This is beneficial as there is a great deal of important information hidden in these databases; however, it is difficult to separate it from the less significant data.

These large databases of magnetic probe data provide a perfect opportunity for knowledge discovery using machine learning techniques such as datamining or clustering. The phase differences between magnetic probes in a Mirnov array provide details of the spatial structure of the fluctuations, which can be used to find clusters of distinct fluctuation types in these large databases. The frequencies of the members of these clusters can then be correlated with plasma parameters to determine details of the dispersion relations of these fluctuations. Using clustering techniques means that no specific structure is imposed on the phase differences between probes. This is particularly important in stellarators where the complexity of the machine (due to their 3D structure), means that a simple model is usually not available.

The phase difference between magnetic probes is 2π periodic, causing significant problems with existing clustering algorithms, which must either distort the high dimensional phase space or ignore the inherent periodicity of these measurements to accommodate this type of data. To overcome these difficulties, a new clustering algorithm was developed, which is based on mixtures of independent von Mises distributions whose parameters are found using the expectation maximisation algorithm. The algorithm has been shown to outperform alternatives on several artificial datasets, and has been used to successfully extract and cluster data from the HMA. Chapter 4 includes a publication describing the algorithm and its application to H-1NF data. A paper which describes an extension to this algorithm to deal with imaging diagnostics such as soft x-ray arrays and interferometers is nearing completion.

Each of the clusters identified using these algorithms represent distinct classes of fluctuation and are compared with state-of-the-art theoretical modelling from the CAS3D and CONTI codes (chapter 6) in an effort to understand the underlying nature of modes that

spontaneously form in 0.5T H/He H-1NF plasmas.

Thread 2 : The radial structure of modes on H1-NF

While magnetic probe arrays are reliable and provide extremely useful information on toroidal and poloidal mode numbers, they do not provide information on the radial structure of plasma fluctuations, which is crucial for understanding these modes. To provide this information a state-of-the-art synchronous imaging technique (based on a technique pioneered and successfully demonstrated by Professor John Howard) was developed, in which the fluctuation signal from a magnetic probe is used as the input to a phase locked loop which then generates gating pulses for an intensified CCD camera. Using this technique it is possible in principle to image high frequency MHD modes in the kHz to MHz range using soft x-rays (with a scintillation plate), spectral lines, broadband light, or bremsstrahlung, depending on the plasma conditions. This is the first time that modes have been imaged in this resolution and at these frequencies in magnetic confinement experiments. The description of the technique and its application to imaging modes in H-1NF in CII 514nm light using an interference filter is described in detail in the paper in chapter 3.

The high resolution 2D images acquired using the synchronous imaging technique provide highly detailed information about the mode being imaged. In H-1NF, the images cover a wedge shaped slice of plasma, providing toroidal, poloidal, and radial mode structure information, which are all important in a fully 3D machine like H-1NF. To extract the radial mode structure and mode number information from these images, a tomographic inversion technique which has minimal assumptions about the structure of the mode, was developed and is described in chapter 5. The radial mode structures presented in this chapter are the most detailed tomographic reconstructions of MHD fluctuation in magnetic confinement experiments to date.

The combination of these novel imaging and tomographic inversion techniques provides extremely detailed radial eigenmode structures. These are used along with the data from the magnetic probes and clustering to provide the detailed comparison with theory in chapter 6.

Thread 3 : The effects of 3D magnetic perturbations on tokamaks (DIII-D)

Tokamaks are currently the most advanced magnetic confinement approach to controlled nuclear fusion and the next-step machine, ITER, which is currently under construction, is a tokamak. In contrast to the highly complex shapes of stellarators, tokamaks are essentially axisymmetric machines (2D), which greatly simplifies their construction and analysis of their plasmas. However, this simplicity comes with two main costs: steady state operation is difficult, and tokamaks are highly susceptible to current driven instabilities due to the required large plasma currents.

Historically great efforts have been made to reduce any non-axisymmetric (or error) field that violated a tokamak's axisymmetry. However, recently it has been found that specially tailored 3D magnetic perturbations (MPs) are extremely useful for suppressing type-I edge localised modes (ELM) (appendix A), which is of considerable importance for future experiments such as ITER as well as future nuclear fusion power plants because the anticipated heat loads will severely limit the lifetime of plasma facing components. MPs have also been used to control resistive wall modes and neoclassical tearing modes, perform magnetic spectroscopy, and correct error fields. Consequently, thorough studies of the plasma response dependence on MP coil and plasma parameters are of significant importance.

The publications in chapters 7 and 8 present in-depth analysis of the linear plasma response to these 3D magnetic fields in both the ideal MHD and resistive MHD cases. The results demonstrate how to tailor the applied field to meet certain goals such as maximising the chance of magnetic island formation through direct coupling, or by driving global modes such as the kink mode, more strongly. The effects of safety factor profile, plasma pressure, toroidal rotation, and plasma resistivity are studied in the linear regime. Additionally, the regions of parameter space where the plasma response transitions from ideal to resistive/rotation dependent are clearly demonstrated. These results are particularly important for guiding experiments and providing interpretation of observations in ELM suppression experiments.

The paper in appendix C includes details of recent DIII-D experiments which examine the dependence of ELM suppression on the applied field spectrum. These experiments are closely related to the modelling presented in chapter 7, and the comparisons appear to show that ELM suppression is more strongly correlated with MPs that couple strongly

to the kink mode. These findings have a very significant impact on how best to tailor the applied field structure to achieve ELM suppression.

Application of 3D methods to Tokamaks

The flexibility, shot reproducibility, and challenges introduced by the fully 3D H-1NF heliac/stellarator have provided the perfect test bed for the design of advanced diagnostics and plasma analysis techniques which are increasingly more useful to tokamaks as well as stellarators. The diagnostic and analysis techniques developed as part of this PhD research were originally designed to deal with the challenging task of diagnosing MHD fluctuations on the H-1NF heliac; however, their generality means that they are also very useful for tokamaks.

The synchronous imaging technique coupled with the 3D tomographic reconstruction method provides the perfect opportunity to obtain highly detailed radial eigenmode structures of modes that affect stability and particle transport in all types of magnetic confinement machines. The generality of the method means the technique is easily adapted to unconventional viewing geometries and takes full advantage of the high resolution offered by modern CCDs. This is particularly important, considering the limited port space available on modern machines.

The periodic datamining technique is particularly useful to the new generation of long pulse superconducting machines, where the quantity of data collected is growing exponentially. Because there is no need to assume a mode structure, the technique is well suited to clustering modes, where the mode structure may be difficult to define *a priori* as is often the case for stellarators. This is also applicable to poloidal arrays on tokamaks, where the mode structure is more difficult to calculate than the toroidal direction because of a lack of symmetry. These types of machine learning techniques are becoming increasingly important, as traditional analysis methods become more difficult and time consuming. The technique also offers the opportunity for knowledge discovery using the existing databases of shots for many of the machines around the world which continue to grow at an accelerating pace.

Contents

Declaration	iii
Acknowledgements	v
Publications	vii
Abstract	ix
Synopsis	xi
1 Introduction	1
1.1 The energy challenge	1
1.2 Motivation and status of nuclear fusion research	4
1.3 Plasma state and the physics of magnetically confined plasma	6
1.4 MHD waves	9
1.5 Magnetic confinement devices: stellarators and tokamaks	13
1.6 The H-1NF flexible heliac	15
1.7 The DIII-D tokamak	17
1.8 Thesis scope and structure	20
2 (Published) Multichannel magnetic probe system	21
3 (Published) Synchronous imaging	31
4 (Published) Clustering of periodic timeseries data	39
5 (Published) 3D tomography of MHD fluctuations	53
6 (In preparation) Analysis of modes on H-1NF	65
7 (Published) Linear ideal MHD predictions for n=2 MPs on DIII-D	81
8 (Published) Effects of resistivity and rotation on MPs	93

9 Conclusions and future work	105
9.1 Future work	108
Appendix A (Published) Sustained suppression of ELMs in DIII-D (n=2)	117
Appendix B (Published) An upgrade of the DIII-D magnetic diagnostics	119
Appendix C (Accepted) Observation of multi-component plasma response	121
Appendix D Code repositories	123
D.1 Obtaining copies of the code repositories	123
D.2 Details of the H1 module	124
Appendix E Supplementary HMA details	127
E.1 Location of the HMA probes	127
E.2 Orientation of the HMA probes	129
E.3 HMA polarisation calculations	131
E.4 Digital control of the amplifier settings	136
Appendix F Supplementary imaging and tomography details	143
F.1 Location of the camera	143
F.2 Shot numbers for the important modes	144
F.3 Details of the PLL and FPGA	146
F.4 Running the tomographic routines	151
Appendix G Supplementary details for the datamining chapter	153
G.1 Using the feature extraction and clustering algorithms	153
G.2 Covariance between phase difference measurements	156
Appendix H Supplementary details for the H-1NF mode analysis chapter	161
H.1 Plotting the spectra from CAS3D and CONTI	161
H.2 Running the polarisation and mode number analysis	162
H.3 Code compilation notes	163
Appendix I Attempts to actively drive modes in H-1NF	169
I.1 Active excitation experiments	169
I.2 Details of the broadband power amplifier design	171

Appendix J Supplementary details for the MP chapters	173
J.1 The pyMARS module	174
J.2 The pyMARS input file	177
J.3 Examples	184

Introduction

1.1 The energy challenge

The high standard of living enjoyed in developed countries depends on readily available and cost effective sources of energy. Figure 1.1 shows the strong correlation between annual per capita electricity usage and the human development index (HDI), which is based on longevity, educational attainment, and standard of living [1]. The human cost due to insufficient access to energy is enormous. In 2010, approximately 1.2 billion people lived without access to electricity, 2.6 billion people were still using traditional biomass for cooking, and a further 0.4 billion people relied on coal for cooking and heating [2]. 1.97 million annual deaths [3] have been attributed to indoor air pollution which is caused by the burning of biomass and coal.

Under three different projections to 2035, the international energy agency (IEA) predicts that world energy demand will continue to rise (figure 1.2). These scenarios range from the continuation of current policies, the adoption of new policies, and a fundamental transformation of the energy sector to keep CO₂ levels below 450ppm, which is anticipated to provide a 50% chance of limiting long term global average temperature increases to 2°C above pre-industrial levels. The “human development scenario” in [1] corresponds to raising the HDI of the world to the plateau that occurs at approximately 0.9, requiring 4000kWh annual per capita electricity consumption. Achieving this goal by 2020 is predicted to require 26,000Mtoe ¹, doubling the current demand.

Meeting this increased energy demand poses several large problems including sourcing enough fuel and using the fuel without incurring significant environmental damage. Currently, fossil fuels make up approximately 80% of OECD (organisation for economic co-operation and development) energy demand, with this amount dropping to 70% in 2035 in the IEA new policies scenario (figure 1.3). Because fossil fuels take millions of years to

¹Millions of tons of oil equivalent is a unit of energy approximately equivalent to 42GJ.

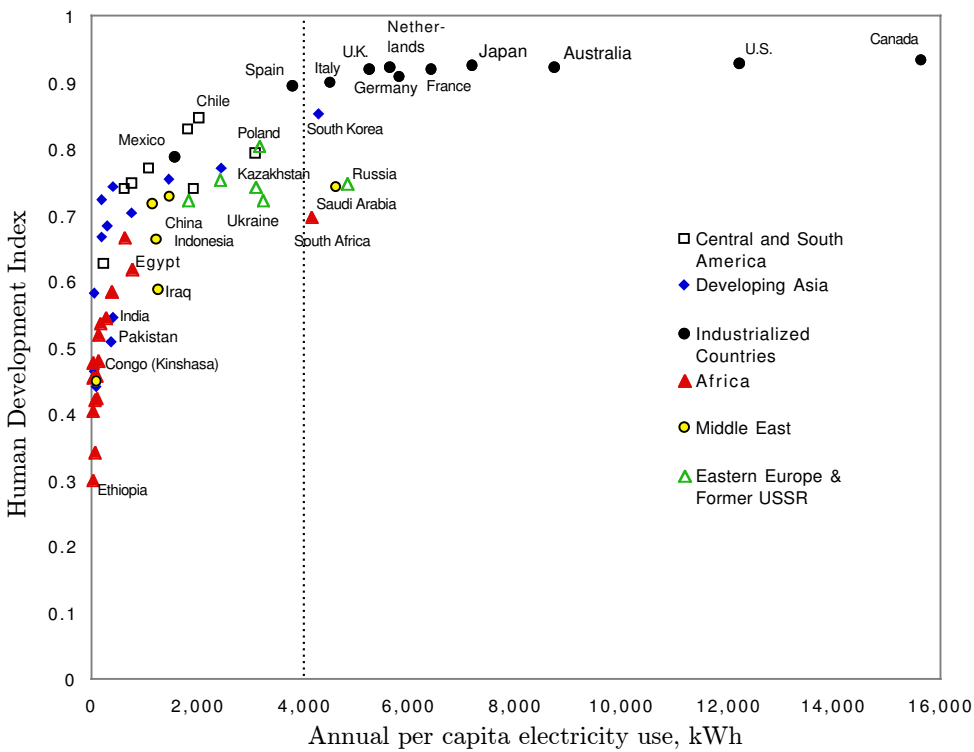


Figure 1.1: The relationship between the human development index and electricity consumption shows a strong positive correlation up to an annual per capita use of 4000kWh. Above 4000kWh there are only marginal increases in the HDI. Figure is from <https://e-reports-ext.llnl.gov/pdf/239193.pdf> [1].

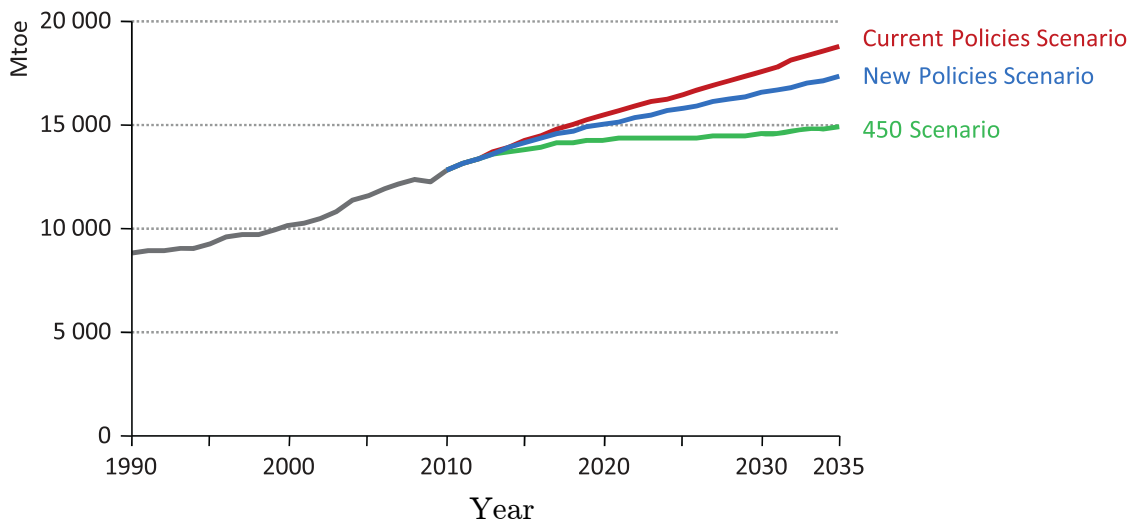


Figure 1.2: The predicted world energy demand under three difference scenarios. All scenarios show increased energy demand. The 450 scenario is a projection based on actions consistent with a 50 % chance of meeting the goal of limiting long term global average temperature increases to 2°C above pre-industrial levels (450ppm of CO₂). Figure is from [2] p50.

Table 1.1: Proven and recoverable reserves of various fossil fuels at current rates of production. Data from [2] p64.

Fossil Fuel	Proven (Yr)	Recoverable (Yr)
Coal	132	2780
Gas	71	240
Oil	55	189

form and reserves are being consumed significantly faster than they are generated, they are a non-renewable resource. Table 1.1 details the number of year's worth of proven and recoverable reserves for various fossil fuels, demonstrating that on a 50-100 year timescale, the world's population is likely to face fuel shortages which are likely to lead to serious geo-political consequences. Additionally, prices will increase as it becomes more difficult to meet demand, leading to many of the world's poor, who would benefit most, being priced out of the market.

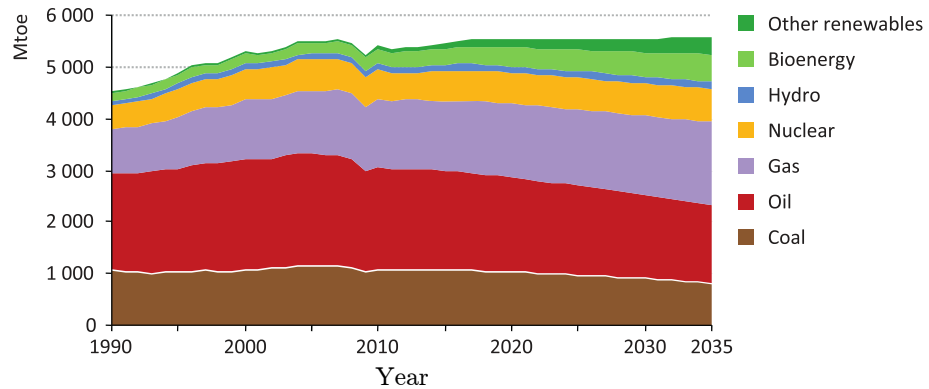


Figure 1.3: OECD primary energy demand by fuel type. Historical demand and projections using the new policies scenario. While fossil fuel use falls, it still constitutes three quarters of the energy mix in 2035. Figure is from [2] p60.

In addition to supply problems, the environmental and health impacts of burning fossil fuels are extremely significant. For example, 4.3 million deaths in 2012 were attributed to outdoor air pollution [4] in addition to the damage to the world climate system. As detailed in the fourth report from the Intergovernmental Panel on Climate Change (IPCC) [5], “[w]arming of the climate is unequivocal, as is now evident from observations of increases in global average air and ocean temperatures, widespread melting of snow and ice and rising global average sea level”, and “[m]ost of the observed increase in global average temperatures since the mid-20th century is very likely due to the observed increase in anthropogenic greenhouse gas concentrations”. Additionally, “[u]nmitigated climate change

would, in the long term, be likely to exceed the capacity of natural, managed and human systems to adapt” where very likely and likely mean “the assessed likelihood, using expert judgment” are over 90% over 66%, respectively. Climate change raises serious ethical concerns because those who face the largest impact of climate change, such as the world’s poor and future generations, played little to no role in the creation of the problem.

To meet the challenges of increased energy use without excessive health and environmental consequences, the current mix of energy sources must undergo a drastic change. Nuclear fission offers several benefits including large fuel reserves and the ability to provide base load power; however, there are several serious concerns including waste disposal, nuclear proliferation, and large scale incidents, particularly in the wake of the Chernobyl, Three Mile Island and Fukushima nuclear disasters. Renewable energy sources are starting play a more significant role in electricity generation; however as can be seen in figure 1.3, the rate of renewable energy uptake must drastically increase to make any significant impacts. Additionally, many of the renewable energy sources, such as solar and wind, are subject to issues of uncertain output, although this could be overcome with the development of economical large scale energy storage systems.

Nuclear fusion offers an attractive alternative. It does not involve any green house gas emission or nuclear weapon proliferation opportunities, and the amount of nuclear waste is substantially reduced and short lived compared to nuclear fission. Additionally, it is passively safe and the reserves of fuel are enormous: 6×10^8 TW-years for the deuterium-tritium reaction and 2×10^{11} TW-years for the deuterium-deuterium reaction. However, while there has been significant progress towards a fusion power plant, the technical and economic feasibility of a fusion power remains uncertain and is the subject of intense research.

1.2 Motivation and status of nuclear fusion research

Nuclear fusion is the process which powers the stars and is responsible either directly or indirectly for all the sources of energy available on Earth. For example, solar radiation, “stored solar radiation” (coal, oil, gas, wood, food), wind, fissionable materials, and hydro electric power can all be traced back to a fusion reaction. While our energy sources come indirectly from fusion reactions, with the exception of thermonuclear bombs, net energy has yet to be liberated from nuclear fusion reactions on Earth. Achieving this goal has been a subject of considerable interest since fusion possesses a great deal of environmental,

social, and political benefits including highly abundant and cheap fuel, inherent safety, no greenhouse gas byproducts, limited short lived nuclear waste, and it does not produce fissionable materials which are suitable for nuclear weapons.

For elements lighter than iron, nuclear fusion reactions are exothermic, with the difference between the binding energies of reactants and products released as kinetic energy of the products. For a reaction to occur, the Coulomb barrier must be overcome. This occurs when the nuclei of the reactants are moving fast enough to overcome the electrostatic repulsion between the two positively charged nuclei and come sufficiently close together for the strong interaction to bind the nuclei together. For useful amounts of energy to be extracted from this process, many particles are required and the fuel must be heated to sufficient temperatures. These temperatures are orders of magnitude larger than the ionisation energies, so the fuel is in an ionised gaseous state known as the plasma state.

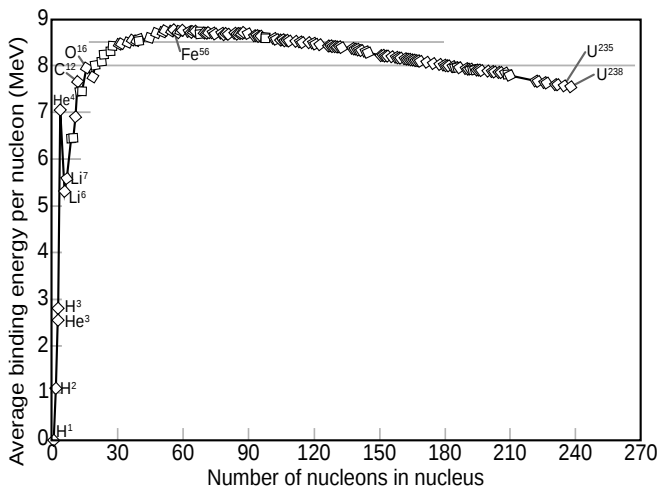


Figure 1.4: The binding energy per nucleon for common isotopes. Fusion (fission) reactions are exothermic for elements lighter (heavier) than iron.

The “triple product” of density, temperature, and confinement time (an extension of the Lawson criterion [6]) describes the minimum conditions required to reach ignition. This occurs when the temperature of the plasma is maintained against losses (due to heat conduction and radiative losses for example) by the products of the fusion reactions. A plot of the triple product as a function of temperature for three of the most accessible fusion reactions is shown in figure 1.5.

D-T fusion ($D + T \rightarrow He + n + 17.6\text{MeV}$) is the most accessible reaction with a minimum triple product of $n_e T \tau_E \geq 10^{21}\text{keV s/m}^3$. While these conditions have been achieved separately by different experiments, they are yet to be achieved simultaneously

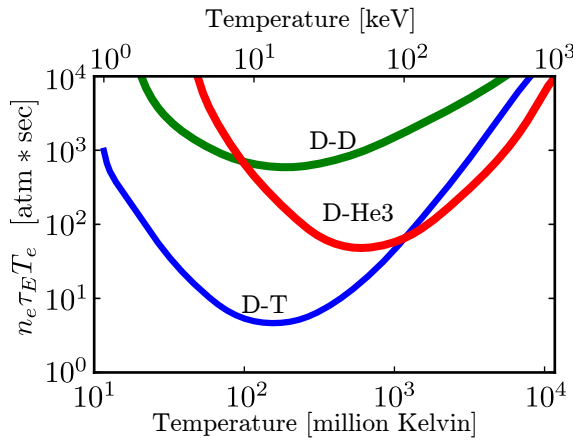


Figure 1.5: The triple product for three different types of fusion reaction as a function of temperature. D-T is clearly the most accessible reaction.

in one machine. The ITER project aims to achieve these conditions and is currently under construction with a first plasma planned for 2020, and the start of D-T experiments in 2027.

1.3 Plasma state and the physics of magnetically confined plasma

At the temperatures required for nuclear fusion, the reactants are in a fully ionised gaseous state known as a plasma. The study of this state of matter is known as plasma physics and an excellent introduction is given in [7] and [8]. Some key details are highlighted in this section.

1.3.1 General description of the plasma state

A plasma is a quasi-neutral gas of charged and neutral particles which exhibits collective behaviour. Collective behaviour refers to particle motions that depend on the plasma state in remote regions as well as local conditions. The key parameters which define a plasma are the Debye length (λ_D), number of particles in a Debye sphere (N_D), and plasma

frequency (ω_p) which are defined as follows:

$$\lambda_D = \sqrt{\frac{\epsilon_0 T_e}{n_e e^2}}, \quad (1.1)$$

$$N_D = \frac{4\pi}{3} n \lambda_D^3, \quad (1.2)$$

$$\omega_p = \sqrt{\frac{n_e e^2}{\epsilon_0 m_e}}, \quad (1.3)$$

where ϵ_0 , n , T_e , n_e , e , m_e are the vacuum permittivity, particle density, and the electron temperature, density, charge, and mass respectively. Using these parameters, the conditions that describe a plasma can more precisely defined as follows: $\lambda_D/L \ll 1$, $N_D \gg 1$ and $\omega_p \tau \gg 1$, where τ and L are the time and length scales of interest.

A charged particle in a uniform magnetic field follows a helical path with the magnetic field line as the center. This is known as cyclotron motion and is a result of the Lorentz force,

$$\mathbf{F} = q(\mathbf{v} \times \mathbf{B} + \mathbf{E}), \quad (1.4)$$

which shows that the force the particle experiences in a uniform magnetic field and no electric field, is perpendicular to the magnetic field and the velocity of the particle. The frequency and radius of the cyclotron motion are given by $\omega_c = |q\mathbf{B}|/m$ and $r_c = mv_\perp/|q\mathbf{B}|$. While variations in \mathbf{B} and the presence of \mathbf{E} complicate the particle motions, this tendency to follow magnetic field lines forms the basis for magnetic confinement fusion.

1.3.2 Particle, kinetic and fluid models of a plasma

It is possible to consider each of the particles in the plasma separately. Their individual motions will be governed by the Lorentz force,

$$m \frac{d\mathbf{v}}{dt} = q(\mathbf{v} \times \mathbf{B} + \mathbf{E}), \quad (1.5)$$

and the magnetic and electric fields can then be calculated using a summation of the contributions from each of the particles in addition to any externally applied fields. While this is a complete description of the plasma, solving this problem is clearly an impossible task for any realistic number of particles.

An alternative is to represent each of the species with a distribution function which describes the number of particles as a function of their position, velocities, and time:

$f(\mathbf{r}, \mathbf{v}, t)$. A kinetic model can then be developed,

$$\frac{\partial f}{\partial t} + \mathbf{v} \cdot \nabla f + \frac{\mathbf{F}}{m} \cdot \frac{\partial f}{\partial \mathbf{v}} = \left(\frac{\partial f}{\partial t} \right)_c , \quad (1.6)$$

where $(\partial f / \partial t)_c$ is the collision operator which describes changes in f due to particle collisions. Ignoring collisions leads to the Vlasov equation. At this stage, none of the physics that was contained in the particle model has been lost, but solving for f is still an impossible task; however, the kinetic model has the great benefit of allowing f to take certain analytic forms, such as Maxwellian distributions. This allows substantial headway to be made if the required assumptions are satisfied.

An alternative approach is to model the plasma as a conducting fluid where the electrons and ions lose their separate identities. The fluid description is known as magnetohydrodynamics (MHD) and can be derived by taking moments of the kinetic equation. This is the simplest description of the plasma state; however, in realistic geometries, solutions still represent a considerable computational challenge.

1.3.3 MHD

The resistive single fluid MHD equations are:

$$\frac{\partial \rho}{\partial t} + \rho \nabla \cdot \mathbf{v} = 0 , \quad (1.7)$$

$$\rho \frac{d\mathbf{v}}{dt} + \nabla p - \mathbf{J} \times \mathbf{B} = 0 , \quad (1.8)$$

$$\frac{d}{dt} \left(\frac{p}{\rho^\gamma} \right) = 0 , \quad (1.9)$$

$$\mathbf{E} + \mathbf{v} \times \mathbf{B} = \eta \mathbf{J} , \quad (1.10)$$

$$\nabla \times \mathbf{B} = \mu_0 \mathbf{J} , \quad (1.11)$$

$$\nabla \times \mathbf{E} + \frac{\partial \mathbf{B}}{\partial t} = 0 , \quad (1.12)$$

where \mathbf{J} , \mathbf{B} , \mathbf{E} , \mathbf{v} , γ , ρ , p , η are the current density, magnetic field, electric field, fluid velocity, adiabatic index, mass density, pressure, and plasma resistivity respectively and $d/dt = \partial/\partial t + \mathbf{v} \cdot \nabla$ is the convective derivative. This model is applicable when the particle distributions are close to Maxwellian, the length scales of interest are much longer than the Larmor radius, and the time scales of interest are much longer than the ion cyclotron period.

If the magnetic diffusion time over the length scales of interest are longer than the

time scales of interest, we can neglect the plasma resistivity ($\eta = 0$). This results in the ideal MHD model which is the starting point for many equilibrium and stability calculations. While ideal MHD represents one of the simplest models of a plasma, in realistic magnetic confinement geometries, equilibrium and stability calculations are still complex and generally require reasonably large computational resources.

To calculate an ideal MHD equilibrium without flow, we set $\partial/\partial t = 0$ and $\mathbf{v} \rightarrow 0$ leading to the following equations:

$$\nabla p_0 = \mathbf{J} \times \mathbf{B} , \quad (1.13)$$

$$\nabla \times \mathbf{B} = \mu_0 \mathbf{J} , \quad (1.14)$$

$$\nabla \cdot \mathbf{B} = 0 , \quad (1.15)$$

which, in 3D, are solved using an equilibrium code such as VMEC [9].

1.4 MHD waves

By examining the time evolution due to a small displacement perturbation ($\boldsymbol{\xi}(\mathbf{r}, t)$), the stability properties and linear wave physics of an equilibrium can be studied. This allows the plasma quantities to be represented as an equilibrium value and a perturbed quantity, due to the displacement (i.e $\mathbf{B} = \mathbf{B}_0 + \mathbf{B}_1$). Substituting into the ideal-MHD equations and neglecting second order terms leads to the linearized ideal-MHD equations:

$$\frac{\partial \rho_1}{\partial t} = -\mathbf{v}_1 \cdot \nabla \rho_0 - \rho_0 \nabla \cdot \mathbf{v}_1 , \quad (1.16)$$

$$\rho_0 \frac{\partial \mathbf{v}_1}{\partial t} = -\nabla p_1 + \mathbf{J}_0 \times \mathbf{B}_1 + \mathbf{J}_1 \times \mathbf{B}_0 , \quad (1.17)$$

$$\frac{\partial p_1}{\partial t} = -\mathbf{v}_1 \cdot \nabla p_0 - \gamma p_0 \nabla \cdot \mathbf{v}_1 , \quad (1.18)$$

$$\mathbf{E}_1 = -\mathbf{v}_1 \times \mathbf{B}_0 , \quad (1.19)$$

$$\frac{\partial \mathbf{B}_1}{\partial t} = -\nabla \times \mathbf{E}_1 , \quad (1.20)$$

$$\mathbf{J}_1 = \frac{1}{\mu_0} \nabla \times \mathbf{B}_1 . \quad (1.21)$$

Here subscripts of 0 and 1 represent the equilibrium and perturbed quantities respectively.

The perturbed magnetic field, electron density, electron temperature, and pressure can

be represented in terms of the displacement and equilibrium quantities:

$$\mathbf{B}_1 = \nabla \times (\boldsymbol{\xi} \times \mathbf{B}_0) , \quad (1.22)$$

$$n_{1e} = -\boldsymbol{\xi} \cdot \nabla n_{0e} - n_{0e} \nabla \cdot \boldsymbol{\xi} , \quad (1.23)$$

$$T_{1e} = -\boldsymbol{\xi} \cdot \nabla T_{0e} - (\gamma - 1) T_{0e} \nabla \cdot \boldsymbol{\xi} , \quad (1.24)$$

$$p_1 = -\boldsymbol{\xi} \cdot \nabla p_0 - \gamma p_0 \nabla \cdot \boldsymbol{\xi} . \quad (1.25)$$

These relations are important for the comparisons between the theoretical predictions and tomographic reconstructions presented in chapter 6.

The momentum equation can be represented in the following form:

$$\rho_0 \frac{\partial^2 \boldsymbol{\xi}}{\partial t^2} = \mathbf{F}(\boldsymbol{\xi}) , \quad (1.26)$$

where

$$\mathbf{F}(\boldsymbol{\xi}) = \frac{1}{\mu_0} (\nabla \times \mathbf{B}_1) \times \mathbf{B}_0 + \frac{1}{\mu_0} (\nabla \times \mathbf{B}_0) \times \mathbf{B}_1 + \nabla (\boldsymbol{\xi} \cdot \nabla p_0 + \gamma p_0 \nabla \cdot \boldsymbol{\xi}) . \quad (1.27)$$

Solutions to this equation that have the following form:

$$\boldsymbol{\xi}(\mathbf{r}, t) = \boldsymbol{\xi}(\mathbf{r}) \exp(-i\omega t) \quad (1.28)$$

are known as the normal modes of the system and can be found by solving the following eigenvalue problem:

$$-\omega^2 \rho_0 \boldsymbol{\xi} = \mathbf{F}(\boldsymbol{\xi}) . \quad (1.29)$$

1.4.1 Sound, torsional Alfvén, and compressional Alfvén waves

In the case of an infinite uniform plasma, there are three solution branches to equation 1.29. These waves are described in more detail below.

Waves that propagate parallel to the magnetic field and whose displacement is parallel to the magnetic field (longitudinal waves) are known as sound waves and are analogous to sound waves in a neutral gas. The dispersion relation for this type of wave is:

$$\omega = v_s k_{||} , \quad (1.30)$$

where $k_{||}$ is the wave vector parallel to the magnetic field and v_s is the sound speed which

depends on the pressure and density:

$$v_s = \sqrt{\gamma p_0 / \rho_0} . \quad (1.31)$$

The thermal pressure provides the restoring force for this wave.

The solution branch for waves propagating parallel to the magnetic field with a displacement perpendicular to the magnetic field describes (transverse wave) are known as shear or torsional Alfvén waves. The dispersion relation for the shear Alfvén wave is given as follows,

$$\omega = v_A k_{||} , \quad (1.32)$$

where v_A is the Alfvén velocity:

$$v_A = \sqrt{\frac{|\mathbf{B}_0|^2}{\mu_0 \rho_0}} . \quad (1.33)$$

This type of wave is similar to waves on a string with a restoring force due to the effective tension of the magnetic field lines.

The third solution branch describes waves propagating in any direction relative to the magnetic field. These are known as compressional Alfvén waves and have the following dispersion relation:

$$\omega^2 = k^2(v_s^2 + v_A^2) , \quad (1.34)$$

where v_s and v_A are the sound and Alfvén speeds given in equations 1.31 and 1.33 respectively. The restoring force is provided by compression of the magnetic field and plasma, which is why this wave is often referred to as the magnetosonic wave.

In more realistic geometry, significant coupling may occur between the various branches, leading to a substantially more complicated set of normal modes.

1.4.2 Alfvén waves in a torus

In the limit of a large aspect ratio torus, the periodicity constraints in the toroidal and poloidal directions give rise to toroidal (n) and poloidal (m) mode numbers. In this case, $k_{||}$ is given as follows,

$$k_{||} = \mathbf{k} \cdot \hat{\mathbf{B}} = \frac{|n - \ell m|}{R} . \quad (1.35)$$

The rotational transform is defined as follows,

$$\ell = \frac{\iota}{2\pi} = \frac{1}{2\pi} \frac{d\psi_p}{d\psi_t} , \quad (1.36)$$

where ψ_p and ψ_t are the poloidal and toroidal flux within a specific flux surface. The rotational transform can be thought of as the number of poloidal rotations a field line undergoes for each toroidal rotation. Rational flux surfaces occur when a field line closes on itself after a fixed number of toroidal rotations and can be identified by rational values of τ .

If the rotational transform and/or mass density vary with flux surface, the frequency of the shear Alfvén wave also varies, giving rise to the shear Alfvén continuum,

$$\omega_A = \frac{B|n - tm|}{R\sqrt{\mu_0 \sum n_i m_i}} . \quad (1.37)$$

It is difficult to excite instabilities that are part of the Alfvén continuum because waves at different radii have different velocities, causing phase mixing. This process contributes to continuum damping and scales with the radial gradient of the phase velocity ($\gamma \propto d/dr(k_{||}v_A)$) [10]. Normally, energetic particles cannot deliver enough drive to overcome this damping.

As detailed in [10], gaps can exist in the continuum because of extrema, or due to the destructive interference between counter propagating waves reflecting off periodic modulations. Counter propagating waves with different mode numbers can have the same continuum frequency at the same radius in a cylinder. In a torus, periodic modulations occur because of variations in the Alfvén speed due to the different magnetic field strength along field lines. These modulations cause a gap to be formed at the frequency crossing, with the size of the gap depending on the variation in the field strength. Within these gaps, modes with significant radial extent can exist that are free from continuum damping. Extremum type gap modes will have a single dominant toroidal and poloidal mode number, while gaps that exist due to counter propagating waves will have two dominant sets of mode numbers, one for each of the counter propagating waves. Table 1.2 lists several different types of gap mode.

Improved understanding of these gap modes is critical because they can be driven to large amplitude by energetic particles from neutral beam injection (NBI), ion cyclotron resonance heating (ICRH), or fusion born alpha particles. These gap modes interact with energetic particles because the Alfvén velocity is similar to the speed of the energetic particles in typical magnetic confinement experiments. The interaction between these waves and the high energy particles can lead to several adverse effects such as damage to the vacuum vessel and significant reduction to the self-heating efficiency, which may prevent

Table 1.2: Various Alfvén gap modes and their cause. Extremum type modes are underlined. Table is reproduced from [10], see the references therein for more information.

Acronym	Name	Cause
RSAE	Reversed Shear Alfvén eigenmode	q_{min}
BAE	Beta Alfvén eigenmode	<u>Compressibility</u>
GAE	Global Alfvén eigenmode	<u>Generic term</u>
TAE	Toroidal Alfvén eigenmode	m and $m + 1$
EAE	Elliptical Alfvén eigenmode	m and $m + 2$
NAE	Noncircular Alfvén eigenmode	m and $m + 3$ (or higher)
MAE	Mirror Alfvén eigenmode	n and $n + 1$
HAE	Helical Alfvén eigenmode	n and m combinations

future machines from reaching ignition [11, 12, 13]. Additionally, improved understanding of these waves is used in the field of MHD spectroscopy to diagnose underlying plasma parameters [14, 15].

In chapter 6, the 3D compressible ideal spectrum on H-1NF is calculated using the continuous spectrum code CONTI [16] and the linear eigenmode solver, CAS3D [17, 18].

1.5 Magnetic confinement devices: stellarators and tokamaks

The simplest type of magnetic confinement device is a solenoid; however, such a device suffers from large losses at the ends of the cylinder. This can be reduced using a magnetic mirror; however, the losses are still large. Another approach is to bend the cylinder into a torus, which removes losses from the ends but suffers from poor confinement due to $\nabla|\mathbf{B}|$ drifts. To counter the $\nabla|\mathbf{B}|$ drift, a poloidal component to the magnetic field is required, causing magnetic field lines to twist around nested toroidal flux surfaces. This field can be generated using a large toroidal plasma current, or using specially shaped external field coils, leading to the two most investigated magnetic confinement devices: the tokamak and stellarator.

On a tokamak, the external field coils are planar and the plasma is approximately axisymmetric (2D). This has significant advantages for the construction of these devices as well as the analysis of their plasmas. However, requiring a large toroidal current means that tokamaks are subject to current-driven instabilities and disruptions, as well suffering from difficulties with steady state operation. Stellarators, on the other hand, can operate in a steady state and are free from current-driven instabilities and disruptions because the

external field coils generate the required poloidal magnetic field. However, this leads to fully 3D components, which complicates the design and construction of these machines as well as the analysis of their plasmas.

While some aspects of the performance of tokamaks are currently better than stellarators, the advantages offered by the stellarator in terms of stability and steady state operation means that the generation of devices following ITER may be stellarators. The barriers to optimising the design, construction, and analysis of stellarators continue to be lowered due to advances in computation and manufacturing technologies. When designing a stellarator, the significant number of free parameters allows for a high degree of optimisation compared with tokamaks and leads to several different types of stellarator including the torsatron, heliotron, heliac, and helias.

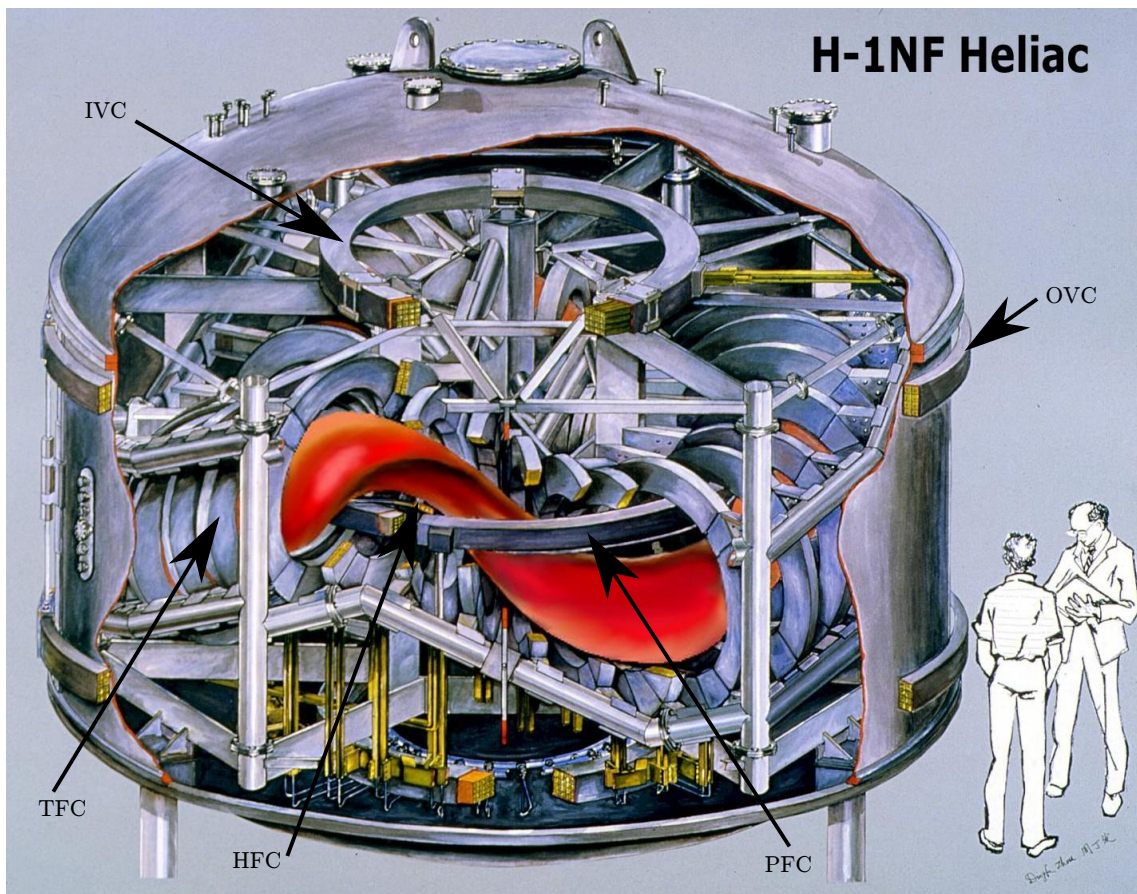


Figure 1.6: A 3D drawing of H-1NF showing the coil-in-tank design and several of the field coils.

Table 1.3: Typical H-1NF ICRH operating parameters.

Parameter	Value
Major radius	1.0m
Minor radius	0.1-0.2m
Magnetic Field	< 1T
Rotational transform	$1 < \tau < 2$
Central electron density	$1 - 4 \times 10^{18} \text{ m}^{-3}$
T_e	$\sim 30 \text{ eV}$
β	0.01 - 0.1 %
Heating	ICRH, 4-20MHz, 2x200kW
Gas	H/He, Ar

1.6 The H-1NF flexible heliac

The first machine that is considered in this thesis is H-1NF: a three period helical axis stellarator (heliac) at the Australian National University whose construction was completed in 1992. It was the first large heliac and is a coil in tank design with 36 toroidal field coils (TFCs), two inner vertical coils (IVCs), one poloidal field coil (PFC), a helical field coil (HFC), and two outer vertical coils (OVCs), as shown in figure 1.6 and 1.7. Typical machine and operating parameters are shown in table 1.3.

The ICRH heating system on H-1NF consists of a pair of phased unshielded antennas that conform approximately to the plasma shape as shown in figure 1.8. While the longer antenna straps are in a single poloidal plane, they are neither parallel or perpendicular to the field lines due to the rotational transform of the magnetic field.

Varying the current in the HFC allows a range of rotational transform profiles to be accessed with great accuracy, making H-1NF well-suited to explore the relationship between plasma behaviour and magnetic configuration [19]. The operating parameter κ_H is the ratio of the currents in the HFC to the TFCs. The variation in the rotational transform profile with κ_H is shown in figure 1.9 (b). The changes in τ significantly impact the types and frequency of fluctuations that are observed with magnetic probes in RF heated H/He plasmas as shown in figure 1.9 (a).

This behaviour has been observed previously with two poloidal Mirnov arrays and analysed using datamining techniques [20, 21]. Analysis using the poloidal arrays is difficult due to the lack of toroidal mode number information caused by toroidal under sampling and substantial variation in the distance from the array to the plasma. The probes which are furthest away from the plasma have a very poor signal to noise ratio, provide a less localised measurement, and the additional distance to the plasma increases the uncertainty

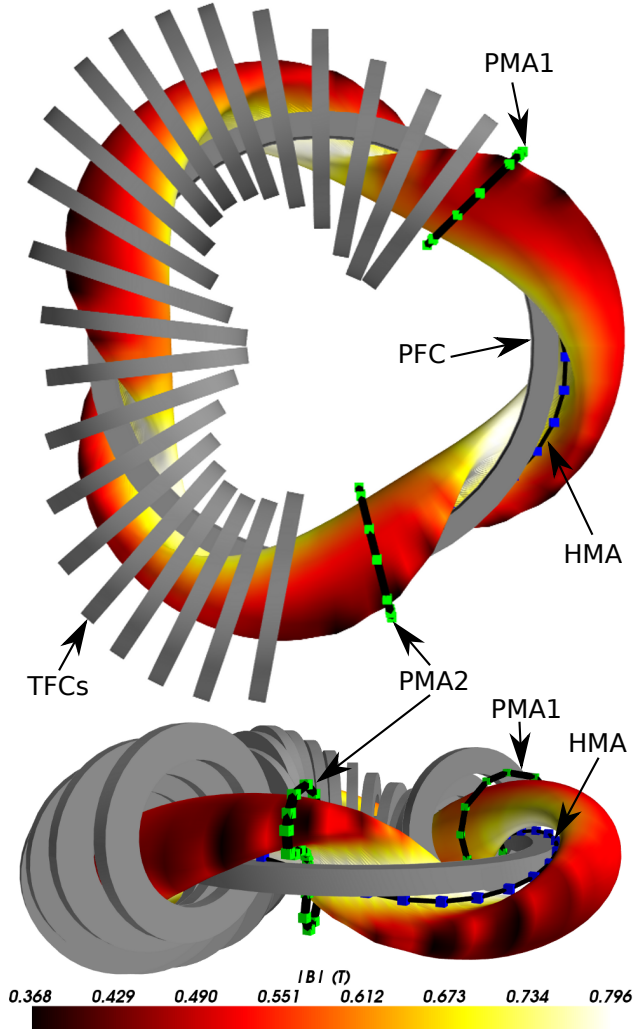


Figure 1.7: An overview of the H-1NF heliac showing a subset of the equilibrium magnetic field coils including the poloidal field coil (PFC) and toroidal field coils (TFCs). The location of the two existing poloidal Mirnov arrays (PMA1 and PMA2) are marked with green cubes, and the helical Mirnov Array (HMA) is marked with blue cubes. The last closed flux surface for a particular H-1NF configuration is shown, with the surface color representing the magnitude of the equilibrium magnetic field.

in the probes' magnetic coordinates. Significant headway was made in the theoretical modelling of this mode activity [23, 24], resulting in the tentative conclusion that these modes may be beta-induced Alfvén eigenmodes.

These uncertainties motivated part of the work presented in this thesis, including the design and installation of new diagnostics (chapter 2: helical Mirnov array, chapter 3: synchronous imaging), the development of advanced analysis techniques (chapter 4: datamining, chapter 5: tomography), and an extension of the theoretical work along with a significant theory-experiment comparison (chapter 6).

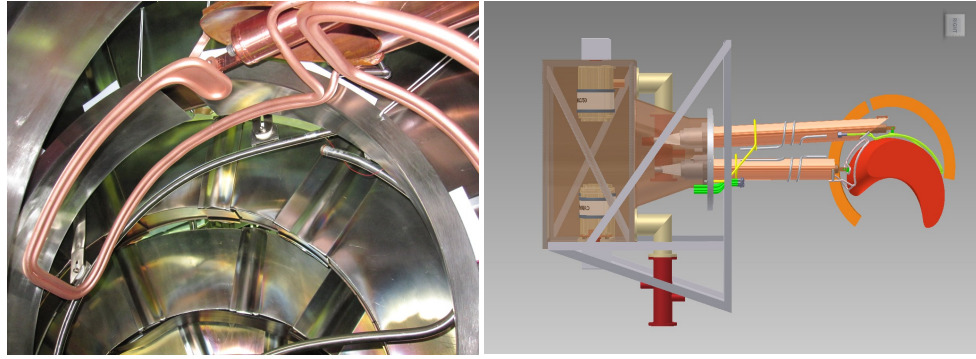


Figure 1.8: The H-1NF ICRH antenna as installed (left) and including feedthroughs and matching box (right).

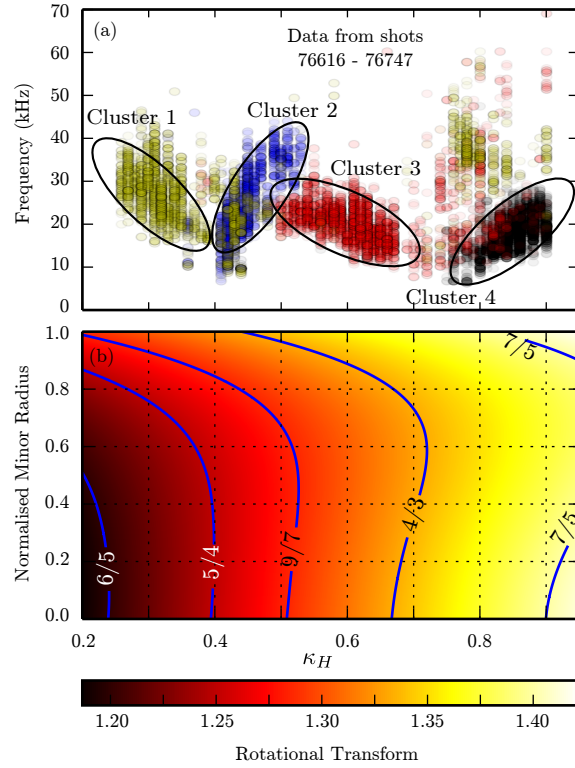


Figure 1.9: (a) Mode activity on H-1NF observed with the magnetic probe array described in chapter 2 and analysed using the datamining technique described in chapter 4. These modes were originally described in [20, 21, 22]. The installation of the new array has provided substantially more information to improve the understanding of these modes. (b) Variation of the rotational transform as a function of κ_H , showing a strong relationship with the type of modes observed.

1.7 The DIII-D tokamak

The second machine that is considered in this thesis is the DIII-D tokamak, which is one-quarter the scale of ITER and is based at General Atomics in San Diego, CA. The key

Table 1.4: Typical DIII-D operating parameters.

Parameter	DIII-D value
Major Radius	1.66m
Minor Radius	0.67m
Magnetic field	2.2T
Plasma current	5MA
Pulse length	10s
Heating Power (NBI)	10MW
Ion temperature	$\sim 5\text{keV}$
Electron temperature	$\sim 5\text{keV}$
Density	$\sim 5 \times 10^{19}\text{m}^{-3}$

parameters of this machine are shown in table 1.4 and a 3D drawing and cross section are displayed in figure 1.10. The combination of advanced diagnostics and the ability to reach ITER relevant conditions means that DIII-D is at the forefront of nuclear fusion research.

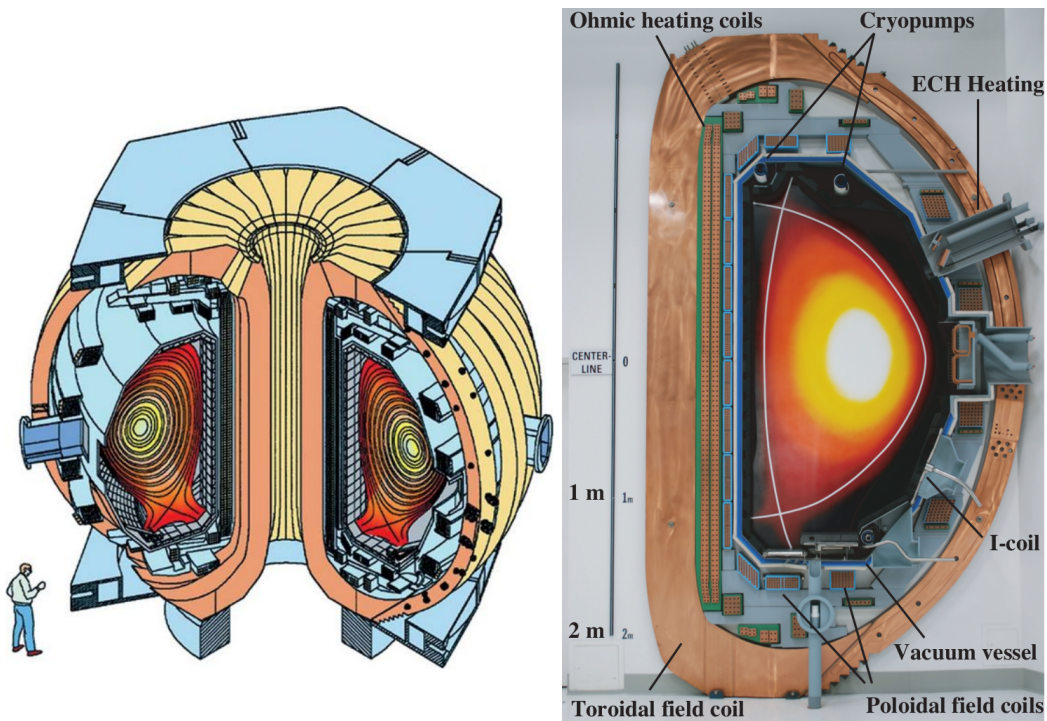


Figure 1.10: A 3D drawing of the DIII-D tokamak and a poloidal cross section showing the field coils and several other aspects of the machine.

While a tokamak is ideally a 2D machine, there are unavoidable departures from symmetry due the finite number of toroidal field coils, manufacturing tolerances, and current supplying structures such as busbars. Historically, great effort was invested to minimise the departures from symmetry using various error field correction coils which can apply

non-axisymmetric perturbations that cancel the existing asymmetry.

Recently, the controlled application of non-axisymmetric fields has been found to be extremely useful for the suppression of type-I edge localised modes (ELMs). This topic is of considerable importance for future experiments such as ITER, as well as future nuclear fusion power plants, because the anticipated heat loads will severely limit the lifetime of plasma facing components.

Non axisymmetric magnetic perturbation (MP) coils have been used to suppress [25, 26, 27, 28, 29, 30], mitigate [31, 32, 33], pace [34], and destabilise [35] ELMs. The underlying mechanism for this behaviour is an active area of research, with one current working hypothesis suggesting that the MP forms a stochastic layer which enhances radial transport, limiting the expansion of the pedestal width and height, and consequently stabilising the ballooning part of the peeling-balloonning type-I ELM [36]. MPs have also been used to control resistive wall modes [37, 38] and neoclassical tearing modes [39], perform magnetic spectroscopy [40, 41], and correct error fields [42, 43]. This motivated the thorough studies of the plasma response dependence on MP coil and plasma parameters presented in chapters 7 and 8.

1.7.1 3D magnetic perturbation coils on DIII-D

Two separate coil sets on DIII-D can apply non-axisymmetric magnetic perturbations: the C-coils and I-coils. This work focuses on the I-coils, which are a set of six coils above and six coils below the midplane, that were installed in 2003. Each coil has an area of approximately 1m^2 and occupies a toroidal extent of $\sim 60^\circ$ as shown in figure 1.11. They are located between the vacuum vessel and plasma-facing carbon tiles, allowing a good degree of coupling to the plasma.

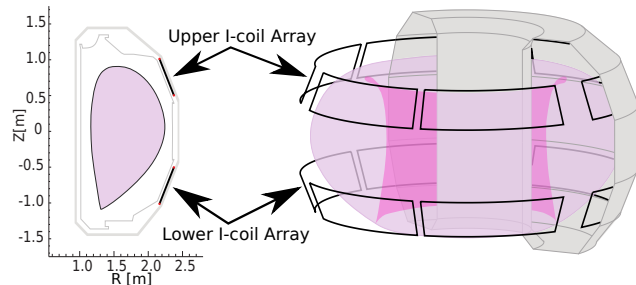


Figure 1.11: 3D cutaway view showing the radial location of the I-coils with respect to the DIII-D vacuum vessel. Poloidal cross section shows the location of the I-coils above and below the mid-plane.

Table 1.5: Various parameters for the I-coil power supplies.

Power supply	Current limit (kA)	Frequency limit (kHz)	Latency (μ s)
Coil PS	6.3-6.5	0.025	\sim ms
SPA	4.5	2	300
A. Amp.	1.5	20-100	9

The I-coils can apply magnetic fields with frequencies up to \sim 300Hz, which is limited by shielding due to induced eddy currents in the vacuum vessel. The current in the coils is limited to 7kA due to a combination of cabling, thermal loads, resonances, and mechanical forces on the coil support structure. The current in the coils is driven by coil power supplies, switched power amplifiers (SPAs), and high bandwidth audio amplifiers which offer various trade-offs between latency and current limit, leading to different supplies being preferred for different applications. The specifications for these power supplies is given in table 1.5.

The six separate toroidal coil locations allow magnetic fields with dominant toroidal mode numbers $n = 1, 2,$ and 3 to be applied to the plasma. Additionally, by varying the phase difference between the currents in the upper and lower I-coil arrays ($\Delta\phi$), it is possible to significantly alter the poloidal spectrum of the applied field. This degree of flexibility has motivated the extensive studies of the dependence of the plasma response to the 3D structure of the applied field, which are presented in chapters 7 and 8. A comprehensive set of radial and poloidal magnetic probe arrays measure the plasma response to the applied non-axisymmetric fields [44, 45]. An upgrade to these probes is described in appendix B.

1.8 Thesis scope and structure

This thesis is written as a thesis by publication. Refer to the synopsis (pxi–xvii) at the start of this thesis for a detailed description of the connection between the following chapters as well as the general thesis layout. The forewords at the beginning of each chapter provide additional context.

A multichannel magnetic probe system for analysing magnetic fluctuations in helical axis plasmas

The paper in this chapter covers the design, calibration and preliminary analysis of the data from a 48-probe helical Mirnov array (HMA) for the H-1NF heliac. This work was carried out as part of this PhD research in order to provide more information on global modes that appear spontaneously in 0.5T H/He ICRH plasmas on H-1NF. The probes were designed to complement two existing poloidal Mirnov arrays by providing higher frequency response and information on the toroidal and poloidal mode numbers and mode polarisation.

The HMA is a unique Mirnov array that has been designed to deal with the difficulties of the fully 3D geometry of H-1NF. While on essentially 2D machines such as tokamaks, a toroidal array would suffice, such an array is difficult, if not impossible, on many stellarators such as H-1NF. The data from this array is analysed using the clustering techniques presented in chapter 4 and the results of this are compared with theoretical modelling from the CAS3D code in chapter 6. Supplementary information which may be useful for future research is included in appendix E. 80% of the research and 85% of the writing presented in this paper are my own work. The paper is also available from <http://dx.doi.org/10.1063/1.4819250>.



A multichannel magnetic probe system for analysing magnetic fluctuations in helical axis plasmas

S. R. Haskey, B. D. Blackwell, B. Seiwald, M. J. Hole, D. G. Pretty, J. Howard, and J. Wach
Plasma Research Laboratory, Research School of Physical Sciences and Engineering, The Australian National University, Canberra, ACT 0200, Australia

(Received 15 May 2013; accepted 12 August 2013; published online 3 September 2013)

The need to understand the structure of magnetic fluctuations in H-1NF heliac [S. Hamberger *et al.*, *Fusion Technol.* **17**, 123 (1990)] plasmas has motivated the installation of a sixteen former, tri-axis helical magnetic probe Mirnov array (HMA). The new array complements two existing poloidal Mirnov arrays by providing polarisation information, higher frequency response, and improved toroidal resolution. The helical placement is ideal for helical axis plasmas because it positions the array as close as possible to the plasma in regions of varying degrees of favourable curvature in the magnetohydrodynamic sense, but almost constant magnetic angle. This makes phase variation with probe position near linear, greatly simplifying the analysis of the data. Several of the issues involved in the design, installation, data analysis, and calibration of this unique array are presented including probe coil design, frequency response measurements, mode number identification, orientation calculations, and mapping probe coil positions to magnetic coordinates. Details of specially designed digitally programmable pre-amplifiers, which allow gains and filters to be changed as part of the data acquisition initialisation sequence and stored with the probe signals, are also presented. The low shear heliac geometry [R. Jiménez-Gómez *et al.*, *Nucl. Fusion* **51**, 033001 (2011)], flexibility of the H-1NF heliac, and wealth of information provided by the HMA create a unique opportunity for detailed study of Alfvén eigenmodes, which could be a serious issue for future fusion reactors. © 2013 AIP Publishing LLC. [<http://dx.doi.org/10.1063/1.4819250>]

I. INTRODUCTION

Magnetic coil probe arrays (Mirnov arrays) are an integral part of the diagnostic suites installed on stellarators and tokamaks.^{3–6} They are routinely used to determine the frequency, mode numbers, polarisation, and growth rates of plasma perturbations such as shear and compressional Alfvén waves in the kHz to MHz range. This valuable information is also used to infer underlying plasma parameters.^{7,8} Additionally, the raw output of the probes can provide a low latency input to control systems, and supply frequency locking information to other diagnostics.

A single magnetic probe only provides spectral information. To obtain spatial information, such as mode numbers, arrays of probes are used, encoding spatial information in the phase differences between probe signals. In toroidal geometry, separate arrays are often arranged in the toroidal and poloidal directions because these are two natural periodic directions for the decomposition of mode numbers. On helical axis plasmas, a toroidal placement is difficult, and in many cases may be impossible due to access issues. A helical array offers an attractive alternative that provides both toroidal and poloidal mode number information as well as advantages such as minimal and relatively constant distance to the plasma.

The H-1NF heliac^{1,2} is a three field-period helical axis stellarator with major radius $R = 1\text{ m}$ and average minor radius $\langle r \rangle \approx 0.2\text{ m}$. The design of the machine allows access to an extensive range of magnetic configurations, making H-1NF well-suited to explore the relationship between

plasma behaviour and magnetic configuration.⁹ A substantial variety of magnetic fluctuations have been observed with two existing poloidal Mirnov arrays (PMAs) in RF heated H/He plasmas.^{10,11} Analysis using the existing arrays is difficult due to the lack of toroidal mode number information caused by toroidal under sampling and substantial variation in the distance from the array to the plasma. The probes which are further away from the plasma have significantly smaller signals and a very low signal to noise ratio, provide a less localised measurement, and the additional distance to the plasma increases the uncertainty in the probe's magnetic coordinates. These uncertainties motivated the installation of a new helical array to provide additional toroidal and poloidal mode number information, polarisation information, and higher frequency response.

The helical Mirnov array (HMA) consists of 16 tri-axis magnetic probes (48 probe coils), which follow the helical winding of H-1NF through one of its three revolutions. This places the array as close as possible to the plasma in areas where strong probe signals have been experimentally observed. The relatively equal spacing of the probes allows better mode separation using singular value decomposition (SVD) analysis. An overview of H-1NF including the location of the HMA and poloidal Mirnov arrays are shown in Figures 1 and 2. A single tri-axis probe is shown in Figure 3. The array is encased in a thin stainless steel bellows to minimise attenuation, provide vacuum integrity, and minimise vacuum seal breaks for cabling. The frequency response of the probes inside the bellows is maximised around 100 kHz or 400 kHz depending on probe orientation. Pre-amplifiers with digitally

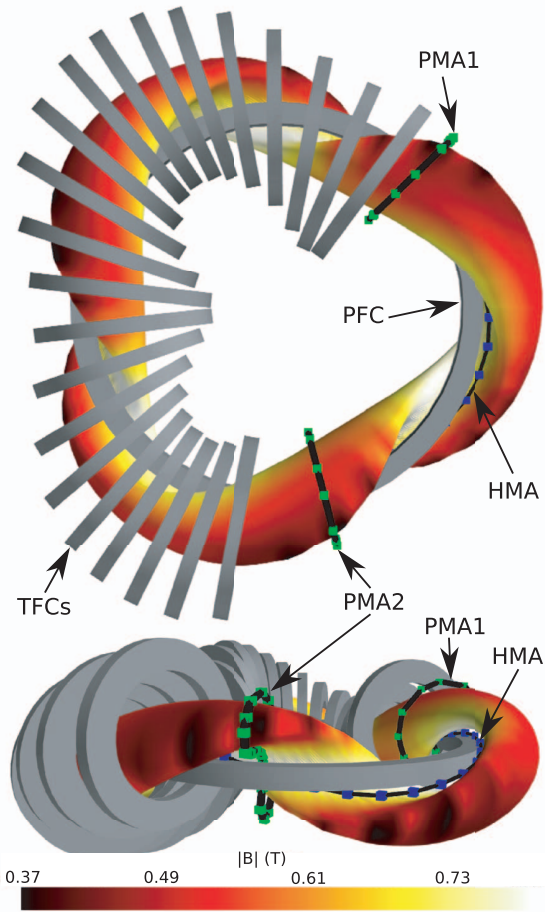


FIG. 1. An overview of the H-1NF heliac showing a subset of the equilibrium magnetic field coils including the poloidal field coil (PFC) and toroidal field coils (TFCs). The locations of the two existing poloidal Mirnov arrays (PMA1 and PMA2) are marked with green cubes, and the helical Mirnov array (HMA) is marked with blue cubes. The last closed flux surface for a particular H-1NF configuration is shown, with the surface color representing the magnitude of the equilibrium magnetic field.

switchable filters and gain allow settings for each shot to be easily modified and stored.

This paper is organised as follows. Section II covers the vacuum considerations, stainless steel bellows housing, probe design, signal amplification, and data acquisition systems. Section III describes the location of the magnetic probes in real space and magnetic coordinates as well as probe orientation calculations. Finally, in Sec. IV, we discuss some of the recent results from the array.

II. ARRAY DESIGN AND SPECIFICATIONS

A. Array housing and vacuum considerations

The H-1NF structure including most magnetic field coils is housed inside a large stainless steel vacuum vessel. Any diagnostic that needs to be placed near the plasma, such as magnetic probes, must be placed inside the vacuum vessel and will be subject to vacuum conditions, imposing considerable constraints on the diagnostic. The decision was made in the early stages of the design to place the array inside a vacuum tight housing allowing the inside of the housing to be at atmos-

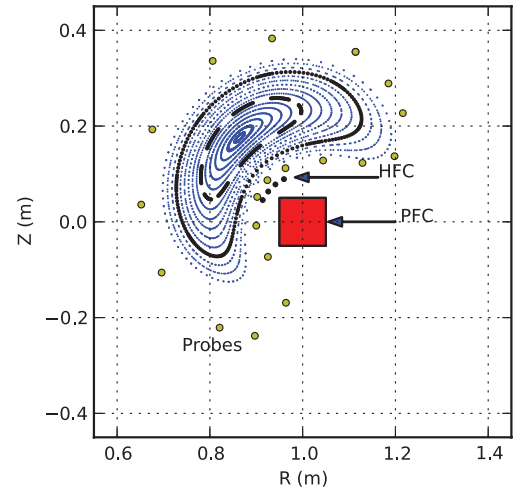


FIG. 2. A Poincaré plot of a poloidal cross-section with the location of the magnetic probes in an existing poloidal array located at a toroidal angle of 44.3°. The locations of the helical field coil conductors (HFC) and poloidal magnetic field coil casing (PFC) are shown along with several flux surfaces for a typical machine configuration. This is for a reversed shear configuration. The closest surfaces to the 4/3 rational surface are marked with black dots. The variable spacing of the probes relative to the plasma causes difficulties in the analysis of the data from this array.

spheric pressure. This has several advantages including protection from the plasma, fewer mounting points to the H-1NF structure, simplified cable routing, one vacuum feed-through for all cabling, and the ability to use non-vacuum compatible materials for the probe coil construction.

A thin (≈ 0.26 mm wall thickness) austenitic stainless steel bellows was chosen for the housing due to its flexibility (must be able to follow a helical path), low magnetic permeability, ability to withstand sputtering by the plasma, good vacuum properties, and low conductance relative to other metallic options. The bellows provides electrostatic shielding as well as some magnetic shielding at higher frequencies. The effect this has on the overall frequency response of the system is discussed in Sec. II B.

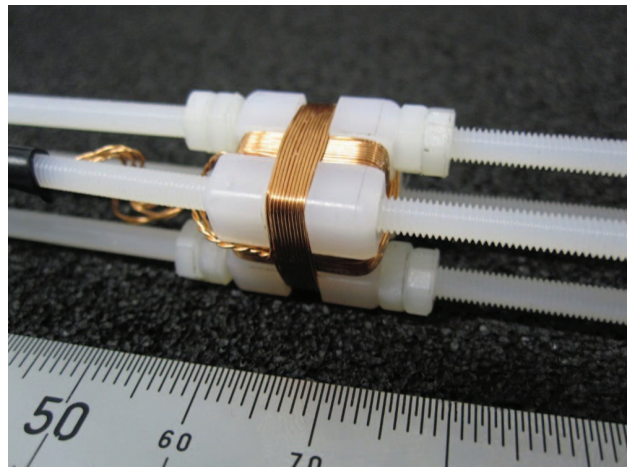


FIG. 3. One of the sixteen tri-axis magnetic probes. The probe coils are wound onto a nylon former. All formers are located on threaded nylon shafts, maintaining their spacing when the array is placed inside the stainless steel bellows housing, shown in Figure 5.



FIG. 4. The last former in the HMA is enclosed inside a copper sputtered borosilicate tube instead of the bellows. This increases the frequency response of the probes, while still providing electrostatic shielding.

Nichrome wire attaches the bellows to mounts, located next to the helical field coil (HFC). Nichrome maximises the resistance of the HMA mounting structure, minimising the effect on the frequency response. At the end of the bellows, a copper sputtered borosilicate tube, shown in Figure 4, houses the final probe in the array. The copper sputtering provides electrostatic shielding, but is thin enough to prevent attenuation of the magnetic field at higher frequencies. Consequently, this probe has a higher frequency response, and can be used to calibrate the effect of the bellows on the response of the other probes. The installed array is shown in Figure 5.

The bellows has an internal diameter of 20.8 mm and an external diameter of 25.8 mm allowing a ≈ 14 mm cube shaped former to fit comfortably inside the bellows. The maximum size probe coil that can be wound onto this former has a square 12 mm \times 12 mm face. Using a cube shaped former centralises the probe coils, and leaves room on the sides of the former to route the twisted pair cables to the other probes.

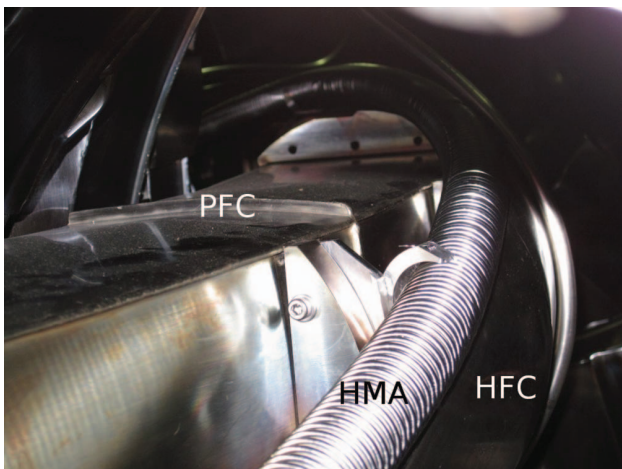


FIG. 5. The installed HMA housed in the stainless steel bellows. The array is attached to the side of the helical magnetic field coil (HFC) causing it to follow a helical path and wrap around the poloidal field coil (PFC).

B. Probe design and frequency response

The magnetic probe formers are made from nylon whose heat resistance is too low for long pulse high temperature machines. H-1NF has short pulses (≈ 100 ms), so the heat load on the formers is low. Two temperature sensors, which monitor the temperature near the formers, have confirmed that the temperatures near the formers remain below 30 °C.

The magnetic probe dimensions are greatly constrained by the bellows housing; however, selecting the number of turns on the probe coils allows us to optimise the frequency response for our application. Ideally, the probes should produce as large an output as possible to minimise the pre-amplification required and have a high frequency response. Unfortunately, these requirements conflict with one another and compromises must be made. Based on observations from the existing PMAs,^{10,11} magnetic fluctuations exist up to 150 kHz. Additionally, theoretical modelling has shown the existence of significant Alfvén continuum gaps in the low hundreds of kHz range^{12,13} suggesting we want the frequency response to be maximum at these frequencies.

As discussed in Ref. 4, the voltage output of a magnetic probe up to its first self resonant frequency can be modelled by $V(\omega) = -j\omega NAB_c(\omega)$. Here, $j^2 = -1$ and N , A , $B_c(\omega)$, and ω represent the number of turns, probe area, magnetic fluctuation amplitude, and frequency of the oscillation, respectively. The probe can be modelled as a RLC circuit where R_c , L_c , and C_c represent probe resistance, self inductance, and stray capacitance, respectively. A transmission line with impedance Z_0 can be included to model the effect of the cabling from the probe to the pre-amplifiers. The voltage across a terminating resistor (R_t) is used as the input to pre-amplifiers or digitisers. A schematic of this lumped circuit element model is shown in Figure 6(a). Impedance matching between the digitiser or pre-amplifier and the transmission line is achieved by setting $R_t = Z_0$. This prevents reflections and allows us to eliminate the transmission line from the model, reducing the circuit to the simple RLC circuit shown in Figure 6(b). This model allows us to easily calculate the self resonant frequency and -3 dB point of the probe once L_c and C_c , and Z_0 are known.

A trade-off exists between high frequency response and probe output at lower frequencies. The cutoff frequency of

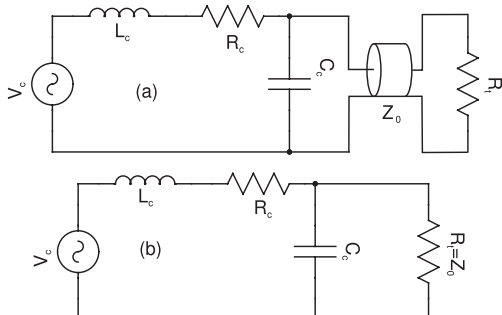


FIG. 6. (a) A lumped circuit element representation of a magnetic probe, transmission line, and terminating resistor. (b) Setting the terminating resistance to match the impedance of the transmission line allows us to model the system using a simpler RLC circuit.

TABLE I. Measured parameters for magnetic probes with 11, 22, and 33 turns representing single, double, and triple layer probes. The -3 dB point assumes termination into 60Ω , matching the impedance of the twisted pair transmission line.

Parameter	11 turns	22 turns	33 turns
R_p ($\text{m}\Omega$)	110	220	340
L_p (μH)	2.8	10	22
C_p (pF)	1.3	17	17
F_r (MHz)	82.0	12.3	8.5
NA (cm^2)	15.8	31.7	47.5
-3 dB (kHz)	3400	960	430

the probe is constrained by the probe inductance which increases with N^2A , while the probe output at lower frequencies increases with NA . Therefore, to maximise the probe output at lower frequencies, while still maintaining as high a cutoff frequency as possible, we want to maximise the area of the probe within the constraints imposed by the internal diameter of the bellows housing. Therefore, we choose a square shaped coil with a side length of 12 mm, which maximises the use of the available area, allows room for routing cables past the probe, and leaves the number of coil turns as a free variable. The choices shown in Table I correspond to single, double, and triple layer windings using AWG30 enamelled copper wire, which was the thinnest wire that could reliably withstand the possible stresses during the installation of the array. The measured probe resistance, self inductance, and stray capacitance of each of these options, along with the calculated -3 dB point and first resonant frequency are shown.

The 22 turn probe was chosen as the best compromise between low frequency probe output (NA) and cutoff frequency. The 11 turn probe provides an unnecessarily high cutoff frequency when the effect of the bellows is taken into account, and the 33 turn probe does not provide a high enough cutoff. The double layer winding offers additional benefits such as having the transmission line leads line up, and cancellation of the off-normal sensitivity due to the slight winding pitch.

The magnetic probes are located roughly 6 m from the pre-amplifiers and are connected using a twisted pair transmission line. The probe coils and transmission line are constructed from a single length of enamelled copper wire. This improves the reliability of the system by eliminating joins, and removes impedance changes that could cause signal reflections. The impedance of the transmission line was measured by time domain reflectometry as 60Ω and the terminating resistor was chosen to match this. Additionally, the length of each transmission line is the same for all probes to minimise the effect of slight impedance mismatches with the terminating resistor.

The ribbed shape of the bellows complicates the attenuation of the magnetic field. The ribs cause an increase in the resistivity per unit length for eddy currents flowing axially along the bellows, and a reduction for currents flowing around the bellows. This decreases (increases) the diffusion time for transverse (axial) magnetic fields, which increases (decreases) the high frequency response relative to a plain cylindrical housing with a similar wall thickness. A

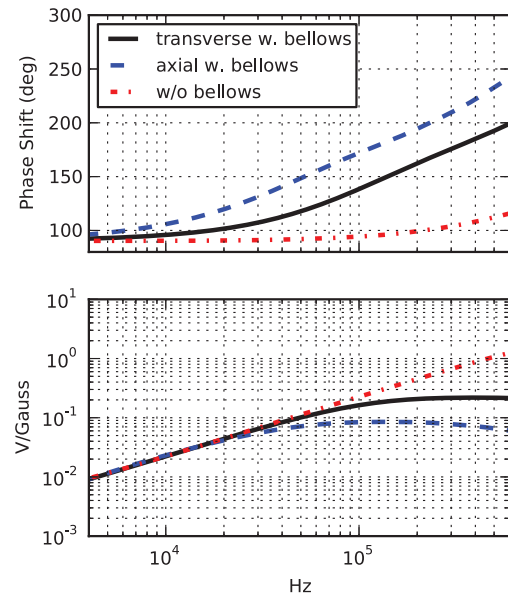


FIG. 7. The measured frequency response of the magnetic probes. The response without the bellows housing is shown—this is valid for the probes in the borosilicate tube. For the rest of the array inside the bellows, the response depends on whether the probe is pointing in the axial or transverse direction.

Helmholtz coil was used to measure the frequency response for the unshielded probe, and the two different orientations inside the bellows. Figure 7 shows the measured frequency response of the magnetic probes. The response of the axially oriented probes is maximised at ≈ 100 kHz, while the transversely oriented probes response is maximised at ≈ 400 kHz.

C. Signal amplification and data acquisition

Custom designed programmable pre-amplifiers with several special features increase the probe output to fully use the dynamic range of the digitisers. The probe output varies considerably depending on the plasma conditions and magnetic configuration.^{9,14} Therefore, it is necessary to have several different gain settings that prevent the pre-amplifiers from clipping, while providing sufficient pre-amplification of the signal for the digitisers. Discrete gain settings of ≈ 125 , 250, 625, and 1250 were chosen based on the analysis of the probe data from the existing magnetic probes and data from prototype pre-amplifiers.

In addition to providing gain, the pre-amplifiers include several passive and active filters to minimise the contribution from several unwanted signals such as high frequency pickup from the 5–8 MHz RF heating system, which is aliased due to the 2 MHz sampling rate, and low frequency field coil power supply switching noise. The impulse switching noise from the magnetic field coil power supplies is very weak as seen in Figure 14 and depends on their current output; however, the frequency is usually 2 or 2.4 kHz, with weaker harmonics at 4 and 6 kHz. There is also some ripple in the magnetic field coil currents. The field coil power supplies have a ripple of ≈ 1 A at 10 Hz, except for the secondary power supply which has a ripple of ≈ 20 A at 30 Hz when supplying the helical winding alone. All active filters and gain settings can be manually or

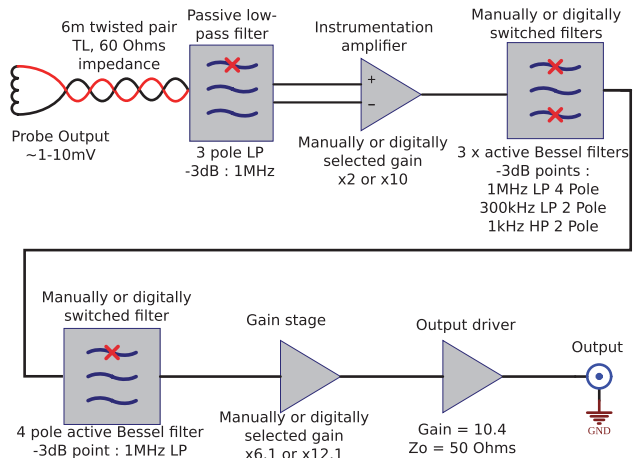


FIG. 8. Block diagram of the pre-amplifiers illustrating the various stages and the overall signal path.

digitally controlled (or bypassed) providing a high degree of flexibility.

The pre-amplifier gain and filter stages are shown in Figure 8. The probe signal passes through a three pole low pass passive filter with a -3 dB point of 1 MHz. This prevents overloading the first stage of the pre-amplifier with pickup from the RF plasma heating. The signal then passes through an instrumentation amplifier (Analog Devices AD8250) providing the first adjustable gain stage ($\times 2$ or $\times 10$), converting the balanced signal to single ended and buffering the signal for the following stages. Following this, the signal passes through two active low pass (LP) and one active high pass (HP) filters, all of which are Bessel filters (for optimal phase response) with -3 dB points of 1 MHz (LP 4 pole), 300 kHz (LP 2 pole), and 1 kHz (HP 2 pole), respectively. The signal then passes through a 4 pole low pass Bessel filter with a 1 MHz -3 dB point before passing through another gain stage (AD8034) with gain selections of $\times 6.1$ or $\times 12.1$ and an output driver stage with a gain of $\times 10.4$ (AD8397). The second 1 MHz low pass filter is included before the major gain stages for situations when the pickup from the RF plasma heating system is exceptionally large. The active filters are implemented using unity gain Sallen-Key designs. A picture of a pre-amplifier is shown in Figure 9(b).

It is possible that certain probes may require different gain and filter settings for the same shot due to their different locations and orientations. Given the large number of probes and the difficulty in manually recording or changing all of the settings for each shot, all pre-amplifier settings are digitally controlled (with the option for manual override). This allows the settings to be chosen before a shot, transmitted to the pre-amplifiers, and recorded with the shot data. All of this happens automatically as part of the H-1NF initialisation and store phases for each shot, and allows the effect of the pre-amplifier settings on the signal to be accounted for in the post shot processing.

Digital switching of the gain and filters is implemented using ADG714 analog switches connected via a buffered serial peripheral interface bus (SPI) interface, run by a microcontroller. The pre-amplifiers are connected to a backplane

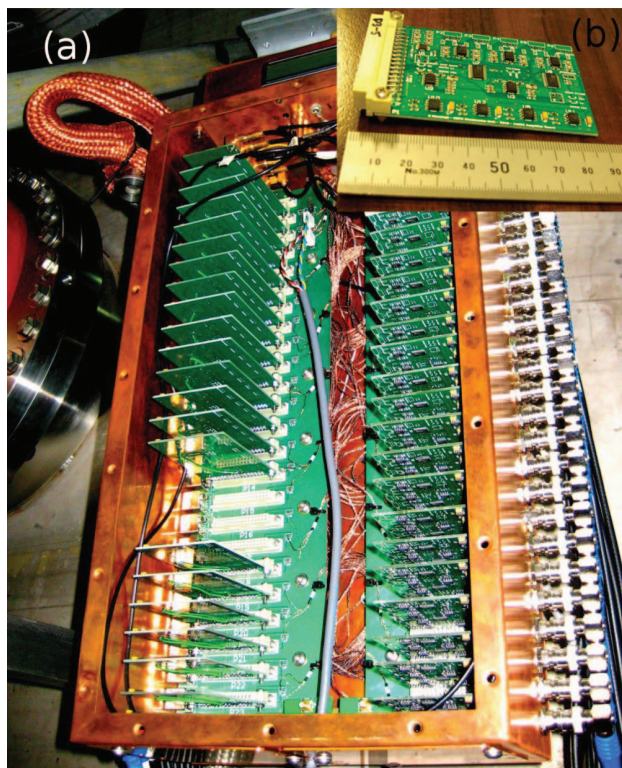


FIG. 9. (a) The 48 pre-amplifiers housed in a copper box, and installed on backplanes to allow communication signals for the digital switching of filters and gains. Three amplifiers have been removed to show the backplane. (b) A single pre-amplifier.

allowing the boards to access the control signals. All pre-amplifiers are placed inside a copper housing, shown in Figure 9(a), to prevent unwanted pickup from a nearby high power RF matching box. The pre-amplifier output is usually digitised at 2 MHz using D-TACQ ACQ132 digitisers with the option to digitise the higher frequency response probes at 16 MHz or 32 MHz. In the higher frequency case, the pre-amplifiers are bypassed and the raw Mirnov signal is acquired. The Mirnov signals are recorded in an MDSplus database¹⁵ along with the pre-amplifier settings. Automatic storage of the pre-amplifier settings simplifies data analysis and eliminates errors that can occur with manual record keeping.

III. ARRAY POSITIONING AND ORIENTATION CALCULATIONS

A. Probe locations in real space and magnetic coordinates

The HMA is placed alongside the helical field coil in H-1NF as shown in Figures 5 and 10, locating the probes as close as possible to the plasma. The variation of the radial position of the probes with toroidal angle, relative to the plasma, is small simplifying the analysis of the signals compared with the PMA (Figure 2). While it is possible to vary the toroidal spacing of the probes to maximise the mode resolving power of the array,⁴ this was not done because there was uncertainty in the final installed location of the probes when the array was manufactured and equal spacing of probes is in general more

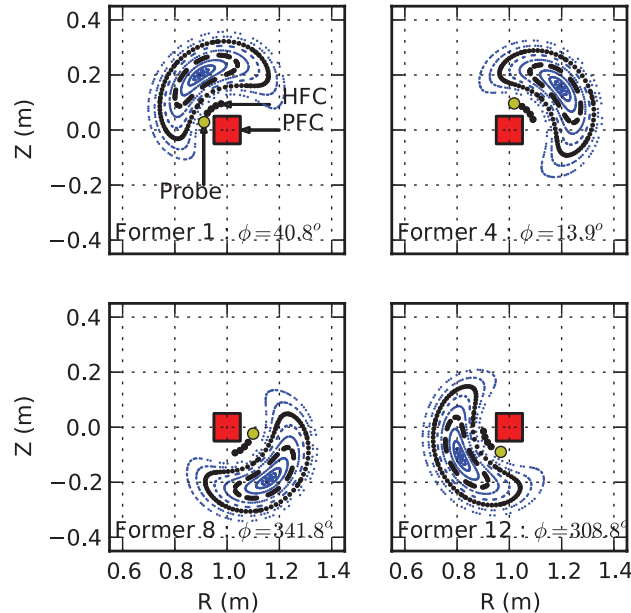


FIG. 10. Poincaré plots of the poloidal cross-sections for a typical H-1NF configuration at the toroidal location (ϕ) of selected probes in the HMA, marked by yellow circles, illustrating their proximity to the plasma. The helical field coil (HFC) and poloidal field coil (PFC) are also shown. This is for a reversed shear configuration. The closest surfaces to the 4/3 rational surface are marked with black dots.

insensitive to probe failure than uneven spacing. The probes have a 15.6 cm spacing along the helical path of the bellows, which is controlled by threaded nylon rods that connect the probes to one another (Figure 3). This causes a slight bunching up (in toroidal angle) of the probes on the outside of the poloidal field coil (PFC), and a stretching on the inside.

When analysing the array outputs to determine mode numbers, the location of the magnetic probes needs to be mapped to a coordinate system where the magnetic field lines follow straight lines. One such coordinate system for the fully three-dimensional plasmas produced in H-1NF is the Boozer coordinate system (s, θ_B, ϕ_B).^{16,17} Here, s is closely related to a radial variable squared, while θ_B and ϕ_B are angle like variables similar to poloidal and toroidal coordinates, respectively. Transformation of the probe coordinates in real space to Boozer coordinates is not simple as Boozer coordinates are not defined at the probe locations since they are outside the last closed flux surface (LCFS). To overcome this problem, we map the real space location of the probes to their nearest point on the LCFS, and transform this location into Boozer coordinates. The mapping of the probes' locations is particularly useful because it allows comparisons with the predicted eigenfunctions from codes such as CAS3D.^{18,19} The VMEC code²⁰ solves the plasma equilibrium, which is used for the coordinate transformation. The BOOZ_XFORM code (part of the STELLOPT package, which includes VMEC) uses this equilibrium to provide the transformation to Boozer coordinates.

The location of the helical and poloidal arrays in Boozer coordinates for a particular magnetic configuration is shown in Figure 11(a). Although not shown for clarity, the location

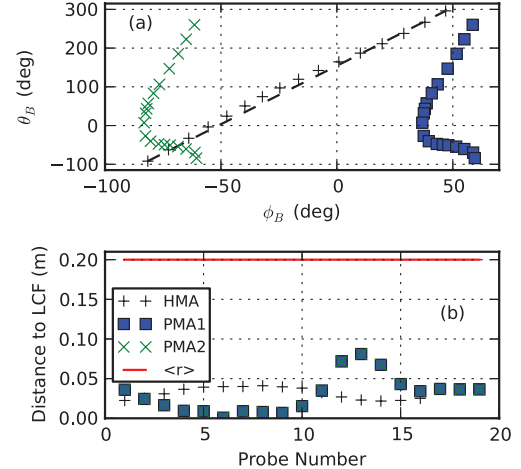


FIG. 11. (a) Probe locations in Boozer coordinates for the two poloidal Mirnov arrays (PMA1, PMA2) and the helical Mirnov array (HMA), based on the closest location on the last closed flux surface for a typical H-1NF magnetic configuration. The probes in the HMA follow an almost straight path (marked by the dashed line) in (θ_B, ϕ_B) space. (b) Distance from the probes to the nearest point on the last closed flux surface. The plasma average minor radius is included for comparison. The distance for the HMA is small and relatively constant along the array, while the distance for the PMAs varies considerably between probes. PMA1 and PMA2 have identical construction and their toroidal location is offset by one field period which is why they overlay.

of the probes varies slightly for different magnetic configurations. This is taken into account when analysing data from different configurations. The HMA follows an almost straight line in (θ_B, ϕ_B) space allowing the array to provide toroidal and poloidal mode number information which is relatively easy to analyse. The almost equal spacing of the probes allows better mode separation using SVD analysis. Figure 11(b) shows how the distance to the nearest point on the LCFS changes along the arrays demonstrating the consistent spacing for the HMA compared with the PMAs. Additionally, Figure 11(a) clearly shows how the HMA provides toroidal information that is missing from the PMAs.

The probe output to a mode that consists of dominantly one component such as a global Alfvén eigenmode²¹ can be described as follows:

$$V_i \propto \cos(n\phi_{B,i} + m\theta_{B,i} - \omega t).$$

Here, n represents the toroidal mode number, m the poloidal mode number, ω is the mode frequency, i an index for the toroidally successive probes, and $\phi_{B,i}$ and $\theta_{B,i}$ are the toroidal and poloidal Boozer angles of the i th probe, respectively. Using this representation, we can simulate the phase difference at the frequency of interest (ω), between toroidally successive probe ($D(n, m, i)$) and the cumulative phase along the array up to the j th probe (C_j) as follows:

$$D(n, m, i) = n(\phi_{B,i} - \phi_{B,i-1}) + m(\theta_{B,i} - \theta_{B,i-1}), \quad (1)$$

$$C_j = \begin{cases} 0 & \text{for } j = 0 \\ \sum_{i=2}^{j+1} D(n, m, i) & \text{for } 1 \leq j \leq n_p - 1 \end{cases}, \quad (2)$$

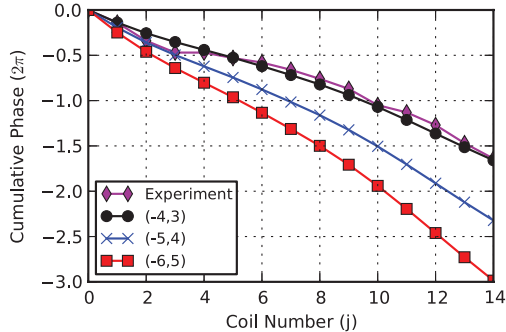


FIG. 12. Simulated cumulative phase, C_j (Eq. (2)), for three different modes in Boozer coordinates. An experimentally obtained mode that is a close fit to ($n = -4, m = 3$) is shown. The spectrogram and time traces for the experimental data are shown in Figures 14 and 15.

where n_p is the number of probes in the array. Figure 12 shows the simulated values of C_j for several mode numbers demonstrating how the HMA can be used to identify mode numbers. The experimentally obtained cumulative phase for a mode that was identified using SVD techniques¹¹ is also shown. A spectrogram and time varying traces from the probes for this particular mode are shown in Figures 14 and 15 in Sec. IV. In this case, the experimental data are a close fit to a ($n = -4, m = 3$) mode.

One of the difficulties of analysing data from the HMA is that certain mode numbers are difficult to differentiate from one another if

$$n_1 + (\Delta\theta_{B,i}/\Delta\phi_{B,i})m_1 = n_2 + (\Delta\theta_{B,i}/\Delta\phi_{B,i})m_2, \quad (3)$$

where $\Delta\theta_{B,i} = (\theta_{B,i} - \theta_{B,i-1})$ and $\Delta\phi_{B,i} = (\phi_{B,i} - \phi_{B,i-1})$. This can be obtained from Eq. (1) by setting $D(n_1, m_1, i) = D(n_2, m_2, i)$. For the HMA, $\Delta\theta_{B,i}/\Delta\phi_{B,i} \approx 3$ for all i , which means that the phase of two modes satisfying $n_1 + 3m_1 = n_2 + 3m_2$ will look similar. The reason they do not look identical is because $\Delta\theta_{B,i}/\Delta\phi_{B,i}$ varies slightly between pickup coils. For example, a ($n = -4, m = 3$) mode will look similar to any other modes where $n + 3m = 5$ such as ($-1, 2$) or ($2, 1$). Therefore, information from the HMA should be supplemented with other information such as data from the PMAs to provide more confidence in the mode numbers. While the HMA provides information about both toroidal and poloidal mode numbers, analysis is more complicated than for separate toroidal and poloidal arrays.

B. Probe orientation calculations

The orientation of the three probes on all 16 formers must be calculated after installation because the formers are free to rotate, within limits, inside the bellows during installation. A dominantly 4 Hz, 50 A current was applied individually to the five magnetic field coil sets (outer vertical coils (OVC), inner vertical coils (IVC), helical coil (HFC), toroidal coils (TFC), and poloidal coil (PFC)) and the probe outputs due to these fields were integrated and recorded. The HELIAC code^{22,23} was used to calculate the applied magnetic field corresponding to each of the probe measurements. Using this information, we calculated the orientation of the probes using

two different methods: the preferred method, which is based on Euler rotations and assumes that the probes are orthogonal, and a second method, which solves for the orientations directly, but does not enforce that the probes are orthogonal to one another. These methods are described and compared below.

We start by defining a matrix, \mathbf{N} , for each tri-axis magnetic probe, describing the orientations of the three probe coils on a tri-axis probe. The directions normal to the faces of the probe coils, $\hat{\mathbf{n}}_1$, $\hat{\mathbf{n}}_2$, and $\hat{\mathbf{n}}_3$, are represented as follows:

$$\mathbf{N} = \begin{bmatrix} \hat{\mathbf{n}}_1 \\ \hat{\mathbf{n}}_2 \\ \hat{\mathbf{n}}_3 \end{bmatrix} = \begin{bmatrix} n_{1,x} & n_{1,y} & n_{1,z} \\ n_{2,x} & n_{2,y} & n_{2,z} \\ n_{3,x} & n_{3,y} & n_{3,z} \end{bmatrix} \begin{bmatrix} \hat{\mathbf{x}} \\ \hat{\mathbf{y}} \\ \hat{\mathbf{z}} \end{bmatrix}, \quad (4)$$

where $\hat{\mathbf{x}}$, $\hat{\mathbf{y}}$, and $\hat{\mathbf{z}}$ represent the standard Cartesian coordinate basis vectors.

The integrated probe output due to the field created by one of the equilibrium field coil sets can be represented in the following matrix, $\mathbf{V} = [V_{p,f}]$. Here p represents one of the three probe coils on a tri-axis probe and f represents the magnetic field coil set responsible for generating the measurement (OVC, PFC, IVC, HFC, or TFC). The applied magnetic field, which generated these measurements, is calculated by HELIAC and can be represented in the following matrix, $\mathbf{B} = [B_{a,f}]$, where a represents the components of the applied field in the $\hat{\mathbf{x}}$, $\hat{\mathbf{y}}$, or $\hat{\mathbf{z}}$ direction. We normalise the measurements and applied field ($\sum_p (V_{p,f})^2 = 1$ and $\sum_a (B_{a,f})^2 = 1$) to remove the effect of the probe and integrator responses.

Representing \mathbf{N} as a rotation matrix, which is constructed using Euler rotations, enforces that the probes on a single former are orthogonal to one another. For any given set of Euler rotations, the predicted probe outputs are given by $\mathbf{Z} = \mathbf{NB}$. A measure of the error between the predicted probe outputs and measured outputs is given by

$$E = \sqrt{\sum_{p,f} ((Z_{p,f} - V_{p,f})^2) / n_f}, \quad (5)$$

where n_f is the number of separate field coils used for the measurements. We can find the Euler rotations, and consequently, \mathbf{N} that minimises E using standard minimisation techniques. This is then chosen as the correct orientation of the probe coils on the tri-axis former. An approximation of the orientation error in the calculation is given by $\arcsin(E)$. This orientation error is shown in Figure 13 for all of the tri-axis formers, demonstrating a maximum rms error of $\approx 6^\circ$.

An alternate and less preferred method in this situation is to remove the assumption of orthogonality and solve for the probe orientations directly. Representing the probe outputs to the various fields, $\mathbf{V} = \mathbf{NB}$, allows us to calculate the probe orientations, $\mathbf{N} = \mathbf{VB}^{-1}$. If we include more than three separate field coil sets in the calculation, the solution can be found using the pseudo inverse of \mathbf{B} . The accuracy of the result can be checked by comparing how close to 90° the angles between $\hat{\mathbf{n}}_1$, $\hat{\mathbf{n}}_2$, and $\hat{\mathbf{n}}_3$ are. These angles (three per tri-axis probe) are shown in Figure 13 for all the tri-axis probes.

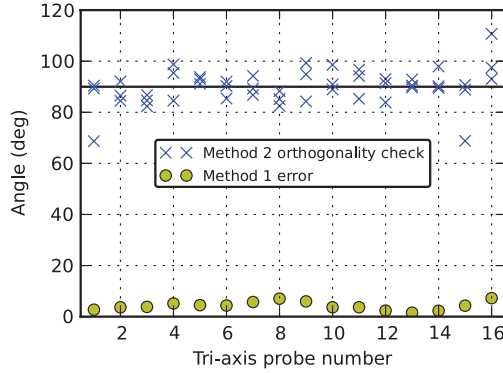


FIG. 13. The orientation error from the Euler rotation method (method 1) is approximated using $\arcsin(E)$ where E is defined in Eq. (5). The angles between \hat{n}_1 , \hat{n}_2 , and \hat{n}_3 on a tri-axis former are used as an orthogonality check for the second method (three possible angles can be calculated for each tri-axis probe).

Both methods produce similar results for many of the probes; however, the first method (Euler rotation method), which enforces the orthogonality of the probes, is preferred, as this is known to be the case to high accuracy and provides additional information for the calculation. This extra information is particularly important if the fields from several field coil sets have similar directions at the probe location, which is the case for probes 1 and 15 in Figure 13. This similarity (or degeneracy) causes the second method to incorrectly imply that the probes on two formers are as far as 20° off normal which is known to be false. However, in situations, where it is possible to apply sufficiently different fields, both methods give the same result, and the second method is substantially faster.

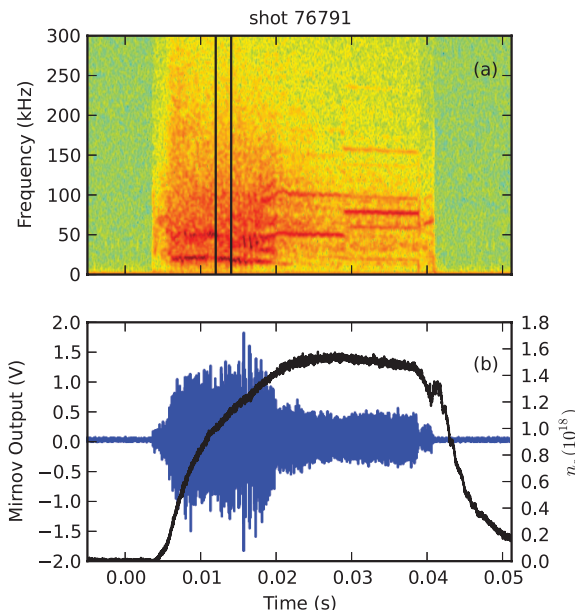


FIG. 14. (a) Spectrogram of one probe output during a shot. Analysis of the ≈ 20 kHz mode between the two vertical bars is shown in Figures 12 and 15. (b) Raw time signal output from the pre-amplifiers (blue) and line averaged electron density trace (black).

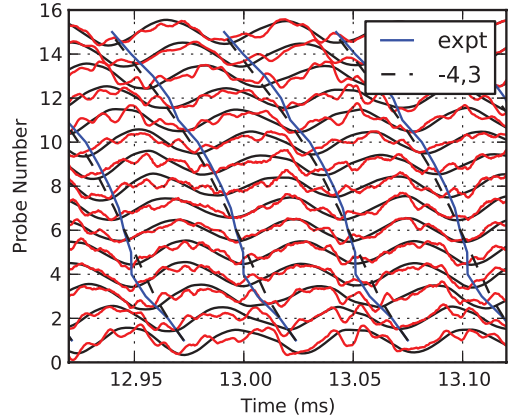


FIG. 15. The raw probe signals for the axially oriented probes are plotted in red. SVD is used to identify the dominant component. Band-pass filtering around the dominant component's frequency creates the black traces. The blue diagonal line marks the same phase in the dominant frequency and clearly illustrates the phase difference in the probe signals at the frequency of interest. Also shown is the expected phase difference for a ($n = -4$, $m = 3$) mode showing a good fit. The cumulative phase across the array for these data is shown in Figure 12.

IV. RESULTS

The initial results from the HMA have been very promising with a large variety of magnetic fluctuations being observed. An example of strong mode activity in the spectrogram from a magnetic probe is shown in Figure 14(a). This particular shot was for a reversed shear magnetic configurations which contains $4/3$ rational surfaces whose location is shown in Figures 2 and 10.

The array has been successful in identifying mode numbers. Analysis of the ≈ 20 kHz signal between the two vertical bars in Figure 14(a) gives the experimentally obtained cumulative phase shown in Figure 12. Comparison with the simulated mode numbers shows that in this case, a ($n = -4$, $m = 3$) mode is clearly the best fit. Previously, using just information from the PMAs, there was a great deal of uncertainty in n . This particular mode was identified using SVD techniques.¹¹ The raw probe signals from this mode are plotted in Figure 15. Also shown in Figure 15 are the probe signals passed through a digital band-pass filter centered on the mode frequency (as obtained from the SVD analysis). The diagonal lines mark the same phase in the signals illustrating the clear phase difference in the signals between probes along the array, which provides spatial information about the mode and confirms the mode numbers.

V. CONCLUSION

Many of the uncertainties in the spatial information of magnetic fluctuations in H-1NF helical axis plasmas have been resolved with the installation of a helical Mirnov array. Figure 1 shows that the array follows the helical winding of H-1NF through one of its three revolutions, placing it as close as possible to the plasma, which results in larger more uniform amplitudes compared with the PMAs. The new array complements two existing poloidal Mirnov arrays by providing polarisation information, higher frequency response, and

093501-9 Haskey *et al.*Rev. Sci. Instrum. **84**, 093501 (2013)

toroidal resolution. The location of the probes in magnetic coordinates is shown to be near linear with almost equal probe spacing. This makes phase variation with probe position approximately linear, greatly simplifying the analysis of the spatial nature of the modes and allowing better mode separation using SVD analysis.

Calibration of the frequency response, orientation, and position of the array in real and magnetic coordinates has been presented. The effect of the thin stainless steel bellows, which surrounds the array, has been measured and reduces the maximum frequency response to ≈ 400 kHz or ≈ 100 kHz depending on the orientation of the probe within the bellows. A single former, placed inside a copper sputtered borosilicate tube, has provided useful signals up to 7 MHz. Two methods for calculating the orientation of the probes using the equilibrium magnetic field coil sets provide complimentary and crosschecking information. Additionally, details of the mapping of the coil locations to magnetic coordinates, based on the nearest location on the last closed flux surface were presented. Pre-amplifiers with digitally switchable filters and gain settings, developed for the HMA, have performed very well under expected conditions. Data analysis confirms that the pre-amplifier settings are controlled reliably for each shot and recorded along with the digitised signals in a MDSplus database, simplifying data analysis and eliminating record keeping errors.

In summary, initial results from the HMA have been very promising, with it performing as designed. The array successfully provides information which is crucial for identifying mode numbers and determining the spatial nature of the observed fluctuations. The higher frequency response, polarisation information, and improved toroidal resolution of the HMA combined with the flexibility of the H-1NF heliac will allow the observed waves dependence on parameters, such as magnetic field geometry, density, and heating power to be explored in great detail.

ACKNOWLEDGMENTS

The authors would like to thank the H-1NF team for continued support of experimental operations. The RSPE Elec-

tronics Unit, and Steven Marshall in particular, contributed a great deal towards the pre-amplifier design and construction. This work was supported by the Education Investment Fund under the Super Science Initiative of the Australian Government. S.R.H. wishes to thank AINSE Ltd. for providing financial assistance to enable this work on H-1NF to be conducted.

- ¹S. Hamberger, B. Blackwell, L. Sharp, and D. Shenton, *Fusion Technol.* **17**, 123 (1990).
- ²R. Jiménez-Gómez, A. Könies, E. Ascasíbar, F. Castejón, T. Estrada, L. Eliseev, A. Melnikov, J. Jiménez, D. Pretty, D. Jiménez-Rey *et al.*, *Nucl. Fusion* **51**, 033001 (2011).
- ³E. Strait, *Rev. Sci. Instrum.* **77**, 023502 (2006).
- ⁴M. Hole, L. Appel, and R. Martin, *Rev. Sci. Instrum.* **80**, 123507 (2009).
- ⁵R. F. Heeter, A. F. Fasoli, S. Ali-Arshad, and J. M. Moret, *Rev. Sci. Instrum.* **71**, 4092 (2000).
- ⁶H. Takahashi, S. Sakakibara, Y. Kubota, and H. Yamada, *Rev. Sci. Instrum.* **72**, 3249 (2001).
- ⁷S. Sharapov, D. Testa, B. Alper, D. Borba, A. Fasoli, N. Hawkes, R. Heeter, M. Mantsinen, M. Von Hellermann *et al.*, *Phys. Lett. A* **289**, 127 (2001).
- ⁸B. Breizman and S. Sharapov, *Plasma Phys. Control. Fusion* **53**, 054001 (2011).
- ⁹J. Harris, M. Shats, B. Blackwell, W. Solomon, D. Pretty, S. Collis, J. Howard, H. Xia, C. Michael, and H. Punzmann, *Nucl. Fusion* **44**, 279 (2004).
- ¹⁰D. Pretty, "A study of MHD activity in the H-1 heliac using data mining techniques," Ph.D. thesis, The Australian National University, 2007.
- ¹¹D. Pretty and B. Blackwell, *Comput. Phys. Commun.* **180**, 1768 (2009).
- ¹²J. Bertram, M. Hole, D. Pretty, B. Blackwell, and R. Dewar, *Plasma Phys. Control. Fusion* **53**, 085023 (2011).
- ¹³J. Bertram, B. Blackwell, and M. Hole, *Plasma Phys. Control. Fusion* **54**, 055009 (2012).
- ¹⁴B. Blackwell, D. Pretty, J. Howard, R. Nazikian, S. Kumar, D. Oliver, D. Byrne, J. Harris, C. Nuhrenberg, M. McGann *et al.*, preprint [arXiv:0902.4728v1](https://arxiv.org/abs/0902.4728v1) (2009).
- ¹⁵T. Fredian and J. Stillerman, *Fusion Eng. Des.* **60**, 229 (2002).
- ¹⁶A. H. Boozer, *Phys. Fluids* **23**, 904 (1980).
- ¹⁷W. D. D'haeseleer, W. N. G. Hitchon, J. D. Callen, and J. L. Shohet, *Flux Coordinates and Magnetic Field Structure: A Guide to a Fundamental Tool of Plasma Structure*, Springer Series in Computational Physics (Springer-Verlag, Berlin, 1991).
- ¹⁸C. Schwab, *Phys. Fluids B* **5**, 3195 (1993).
- ¹⁹C. Nührenberg, *Phys. Plasmas* **6**, 137 (1999).
- ²⁰S. Hirshman and J. Whitson, *Phys. Fluids* **26**, 3553 (1983).
- ²¹W. W. Heidbrink, *Phys. Plasmas* **15**, 055501 (2008).
- ²²A. Ehrhardt, *Algorithms for Real Time Magnetic Field Tracing and Optimization* (Princeton Plasma Physics Laboratory, Princeton, NJ, 1985).
- ²³B. Blackwell, B. McMillan, A. Searle, and H. Gardner, *Comput. Phys. Commun.* **142**, 243 (2001).

Synchronous imaging of coherent plasma fluctuations

The paper in this chapter describes a technique that allows, for the first time, high resolution imaging of high frequency MHD modes in the kHz to MHz range using spectral lines, broadband light, bremsstrahlung, and, with a scintillation plate, soft x-rays. This technique, which was originally pioneered by Professor John Howard was used to acquire a phase-resolved sequence of images of CII 514nm emission for several of the modes that appear spontaneously in 0.5T H/He ICRH plasmas on H-1NF. These modes are described in more detail in chapter 6.

The technique relies on a reference signal from a magnetic probe, such as those described in chapter 2, to generate the phase-locked camera gating signal. The high resolution 2D images that are acquired in this way required the development of a new tomographic inversion technique, which is described in the paper in chapter 5. This combination of imaging and tomographic inversion techniques provides extremely useful radial eigenmode structures which can be compared with theory. This comparison is presented in chapter 6. Supplementary information which may be useful for future research is included in appendix F. 80% of the research and 80% of the writing presented in this paper are my own work. The paper is also available from <http://dx.doi.org/10.1063/1.4868504>.



Synchronous imaging of coherent plasma fluctuations

S. R. Haskey,^{a)} N. Thapar, B. D. Blackwell, and J. Howard
*Plasma Research Laboratory, Research School of Physics and Engineering,
The Australian National University, Canberra, ACT 0200, Australia*

(Received 13 December 2013; accepted 1 March 2014; published online 20 March 2014)

A new method for imaging high frequency plasma fluctuations is described. A phase locked loop and field programmable gate array are used to generate gating triggers for an intensified CCD camera. A reference signal from another diagnostic such as a magnetic probe ensures that the triggers are synchronous with the fluctuation being imaged. The synchronous imaging technique allows effective frame rates exceeding millions per second, good signal to noise through the accumulation of multiple exposures per frame, and produces high resolution images without generating excessive quantities of data. The technique can be used to image modes in the MHz range opening up the possibility of spectrally filtered high resolution imaging of MHD instabilities that produce sufficient light fluctuations. Some examples of projection images of plasma fluctuations on the H-1NF heliac obtained using this approach are presented here. © 2014 AIP Publishing LLC. [<http://dx.doi.org/10.1063/1.4868504>]

I. INTRODUCTION

MHD instabilities such as Alfvén eigenmodes,¹ tearing modes, and sawteeth can limit achievable plasma parameters, and cause detrimental disruptions.^{2,3} The identification and control of these modes relies on accurate measurements of their internal structure, and comparison with modelling. Soft x-ray arrays, and ECE, are often used to provide line of sight measurements which can be tomographically inverted. However, these arrays offer a limited number of line-integrated samples, so *a priori* assumptions are required for useful inversion. Optical CCD cameras have been deployed for imaging and tomography of plasma structures, but frame rates are often limited by plasma light fluxes to around 100 frames per second.^{4,5}

High resolution imaging with fast framing cameras has been used to image the evolution of filament structures during edge localised modes⁶ as well as filaments/blobs near the last closed flux surface.⁷ Additionally, fast 2D imaging of bremsstrahlung emissions from modes with frequencies up to ≈10 kHz has been achieved using a fast framing camera.^{8–11} These approaches require sufficient light emission from the plasma per exposure, generate large amounts of data and are band-limited to resolving fluctuations with period of order twice the exposure time.

The synchronous imaging (SI) technique is quite general and provided enough signal is available, can be used to image mode related fluctuations in bremsstrahlung,⁸ soft x-rays (using a scintillator plate to convert the soft x-rays to visible light¹²), or spectral lines using interference filters. The use of an intensified camera with gated exposure phase-locked to the mode fluctuation period allows imaging of quasi-coherent fluctuations with frequencies from the low kHz to MHz range. This opens up the possibility of directly imaging MHD instabilities that produce sufficient light fluctuations which can have frequencies in the hundreds of kHz, without requiring bright emission from the plasma. The key to the technique is

the generation of camera timing pulses that are phase-locked to the mode. This allows the camera to accumulate enough charge to produce a high fidelity image by accumulating many phase-locked gated exposures. By changing the phase of the clock pulses between frames, the process can be repeated and a phase-resolved set of projection images spanning a full cycle of the mode is generated. With modern CCD's, these images represent millions of lines of sight and can provide sufficient information to obtain a reliable tomographic reconstruction of the fluctuation structure.

The motivation for this work is to better understand the nature of global MHD wave modes observed in the H-1NF heliac.¹³ These fluctuations exhibit a systematic relationship between mode structure and frequency and the magnetic configuration.^{14–17} The ultimate goal of the work is to image the mode-associated perturbations in the emission of various helium atomic transition lines and to use this information, in conjunction with collisional radiative models,^{18,19} to infer the structure of the electron density and temperature perturbations for comparison with theoretical predictions.^{20,21}

This paper is organised as follows. Section II describes the synchronous imaging system, including details of the hardware, system performance, and timing considerations. Section III shows first results of the synchronous imaging on H-1NF using emission from singly charged carbon impurity ions at 514 nm.

II. THE SYNCHRONOUS IMAGING TECHNIQUE

A. Description of hardware

An overview of the SI approach is shown in Figure 1. A low latency signal from another diagnostic provides the reference signal (Figure 1(a)). For magnetohydrodynamic waves, an obvious choice is the signal from one of an array of magnetic pickup coils which are often used to detect and analyse plasma perturbations.²² This signal is amplified and appropriately filtered before providing the reference input to the phase comparator section of an analog PLL (Figure 1(b)). We have

^{a)}shaun.haskey@anu.edu.au

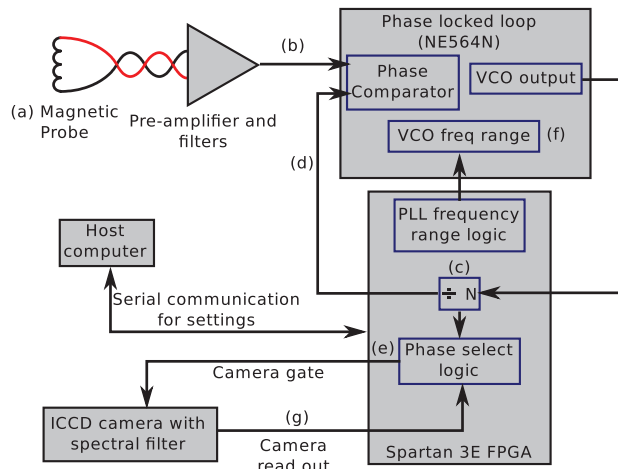


FIG. 1. Overview of the SI system consisting of a magnetic probe which provides the reference signal, a phase locked loop (PLL) for locking to the mode frequency, and field programmable gate array (FPGA) for the logic and generating the intensified CCD (ICCD) gate trigger signals.

used the NE564N PLL which has guaranteed operation up to 50 MHz.

A Xilinx Spartan 3E field programmable gate array (FPGA) generates the ICCD gate triggers and provides the logic to select the relative phase that is being imaged for each camera frame. It does this by acting as a clock divisor for the voltage controlled oscillator (VCO) output of the PLL. The divisor, N , is set to the number of phases to be captured across the fluctuation cycle (Figure 1(c)). For example, if we want 16 frames (an image for every $\pi/8$ radians), then $N = 16$. The VCO clock divided signal is fed back into the phase comparator input of the PLL (Figure 1(d)). This forces the VCO clock output to be upshifted to N times the frequency of the input reference signal, and it will track the changes in the reference signal as the frequency of the mode varies. Using this high frequency clock, the FPGA can output a ICCD gate trigger every N VCO clock cycles. These triggers will occur at the same phase with respect to the reference signal (Figure 1(e)). Changing the initial count changes the phase when the gate trigger occurs with respect to the reference signal allowing the ICCD to be repetitively gated at the phase of choice.

The frequency range that the PLL can lock, and remain locked is determined by a capacitance which the FPGA controls by switching an array of capacitors in and out (Figure 1(f)). This is generally set before a plasma pulse, because the frequency of the mode can be generally anticipated, although the possibility of actively changing the frequency range during a shot exists. The camera read output is provided as an input to the FPGA (Figure 1(g)), so that the phase that is being imaged can be changed after the camera is finished downloading the previous image to a host computer (or local memory). This allows several images at different phases to be acquired in quick succession, limited by the image transfer rate and the plasma pulse duration. A host computer communicates with the FPGA over a serial link ahead of a shot, and uploads the number and sequence of phases to be imaged along with the desired frequency range of the VCO.

B. Performance of the phase locked loop

The performance of the PLL and FPGA is demonstrated in Figure 2. A magnetic probe from the helical Mirnov array on H-1NF²² is used as the reference signal for the PLL. The top plot shows a coherent mode oscillation in the probe signal, while the PLL and FPGA generated ICCD gate triggers derived from this reference signal are over-plotted. The bottom plot shows the phase obtained from the Hilbert transform of the probe signal. The times of the camera gates as marked by the solid dots clearly demonstrate a high mutual coherence.

Typical data for an experimental pulse are shown in Figure 3. Here the FPGA was programmed to step through four different phases during a plasma pulse on H-1NF. The top plot shows the spectrogram of the reference magnetic probe signal. There is a strong coherent mode from 55 ms onwards at a frequency close to 60 kHz. The center plot shows the ICCD gate trigger signals and ICCD readout signals. Commencing at 50 ms, the first frame accumulates 30 exposures. Once the exposures are finished, the camera waits a fixed amount of time to allow the phosphor to decay, and then starts to download the frame to a host computer (signified by the high camera readout signal). The phosphor decay time is due to the intensifier, and its value can vary depending on the phosphor used (for example, P43, P46, and P47 phosphors have decay times of 3 ms, 2 μ s and 0.5 μ s, respectively). As soon as the camera has finished reading out, the FPGA switches to the next programmed phase, and produces the desired camera gate pulse sequence. The process repeats itself for as many different phases and images as required. The bottom plot shows the phase of the probe signal at the camera gate time. The phases of the 2nd, 3rd, and 4th images are clustered at the pre-programmed phases as required. The phases for the first image appear to be random because the mode amplitude is not sufficient to lock the PLL at 50 ms.

Analysis of phase jitter of the ICCD gate triggers for 16 frames obtained during an experimental sequence is

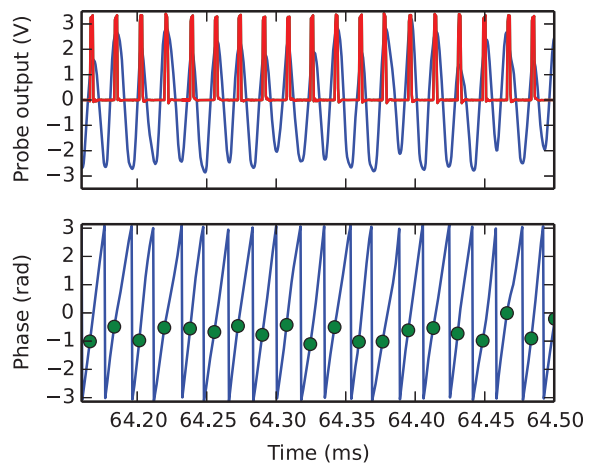


FIG. 2. Performance of the phase locked loop during a single shot. Top: Magnetic probe output and the camera gating trigger signal generated by the FPGA (red pulses). Bottom: Phase of the mode as a function of time calculated using the argument of the Hilbert transform of the probe signal. The dots represent camera gating times, which are all at approximately the same phase showing a good lock to the magnetic probe signal.

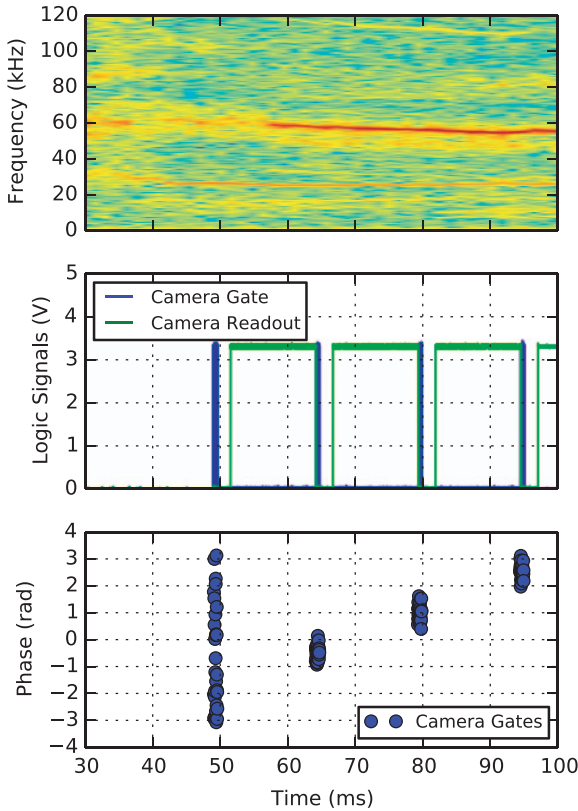


FIG. 3. Top: Spectrogram of the reference magnetic probe signal. Middle: ICCD gate trigger signals (too closely spaced to separate on this scale), and ICCD readout signal. Bottom: Phase of the mode at the ICCD gate trigger times showing consistent phase. The first frame at 50 ms has random phasing because there is no mode to lock to until 55 ms.

presented in Figure 4. The observed mean and standard deviation of the mode phase at the time of the ICCD gating trigger for each frame demonstrates that the system can successfully track the mode phase with small jitter. Simple analysis, by assuming that phase jitter causes an averaging over a portion of a sine wave shows that the phase jitter has a

minimal effect. For example, phase jitter of the order 1 radian peak to peak, like that shown in Figure 4, causes a smoothing that results in a small 5% reduction in the amplitude of the signals. Because the phase is a periodic quantity, the maximum likelihood estimates of the mean and standard deviation are calculated as $\hat{\mu} = \arg(R)$, and, $\hat{\sigma} = \sqrt{-2 \ln(|R|)}$, where $R = \frac{1}{n} \sum_{j=1}^n \exp(i x_j)$, x_j represent the phases, $i = \sqrt{-1}$ and n is the number of gate triggers for the particular phase.^{23,24}

C. Timing considerations

Using this technique it is possible to obtain extremely high effective frame rates. For example, a conventional fast framing camera would need to operate at 16 million fps to image a 1 MHz mode with 16 frames per cycle, generating enormous quantities of data in the process. A camera operating at this speed would require an exceptionally strong light source especially if interference filters are being used to isolate spectral lines. Without strong gain, a plasma fluctuation is highly unlikely to be able to produce sufficient light. The ability to accumulate multiple exposures as in the SI technique allows one to obtain high fidelity images, even in relatively light poor situations.

The main limitation of the technique is the requirement that the coherent oscillation and plasma conditions remain stable over the duration of the imaging sequence, or alternatively, that the mode and plasma conditions are reproducible enough that the phase-resolved sequence can be acquired over multiple discharges. The time required to acquire the data, T , is approximately:

$$T = N^2 t_e + N(t_r + t_d), \quad (1)$$

where N is the number of phases we wish to acquire, t_e is the exposure time required to obtain enough counts, t_r is the readout time for each frame, and t_d is the decay time for the phosphor. It is worth noting that the time required to acquire the data is independent of the mode frequency. Here we choose the gate time to be approximately equal to the wave period divided by the number of frames to be acquired to obtain the phase resolved sequence (3.5 μ s was used for the data shown in Sec. III).

As the gate time increases compared with the mode period, the SI signal level of the mode is reduced. An approximation to the loss of contrast (found by integrating a sine wave over a fixed interval) is given by $1 - \text{sinc}(\tau)$ where τ is the gate time as a proportion of the wave period. Using this approximation, gate times of 1/16, 1/4, and 1/2 of the wave period result in 1%, 10%, and 36% reduction in the mode signal strength, respectively. The minimum available gating time on an ICCD camera such as the Princeton Instruments PiMAX4 is of the order 3ns, so this does not limit the technique.

Calculating the required exposure time (t_e) depends on many variables related to the camera setup, intensifier gain and plasma parameters. We set the exposure time, and number of sequence phases empirically, so that there are sufficient photo-counts to resolve the fluctuation above shot noise while ensuring that the camera does not saturate and that the mode activity remains steady throughout the exposure sequence.

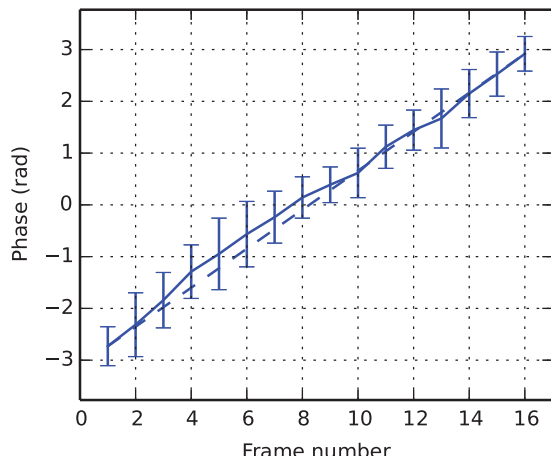


FIG. 4. Performance of the phase locked loop for a 16 frame experimental sequence. The mean phase for each frame is shown along with the standard deviation. The phase shifts between frames is $\pi/8$ as expected for 16 frames. The dashed line is the ideal case with perfect spacing.

For applications on H-1NF imaging 514 nm CII light, t_e was of the order 350 μ s when using a relatively low intensifier gain and 4 \times 4 pixel binning on a 1024 \times 1024 CCD array. This means the first term in Eq. (1) is 90 ms for 16 frames. In many situations this time is sufficiently short for the mode and plasma conditions to remain stable. The second term in Eq. (1) depends on the camera capabilities. The PiMAX 4 camera with P43 phosphor used for the data in this paper has a readout time of 13 ms for 256 \times 256 resolution and a phosphor decay time of 3ms. This gives 256 ms for the second term in Eq. (1) which is significantly larger than the first term. This is evident in Figure 3 where the ICCD readout time is substantially greater than the total gate time. On H-1NF, the discharges are reproducible, \approx 100 ms in length and the time between shots is roughly a minute so separate discharges were used to acquire each of 16 independent phase-locked frames. On longer pulse plasma devices, and provided the light fluxes are sufficiently high, and the structure sufficiently steady, it is feasible to obtain an entire phase-resolved sequence within a single discharge.

III. IMAGING RESULTS FROM H-1NF

The projection images shown here were obtained using a Princeton Instruments PiMAX 4 intensified gated camera. The experimental geometry is illustrated in Figure 5. The camera views the plasma radially in a gap between the toroidal field coils. The lines of sight therefore cover the poloidal cross-section of the H-1NF device and extend over a

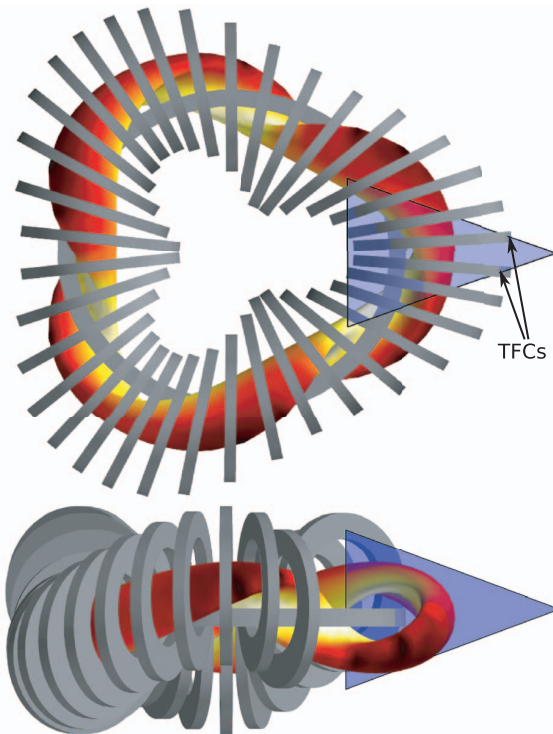


FIG. 5. Details of the camera view. The top plot shows how the toroidal field coils (TFCs) limit the field of view. A typical H-1NF plasma is shown, with the surface colour representing the magnetic field strength.

small range of toroidal angles. The images presented here are obtained in impurity carbon ion emission at 514 nm. Because of the relatively cool electron temperatures in 0.5 T H/He plasmas in H-1NF, this emission emanates from all regions in the plasma, and so is suitable for revealing the structural details of the mode.

For emission line radiation, the brightness is proportional to the product of the electron and impurity ion densities, and, in our case, only weakly dependent on the electron temperature through the collisional excitation rate coefficient. Mode related fluctuations in temperature and density, which are small compared to the background will therefore result in linear changes to the brightness detected by the camera.

The first and fourth frames in a 16 phase sequence for a 15 kHz mode are shown in Figure 6. The discharges are short but very repeatable, so for this data, each frame was obtained using a separate shot, with the image exposure commencing at the same time in each discharge. Also shown is the DC level across all frames, and the difference between the fourth and first frames. To account for shot-to-shot variability, the images are generally normalized for equal integrated photo-electron counts. A white calibration removes systematic variations in the camera response and a black image is used to

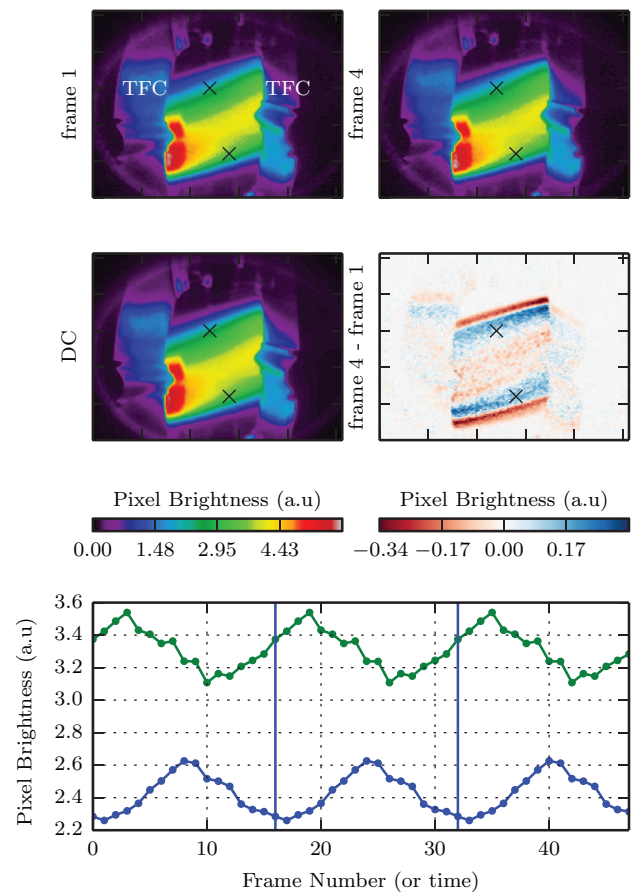


FIG. 6. Top: Frames 1 and 4 from a 16 frame sequence. Middle left: DC component of all 16 frames. Middle right: Difference between frames 1 and 4. Bottom: Evolution of the pixels marked with crosses as a function of frame, or time, showing clear sinusoidal behaviour. The sequence is repeated three times to clearly demonstrate the sinusoidal pattern.

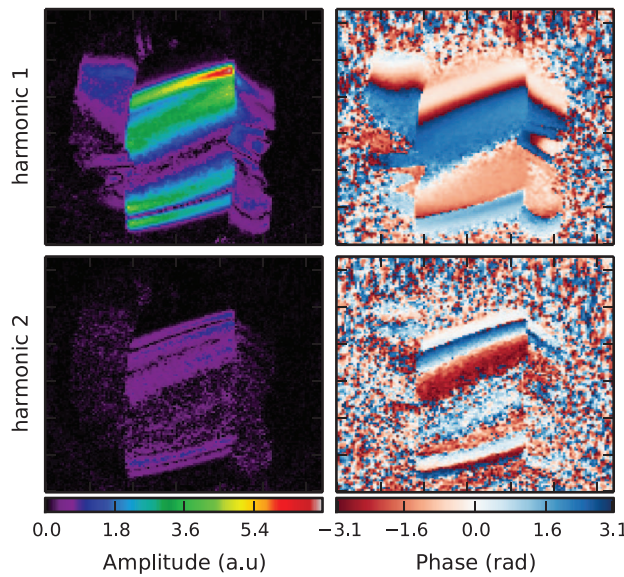


FIG. 7. The amplitude (envelope) and phase of the first two harmonics from the Fourier decomposition of the frames shown in Figure 6.

remove offsets and fixed pattern noise. The intensity variation over a cycle of the pixels marked with crosses is shown in the bottom plot. The 16-frame pattern is repeated three times to make apparent the sinusoidal variation and depth of the first harmonic component intensity modulations.

Figure 7 shows the amplitude (envelope) and phase of the first two harmonics obtained by Fourier processing of the frame sequence shown in Figure 6. Almost all of the power appears in the first harmonic as expected, and the structure of the mode is clear. For this mode, the small amplitude at the center of the projection indicates that this mode has an odd poloidal mode number. This agrees with the toroidal mode number ($n = 4$) and poloidal mode number ($m = -3$) obtained from analysis of the magnetic probe array data. The slightly different structure of the second harmonic image suggests that this is not an artifact or distortion in the image acquisition process.

Projections of another mode which has been identified magnetically as having mode numbers $n = 5$ and $m = -4$ and has a frequency of 20 kHz, are shown in Figure 8. This

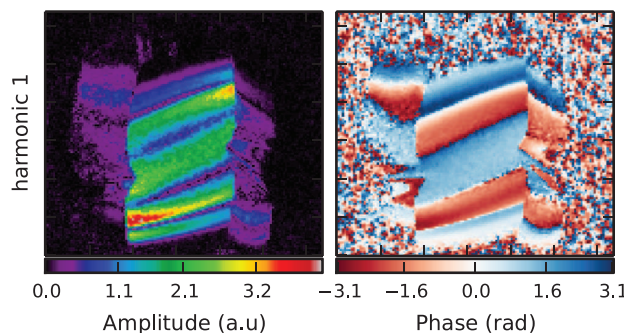


FIG. 8. The amplitude (envelope) and phase of the first harmonic from the Fourier series decomposition of another set of frames from a mode identified as $n = 5$ and $m = -4$ using a magnetic probe array.

mode has a significantly different structure to the one shown in Figure 7. In this case, the amplitude across the middle is an antinode which is expected for a plasma structure having even poloidal mode number.

IV. CONCLUSION

By phase locking to a coherent plasma oscillation and synchronously accumulating photons at a fixed phase in the mode cycle, SI is capable of phase-resolved imaging of coherent plasma instabilities with frequencies in the low kHz to MHz range. With current camera technology, these images represent millions of lines of sight that can facilitate detailed tomographic reconstruction of the mode radial structure. The utility of the technique has been demonstrated by imaging in 514 nm carbon ion impurity light, the MHD eigenmodes that appear spontaneously in 0.5 T H/He discharges on the H-1NF heliac.

ACKNOWLEDGMENTS

The authors would like to thank the H-1NF team for continued support of experimental operations. This work was supported by the Education Investment Fund under the Super Science Initiative of the Australian Government. S.R.H. wishes to thank AINSE Ltd. for providing financial assistance to enable this work on H-1NF to be conducted. J.H. and B.B. acknowledge support from the Australian Research Council Discovery, Grant Nos. DP110104833 and DP0666440, respectively.

- ¹W. W. Heidbrink, *Phys. Plasmas* **15**, 055501 (2008).
- ²K. L. Wong, R. J. Fonck, S. F. Paul, D. R. Roberts, E. D. Fredrickson, R. Nazikian, H. K. Park, M. Bell, N. L. Bretz, R. Budny, S. Cohen, G. W. Hammett, F. C. Jobes, D. M. Meade, S. S. Medley, D. Mueller, Y. Nagayama, D. K. Owens, and E. J. Synakowski, *Phys. Rev. Lett.* **66**, 1874 (1991).
- ³R. B. White, E. Fredrickson, D. Darrow, M. Zarnstorff, R. Wilson, S. Zweber, K. Hill, Y. Chen, and G. Fu, *Phys. Plasmas* **2**, 2871 (1995).
- ⁴J. Howard, *Rev. Sci. Instrum.* **77**, 10F111 (2006).
- ⁵J. Howard, *J. Phys. B: At. Mol. Opt. Phys.* **43**, 144010 (2010).
- ⁶A. Kirk, B. Koch, R. Scannell, H. Wilson, G. Counsell, J. Dowling, A. Herrmann, R. Martin, and M. Walsh, *Phys. Rev. Lett.* **96**, 185001 (2006).
- ⁷Z. Linge, M. Takeuchi, N. Nishino, T. Mizuchi, S. Ohshima, K. Kasajima, M. Sha, K. Mukai, H. Lee, K. Nagasaki *et al.*, *Plasma Sci. Technol.* **15**, 213 (2013).
- ⁸M. Van Zeeland, J. Yu, M. Chu, K. Burrell, R. La Haye, T. Luce, R. Nazikian, W. Solomon, and W. West, *Nucl. Fusion* **48**, 092002 (2008).
- ⁹M. Van Zeeland, J. Yu, N. Brooks, W. Heidbrink, K. Burrell, R. Groebner, A. Hyatt, T. Luce, N. Pablant, W. Solomon *et al.*, *Plasma Phys. Controlled Fusion* **52**, 045006 (2010).
- ¹⁰J. Yu and M. Van Zeeland, *Rev. Sci. Instrum.* **79**, 10F516 (2008).
- ¹¹J. Yu, M. Van Zeeland, M. Chu, V. Izzo, and R. La Haye, *Phys. Plasmas* **16**, 056114 (2009).
- ¹²S. Ohdachi, K. Toi, G. Fuchs, S. von Goeler, and S. Yamamoto, *Rev. Sci. Instrum.* **74**, 2136 (2003).
- ¹³S. Hamberger, B. Blackwell, L. Sharp, and D. Shenton, *Fusion Technol.* **17**, 123 (1990).
- ¹⁴B. Blackwell, D. Pretty, J. Howard, R. Nazikian, S. Kumar, D. Oliver, D. Byrne, J. Harris, C. Nuhrenberg, M. McGann *et al.*, preprint [arXiv:0902.4728](https://arxiv.org/abs/0902.4728) (2009).
- ¹⁵J. Harris, M. Shats, B. Blackwell, W. Solomon, D. Pretty, S. Collis, J. Howard, H. Xia, C. Michael, and H. Punzmann, *Nucl. Fusion* **44**, 279 (2004).
- ¹⁶D. Pretty, "A study of MHD activity in the H-1 heliac using data mining techniques," Ph.D. thesis, The Australian National University, 2007.

- ¹⁷D. Pretty and B. Blackwell, *Comput. Phys. Commun.* **180**, 1768 (2009).
- ¹⁸S. Ma, J. Howard, B. D. Blackwell, and N. Thapar, *Rev. Sci. Instrum.* **83**, 033102 (2012).
- ¹⁹S. Ma, J. Howard, and N. Thapar, *Phys. Plasmas* **18**, 083301 (2011).
- ²⁰J. Bertram, B. Blackwell, and M. Hole, *Plasma Phys. Controlled Fusion* **54**, 055009 (2012).
- ²¹J. Bertram, M. Hole, D. Pretty, B. Blackwell, and R. Dewar, *Plasma Phys. Controlled Fusion* **53**, 085023 (2011).
- ²²S. R. Haskey, B. D. Blackwell, B. Seiwald, M. J. Hole, D. G. Pretty, J. Howard, and J. Wach, *Rev. Sci. Instrum.* **84**, 093501 (2013).
- ²³K. V. Mardia and P. E. Jupp, *Directional Statistics* (Wiley, 2009), Vol. 494.
- ²⁴N. I. Fisher, *Statistical Analysis of Circular Data* (Cambridge University Press, 1995).

Clustering of periodic multichannel timeseries data with application to plasma fluctuations

Arrays of magnetic probes, such as the one described in chapter 2, generate large quantities of multidimensional timeseries data and are among the “always on” diagnostics on major experiments. These large databases of information provide a perfect opportunity for knowledge discovery using machine learning techniques such as clustering. The *phase differences* between magnetic probes in a Mirnov array provide details on mode structure. These phase differences are 2π periodic, causing significant problems with existing clustering techniques. To overcome these difficulties, a new clustering algorithm was developed which is based on mixtures of independent von Mises distributions whose parameters are found using the expectation maximisation algorithm. This new clustering technique is applied to the data obtained from the helical Mirnov array (described in chapter 2) to discover physically interesting information on the variety of modes that exist in H-1NF. Using clustering techniques means that no specific assumptions of the structure are imposed on the phase differences between probes. This is particularly important in stellarators where the complexity of the machine, which is introduced by their 3D structure, means that a simple analytic model of the mode structure can not be found, especially in highly 3D devices. Typical modes from the clusters are imaged and tomographically inverted in chapters 3 and 5, and the identified clusters are examined and compared with theory in chapter 6. Supplementary information which may be useful for future research is included in appendix G. 90% of the research and 85% of the writing presented in this paper are my own work. The paper is also available from <http://dx.doi.org/10.1016/j.cpc.2014.03.008>.



Clustering of periodic multichannel timeseries data with application to plasma fluctuations



S.R. Haskey*, B.D. Blackwell, D.G. Pretty

Plasma Research Laboratory, Research School of Physics and Engineering, The Australian National University, Canberra, ACT 0200, Australia

ARTICLE INFO

Article history:

Received 11 November 2013

Received in revised form

3 March 2014

Accepted 10 March 2014

Available online 17 March 2014

Keywords:

Clustering

Periodic datamining

Von Mises distribution

Magnetic fluctuations

Plasma physics

ABSTRACT

A periodic datamining algorithm has been developed and used to extract distinct plasma fluctuations in multichannel oscillatory timeseries data. The technique uses the Expectation Maximisation algorithm to solve for the maximum likelihood estimates and cluster assignments of a mixture of multivariate independent von Mises distributions (EM-VMM). The performance of the algorithm shows significant benefits when compared to a periodic k-means algorithm and clustering using non-periodic techniques on several artificial datasets and real experimental data. Additionally, a new technique for identifying interesting features in multichannel oscillatory timeseries data is described (STFT-clustering). STFT-clustering identifies the coincidence of spectral features over most channels of a multi-channel array using the averaged short time Fourier transform of the signals. These features are filtered using clustering to remove noise. This method is particularly good at identifying weaker features and complements existing methods of feature extraction. Results from applying the STFT-clustering and EM-VMM algorithm to the extraction and clustering of plasma wave modes in the time series data from a helical magnetic probe array on the H-1NF heliac are presented.

© 2014 Elsevier B.V. All rights reserved.

1. Introduction

The identification and characterisation of plasma wave modes as a function of machine and plasma parameters is a subject of considerable interest for plasma magnetic confinement devices. As has been observed with Alfvén waves [1], high energy fusion alphas or neutral beam injection ions can interact with these modes, severely degrading their confinement and driving the modes to large amplitude [2]. This causes significant problems such as damage to the first wall [3], and may prevent fusion plasmas from reaching ignition. Diagnostics such as arrays of magnetic probes are critical for identifying and characterising the spectral and spatial nature of these modes. These diagnostics are “always on” on major experiments, generating extremely large databases of time-series data which provides a perfect opportunity for knowledge discovery using datamining techniques.

Data clustering, a recognised technique for unsupervised classification, has recently been applied to the field of plasma physics for intelligent data retrieval from large fusion device databases [4–7] and for the identification and classification of wave modes [8–10] using non-periodic clustering algorithms.

The techniques described in this paper address the problem of dealing with periodic data and can be applied to many applications where multichannel diagnostics produces periodic signals. Applications within plasma physics include interferometers, soft X-ray arrays, arrays of magnetic probes and imaging diagnostics. For simplicity we will focus on the application to magnetic probe signals where the spatial information, such as mode numbers, is encoded in the phase differences between magnetic probe signals at the frequency of the mode. These phase differences ($\Delta\psi$) are periodic, $(-\pi, \pi]$, causing problems with standard clustering techniques. Additionally, the number of probes available is often quite large giving rise to high dimensional data. These constraints require the application of specialised clustering techniques. Two options that have good memory scalability are a periodic version of the k-means algorithm and expectation maximisation (EM) using mixtures of multivariate independent von Mises distributions (EM-VMM). Minimal information is available in the literature about the application of EM to multivariate independent von Mises distributions with more than 3 variables, so this is described in detail in Section 4. Previously [8–10], clustering on timeseries data was performed using standard non-periodic clustering techniques by trigonometrically encoding the data ($\sin(\Delta\psi)$ and $\cos(\Delta\psi)$). This method has several drawbacks including artificially creating structure, encoding systematic errors in the data, and doubling the dimensionality of the problem.

* Corresponding author. Tel.: +61 428778853.
E-mail address: shaun.haskey@anu.edu.au (S.R. Haskey).

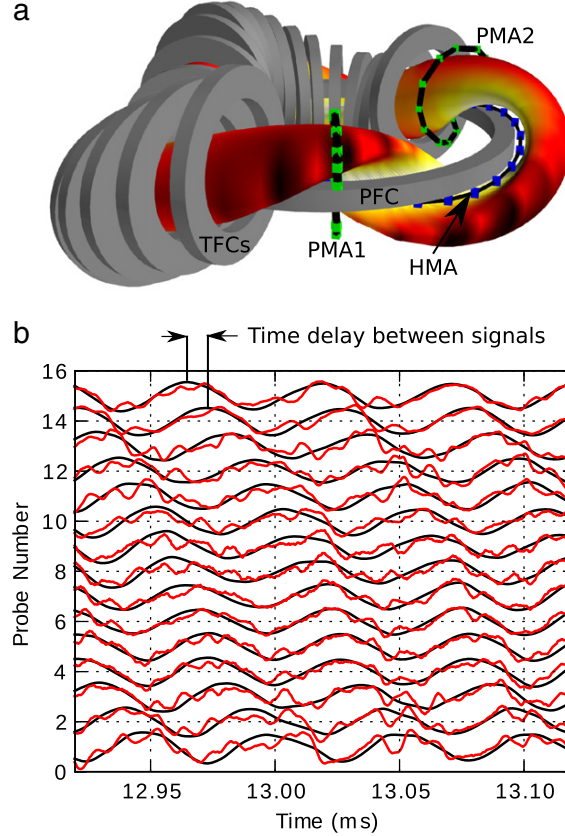


Fig. 1. (a) An overview of the H-1NF heliac including a subset of the equilibrium magnetic field coils (poloidal field coil (PFC), toroidal field coils (TFC)), the poloidal Mirnov arrays (PMA1, PMA2) and the helical Mirnov array (HMA). The surface colour represents the equilibrium magnetic field strength on the last closed flux surface. (b) Examples of the timeseries signals from the probes in the HMA, red is the raw signal and black is a bandpass filtered signal. The time delay in the signal between channels can be converted to a phase difference which represents the spatial structure of the mode. (For interpretation of the references to colour in this figure legend, the reader is referred to the web version of this article.)

Using several artificial datasets, we find that the EM-VMM algorithm performs better than the other available algorithms without incurring a significant computational cost. As a case study we successfully apply the EM-VMM algorithm to real data from the H-1NF heliac [11].

H-1NF is a three field-period helical axis stellarator with major radius $R = 1$ m and average minor radius $\langle r \rangle \approx 0.2$ m. The design of the machine allows access to an extensive range of magnetic configurations, making H-1NF well-suited to explore the relationship between plasma behaviour and magnetic configuration [12]. A variety of magnetic fluctuations have been observed with a recently installed helical Mirnov array (HMA) [13], which provides our experimental datasets in this paper. An overview picture of H-1NF including a subset of magnetic field coils and magnetic probe arrays as well as an example of the time trace signals from the HMA when a strong mode is present are shown in Fig. 1(a) and (b) respectively.

Additionally, a pre-processing technique for more robust identification of fluctuations in multichannel oscillatory timeseries data is described. The technique involves a combination of singular value decomposition (SVD) analysis, and an averaged short time Fourier transform followed by clustering (STFT-clustering). The STFT-clustering technique involves finding spectral features using the averaged short time Fourier transform followed by preliminary periodic clustering analysis to identify interesting features.

This paper is organised as follows: Section 2 provides an overview of the feature extraction and clustering process. Section 3 describes the STFT-clustering technique and how combining this with the SVD technique identifies features other techniques miss. Section 4 describes in detail how to apply the expectation maximisation algorithm to a mixture model of multivariate independent von Mises distributions. Section 5 compares the results of applying the periodic and standard clustering techniques to artificial data, and Section 6 shows results from applying STFT-clustering and EM-VMM to experimental data from the H-1NF heliac. Finally we provide some conclusions in Section 7.

2. Overview of the feature extraction and clustering process

For our application, we are ultimately interested in the physical nature of instabilities in plasmas, in particular, their dispersion relations. This information allows us to identify measures that can be taken to prevent these instabilities from growing to destructive amplitudes, and provides information on possible ways to use them beneficially.

Many different types of instabilities give rise to observable fluctuations in a magnetised toroidal plasma, for example ($n = 4$, $m = -3$) global Alfvén eigenmode (GAE), (5, -4) GAE, etc. [1]. Their existence and aspects of their behaviour such as frequency depend on the experimental conditions and plasma parameters such as magnetic field strength and its rotational transform profile and the plasma density. For clustering purposes we assume the spatial structure of a fluctuation instance is what defines it and makes it unique from other fluctuations. Unless the plasma equilibrium is very steady, if a fluctuation exists in a shot it will have different frequencies at different times depending on the plasma parameters such as density and magnetic field strength. Therefore, frequency is not a good identifier of a particular fluctuation and is not used in the clustering process. This and other attributes of each fluctuation instance (time, plasma parameters etc.) are only used later in interpreting the nature of each cluster. Each cluster represents a collection of measurements of the same type of fluctuation that have existed during different experiment conditions which together provide a great deal of information important for interpretation of the underlying physical phenomena.

An overview of the feature extraction, clustering, and analysis process is shown in Fig. 2. The measurements available to identify these instabilities generally consist of timeseries data from arrays of experimental diagnostics such as magnetic pickup probes or multichannel interferometers. In this paper we will focus on magnetic probes but the same technique has been successfully applied to interferometer data.

The magnetic probe signal from a mode that consists primarily of one component such as a global Alfvén eigenmode [1] can be described as follows:

$$V_i \propto \cos(n\phi_{B,i} + m\theta_{B,i} - \omega t). \quad (1)$$

Here, ω is the mode frequency, m represents the poloidal mode number, n the toroidal mode number, i an index in the toroidal array of probes, and, $\phi_{B,i}$ and $\theta_{B,i}$ are the toroidal and poloidal Boozer angles [14,15] of the i th probe, respectively. Examples of the time trace signals from a magnetic probe array due to a mode are shown in Fig. 1(b).

From Eq. (1) we can see that spatial information we are interested in (n and m) is contained in the phase structure of the signal at the frequency of the perturbation (ω). Therefore, the first task is to identify the frequencies of the perturbations over discrete time intervals, and extract the phase structure of the signal at those frequencies for each of the magnetic probes in the array. To make the data independent of the choice of time origin, we calculate the phase difference between successive coils in the array. This forms a

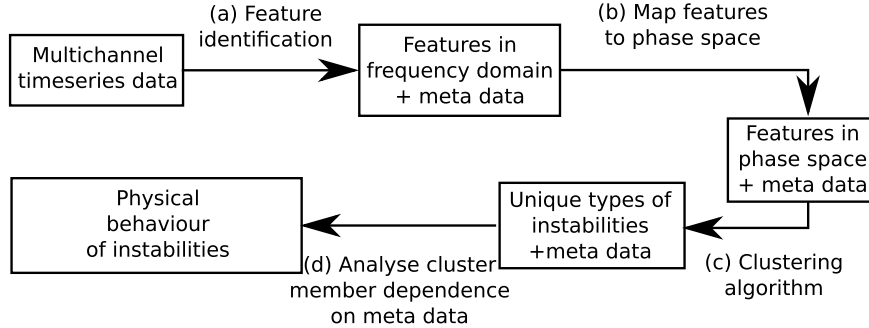


Fig. 2. Overview of the stages involved in the feature extraction and clustering process.

$N_c - 1$ set of nearest neighbour phase differences for each measurement, where N_c is the number of channels or probes in the array ((a) in Fig. 2). This maps the identified features to the $(-\pi, \pi]^{N_c-1}$ hyper-torus which we call $\Delta\psi$ -space (step (b) in Fig. 2).

Options for this extraction step include the SVD techniques [16,8,17], the STFT-clustering technique described in Section 3, or a combination of techniques. We also record any meta-data such as frequency, electron density profile, heating power and magnetic configuration that is not used in the clustering process but is useful for analysing the identified clusters dependence on physical parameters.

In the final clustering stage, we partition the identified features (measurements) into meaningful subgroups, where each subgroup consists of similar phase difference measurements, and therefore represents a different type of fluctuation ((c) in Fig. 2). Clustering methods usually follow either a hierarchical strategy, such as agglomerative hierarchical clustering, or a relocating strategy such as k -means or clustering via mixture models based on the EM algorithm [18]. In this paper, we focus on the relocating method as we have found that the hierarchical methods with reasonable run times are very memory intensive when dealing with the substantial number of instances we usually have in our datasets. The final stage of the analysis is to use the meta-data of each cluster to investigate the physical dependence of the observed features.

3. Feature extraction using the STFT-clustering pre-processing technique

The first step in the clustering process is to extract interesting measurements (or instances) from the time-series probe data which will be used in the final clustering process. This step is essentially a coarse filtering which reduces the number of instances used in the main clustering stage to a manageable level. Several methods are available to extract interesting features from the time series data [19] and map them to $\Delta\psi$ -space for clustering. One successful option that we have applied extensively is the SVD “fluctstruc” identification technique [17,8]. While this process works well, it fails to identify lower power fluctuations whose singular values are small, or are dwarfed by other fluctuations that exist at the same time.

Another option which is described in detail below is to break the probe time series data into short time intervals and apply the DFT to these intervals (equivalent to the short time Fourier transform (STFT)). By identifying peaks in the magnitudes in the STFT, we can locate data that is likely related to fluctuations. Using this approach, it is possible to select a large number of peaks for each discrete time step in a single experimental discharge (or shot) to ensure that lower power fluctuations are also included. By including the lower power peaks a significant number of measurements due to noise will also be included. To filter out the noise measurements a primary or “filtering” clustering step is performed on each

shot individually. Those features that are assigned to poorly defined or very broad clusters are removed because they are likely to be noise. The primary clustering step for each shot is separate from the final clustering of the data which uses the surviving measurements from all shots. Both the primary and final clustering use the technique described in Section 4. The whole process for a single shot is shown in Fig. 3. Combining the SVD and STFT-clustering techniques allows substantially more useful measurements to be extracted from the magnetic probe array data.

3.1. Multi channel averaged STFT feature extraction using clustering as a filter

The time-series data for a single shot consisting of N_s samples from N_c diagnostic channels, sampled at $(1/\tau)$ Hz can be represented in the following $N_c \times N_s$ matrix:

$$\boldsymbol{s} = \begin{pmatrix} s_0(t_0) & s_0(t_0 + \tau) & s_0(t_0 + 2\tau) & \dots & s_0(t_0 + (N_s - 1)\tau) \\ s_1(t_0) & s_1(t_0 + \tau) & s_1(t_0 + 2\tau) & \dots & s_1(t_0 + (N_s - 1)\tau) \\ \vdots & \vdots & \vdots & \ddots & \vdots \\ s_{N_c-1}(t_0) & s_{N_c-1}(t_0 + \tau) & s_{N_c-1}(t_0 + 2\tau) & \dots & s_{N_c-1}(t_0 + (N_s - 1)\tau) \end{pmatrix}. \quad (2)$$

This assumes that each channel has the same time base or has been interpolated onto a common time base before assembling \boldsymbol{s} .

The frequency and phase content of the signals we are interested in change over time. To capture the time dependence of the spectral content of the signals, we apply the STFT to our time series data ((a) in Fig. 3). To do this, we break up the time series data in \boldsymbol{s} into T small time chunks consisting of N_f samples each. A window function (typically Hanning) is applied to each time chunk. This data is referenced as, $x_{c,\tau}$ where $c = 1, 2, \dots, N_c$ represents the channel number, and $\tau = 0, 1, \dots, T$ identifies the time chunk. The discrete Fourier transform (DFT) of each time chunk for each channel is taken:

$$X_c[\tau, k] = \sum_{n=0}^{N_f-1} x_{c,\tau}[n] \exp(-i2\pi kn/N_f). \quad (3)$$

For our purposes 0.5 ms time chunks corresponding to $N_f = 1024$ samples at a 2 MHz sampling rate provides the best compromise between temporal and frequency resolution for data from the H-1NF heliac.

The next step is to identify the frequencies of interesting features from the multi-channel STFT of the shot. Using a single reference channel and searching for peaks in its STFT biases the reference channel, may miss features that are seen on other channels, and does not take advantage of the reduction in signal to noise that is available by using multiple channels. An attractive

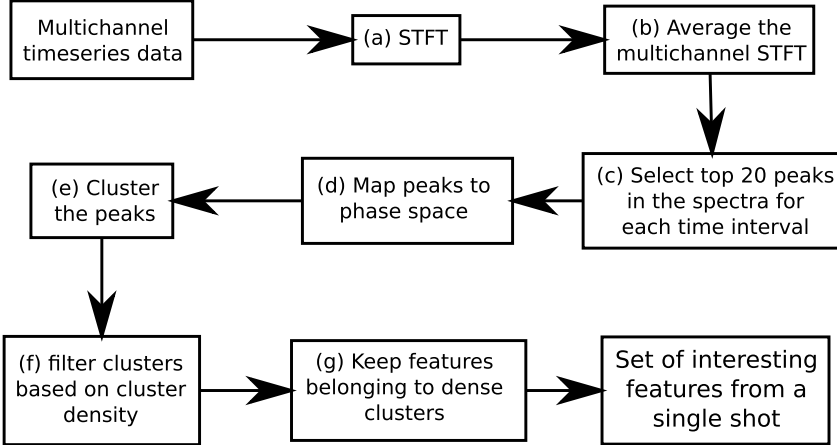


Fig. 3. Overview of the STFT-clustering process for a single shot. The retained features from each shot are combined to form the dataset for the major clustering stage.

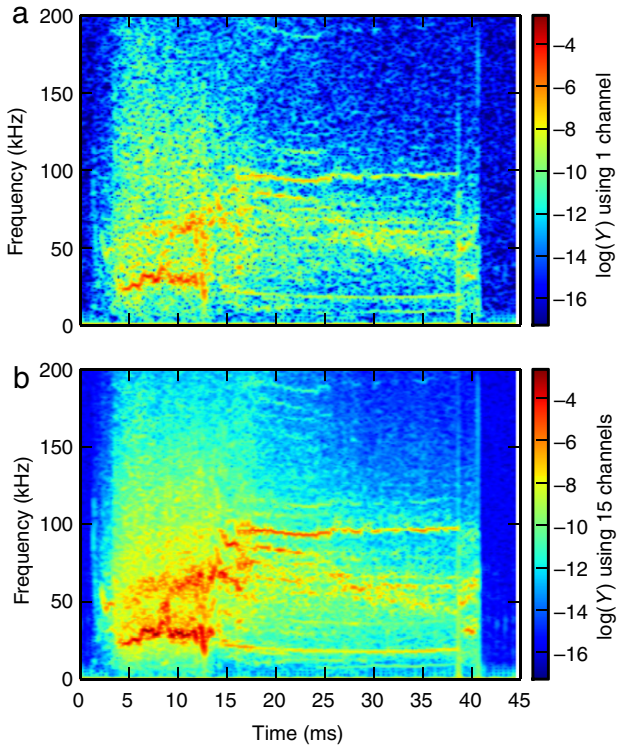


Fig. 4. Averaged STFT ($\log(Y)$) using 15 channels (b) and just a single channel (a) showing the improved signal to noise when using multiple channels, particularly for the ≈ 100 kHz signal at 20 ms. (For interpretation of the references to colour in this figure legend, the reader is referred to the web version of this article.)

alternative is to average the magnitude squared of the STFT from all channels ((b) in Fig. 3):

$$Y[\tau, k] = \frac{1}{N_c} \sum_{c=1}^{N_c} |X_c[\tau, k]|^2. \quad (4)$$

This is similar to the method of averaged periodograms (Bartlett's method) for a single channel. Instead of splitting up a longer time window, we use multiple channels, which reduce the variance of the periodogram without the usual reduction in temporal resolution. Fig. 4(a) and (b) show the magnitude squared of a single probe channel and the average magnitude squared of the multi-

channel STFT respectively clearly demonstrating the improved signal to noise for the multichannel case using this method.

The next step is to identify peaks in $Y[\tau, k]$ ((c) in Fig. 3). This is achieved by comparing the amplitude of each datapoint with the amplitude of the five point moving average:

$$P[\tau, k] = Y[\tau, k] - \frac{1}{5} \sum_{j=k-2}^{k+2} Y[\tau, j]. \quad (5)$$

The 5-point moving average was optimum for this application as it was small enough to provide a local average, without covering multiple peaks at once. For applications where the frequencies are known to be well separated, a greater number of points can be included in the moving average. We then select peaks in $P[\tau, k]$ (i.e. $Y[\tau, k]$ must satisfy $Y[\tau, k-1] < Y[\tau, k] > Y[\tau, k+1]$). For each interval τ , we rank the peaks, k , by how peaked the points are by ordering $P[\tau, k]$ and select the largest 20 peaks to ensure that we capture all the available interesting features. This creates a list of tuples, $Z = [(\tau_1^*, k_1^*), (\tau_2^*, k_2^*), \dots]$, which identifies peaks we are interested in. At this stage we are not concerned if we include points which may be noise because we are about to apply a clustering technique to filter them based on their structure in $\Delta\psi$ -space. We map each τ_j^*, k_j^* in Z to $\Delta\psi$ -space by extracting the $\psi = (\psi_1, \psi_2, \dots, \psi_c)$ where $\psi_i = \arg(X_i[\tau_j^*, k_j^*])$. The elements of $\Delta\psi = (\Delta\psi_1, \Delta\psi_2, \dots, \Delta\psi_{N_c-1})$ are calculated as follows: $\Delta\psi_i = \psi_{i+1} - \psi_i$ ((d) in Fig. 3).

We are now ready to apply the periodic clustering based feature extraction filter to these datapoints from a single shot ((e) in Fig. 3). We apply the EM-VMM algorithm described in Section 4 with a large number of clusters (typically 16) to ensure that interesting features can be separated out into clusters, we then analyse the resulting clusters to see how well-defined they are using the average circular standard deviation $\bar{\sigma}$ which is defined in Eqs. (14) and (10) in Section 4. The phase difference measurements that belong to clusters that have $\bar{\sigma} < 20^\circ$ are likely to be due to fluctuations so they are kept. The phase difference measurements in the other low density, broader clusters are likely to be noise so they are discarded. The cutoff value for $\bar{\sigma}$ was chosen as the point at which the rate of increase in the number of features with $\bar{\sigma}$ fell markedly (steps (f) and (g) in Fig. 3).

An example of these two techniques applied to a single shot is shown in Fig. 5. Fig. 5(a) shows the features identified using the standard SVD technique, (b) shows the features identified using the peaks in the averaged STFT (black dots), and the features which survive the cluster filtering (green circles). Fig. 5(c) shows the result of combining both the SVD and STFT-clustering techniques

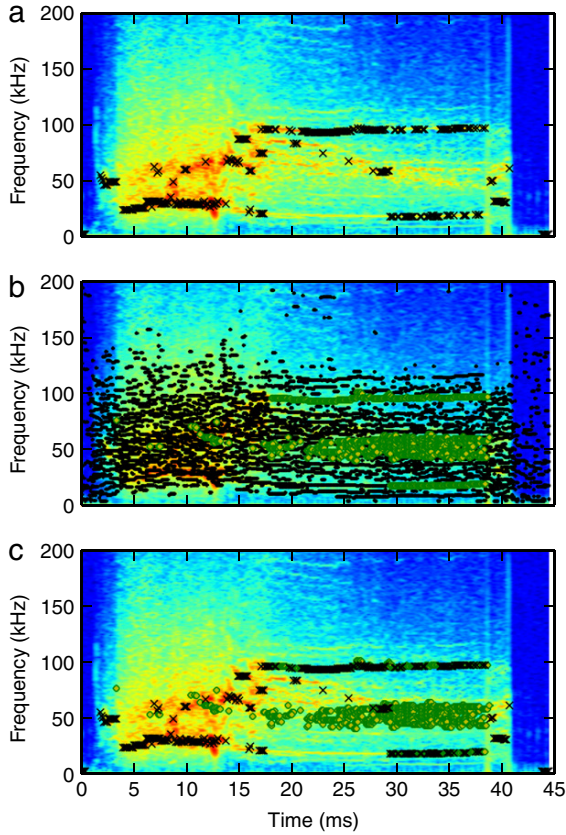


Fig. 5. (a) Black crosses represent features identified using the SVD method. (b) Green circles represent the features identified using STFT-clustering. The top 20 peaks at each timestep before filtering are marked with small black dots. (c) The features identified by the SVD method (black crosses), and the STFT clustering filtered method (green circles), demonstrating that the features identified using the two techniques complement each other. (For interpretation of the references to colour in this figure legend, the reader is referred to the web version of this article.)

using an “inclusive OR” to avoid double counting features that are common to both methods. There are many common features, however, both methods also complement each other allowing us to identify a greater number of real features.

3.2. Comparison with SVD feature extraction

The SVD, STFT-clustering and combination of both methods were used to extract features in a 131 shot database which was part of a magnetic configuration scan on H-1NF. Table 1 shows the number of features that were identified using each technique as well as the number of features that are identified by both techniques (duplicates are only counted once). Using the combination of both techniques provides a significant advantage, allowing us to find approximately twice as many meaningful features as explained below.

In the second and final clustering step, to check the quality of the extracted features using these three techniques, we apply the EM-VMM clustering algorithm described in Section 4 to the entire set of features that was found throughout the scan using each method. Next, we check the number of features that is assigned to clusters below a certain $\bar{\sigma}$ value. The greater the number of features that belong to dense clusters (smaller $\bar{\sigma}$), the higher the quality of the features that have been extracted. A plot of the number of features that are in clusters with a given or smaller value of $\bar{\sigma}$ is shown in Fig. 6. The filtering criterion used in the primary clustering step,

Table 1

Comparison of the SVD and STFT-clustering feature extraction techniques using 131 shots that were part of a magnetic configuration scan. The number of features identified using each method is shown along with the number of identified features that are common to the two methods. Also shown is the number of features obtained by combining the two methods.

	Number of features
SVD	23 000
STFT-clustering	27 000
Common (% SVD, % STFT)	13 000 (57%, 48%)
Combined	37 000

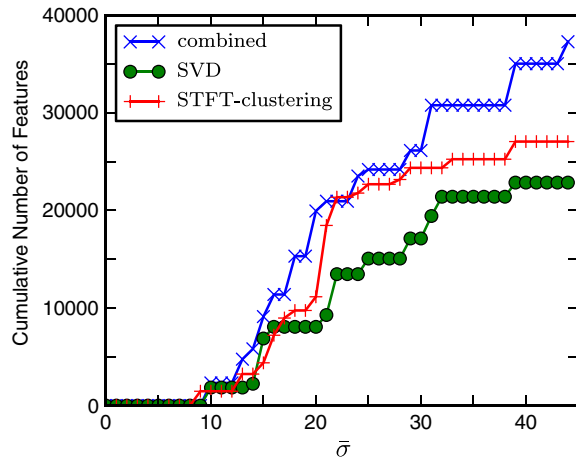


Fig. 6. Clustering the same features shown in Table 1 to check the significance of the features found by each method. Twice as many features are included in the good clusters ($\bar{\sigma} < 20^\circ$) using the combined method compared with only the SVD method signifying a substantial improvement in the feature identification procedure.

$\bar{\sigma} < 20^\circ$, is indicative of a “dense” cluster, but the ultimate criterion of cluster quality is how distinct the cluster is, as discussed in relation to Fig. 15. We find that the STFT-clustering method performs marginally better than the SVD method, and the combined method performs best, identifying 50% more features that form quality clusters compared with the SVD method.

4. Model based clustering using multivariate independent von Mises distributions

4.1. Selecting the correct model for the experimental measurements

As explained in Section 2, we characterise the spatial structure of fluctuations by the set of phase differences between adjacent Mirnov coils ($\Delta\psi_i$). A collection of phase difference measurements due to a single fluctuation has a well-defined mean value, and because it is subject to random processes such as electrical noise in the probe amplifiers, and noise generated by localised plasma turbulence will be distributed about this mean. Therefore, these measurements, which are inherently (2π) periodic, can be modelled using a circular distribution function. Of the several circular distribution functions available, we use the von Mises distribution which is one of the best known and widely used [20, 21]. If the experimental measurements are generated by a variety of fluctuations, each of which produces unique patterns of phase difference between probes, we can use a mixture of von Mises distributions to model the data. The expectation maximisation algorithm [22,23] can then be used to compute the maximum-likelihood estimates (MLE) of the mixture model parameters and the cluster assignments.

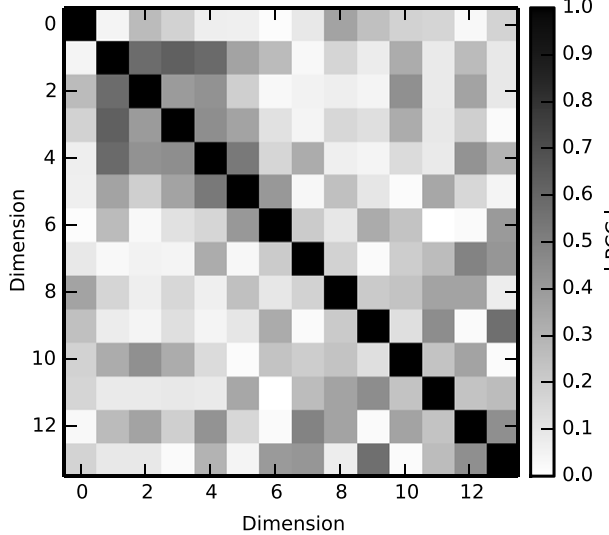


Fig. 7. Graphical representation of the absolute values of the Pearson correlation coefficient for a cluster that was obtained from the H-1NF dataset using EM with Gaussian mixtures with a full covariance matrix. The off diagonal PCCs are generally below 0.5 and have a mean magnitude of 0.21 indicating that covariance is not dominant in this cluster.

In our case, we have an array of such measurements ($\Delta\psi$), which we model using a mixture of *multivariate* von Mises distributions (as described in [24]); however, beyond the bi-variate case the normalising constant becomes intractable when covariance is present. To overcome these difficulties, Mardia et al. [25] described a concentrated multivariate sine (CMS) model. Unfortunately, our experimental data is not sufficiently concentrated causing difficulties with this algorithm.

In the absence of practical methods that include the full covariances, we can use a mixture of multivariate independent von Mises distributions. We expect each of the variables $\Delta\psi$ due to a single type of fluctuation to have a degree of independence due to localised noise from plasma turbulence and uncorrelated electrical noise. Covariances could however exist due to shared noise, or movement of the plasma relative to the pickup probes. To obtain an estimate of the importance of including covariance, we performed a clustering analysis on some of the H-1NF data using EM with a Gaussian mixture model. While this method does not provide the correct distribution for the periodic data, it allows us to include the full covariance matrix to test its importance, and is valid for this dataset because the clusters are well clear of the folding at $-\pi, \pi$. The Pearson correlation coefficients (PCC) between all dimensions of a cluster of interest are shown in Fig. 7. While there is some degree of correlation, the off diagonal elements are generally below 0.5 and have a mean magnitude of 0.21 in this case. This should not have a significant impact on the cluster assignments and suggests that using a multivariate independent von Mises distribution provides a good model for the individual clusters.

The rest of this section describes in detail how to solve for the parameters and cluster assignments in a mixture of multivariate independent von Mises distributions using the EM algorithm.

4.2. The von Mises distribution

The probability density function for the von Mises distribution is defined as follows [20,21]:

$$f(x; \mu, \kappa) = \frac{1}{2\pi I_0(\kappa)} \exp\{\kappa \cos(x - \mu)\} \quad (6)$$

where $-\pi < x \leq \pi$, $I_0(\kappa)$ is the modified Bessel function of the first kind and order 0, μ represents the mean direction and $\kappa \geq 0$ is a concentration parameter that increases with distributions that are more concentrated around the mean. We obtain a uniform distribution on $(-\pi, \pi]$ when $\kappa = 0$. This distribution can be used to model measurements of the phase differences between two probes due to a single type of fluctuation. $f(x; \mu, \kappa)$ describes the probability of obtaining the phase difference measurement x (same as $\Delta\psi$ from Section 3.1) from a particular fluctuation for which μ is the mean value of the measurements, and κ describes how concentrated the measurements are.

Given a random sample (x_1, x_2, \dots, x_n) in the data following, these will be phase difference measurements which is drawn from $f(x; \mu, \kappa)$ (i.e. they are due to a particular type of fluctuation), the maximum likelihood estimates, $\hat{\mu}$, and $\hat{\kappa}$ are given as follows [20]:

$$R = \frac{1}{n} \sum_{j=1}^n \exp(ix_j)$$

$$\bar{R} = |R|$$

$$\hat{\mu} = \arg(R) \quad (7)$$

$$\frac{I_1(\hat{\kappa})}{I_0(\hat{\kappa})} = \bar{R} \quad (8)$$

where $i = \sqrt{-1}$, and $I_1(\hat{\kappa})$ is the modified Bessel function of the first kind and first order. There is no analytical solution to solve Eq. (8) for $\hat{\kappa}$, so one must resort to numerical techniques, a pre-calculated lookup table, or the following approximation [20]:

$$\hat{\kappa} = \begin{cases} 1/(2 - 2\bar{R}), & \text{for } 0.85 < \bar{R} \\ -0.4 + 1.39\bar{R} + 0.43/(1 - \bar{R}), & \text{for } 0.53 < \bar{R} < 0.85 \\ 2\bar{R} + \bar{R}^3 + (5/6)\bar{R}^5, & \text{for } \bar{R} < 0.53. \end{cases} \quad (9)$$

Each of these methods work well, providing various trade-offs between speed and accuracy. We can also calculate a circular standard deviation, which has units of radians and has more intuitive meaning than κ [26]:

$$\sigma = \sqrt{-2 \ln(\bar{R})}. \quad (10)$$

4.3. The multivariate independent von Mises distribution

We can extend Eq. (6) to get the probability density function of the P -variate independent von Mises distribution as follows:

$$f_p(\mathbf{x}; \boldsymbol{\mu}, \boldsymbol{\kappa}) = \left(\frac{1}{2\pi} \right)^P \frac{1}{I(\boldsymbol{\kappa})} \exp\{\boldsymbol{\kappa} \cdot \mathbf{c}(\mathbf{x}, \boldsymbol{\mu})\} \quad (11)$$

where:

$$-\pi < x_i \leq \pi,$$

$$\kappa_i \geq 0,$$

$$\mathbf{x} = (x_1, x_2, \dots, x_P),$$

$$\boldsymbol{\kappa} = (\kappa_1, \kappa_2, \dots, \kappa_P),$$

$$\boldsymbol{\mu} = (\mu_1, \mu_2, \dots, \mu_P),$$

$$\mathbf{c}(\mathbf{x}, \boldsymbol{\mu})^T = (\cos(x_1 - \mu_1), \cos(x_2 - \mu_2), \dots, \cos(x_P - \mu_P)),$$

$$I(\boldsymbol{\kappa}) = \prod_{p=1}^P I_0(\kappa_p).$$

Eq. (11) is the extension of Eq. (6) to phase difference measurements from an array with more than 2 probes. f_p gives the probability of obtaining the phase difference measurement \mathbf{x} consisting of $N_c - 1 = P$ values from an array with N_c probes (same as $\Delta\psi$ from Section 3.1) from a particular fluctuation for which $\boldsymbol{\mu}$ is the

mean value of the phase difference measurements between adjacent coils, and κ describes how concentrated the measurements are.

When dealing with a large number of dimensions, $\exp\{\kappa \cdot c(\mathbf{x}, \boldsymbol{\mu})^T\}$ can become very large, while $(\frac{1}{2\pi})^P \frac{1}{I(\kappa)}$ becomes very small causing computational problems. These problems can be overcome by rewriting Eq. (11) as follows:

$$f_P(\mathbf{x}; \boldsymbol{\mu}, \kappa) = \exp \left\{ \kappa \cdot c(\mathbf{x}, \boldsymbol{\mu}) - P \ln(2\pi) - \sum_{p=1}^P \ln(I_0(\kappa_p)) \right\}. \quad (12)$$

4.4. EM and mixtures of multivariate independent von Mises distributions

The phase difference measurements from K different types of fluctuation each with their own $\boldsymbol{\mu}$ and κ can be represented using a mixture of K , P -variate independent von Mises distributions:

$$M(\mathbf{x}, \boldsymbol{\mu}_1, \boldsymbol{\mu}_2, \dots, \boldsymbol{\mu}_K, \kappa_1, \kappa_2, \dots, \kappa_K) = \sum_{k=1}^K p_k f_P(\mathbf{x}; \boldsymbol{\mu}_k, \kappa_k) \quad (13)$$

where p_k represents the mixing ratios which represent how likely the measurement is to come from the fluctuation represented by k , $p_k > 0$ and $\sum_{k=1}^K p_k = 1$. Given a set of n data points $\{\mathbf{x}_1, \mathbf{x}_2, \dots, \mathbf{x}_n\}$ from a mixture of K , P -variate independent von Mises distributions, we can define the cluster membership in a $n \times K$ matrix, $Z = (z_{ik})$, where $z_{ik} = 1$ if \mathbf{x}_i is a member of group k and zero otherwise.

Two useful measures of the concentration of a P -variate independent distribution are the average circular standard deviation, and the equivalent circular standard deviation:

$$\bar{\sigma} = \frac{1}{P} \sum_{i=1}^P \sigma_i \quad (14)$$

$$\sigma_{eq} = \left(\prod_{i=1}^P \sigma_i \right)^{1/P} \quad (15)$$

where σ is the circular standard deviation of each dimension (as defined in Eq. (10)). The equivalent standard deviation can be thought of as the side length of a hyper cube that has the same the volume as a hyper-cuboid whose side lengths are the circular standard deviation in each dimension. These measures are used to quantify the density of the clusters.

Our aim is to find the MLE estimates of our dataset $(\hat{p}_k, \hat{\boldsymbol{\mu}}_k, \hat{\kappa}_k)$, and \hat{z}_{ik} where $k = 1, 2, \dots, K$ and $i = 1, 2, \dots, n$. The expectation maximisation algorithm [22] which seeks to maximise the log-likelihood can be used to find the MLE values. The log-likelihood of the MLE values is given by:

$$L = \sum_{k=1}^K \sum_{i=1}^n \hat{z}_{ik} \ln(f_P(\mathbf{x}_i; \hat{\boldsymbol{\mu}}_k, \hat{\kappa}_k)). \quad (16)$$

The EM algorithm involves the following two steps which are iterated over until convergence criteria such as minimal changes in $\hat{\boldsymbol{\mu}}_k$ and $\hat{\kappa}_k$ between iterations, are met.

Expectation (E) step: given $\hat{\boldsymbol{\mu}}_k, \hat{\kappa}_k$, and \hat{p}_k from the maximisation step, we calculate \hat{z}_{ik} :

$$\hat{z}_{ik} = \frac{\hat{p}_k f_P(\mathbf{x}_i; \hat{\boldsymbol{\mu}}_k, \hat{\kappa}_k)}{\sum_{l=1}^K \hat{p}_l f_P(\mathbf{x}_i; \hat{\boldsymbol{\mu}}_l, \hat{\kappa}_l)}. \quad (17)$$

This means, $0 \leq \hat{z}_{ik} \leq 1$, and $\sum_{k=1}^K \hat{z}_{ik} = 1$. This is referred to as soft cluster assignment.

The maximisation (M) step: given \hat{z}_{ik} from the expectation step, we calculate $\hat{\kappa}_k = (\hat{\kappa}_{1k}, \hat{\kappa}_{2k}, \dots, \hat{\kappa}_{Pk})$, $\hat{\boldsymbol{\mu}}_k = (\hat{\mu}_{1k}, \hat{\mu}_{2k}, \dots, \hat{\mu}_{Pk})$, and \hat{p}_k for each cluster $k = 1, \dots, K$ in a similar manner to the uni-variate case:

$$\begin{aligned} \hat{p}_k &= \frac{\sum_{i=1}^n \hat{z}_{ik}}{n} \\ R_{jk} &= \frac{1}{\sum_{i=1}^n \hat{z}_{ik}} \sum_{i=1}^n \hat{z}_{ik} \exp(ix_{ip}) \\ \bar{R}_{jk} &= |R_{jk}| \\ \hat{\mu}_{jk} &= \arg(R_{jk}) \end{aligned} \quad (18)$$

$$\frac{I_1(\hat{\kappa}_{jk})}{I_0(\hat{\kappa}_{jk})} = \bar{R}_{jk}. \quad (19)$$

Eq. (19), is solved for $\hat{\kappa}_{jk}$, numerically, using a pre-calculated lookup table, or using the approximation shown in Eq. (9).

We initialise the EM algorithm using the cluster assignments, \hat{z}_{ik} which are obtained from a k -means run. These values are used for the maximisation step. We then alternate between the E and M steps until convergence. Finding a local maximum instead of the global one is a well known problem with the EM algorithm. To overcome this, the algorithm is run several times with different starting points and the solution which maximises the log-likelihood is chosen.

4.5. Implementation and computational requirements

Many software packages exist that include an implementation of Expectation Maximisation for Gaussian mixture models for clustering [27,28]; however, implementations using von Mises distributions appear to be rare. A related approach is implemented in the SNOB code [29,30], which solves for independent von Mises distributions using the minimum message length technique. We have implemented the algorithm described in Section 4 using the Python programming language. Using the Scipy [31] and Numpy [32] modules allows us to achieve close to compiled speeds. Each iteration takes approximately 0.5 s for 37,000 instances, 14 dimensions, and 16 clusters using a single core on a laptop with an Intel core i7 processor. After ≈ 30 iterations, the algorithm is usually well converged. This speed allows many clustering parameters to be tried without excessive delays. The computational cost is roughly the same as performing the clustering with the same parameters using a Gaussian mixture model with trigonometric encoding.

5. Artificial dataset

In this section, we compare the expectation maximisation algorithm using mixtures of multivariate independent von Mises distributions (EM-VMM) with the standard non-periodic datamining techniques: EM with Gaussian mixtures (EM-GMM), EM with Gaussian mixtures using trigonometric encoding (EM-GMM-trig), k -means using trigonometric encoding (k -means-trig) and a periodic k -means variant (k -means-periodic) whose distance measure is $D(\theta, \phi) = \min\{|\theta - \phi|, 2\pi - |\theta - \phi|\}$, and whose new cluster center is calculated in the same way as for the EM-VMM algorithm (Eq. (18)) with hard cluster assignment. For the EM-GMM clustering, we use the implementation in the Python scikit-learn module [27].

For this comparison we have generated three datasets—case 1, case 2 and case 3. For all of the cases, the dataset is generated using the normal distribution, and wrapping the data to $(-\pi, \pi]$

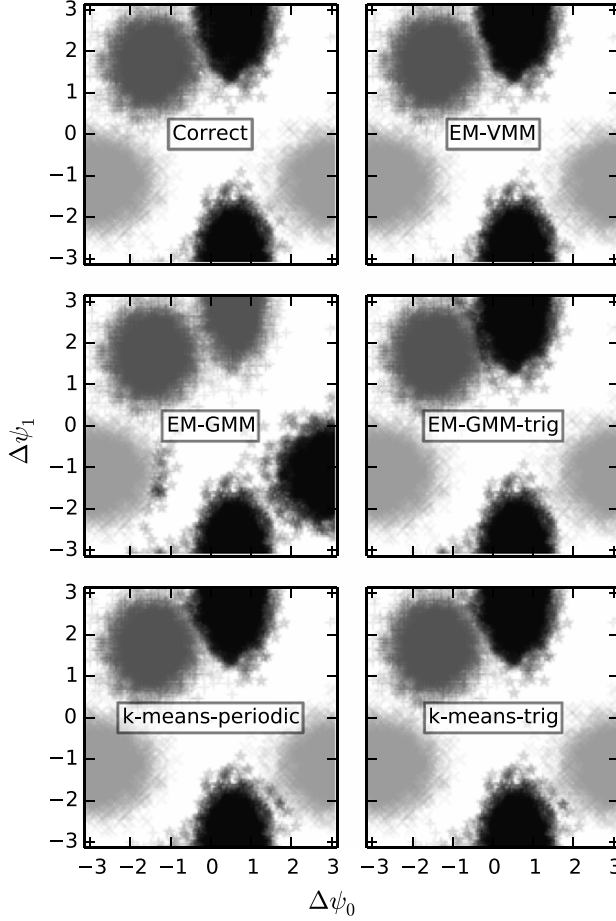


Fig. 8. The performance of the various clustering algorithms for case 1 where the algorithms must deal with the periodicity problems that occur at π and $-\pi$. Each point is a single datapoint in the artificial dataset that is used to test the clustering algorithms. The colour of each datapoint represents the cluster to which it has been assigned by various methods as labelled. The correct assignment is shown in the top left plot.

by adding π , taking modulus 2π and subtracting π . Case 1 consists of 3 clusters in 2 dimensions. Two of the clusters have a single dimension whose mean is close to π to test the performance of the various techniques near the $-\pi$, π discontinuity. Case 2 also consists of 3 clusters in 2 dimensions. For this case, the means of all dimensions are far enough away from π that periodic effects should not be important; however, one of the clusters has a large standard deviation, which is more sensitive to the distortions caused by trigonometric encoding. The third dataset consists of 4 clusters in 4 dimensions to test the performance of the algorithms on higher dimensional data. For this dataset, the means were randomly selected to be $-\pi < \mu < \pi$, and the standard deviation values are chosen to be in the range $\pi/12 < \sigma < \pi/4$ except for one cluster whose σ values are π for all dimensions to simulate noise.

The results from clustering case 1 are shown in Fig. 8, and the percentage of correct identifications is shown in Table 2. The EM-VMM, periodic k -means algorithm, EM-GMM-trig, k -means-trig perform well, with EM-VMM performing the best. EM-GMM performs poorly because it fails to deal with the periodicity problem as expected.

The results from clustering case 2 are shown in Fig. 9 and the percentage of correct identifications is shown in Table 2. Again, EM-VMM performs the best. For this case, EM-GMM also per-

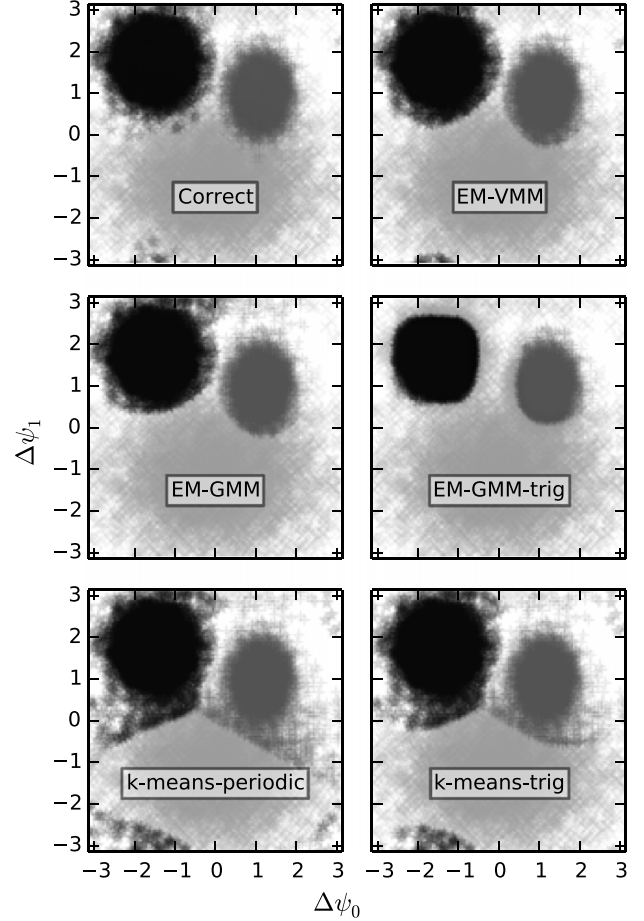


Fig. 9. The performance of the various clustering algorithms for case 2 where problems occur with the distortions caused by trigonometric encoding. The caption for Fig. 8 provides a description of what each datapoint and the colours represent.

Table 2

Performance of the various algorithms based on percentage of correct cluster identification for cases 1–3 which represent difficult cases for periodicity, trigonometric distortion, and multi dimensionality (more in text).

	Case 1 (per)	Case 2 (dist)	Case 3 (dim)
EM-VMM	99.7%	97.1%	95.3%
EM-GMM	71.9%	96.9%	74.1%
EM-GMM-trig	99.4%	93.3%	90.6%
k -means-periodic	99.6%	92.8%	79.5%
k -means-trig	99.6%	94.4%	88.3%

forms well because the periodicity problems are not present. Both the algorithms with trigonometric encoding (EM-GMM-trig and k -means-trig) perform less well due to distortions caused by the trigonometric encoding. The distortions can be seen clearly for the k -means-trig case in Fig. 9. The partitions separating clusters should be along straight lines for k -means, however, the distortions introduced by k -means-trig cause the partition between the clusters to follow an arc.

For the higher dimensionality dataset in case 3, EM-VMM performs substantially better than the other algorithms. The algorithms with trigonometric encoding perform well, while EM-GMMs performs poorly due to its inability to deal with the periodic data.

The results from the artificial datasets clearly show that EM-VMM performs better than the other algorithms. This is because we are fitting an accurate model for periodic data to the datasets.

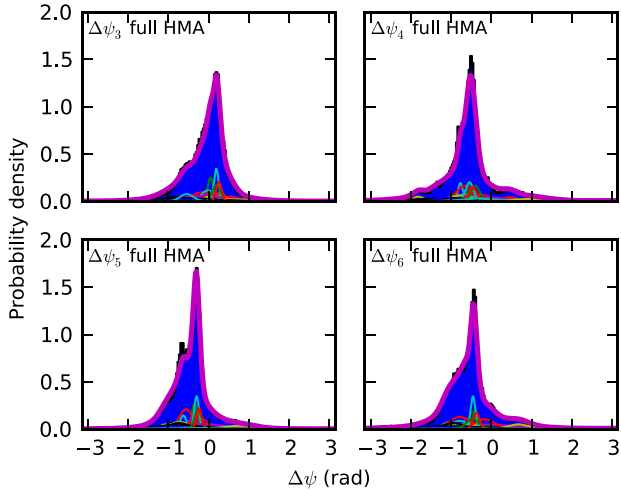


Fig. 10. Histograms for four phase differences when using the full HMA. The blue colour represents a histogram of the raw data. The thick line is the mixture of von Mises distributions that has been fitted to the data using EM. The thin lines represent the probability density functions for each of the clusters that make up the mixture model multiplied by their mixture weights. (For interpretation of the references to colour in this figure legend, the reader is referred to the web version of this article.)

Additionally, while the k -means algorithm is faster than the EM algorithms, it tends to find clusters of comparable spatial extent. This represents a significant disadvantage because we expect the clusters in our experimental data to have a variety of shapes.

6. Application to the H-1NF helical Mirnov array dataset

The flexibility of the H-1NF heliac allows access to different rotational transform profiles by varying the ratio of currents in certain field coils, a parameter represented by κ_H (this has no relation to the κ concentration parameter for the von Mises distributions). The rotational transform is essentially a measure of the twist of magnetic field lines on flux surfaces [33]. It plays an important role in determining the type of magnetic fluctuations that can exist and their frequencies. A scan consisting of 131 separate shots was performed by incrementally increasing κ_H . Data from the helical Mirnov array (HMA) [13] was used to identify approximately 37,000 features in the scan using the combination of SVD and STFT-clustering extraction techniques described in Section 3.

The histograms for $\Delta\psi_3$, $\Delta\psi_4$, $\Delta\psi_5$ and $\Delta\psi_6$ for the 37,000 datapoints are shown in solid blue in Fig. 10. The histograms are normalised to show the proportion of items that fall into each bin so that the area under the histogram is 1 for comparison with the probability distribution functions. The other dimensions, which are not shown have similar histograms. The phase differences are peaked far away from the $(\pi, -\pi)$ discontinuity because the spacing of the HMA is very dense. Data from this array could be clustered using the EM-GMM algorithm without having to resort to trigonometric encoding, although this is not ideal as some important datapoints in low population clusters may still be close to π and $-\pi$.

Spacing the magnetic probes as densely as in the HMA is not always possible and can be prohibitively expensive, especially in larger fully three dimensional stellarators [33]. To simulate a less dense array, we only include every third coil in the HMA. The histograms for $\Delta\psi_1$, $\Delta\psi_2$, $\Delta\psi_3$, and $\Delta\psi_4$ of this reduced array are shown in Fig. 11. In this case, the EM-VMM algorithm has many benefits because the histograms are much less concentrated, and the clustering algorithm must be able to handle periodicity, and minimise the distortion of the phase space.

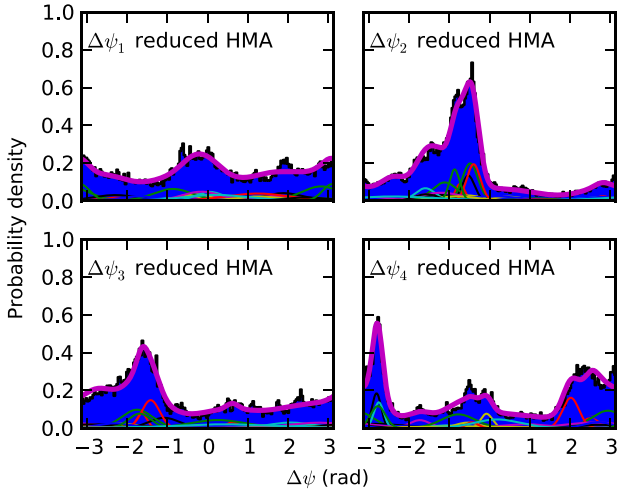


Fig. 11. Histograms for four phase differences (blue) when using every third coil in the HMA to simulate a smaller array. Compared with Fig. 10, the phase differences are generally 3 times larger (as the probes are further away from each other), and a substantial number of datapoints are close to $-\pi$ and π . The thick line is the mixture of von Mises distributions that has been fitted to the data using EM and the thin lines represent the probability density functions for each of the clusters that make up the mixture model multiplied by their mixture weights. (For interpretation of the references to colour in this figure legend, the reader is referred to the web version of this article.)

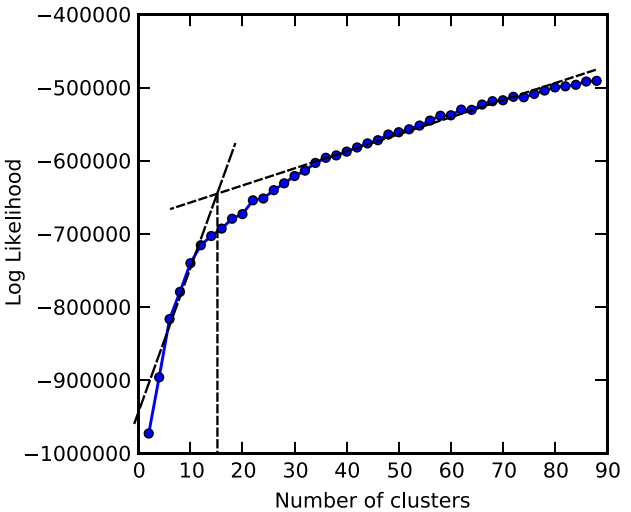


Fig. 12. Plot of log likelihood versus number of clusters. The elbow in the plot occurs at approximately 16 clusters.

One of the main difficulties in clustering is choosing the correct number of clusters. The “elbow” criterion, which identifies a flattening of some error measure versus the number of clusters, is a commonly used heuristic method for identifying the optimal number of clusters [34]. The Bayesian information criterion (BIC) [35] or Aikake information criterion (AIC) are other commonly used measures. A plot of the EM log likelihood versus number of clusters is shown in Fig. 12 suggesting that a good number of clusters is 16. The speed of the algorithm makes it easy to experiment using different numbers of clusters. Visual inspection of the clusters suggests that between 16 and 24 clusters provide the most useful separation of the data.

The results of clustering using the EM-VMM for the full HMA and the reduced HMA (every third coil) are also shown in Figs. 10

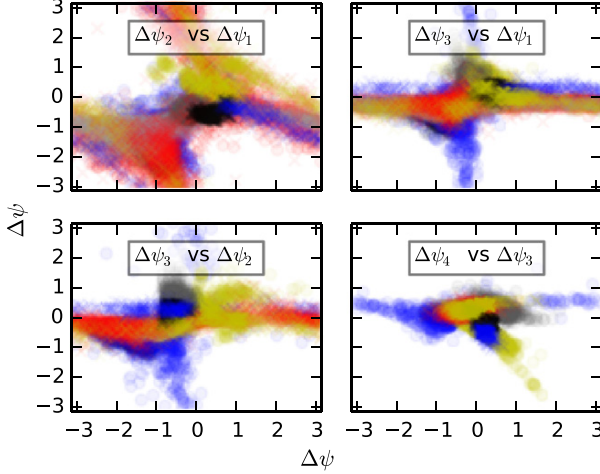


Fig. 13. Each datapoint represents one of the measured phase differences from the full HMA (each measurement consists of $N_c - 1$ numbers). The subplots are different projections of the $N_c - 1$ space needed to plot the measurements. Only the datapoints that are assigned to well-defined clusters are shown to exclude measurements that are noise. Each cluster is identified using a different colour (and marker style in the case of duplicated colours). (For interpretation of the references to colour in this figure legend, the reader is referred to the web version of this article.)

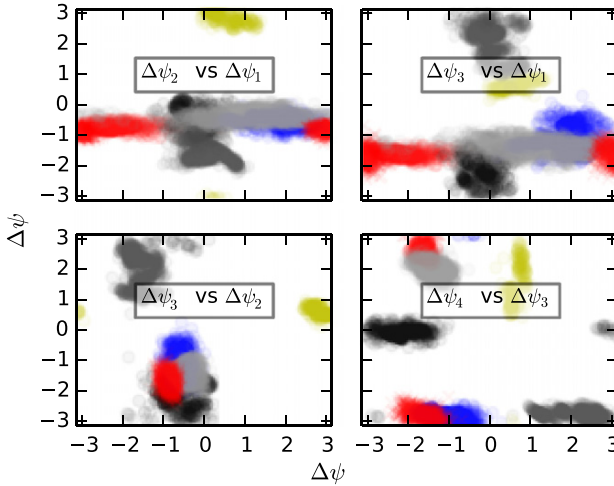


Fig. 14. Same as Fig. 13 except using the measurements from the reduced HMA ($N_c/3 - 1$). Compared with the full HMA (Fig. 13), the clusters are more separated, and closer to the $(-\pi, \pi]$ discontinuity. Each cluster is identified using a different colour (and marker style in the case of duplicated colours). (For interpretation of the references to colour in this figure legend, the reader is referred to the web version of this article.)

and 11. The von Mises distributions for the individual clusters are shown, along with the sum of the mixtures with the appropriate mixing proportions. The sum of the mixtures is very similar to the histograms, indicating that the von Mises mixture model fits the data well.

Plots showing the location of the clusters in the coordinate space of selected phase differences are shown in Figs. 13 and 14, for the full HMA and reduced array respectively. For the full HMA, the majority of phase differences are far from $(-\pi, \pi)$ (as seen in Fig. 10), however, there are clearly a few datapoints which are close to the discontinuity that require including periodicity to treat them properly. The plot for the reduced HMA clearly shows a great deal of spread in the location of the clusters indicating how important

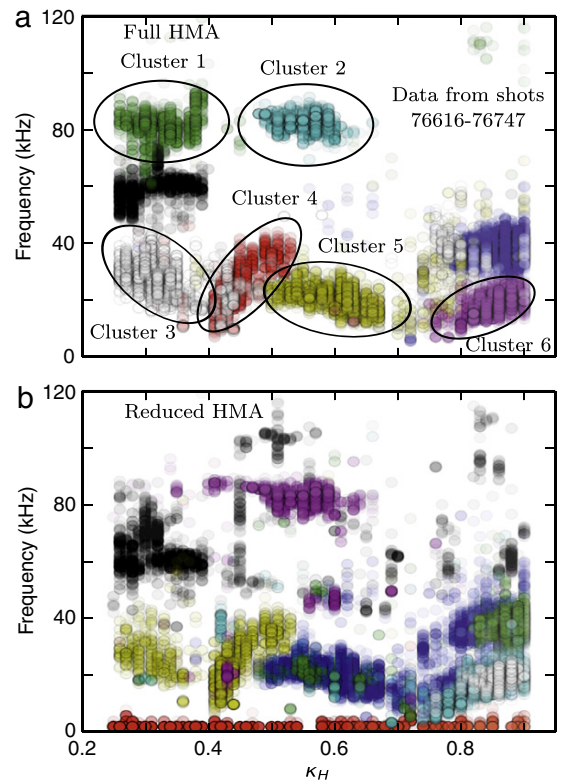


Fig. 15. Plot of dense clusters as a function of magnetic configuration (κ_H) and frequency found using EM-VMM using the full HMA (a) and reduced HMA (b). The clusters are clearly localised in κ_H , and some show a frequency dependence as κ_H changes (clusters 3–6), while others do not have such a strong dependence (clusters 1 and 2). The full HMA produces cleaner, more defined clusters when using the same clustering parameters because there is more information available to separate the clusters for the full array. (For interpretation of the references to colour in this figure legend, the reader is referred to the web version of this article.)

including periodicity is for the case of a less densely spaced array. Note that the apparently reduced overlap of clusters compared to the full HMA is not indicative of better clustering, but is because the phase differences are larger by a factor of 3. The quality of clustering is discussed in relation to Fig. 15.

The final stage of the clustering analysis is to look at the cluster dependence on the meta-data that was recorded with the features. This allows us to determine the dependence of the instability on interesting physical quantities ((d) in Fig. 2). Fig. 15(a) and (b) show several of the most dense clusters plotted against frequency and κ_H for the full HMA and reduced HMA respectively. Each cluster represents a distinct type of fluctuation and by plotting the cluster member's dependence on ω and κ_H we can see what effect magnetic configuration has on the types of fluctuations that exist. The identified clusters show very well-defined behaviour in (ω, κ_H) space even though neither of these parameters were included in the clustering. The full HMA provides better defined clusters and more accurate fluctuation identification. For example, clusters 3 and 4 appear as a single cluster for the reduced HMA, consistent with the loss of information resulting from the omission of two thirds of the signals. This demonstrates the importance of having dense magnetic probe spacing for resolving different types of fluctuations.

Most clusters are limited to particular ranges of κ_H indicating that the magnetic configuration is important in determining whether or not a specific type of fluctuation can exist. For example, cluster 2 only exists for $0.45 < \kappa_H < 0.65$. Some clusters such as 3–6 show a relationship between ω and κ_H . As κ_H increases

the members of these clusters frequency increases or decreases systematically. This shows that the magnetic configuration affects the frequency of these fluctuations providing information about the fluctuations dispersion relation. This is a clear demonstration of the ability of the clustering algorithm to find interesting physical phenomena using just the phase differences between magnetic probes.

7. Conclusion

The application of the expectation maximisation algorithm to mixtures of multivariate independent von Mises distributions (EM-VMM) has been described in detail. Such a model does not distort phase space, and provides an accurate representation of multi-dimensional periodic data. This technique is ideally suited to clustering large multidimensional periodic datasets, such as those obtained from magnetic probe arrays observing instabilities in magnetic confinement plasma devices. The technique would also be useful to the multitude of applications where multichannel arrays of diagnostics record large quantities of periodic signals such as interferometers, soft X-ray arrays, magnetic probe arrays and imaging diagnostics.

The EM-VMM algorithm was shown to have superior performance on several artificial periodic datasets compared with other clustering options such as EM with Gaussian mixtures with and without trigonometric encoding, k -means with trigonometric encoding and a periodic k -means variant. The improved performance does not come with a significant increase in computational requirements. A 14 dimensional, 37,000 instance dataset takes less than a minute to converge when fitting 16 clusters, which is roughly equivalent to the time taken for EM with Gaussian mixtures and trigonometric encoding. This fast convergence is particularly useful for interactive data analysis, where several clustering parameters are varied to find the best combination.

A new method of feature extraction from multi-channel time-series data was described. The method, called STFT-clustering, identifies peaks in the multi-channel averaged short time Fourier transform of the timeseries, and clusters the data using the EM-VMM. Interesting data can then be extracted by selecting clusters with an average circular standard deviation below a threshold. This method was compared to an SVD extraction technique that is currently applied to data from the helical Mirnov array on H-1NF. The two methods complement each other, and when used together identify up to twice as many interesting features in the multichannel time-series data. The STFT-clustering method is particularly good at identifying lower power features.

Results from applying the STFT-clustering for feature extraction, and EM-VMM for clustering, to a 131 shot dataset from a magnetic configuration scan on the H-1NF heliac were presented. The combination of SVD and STFT-clustering identified 37,000 interesting features in the 15 channel helical Mirnov array (HMA) dataset. The EM-VMM clustering then successfully fitted a 14 dimensional, 16 mixture model to the data. Comparing the meta-data for each of the identified clusters showed distinct behaviour as a function of magnetic configuration and frequency, indicating the successful identification of unique, physically interesting instabilities.

Acknowledgements

The authors would like to thank Professors Markus Hegland and Donald Poskitt for valuable suggestions and comments, and the H-1NF team for continued support for experimental operations. This work was supported by the Education Investment Fund under the Super Science Initiative of the Australian Government. SRH wishes to thank AINSE Ltd. for providing financial assistance to enable this work on H-1NF to be conducted.

References

- [1] W. Heidbrink, Basic physics of Alfvén instabilities driven by energetic particles in toroidally confined plasmas, *Phys. Plasmas* 15 (5) (2008) 055501-1–055501-15.
- [2] K.L. Wong, R.J. Fonck, S.F. Paul, D.R. Roberts, E.D. Fredrickson, R. Nazikian, H.K. Park, M. Bell, N.L. Bretz, R. Budny, S. Cohen, G.W. Hammett, F.C. Jobes, D.M. Meade, S.S. Medley, D. Mueller, Y. Nagayama, D.K. Owens, E.J. Synakowski, Excitation of toroidal Alfvén eigenmodes in tftr, *Phys. Rev. Lett.* 66 (1991) 1874–1877. <http://dx.doi.org/10.1103/PhysRevLett.66.1874>.
- [3] R. White, E. Fredrickson, D. Darrow, M. Zarnstorff, R. Wilson, S. Zweber, K. Hill, Y. Chen, G. Fu, Toroidal Alfvén eigenmode-induced ripple trapping, *Phys. Plasmas* 2 (8) (1995) 2871–2873.
- [4] H. Nakanishi, T. Hochin, M. Kojima, Search and retrieval method of similar plasma waveforms, *Fusion Eng. Des.* 71 (1) (2004) 189–193.
- [5] J. Vega, A. Pereira, A. Portas, S. Dormido-Canto, G. Farias, R. Dormido, J. Sánchez, N. Duro, M. Santos, E. Sánchez, et al., Data mining technique for fast retrieval of similar waveforms in fusion massive databases, *Fusion Eng. Des.* 83 (1) (2008) 132–139.
- [6] J. Vega, Intelligent methods for data retrieval in fusion databases, *Fusion Eng. Des.* 83 (2) (2008) 382–386.
- [7] J. Vega, A. Murari, A. Pereira, A. Portas, G.A. Rattá, R. Castro, Overview of intelligent data retrieval methods for waveforms and images in massive fusion databases, *Fusion Eng. Des.* 84 (7) (2009) 1916–1919.
- [8] D. Pretty, B. Blackwell, A data mining algorithm for automated characterisation of fluctuations in multichannel timeseries, *Comput. Phys. Commun.* 180 (10) (2009) 1768–1776.
- [9] R. Jiménez-Gómez, A. Könies, E. Ascasíbar, F. Castejón, T. Estrada, L. Eliseev, A. Melnikov, J. Jiménez, D. Pretty, D. Jiménez-Rey, et al., Alfvén eigenmodes measured in the TJ-II stellarator, *Nucl. Fusion* 51 (3) (2011) 033001.
- [10] S. Yamamoto, D. Pretty, B. Blackwell, K. Nagasaki, H. Okada, F. Sano, T. Mizuchi, S. Kobayashi, K. Kondo, R. Jiménez-Gómez, et al., Studies of MHD stability using data mining technique in helical plasmas, *Plasma Fusion Res.* 5 (2010) 034–1–034–7.
- [11] S. Hamberger, B. Blackwell, L. Sharp, D. Shenton, H-1 design and construction, *Fusion Technol.* 17 (1990) 123–130.
- [12] J. Harris, M. Shats, B. Blackwell, W. Solomon, D. Pretty, S. Collis, J. Howard, H. Xia, C. Michael, H. Punzmann, Fluctuations and stability of plasmas in the H-1NF heliac, *Nucl. Fusion* 44 (2) (2004) 279.
- [13] S.R. Haskey, B.D. Blackwell, B. Seiwald, M.J. Hole, D.G. Pretty, J. Howard, J. Wach, A multichannel magnetic probe system for analysing magnetic fluctuations in helical axis plasmas, *Rev. Sci. Instrum.* 84 (9) (2013) 093501. <http://dx.doi.org/10.1063/1.4819250>. URL <http://link.aip.org/link/?RSI/84/093501/1>.
- [14] A.H. Boozer, Guiding center drift equations, *Phys. Fluids* 23 (5) (1980) 904–908. <http://dx.doi.org/10.1063/1.863080>. URL <http://link.aip.org/link/?PFL/23/904/1>.
- [15] W.D. Dhaeseleer, Flux coordinates and magnetic field structure: a guide to a fundamental tool of plasma structure, in: Springer Series in Computational Physics, 1991.
- [16] C. Nardone, Multichannel fluctuation data analysis by the singular value decomposition method. Application to MHD modes in jet, *Plasma Phys. Control. Fusion* 34 (9) (1992) 1447.
- [17] D. Pretty, A study of mhd activity in the h-1 heliac using data mining techniques, Ph.D. Thesis, 2007.
- [18] C. Fraley, A.E. Raftery, How many clusters? which clustering method? answers via model-based cluster analysis, *Comput. J.* 41 (8) (1998) 578–588.
- [19] T. Warren Liao, Clustering of time series data a survey, *Pattern Recognit.* 38 (11) (2005) 1857–1874.
- [20] K.V. Mardia, P.E. Jupp, Directional Statistics, vol. 494, Wiley, 2009.
- [21] R. Von Mises, über die ganzzahligkeit der atomgewichte und verwandte fragen, *Phys. Z* 19 (1918) 490–500.
- [22] A.P. Dempster, N.M. Laird, D.B. Rubin, Maximum likelihood from incomplete data via the EM algorithm, *J. R. Stat. Soc. Ser. B Stat. Methodol.* (1977) 1–38.
- [23] G. McLachlan, D. Peel, Finite Mixture Models, Wiley-Interscience, 2004.
- [24] K.V. Mardia, G. Hughes, C.C. Taylor, H. Singh, A multivariate von Mises distribution with applications to bioinformatics, *Canad. J. Statist.* 36 (1) (2008) 99–109.
- [25] K.V. Mardia, J.T. Kent, Z. Zhang, C.C. Taylor, T. Hamelryck, Mixtures of concentrated multivariate sine distributions with applications to bioinformatics, *J. Appl. Stat.* 39 (11) (2012) 2475–2492.
- [26] N.I. Fisher, Statistical Analysis of Circular Data, Cambridge University Press, 1995.
- [27] F. Pedregosa, G. Varoquaux, A. Gramfort, V. Michel, B. Thirion, O. Grisel, M. Blondel, P. Prettenhofer, R. Weiss, V. Dubourg, J. Vanderplas, A. Passos, D. Cournapeau, M. Brucher, M. Perrot, E. Duchesnay, Scikit-learn: machine learning in Python, *J. Mach. Learn. Res.* 12 (2011) 2825–2830.
- [28] M. Hall, E. Frank, G. Holmes, B. Pfahringer, P. Reutemann, I.H. Witten, The weka data mining software: an update, *ACM SIGKDD Explor. Newsl.* 11 (1) (2009) 10–18.
- [29] C.S. Wallace, D.L. Dowe, MML clustering of multi-state, Poisson, von Mises circular and Gaussian distributions, *Stat. Comput.* 10 (2000) 73–83.
- [30] C.S. Wallace, D.L. Dowe, Intrinsic classification by MML—the Snob program, in: Proc. 7th Australian Joint Conf. on Artificial Intelligence, World Scientific, 1994, pp. 37–44.

- [31] E. Jones, T. Oliphant, P. Peterson, et al., SciPy: open source scientific tools for Python (2001–). URL <http://www.scipy.org/>.
- [32] T.E. Oliphant, Guide to NumPy, Provo, UT (Mar. 2006). URL <http://www.tramy.us/>.
- [33] A.H. Boozer, What is a stellarator? *Phys. Plasmas* 5 (5) (1998) 1647–1655.
- [34] R. Tibshirani, G. Walther, T. Hastie, Estimating the number of clusters in a data set via the gap statistic, *J. R. Stat. Soc. Ser. B Stat. Methodol.* 63 (2) (2001) 411–423.
- [35] G. Schwarz, Estimating the dimension of a model, *Ann. Statist.* 6 (2) (1978) 461–464.

3D tomography of MHD fluctuations in the H-1NF heliac

The high resolution 2D images acquired using the synchronous imaging technique described in the paper in chapter 3 provide significant amounts of information about the mode being imaged. The 2D images covered a wedge shaped piece of plasma, potentially providing toroidal, poloidal, and radial mode structure information, which are all important in a fully 3D machine like H-1NF. To take advantage of this rich source of information, a new 3D tomographic inversion technique was developed. The tomographic inversion provides radial eigenmode structure information without requiring any radial basis functions. The radial structure is compared with theory in chapter 6. Supplementary information which may be useful for future research is included in appendix F. 90% of the research and 85% of the writing presented in this paper are my own work. The paper is also available from <http://dx.doi.org/10.1088/0029-5515/54/8/083031>.

Visible light tomography of MHD eigenmodes in the H-1NF stellarator using magnetic coordinates

S.R. Haskey, B.D. Blackwell, B. Seiwald and J. Howard

Plasma Research Laboratory, Research School of Physics and Engineering, The Australian National University, Canberra, ACT 0200, Australia

E-mail: shaun.haskey@anu.edu.au

Received 31 March 2014, revised 3 June 2014

Accepted for publication 5 June 2014

Published 23 July 2014

Abstract

A tomographic reconstruction technique is described for the inversion of a set of limited-angle high-resolution 2D visible light emission projections of global MHD eigenmodes in the H-1NF heliac. The technique is well suited to limited viewing access in toroidal devices and the strong shaping of optimized stellarator/heliotron configurations. Fluctuations are represented as a finite sum of Fourier modes characterized by toroidal and poloidal mode numbers having fixed amplitude and phase in a set of nested flux volumes in Boozer coordinates (Boozer 1980 *Phys. Fluids* **23** 904–8). Iterative tomographic inversion techniques and standard linear least-squares methods are used to solve for the complex amplitudes. The method is applied to synchronous camera images of singly charged carbon impurity ion emission at 514 nm obtained at three discrete poloidal viewing orientations (Haskey *et al* 2014 *Rev. Sci. Instrum.* **85** 033505). The 2D amplitude and phase projections provide high quality reconstructions of the radial structure of the fluctuations that are compact in Boozer space and allow clear determination of the poloidal mode number as well as some degree of toroidal mode number differentiation.

Keywords: tomography, plasma fluctuations, MHD, imaging, stellarators

 Online supplementary data available from stacks.iop.org/NF/54/083031/mmedia

(Some figures may appear in colour only in the online journal)

1. Introduction

MHD instabilities such as Alfvén eigenmodes [3, 4], sawteeth, and tearing modes can cause detrimental disruptions [5–7] and limit achievable plasma parameters. In order to identify and control these modes, accurate measurements of their internal structure are required for comparison with modelling.

The structure of MHD fluctuations in the H-1NF heliac [8, 9] exhibits a systematic dependence on magnetic configuration [10–13]. Here the tomographic imaging of the modes based on emission from singly charged carbon impurity ions at 514 nm is reported. This emission is strongly related to electron density fluctuations and weakly related to electron temperature fluctuations at typical H-1NF electron temperatures. Future work based on the ratio of tomographically inverted atomic helium transition-line emission contours at a number of wavelengths will allow absolute measurement of both the electron density and temperature fluctuations [14, 15] for comparison with theoretical predictions [16, 17].

Because of the sparseness of available measurement data in plasma physics applications, tomographic inversion

methods have generally relied on representations in terms of a small set of continuous, orthogonal basis functions such as Zernike [18, 19], and Fourier–Bessel expansions [20, 21]. A recently developed high-resolution optical synchronous imaging technique [2], which uses an intensified camera with gated exposure phase-locked to mode fluctuations allows high-resolution imaging of quasi-coherent global plasma eigenmodes with frequencies in the kHz to MHz range. With modern array detectors, these images represent millions of lines of sight which, subject to viewing access, observe a wedge-shaped volume of plasma. Under appropriate assumptions, the measurements can allow high quality tomographic reconstruction of the fluctuation structure to be obtained.

The novel tomographic technique described in this paper is applied to invert synchronously acquired sequences of 2D visible-light projections of plasma eigenmode structures acquired at multiple poloidal viewing angles [2]. The H-1NF fluctuation structures can generally be represented in terms of a small set of Fourier modes in Boozer coordinates [1, 22] on a high-resolution discretized radial flux grid. The linear mapping between projections and the helical plasma

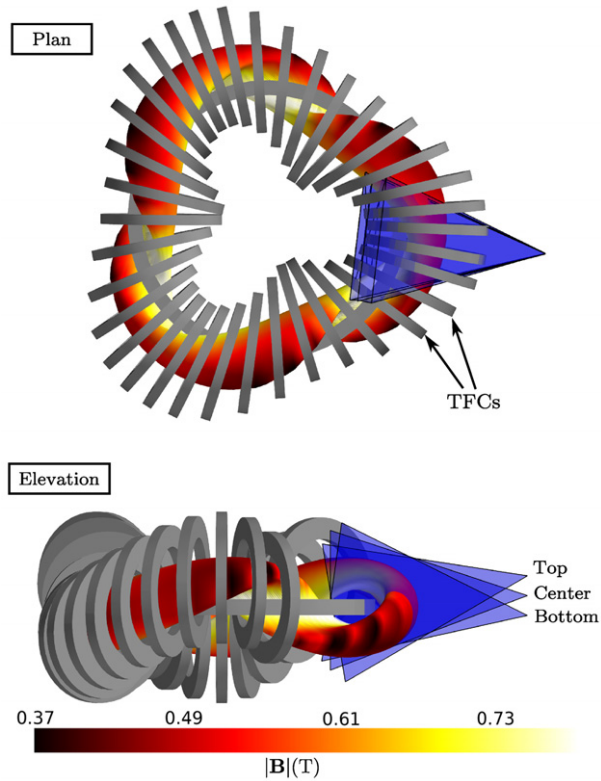


Figure 1. Details of the three different camera views used to acquire the data on H-1NF. The top plot shows how the toroidal field coils (TFCs) limit the field of view. A typical H-1NF plasma is shown, with the surface colour representing the magnetic field strength.

modes can then be inverted using standard least-squares fitting techniques to obtain the mode amplitudes and phases in the discretized flux regions. The availability of three independent views of the plasma helps determine the helical mode numbers by comparing the best fit error between different candidate mode helicities. Alternatively, the basis set of modes can be imposed *a priori* using information from other diagnostics such as magnetic probe arrays [23, 24]. Provided the number of reconstructed mode helicities is small, the radial structure can be recovered with high resolution without the need for additional *a priori* information or smoothing constraints. Here, the Fourier basis functions are represented in Boozer magnetic coordinates, although other magnetic or non-magnetic coordinate systems can be used.

In this work the tomography technique is applied to invert projections of both odd and even parity poloidal modes observed in H-1NF. It is found that the Boozer representation allows the projection data to be closely fitted using only a single helical harmonic component, suggesting that this is an optimal coordinate system for representing these modes in H-1NF. Reconstruction using a Fourier series in Boozer space allows the tomography of strongly shaped plasmas such as H-1NF to be handled in a natural way. The approach is well suited to detector-array-based diagnostic systems that image bremsstrahlung [25], spectral lines [2] or soft x-ray emission [26].

This paper is organized as follows. Section 2 provides details of the experimental data used in the tomographic reconstructions and section 3 describes the tomographic

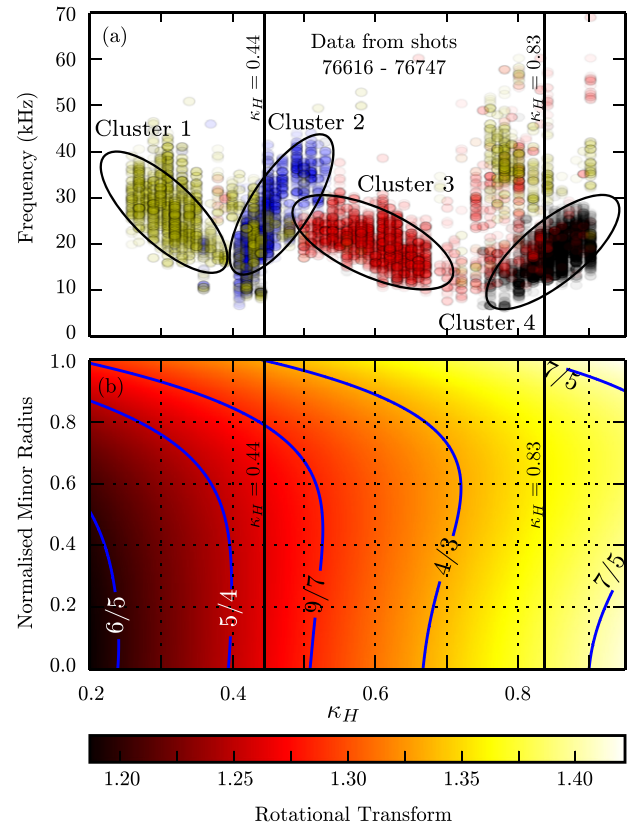


Figure 2. (a) Fluctuation clusters in H-1NF as a function of frequency and machine configuration parameter κ_H . Measurements having similar properties are grouped together using a data mining technique. (b) Rotational transform profile of the magnetic field as a function of κ_H with the location of some low-order rational surfaces shown. See text for more detail.

inversion technique including some of the issues involved in the coordinate transformation of the lines of sight. Section 4 provides details of the tomographic inversion, and mode number identification for both odd and even parity eigenmodes in H-1NF.

2. Data used in the tomographic reconstructions

The H-1NF heliac is a three field-period helical axis stellarator with major radius $R = 1$ m and average minor radius $\langle r \rangle \approx 0.2$ m (figure 1). H-1NF is a flexible machine that allows access to an extensive range of magnetic configurations, making it well suited to explore the relationship between plasma behaviour and magnetic configuration [11]. By varying the ratio of the current in the control helical winding to the current in the TFCs (κ_H) it is possible to modify the rotational transform profile of the magnetic field as shown in figure 2(b).

As seen in figure 2(a), the nature of the magnetic fluctuations in 0.5 T, radio-frequency-heated (7 MHz, 40 kW) H/He plasmas [12, 13] in H-1NF is strongly dependent on rotational transform. The fluctuations measured using a magnetic probe array from a 131 shot κ_H scan are classified into clusters using data mining techniques [27]. Each cluster represents a grouping of measured fluctuations that appear similar in spatial structure to the magnetic probe array, and are therefore likely to be due to the same type of

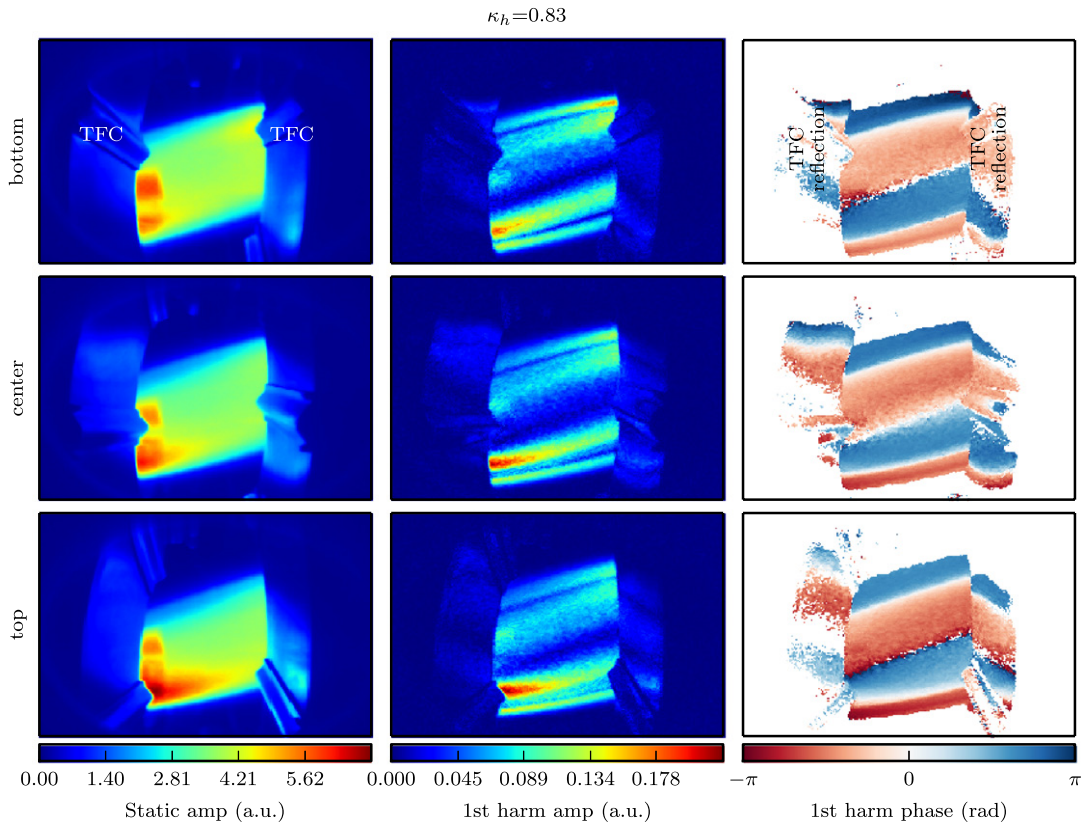


Figure 3. The static amplitude, 1st harmonic amplitude and 1st harmonic phase of the three separate camera views shown in figure 1. The fluctuation shown had a frequency of 20 kHz, and spontaneously appears in H-1NF discharges with a magnetic configuration of $\kappa_H = 0.83$. The phase images have been thresholded based on the amplitude to remove phase measurements due to noise.

fluctuation. Clustering allows the behaviour of certain classes of fluctuations to be studied as a function of plasma parameters.

Tomographic reconstructions of two fluctuation structures at $\kappa_H = 0.44$, and $\kappa_H = 0.83$ are presented here. These are representative of the behaviour of modes that belong to cluster2 and cluster4 in figure 2(a). The waves have frequencies between 20 kHz and 25 kHz and occur where the zero shear in the magnetic rotational transform is near the $t = 5/4$ and $t = 4/3$ resonances respectively.

The relatively cool electron temperatures in these plasmas means that carbon ion emission at 514 nm is radiated from all regions in the plasma, making it suitable for revealing the structural details of the mode, through its dependence on impurity ion density, electron density (n_e) and electron temperature (T_e). Analysis of photon emissivity using ADAS models [28] shows an insensitivity to changes in electron temperature when $T_e > 25$ eV, which is typically the case for a large portion of the plasma on H-1NF [14]. Therefore, the tomographic inversions of the intensity fluctuations presented in this paper are closely related to changes in the electron density.

The projection images of the fluctuation structures were obtained using a Princeton Instruments PiMAX 4 intensified gated camera and a synchronous imaging technique [2]. The camera's gated exposure is phase-locked to the mode fluctuation period using a magnetic probe signal [23] as input to a phased-locked loop that produces the camera timing pulses. The plasma is viewed through the gap between adjacent TFCs at three separate camera inclinations in the poloidal cross-section (figure 1), the range of viewing angles ($\pm 10^\circ$ wrt the

horizontal) being limited by the size of the port window. The available views provide good coverage of the poloidal cross-section, but are of limited toroidal extent as revealed in figure 1.

Sixteen camera images equispaced in phase over one cycle of the fluctuation were acquired over a sequence of shots. The same camera and lens setup is used for all three views. To account for shot-to-shot variability, the images are normalized for equal integrated photo-electron counts with the normalization for each view being treated separately. A white calibration removes systematic variations in the camera response and a black image is used to remove offsets and fixed pattern noise [2]. The images were decomposed into a Fourier series, allowing the static emission level, fundamental harmonic, and higher harmonics (up to 8) to be isolated. The static emission, and the amplitude and phase projections of the first harmonic for the fluctuation at $\kappa_H = 0.83$ are shown in figure 3. The images show a clear fundamental mode structure. The Mirnov probe signal, Mirnov power spectral density and line-averaged central electron density for a typical shot that was part of the acquisition sequence for this set of images is shown in figure 4.

3. The tomographic reconstruction technique

3.1. Representation of the perturbation structure

A scalar perturbation (such as density or light emission) with frequency f_0 can be represented as a sum of modes, each having

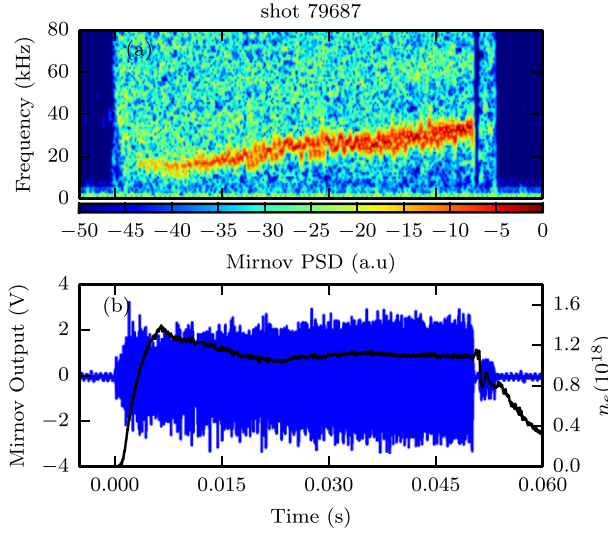


Figure 4. (a) Power spectral density of the Mirnov signal for the mode shown in figure 3. (b) Raw time trace of the amplified Mirnov signal, and line-averaged central electron density.

a toroidal and poloidal mode number (n and m):

$$\epsilon(s, \theta, \phi, t) = \sum_{n,m} G_{n,m}(s) \cos(n\phi + m\theta + 2\pi f_0 t + \psi_{n,m}(s)) \quad (1)$$

where $s = s(x, y, z)$ is the normalized flux (radial variable), and $\phi = \phi(x, y, z)$ and $\theta = \theta(x, y, z)$ are the toroidal and poloidal coordinates in the chosen coordinate system (Boozer coordinates is used for the case studies shown in figure 4). The amplitude (G) and phase (ψ) of the modes are assumed to be flux surface quantities in that they depend only on the ‘radial’ variable s .

Initially we treat the case of a perturbation that can be represented by a single toroidal and poloidal mode number and return to the sum of multiple modes at the end of this section.

3.2. Representation of the projections

The line of sight (LOS) measurement (such as the brightness of a pixel) is given by

$$P = \int_L \epsilon(s, \theta, \phi, t) dl \quad (2)$$

where L is the path along the LOS. Splitting the continuous LOS into J separate intervals of equal length Δl gives an approximate discretized version of the line integral

$$P = \sum_{j=0}^J \epsilon(s_j, \theta_j, \phi_j, t) \Delta l \quad (3)$$

where the subscript j represents the value at the j th interval. This is shown in figure 5 where a LOS passes through a series of nested flux regions.

Using a camera synchronized to the fundamental plasma mode frequency f_0 , it is possible to capture a phase-resolved sequence of projection images [2]. After Fourier transforming

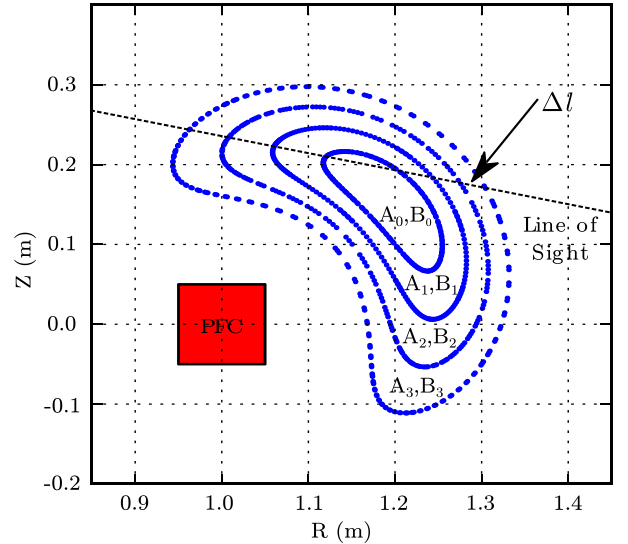


Figure 5. A typical H-1NF plasma cross-section including the poloidal field coil (PFC). The plasma is split into a series of nested flux regions, where the amplitude and phase (G_n, ψ_n), or real and imaginary components of the mode (A_n, B_n) are constant. The lines of sight are broken up into small length elements, Δl . While this image is shown in a single poloidal cross section, the method is generalized to lines of sight in any direction.

this sequence, the resulting complex pixel brightness for the fundamental component is given by

$$\mathcal{P}(f_0) = \sum_{j=0}^J \left\{ \frac{1}{2} G_j \cos(n\phi_j + m\theta_j + \psi_j) + i \frac{1}{2} G_j \sin(n\phi_j + m\theta_j + \psi_j) \right\} \Delta l \quad (4)$$

where $G_j = G(s_j)$ and $\psi_j = \psi(s_j)$ are the amplitudes and phases of the mode at LOS point j .

Separating the real ($M_R = \text{Re}\{\mathcal{P}(f_0)\}$) and imaginary components ($M_I = \text{Im}\{\mathcal{P}(f_0)\}$) and letting $c_j = \cos(n\phi_j + m\theta_j)$, and $\sigma_j = \sin(n\phi_j + m\theta_j)$ gives

$$M_R = \frac{1}{2} \sum_{j=0}^J G_j [c_j \cos(\psi_j) - \sigma_j \sin(\psi_j)] \Delta l \quad (5)$$

$$M_I = \frac{1}{2} \sum_{j=0}^J G_j [\sigma_j \cos(\psi_j) + c_j \sin(\psi_j)] \Delta l. \quad (6)$$

Representing the plasma domain as a set of N discrete nested flux surface regions $\{s_n | n = 0, 1, \dots, N-1\}$, and defining $A_n = \frac{1}{2} G_n \cos(\psi_n)$ and $B_n = \frac{1}{2} G_n \sin(\psi_n)$ allows equations (5) and (6) to be written as

$$M_R = \sum_{n=0}^{N-1} \sum_{j \in J_n} [c_j A_n - \sigma_j B_n] \Delta l \quad (7)$$

$$M_I = \sum_{n=0}^{N-1} \sum_{j \in J_n} [\sigma_j A_n + c_j B_n] \Delta l \quad (8)$$

where the set J_n selects the segments of the LOS that are in the flux region n : $J_n = \{j \in \mathbb{N} | s_n \leq s_j < s_{n+1}\}$.

A set of X pixels corresponding to X lines of sight, provides a set of $2X$ linear equations (equations (7) and (8) for each LOS), which can be represented in matrix form:

$$\mathbf{M} = \mathbf{ST} \quad (9)$$

where:

$$\mathbf{M} = (M_{R,0}, M_{I,0}, M_{R,1}, M_{I,1}, \dots, M_{R,X}, M_{I,X})^T \quad (10)$$

$$\mathbf{T} = (A_0, B_0, A_1, B_1, \dots, A_{N-1}, B_{N-1})^T \quad (11)$$

$$\mathbf{S} = \begin{pmatrix} C_{0,0} & -S_{0,0} & C_{0,1} & -S_{0,1} & \dots & C_{0,N-1} & -S_{0,N-1} \\ S_{0,0} & C_{0,0} & S_{0,1} & C_{0,1} & \dots & S_{0,N-1} & C_{0,N-1} \\ C_{1,0} & -S_{1,0} & C_{1,1} & -S_{1,1} & \dots & C_{1,N-1} & -S_{1,N-1} \\ S_{1,0} & C_{1,0} & S_{1,1} & C_{1,1} & \dots & S_{1,N-1} & C_{1,N-1} \\ \vdots & \vdots & \vdots & \vdots & \ddots & \vdots & \vdots \\ C_{X,0} & -S_{X,0} & C_{X,1} & -S_{X,1} & \dots & C_{X,N-1} & -S_{X,N-1} \\ S_{X,0} & C_{X,0} & S_{X,1} & C_{X,1} & \dots & S_{X,N-1} & C_{X,N-1} \end{pmatrix} \quad (12)$$

The first and second subscripts on $S_{x,n}$ and $C_{x,n}$ refer to the LOS (or pixel), and flux region respectively. The elements of \mathbf{S} are calculated as follows:

$$S_{x,n} = \sum_{j \in J_n} \sigma_j \Delta l, \quad C_{x,n} = \sum_{j \in J_n} c_j \Delta l. \quad (13)$$

The aim of tomographic inversion is to recover \mathbf{T} from equation (9). This gives the values of A_n and B_n in each flux region, allowing the amplitude and phase of the associated Fourier component to be recovered as follows:

$$\psi_n = \text{atan2}(B_n, A_n), \quad G_n = \sqrt{(2B_n)^2 + (2A_n)^2}. \quad (14)$$

The residual error in the tomographic reconstruction can be estimated using

$$E = \sqrt{\sum (M - ST)^2} \quad (15)$$

where $(\cdot)^2$ is performed element-wise and the sum is over all elements. This error is very useful for comparing the quality of various fits as demonstrated in section 4.1.

In practice, it is found that the fluctuation structures in H-1NF can be well fitted by summing over a small number of Fourier modes as given in equation (1). This type of description is generally suitable for many types of plasma waves in toroidal devices, such as TAE, HAE and EAE's [3]. The additional modes, $(n_1, m_1), (n_2, m_2), \dots$, can be accommodated by augmenting the matrices \mathbf{S} and \mathbf{T} : $\mathbf{S} = (S_{n1,m1}, S_{n2,m2}, S_{n3,m3}, \dots)$, $\mathbf{T} = (T_{n1,m1}, T_{n2,m2}, T_{n3,m3}, \dots)$. Subsequent basis modes can be chosen by finding the best fit basis mode to the remaining signal after subtracting the contribution from the dominant mode. If many basis modes are required to fit the fluctuation it may be worth trying different coordinate systems where the representation of the fluctuation may be more compact. The number of radial flux regions should be chosen to maximize the radial resolution given the required number of basis functions and there should be good *a priori* reasons for including multiple basis functions as is discussed in section 4.

The dc emission profile is obtained tomographically by setting $n = 0, m = 0$ and fitting to the dc component of the

pixel intensities. This allows the change in emission due to the mode to be normalised to the dc emission in each flux annulus ($d\epsilon/\epsilon$). Only using the $n = 0, m = 0$ basis function assumes that the dc emissivity is a flux surface quantity. Other mode numbers can be included if this is not a good approximation.

The radial profile information, \mathbf{T} can be recovered from equation (9) in a single step using the Moore–Penrose pseudoinverse of \mathbf{S} which we refer to as the direct solution. If the dimensions of \mathbf{S} , are sufficiently small, this method is very fast, though it scales poorly as the dimensions of \mathbf{S} increase. The approach can deliver less smooth solutions than alternatives, although this can be overcome using some form of regularization. There are also iterative techniques such as the algebraic reconstruction technique (ART) [29, 30] and simultaneous iterative reconstruction technique (SIRT) [31] that perform more efficiently for large \mathbf{S} . A thorough explanation of these techniques and tomography in general is given in [32]. Each of these methods produced similar results when applied to the data shown in section 4. The direct solution approach has been used for all the results presented in this paper because it was found to be sufficiently smooth, and was substantially faster than ART and SIRT.

3.3. Coordinate transformation details

The coordinates (s, θ, ϕ) at each interval along the lines of sight must be known to calculate $S_{x,n}$ and $C_{x,n}$. The chosen coordinate system should minimize the number of basis functions required to represent the fluctuation, simplifying the tomographic inversion. Boozer coordinates, a magnetic coordinate system, are commonly used for fully three-dimensional stellarators and are used for the results in section 4. This transformation can be evaluated numerically using a coordinate system based on the equilibrium plasma magnetic field. The VMEC code [33] is used to solve for the plasma equilibrium, H-1NF plasmas typically have a very low $\beta \approx 10^{-4}$ [16] so the equilibrium magnetic field is generally quite similar to the vacuum magnetic field. The BOOZ_XFORM code (part of the STELLOPT package, which includes VMEC) uses this equilibrium to provide the transformation from Boozer coordinates to lab coordinates (i.e. $x = x(s, \theta, \phi)$, $y = y(s, \theta, \phi)$, $z = z(s, \theta, \phi)$). However, the inverse of this transformation, $s = s(x, y, z)$, $\phi = \phi(x, y, z)$ and $\theta = \theta(x, y, z)$ is required for calculating the projection weight matrix \mathbf{S} .

An efficient method to calculate the inverse transformation uses a dense regular grid in Boozer space that has been transformed to lab coordinates. The forward transformation is relatively fast because the magnetic field is described in terms of a Fourier series. Using the irregular grid in lab coordinates, a three dimensional interpolation routine is used to approximate the Boozer coordinates at the points along the lines of sight. Care is also taken in regions where the plasma surface is concave in order to protect against the algorithm calculating interpolates along lines of sight that have exited the plasma.

Because the coordinates of the LOS are transformed to Boozer coordinates (although another coordinate system can be used if appropriate), the technique is general enough to be applied to unconventional viewing geometries in tokamaks

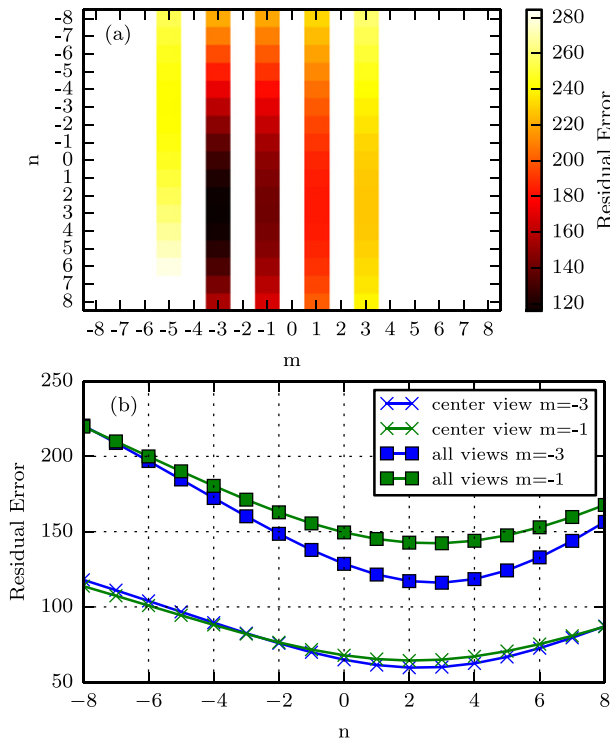


Figure 6. (top) Tomographic reconstruction error (equation (15)) using a single mode with radial phase variation to fit the data from all three views shown in figure 3. Basis modes with large residual errors have been clipped. The technique shows a clear ability to discriminate between poloidal mode numbers using the views on H-1NF. (bottom) The toroidal mode numbers can also be discriminated reasonably well considering the minimal toroidal extent of the views used. This is shown clearly for a variety of n numbers with $m = -3$ and -1 using all three views, and using just the centre view.

and is well suited to strongly shaped devices such as heliotrons/stellarators where simplified viewing geometries are not available. This is of particular importance to fusion relevant devices where there is limited access and port space.

4. Tomography of plasma structures in H-1NF

4.1. Determining mode numbers

Before performing the tomographic inversion, a set of candidate basis modes must be chosen. This choice can be guided by information from other diagnostics such as magnetic probe arrays or from theoretical modelling. The projections also self-consistently include a great deal of information that constrains the set of allowable helical mode numbers.

Using many trial modes, and calculating the error in the best fit (equation (15)), it is possible to determine which combination of mode numbers provide the best fit to the data. This is demonstrated in figure 6(a) where a single mode with $-8 \leq n \leq 8$ and $-8 \leq m \leq 8$ is used in the tomographic inversion of the data from three views shown in figure 3. Odd poloidal harmonics are clearly favoured by virtue of the phase-reversal across the centre of the poloidal projections (see figure 3). Of the odd poloidal harmonics, $m = -3$ gives the best fit. This is in accord with analysis of the magnetic probe arrays. The $m = -1$ modes also show an acceptable degree of

fit, though higher m structures are clearly incompatible with the number of radial nodes in the projection data.

Figure 6 also reveals that, in spite of the restricted toroidal coverage (see figure 1), the system shows some limited ability to discriminate between toroidal mode numbers. Including new views at other toroidal locations would provide substantially more toroidal information that would help to identify unambiguously the toroidal mode numbers. For this particular set of images, a toroidal mode number of 3 is favoured, although 1, 2 and 4 also provide acceptable fits. Analysis of the magnetic probe data indicates a toroidal mode number $n = 4$. The slight inconsistency with the camera projections could perhaps be attributed to small errors in the camera registration.

4.2. Fluctuation radial structure and inversion accuracy

The data shown in the left column of figure 3 is used to calculate the radial structure of the static (dc) emissivity profile figure 7. 30 radial flux regions evenly spaced in \sqrt{s} were used to obtain this reconstruction. The radial profile of the static emissivity (ϵ) is used to normalize the change in emissivity ($d\epsilon$) due to the mode in the following discussion.

The tomographic inversion of the data in figure 3 using a $(4, -3)$ mode and 30 radial flux regions (evenly spaced in \sqrt{s}) is shown in figure 8. This mode was chosen because it agreed best with analysis of magnetic probe data and provides a low reconstruction error (figure 6). The best fit to the projection is accurate across the full toroidal and poloidal extent of all three views. The radial structure of the mode normalized to the dc emissivity (figure 7) is shown in the left column of figure 8. As was discussed in section 2 these radial profiles relate to changes in electron and impurity ion density due to the fluctuation.

The radial profiles are smooth, and show that the mode is radially localized to the outer half of the plasma. The phase of the mode (figure 8(b)) is constant where the amplitude is large ($0.55 < \sqrt{s} < 0.9$) which is to be expected for a propagating wave in a wave guide that is represented in an appropriate coordinate system. The phase starts to vary considerably for $\sqrt{s} < 0.5$, however, this is not surprising because the phase is not a reliable quantity in the presence of noise, when the amplitude is small.

Figure 9 shows the effects of varying the number of flux regions while using the single best fit mode, and the effects of including multiple basis modes for the same data shown in figure 3. In this case, there are only marginal gains when the number of flux regions is increased beyond 20 and there is a small advantage to using two basis modes, however the effect of this second mode is quite small in comparison to the first best fit basis mode. There are minimal benefits to including any more than 2 basis modes.

A basis set of $(4, -3)$ and $(5, -4)$ for the $\kappa_H = 0.83$ fluctuation improves the fit by 30%. However, a similar reduction in reconstruction error is obtained using $(4, -3)$ and $(5, -2)$ modes, even though there is no reason to expect the latter mode to be present. Improved fits can be obtained using a large number of possible second mode helicities, illustrating that there should be good *a priori* reasons for including a second mode in the basis set, and that additional toroidally displaced plasma views are desirable. In spite of the

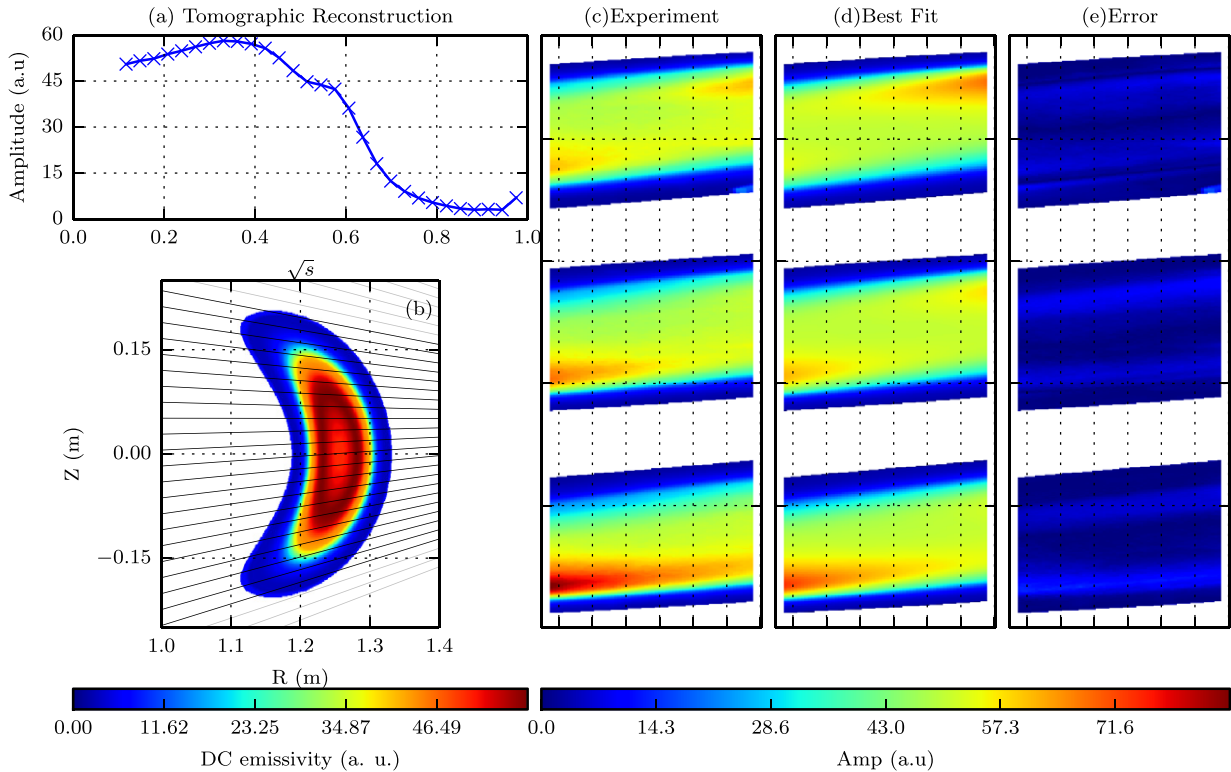


Figure 7. Tomographic inversion of the dc component of the camera images shown in figure 3. The radial structure of the amplitude is shown in (a). (b) shows a poloidal cross-section and a small subset of LOS from the central camera view. The experimental and best fit amplitude (c), (d) and error in the best fit (e) are also shown. Only a $n = 0, m = 0$ basis function was used which assumes the dc emissivity is a flux surface quantity.

improvement to the fit, the amplitude of the second even parity mode is relatively small compared to the $(4, -3)$ component. That the reconstruction of the fluctuation structure is compact (only a single helical mode is required) indicates that the camera view is well registered with respect to the coordinate system, and that Boozer coordinates are a ‘natural’ basis for the plasma wave. Some examples of theoretical eigenmode structures which also consist of a single dominant mode are shown in [16].

For comparison, the tomographic inversion of the even-parity projection data at $\kappa_H = 0.44$ is shown in figure 10. Here a single $(5, -4)$ helical mode was fit satisfactorily to the data. As for the previous case, the fit is excellent, and the mode radial structure is smooth and localized beyond mid-radius. Animated gif files illustrating the quality of the reconstruction using one and two basis mode are available online from stacks.iop.org/NF/54/083031/mmedia and stacks.iop.org/NF/54/083031/mmedia respectively. In this case, the phase variation with the radial coordinate is larger than in figure 8. Performing the tomographic inversions with the phase constrained to be constant results in an almost identical amplitude profile but with a slightly poorer quality of fit.

The tomographic inversions for the $\kappa_H = 0.44$ case (figure 11) were also performed using each of the views separately. In all cases the reconstructions are similar suggesting that one viewing location can provide sufficient information for the tomographic inversion in the case where a single Fourier mode is dominant. This could be important

to fusion relevant devices where viewing access is limited. The multiple views, however, provide a significant advantage when trying to discriminate between different poloidal mode numbers when *a priori* information is unavailable. For example, the difference in the tomographic reconstruction error between the best fit modes with $m = -3$ and $m = -1$ increases threefold when using all three views compared to a single view alone (figure 6(b)).

4.3. Noise tolerance

Gaussian noise of root mean square (rms) amplitude comparable to the mode fluctuation signal was added to the real and imaginary components of the original experimental data shown in figures 3 and 8 to test noise sensitivity. The noise added to each of the views was independent, as was the noise added to the real and imaginary parts. Figure 12 shows the original amplitude from the centre image along with the noisy image. The tomographic inversions are close despite the significant reduction in the signal-to-noise ratio. This tolerance to noise is due to the large number of measurements available and the fact that only a single harmonic component is fitted. This is particularly important for low amplitude modes and high-speed imaging where the reduced exposure time reduces the signal-to-noise ratio.

5. Conclusion

A tomographic reconstruction technique that takes advantage of high-resolution 2D synchronous imaging and high-speed

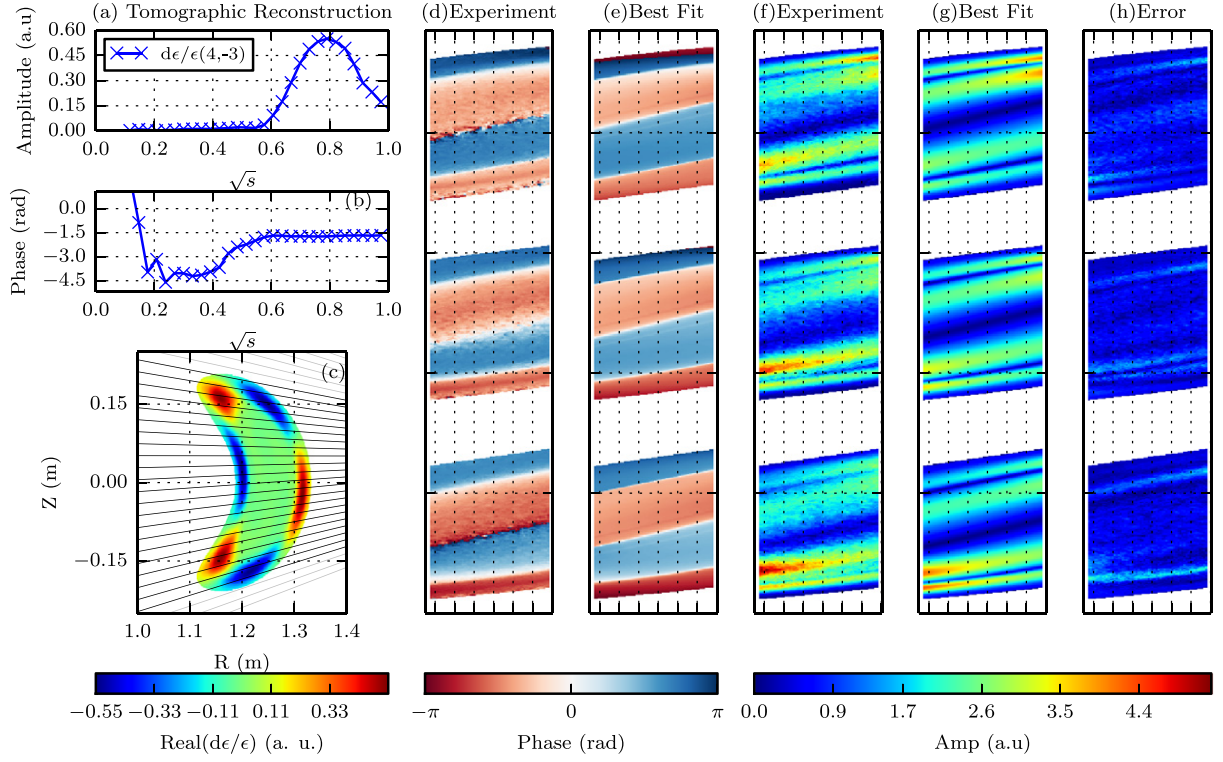


Figure 8. Details of the tomographic inversion of the camera images shown in figure 3 using a $(4, -3)$ mode for a fluctuation at $\kappa_H = 0.83$. The radial structure of the amplitude and phase are shown in (a) and (b). (c) shows a poloidal cross-section with the real part of the mode normalized to the dc emissivity and a small subset of LOS from the central camera view. The experimental and best fit phase (d), (e), amplitude normalized to the dc emissivity (f), (g) and error in the best fit (h) are also shown. The error is the Euclidean distance between the phasors for each pixel in the experimental and best fit re-projection data. The error is generally low demonstrating that the tomographic inversion is extremely good.

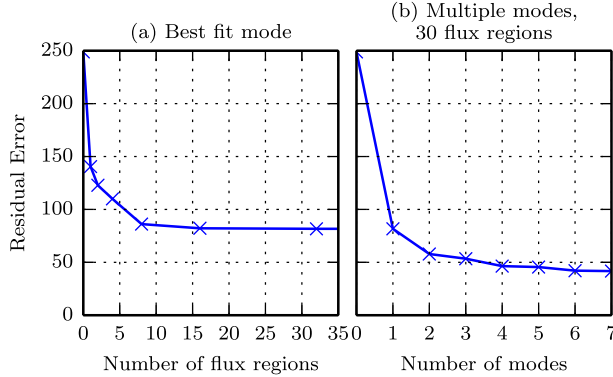


Figure 9. The behaviour of the residual error as the number of flux regions is increased using the best fit basis mode (a), and as the number of basis modes is increased with 30 flux regions (b). For (b), all combinations of basis modes include the best fit basis mode. The residual error for zero flux regions and zero modes is shown to indicate the residual error before trying to fit a mode ($ST = 0$ in equation (15)).

imaging of MHD fluctuations has been described. The MHD structures are represented as a sum of Fourier modes with discrete amplitudes and phases in a series of nested magnetic flux regions. This allows the inversion to be represented as a standard linear algebra problem which can be solved using proven tomographic inversion techniques such as ART, SIRT and standard linear least-squares methods. The examples given in this paper used Boozer coordinates to represent the

modes, although the technique can easily be adapted to other coordinate systems if appropriate. The utility of the technique has been demonstrated on images obtained in 514 nm carbon ion impurity light of two different ≈ 25 kHz MHD structures that appear spontaneously in 0.5 T H/He discharges on the H-1NF heliac.

A single basis mode provides a good quality fit for the fluctuations shown in this paper indicating that their structure is well represented in Boozer coordinates. Including a second mode reduces the residual error further, providing a very high quality fit; however, the amplitude of the second basis mode is small compared to the dominant basis mode and it is not clear which second basis mode should be used as many of them can be used to improve the fit quality. Therefore, for these fluctuations, including a second mode provides minor benefits. For cases where the exact structure of the mode is important, such as in comparisons between a non-linearly saturated MHD mode structure and linearized theoretical predictions, including these additional basis modes may be critical. Additionally, if harmonics of the dominant frequency are generated by the fluctuation, these should also be included in the analysis.

The technique provides information to aid in toroidal and poloidal mode number identification, produces high quality tomographic reconstructions of the radial structure of the fluctuations and is general enough to apply to strongly shaped plasmas such as those in optimized stellarator/heliotron configurations as well as unconventional viewing geometries

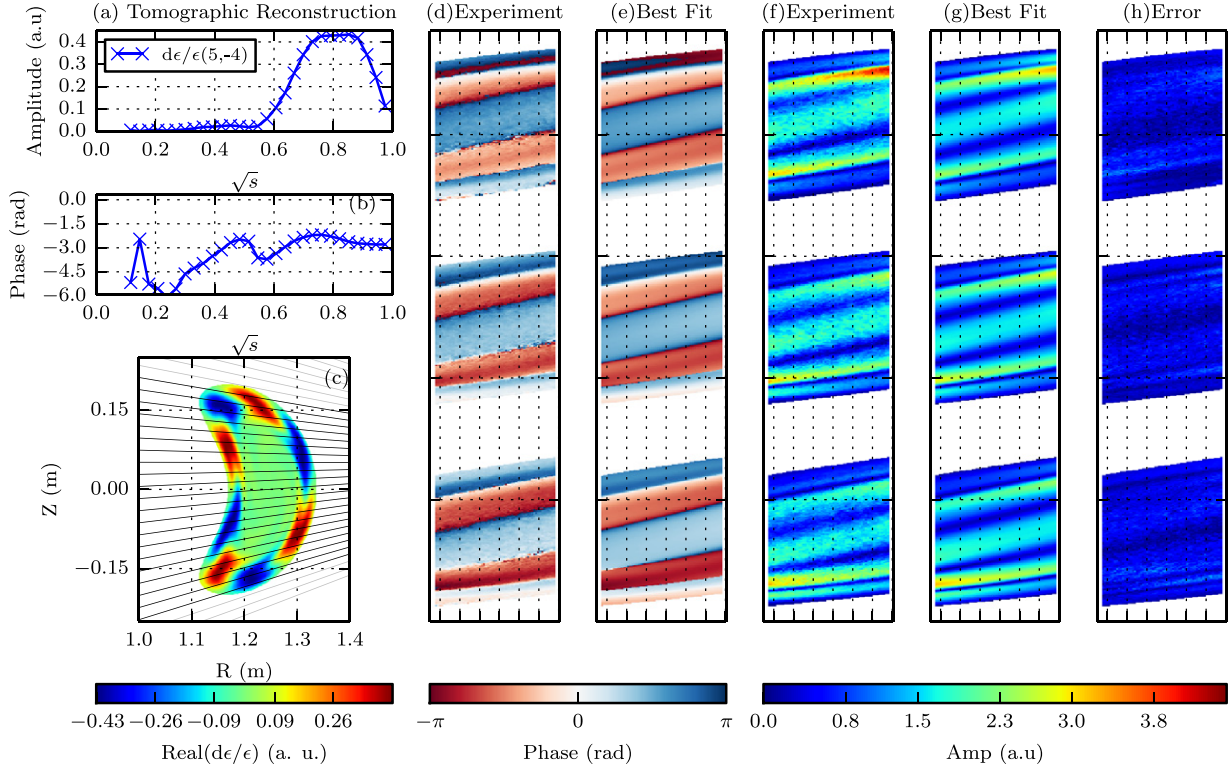


Figure 10. Details of the tomographic inversion of a fluctuation at $\kappa_H = 0.44$. The subplots are the same as in figure 8. The tomographic inversion provides a high quality fit using a $(5, -4)$ mode.

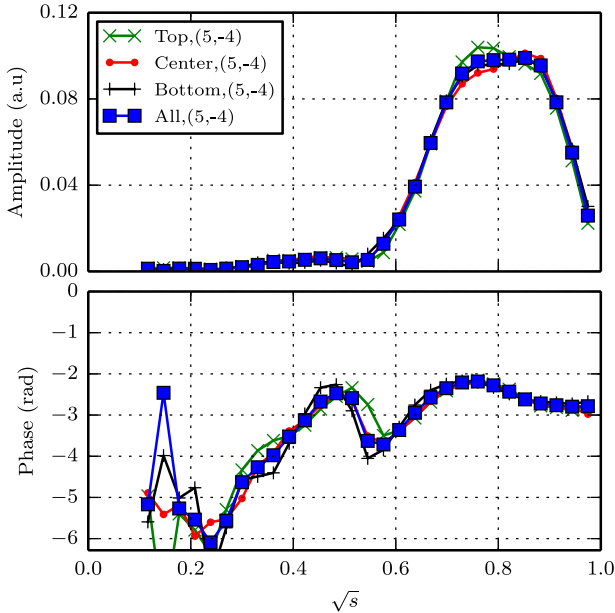


Figure 11. Tomographic reconstruction of the fluctuation at $\kappa_H = 0.44$ using the $(5, -4)$ basis mode for single views, and using all views.

in tokamaks. Additionally, the technique is relatively immune to noise, and can be applied to many different camera systems such as those that measure bremsstrahlung, spectral lines or soft x-ray emission. This combination of uses is particularly important for current and future fusion research devices where there is limited access and port space.

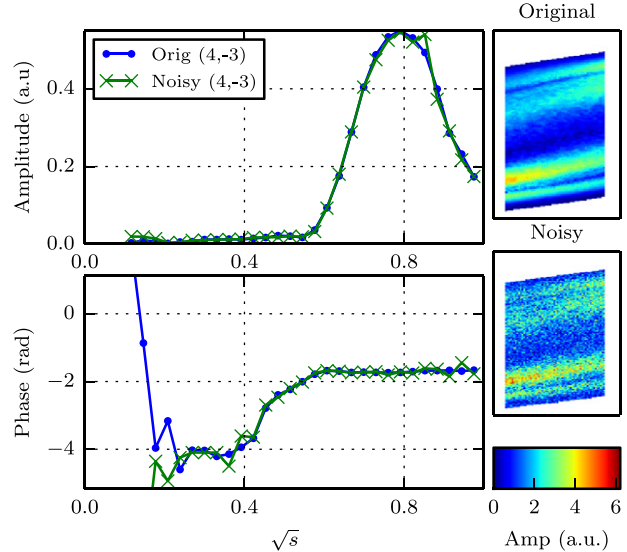


Figure 12. Details of the tomographic inversion using the original experimental data with and without a significant amount of Gaussian noise added. The reconstructions are similar showing a good tolerance to noise. All three viewing locations were used, but only the images from the centre view are shown.

Acknowledgments

The authors would like to thank the H-1NF team for continued support of experimental operations and the referees for comments and suggestions that have improved this paper. This work was supported by the Education Investment Fund under the Super Science Initiative of the Australian

Government. SRH wishes to thank AINSE Ltd. for providing financial assistance to enable this work on H-1NF to be conducted. JH and BB acknowledge support from the Australian Research Council Discovery, grant numbers DP110104833 and DP0666440 respectively.

References

- [1] Boozer A.H. 1980 Guiding center drift equations *Phys. Fluids* **23** 904–8
- [2] Haskey S.R., Thapar N., Blackwell B.D. and Howard J. 2014 Synchronous imaging of coherent plasma fluctuations *Rev. Sci. Instrum.* **85** 033505
- [3] Heidbrink W.W. 2008 Basic physics of Alfvén instabilities driven by energetic particles in toroidally confined plasmas *Phys. Plasmas* **15** 055501
- [4] Fasoli A. et al 2007 Progress in the ITER physics basis: chapter 5. Physics of energetic ions *Nucl. Fusion* **47** S264
- [5] Wong K.L. et al 1991 Excitation of toroidal Alfvén eigenmodes in TFTR *Phys. Rev. Lett.* **66** 1874–7
- [6] White R.B., Fredrickson E., Darrow D., Zarnstorff M., Wilson R., Zweber S., Hill K., Chen Y. and Fu G. 1995 Toroidal Alfvén eigenmode-induced ripple trapping *Phys. Plasmas* **2** 2871–3
- [7] Hender T.C. et al 2007 Progress in the ITER physics basis: chapter 3. MHD stability, operational limits and disruptions *Nucl. Fusion* **47** S128–202 (beginning of chapter)
- [8] Hamberger S.M., Blackwell B.D., Sharp L.E. and Shenton D.B. 1990 H-1 design and construction *Fusion Technol.* **17** 123–30
- [9] Jiménez-Gómez R. et al 2011 Alfvén eigenmodes measured in the TJ-II stellarator *Nucl. Fusion* **51** 033001
- [10] Blackwell B.D. et al 2009 Configurational effects on Alfvénic modes and confinement in the H-1NF heliac arXiv:0902.4728
- [11] Harris J.H., Shats M.G., Blackwell B.D., Solomon W.M., Pretty D.G., Collis S.M., Howard J., Xia H., Michael C.A. and Punzmann H. 2004 Fluctuations and stability of plasmas in the H-1NF heliac *Nucl. Fusion* **44** 279
- [12] Pretty D.G. 2007 A study of MHD activity in the H-1 heliac using data mining techniques *PhD Thesis* The Australian National University
- [13] Pretty D.G. and Blackwell B.D. 2009 A data mining algorithm for automated characterisation of fluctuations in multichannel timeseries *Comput. Phys. Commun.* **180** 1768–76
- [14] Ma S., Howard J., Blackwell B.D. and Thapar N. 2012 Measurements of electron density and temperature in the H-1 heliac plasma by helium line intensity ratios *Rev. Sci. Instrum.* **83** 033102
- [15] Ma S., Howard J. and Thapar N. 2011 Relations between light emission and electron density and temperature fluctuations in a helium plasma *Phys. Plasmas* **18** 083301
- [16] Bertram J., Blackwell B.D. and Hole M.J. 2012 Ideal-magnetohydrodynamic theory of low-frequency Alfvén waves in the H-1 heliac *Plasma Phys. Control. Fusion* **54** 055009
- [17] Bertram J., Hole M.J., Pretty D.G., Blackwell B.D. and Dewar R.L. 2011 A reduced global Alfvén eigenmodes model for Mirnov array data on the H-1NF heliac *Plasma Phys. Control. Fusion* **53** 085023
- [18] Granetz R.S. and Smeulders P. 1988 X-ray tomography on JET *Nucl. Fusion* **28** 457
- [19] Howard J. and Persson M. 1992 Cold bubble formation during density limit disruptions *Nucl. Fusion* **32** 361–77
- [20] Nagayama Y. 1987 Tomography of $m = 1$ mode structure in tokamak plasma using least-square-fitting method and Fourier-Bessel expansions *J. Appl. Phys.* **62** 2702–6
- [21] Franz P., Marrelli L., Murari A., Spizzo G. and Martin P. 2001 Soft x ray tomographic imaging in the RFX reversed field pinch *Nucl. Fusion* **41** 695
- [22] D'haeseleer W.D. 1991 *Flux Coordinates and Magnetic Field Structure: A Guide to a Fundamental Tool of Plasma Structure* Springer Series in Computational Physics (Berlin: Springer)
- [23] Haskey S.R., Blackwell B.D., Seiwald B., Hole M.J., Pretty D.G., Howard J. and Wach J. 2013 A multichannel magnetic probe system for analysing magnetic fluctuations in helical axis plasmas *Rev. Sci. Instrum.* **84** 093501
- [24] Hole M.J., Appel L.C. and Martin R. 2009 A high resolution Mirnov array for the mega ampere spherical tokamak *Rev. Sci. Instrum.* **80** 123507
- [25] Van Zeeland M.A., Yu J.H., Chu M.S., Burrell K.H., La Haye R.J., Luce T.C., Nazikian R., Solomon W.M. and West W.P. 2008 Tearing mode structure in the DIII-D tokamak through spectrally filtered fast visible bremsstrahlung imaging *Nucl. Fusion* **48** 092002
- [26] Ohdachi S., Toi K., Fuchs G., von Goeler S. and Yamamoto S. 2003 High-speed tangentially viewing soft x-ray camera to study magnetohydrodynamic fluctuations in toroidally confined plasmas *Rev. Sci. Instrum.* **74** 2136–43
- [27] Haskey S.R. et al 2014 Clustering of periodic multichannel timeseries data with application to plasma fluctuations *Comput. Phys. Commun.* **185** 1669–80
- [28] Summers H.P. 2004 *The ADAS User Manual* version 2.6; online at <http://adas.phys.strath.ac.uk>
- [29] Gordon R., Bender R. and Herman G.T. 1970 Algebraic reconstruction techniques (ART) for three-dimensional electron microscopy and x-ray photography *J. Theor. Biol.* **29** 471–81
- [30] Herman G.T. 2009 Fundamentals of computerized tomography *Image Reconstruction from Projections* (Berlin: Springer) p 1
- [31] Gilbert P. 1972 Iterative methods for the three-dimensional reconstruction of an object from projections *J. Theor. Biol.* **36** 105–17
- [32] Kak A.C. and Slaney M. 1999 *Principles of Computerized Tomographic Imaging* (online at www.slaney.org/pct/)
- [33] Hirshman S.P. and Whitson J.C. 1983 Steepest-descent moment method for three-dimensional magnetohydrodynamic equilibria *Phys. Fluids* **26** 3553

Analysis of modes on H-1NF

The work shown in this chapter compares theoretical predictions from compressible linearised ideal-MHD using the CAS3D and CONTI codes, which include all three spatial dimensions, with the results from the analysis techniques, diagnostic development, and diagnostic measurements presented in chapters 2, 3, 4, and 5. It brings together all of the work that has been shown in previous chapters, improving the understanding of the impact of 3D magnetic field structure in H-1NF on low frequency Alfvén waves. In particular, experimental measurements of the frequency, polarisation, and radial structure are compared with global Alfvén eigenmodes (GAE) as well as compressibility induced gap modes such as BAEs, and modes due to Alfvén -acoustic interaction such as BAAEs.

Supplementary information which may be useful for future research is included in appendix H, along with details of attempts at active excitation of these modes in appendix I. 75% of the research and 85% of the writing presented in this chapter are my own work. In the coming weeks, this draft paper will be reduced in length and submitted to a journal. The long form of the paper is included here because it is a more complete reference for future work.

Experiment-theory comparison for low frequency modes on the H-1NF stellarator

S. R. Haskey,^{1,*} B. D. Blackwell,¹ C. Nührenberg,² A. Könies,² J. Bertram,¹ C. Michael,¹ M. J. Hole,¹ and J. Howard¹

¹*Plasma Research Laboratory, Research School of Physics and Engineering,*

The Australian National University, Canberra, ACT 0200, Australia

²*Max-Planck-Institut für Plasmaphysik, Greifswald, Germany*

(Dated: September 30, 2014)

The experimentally observed behaviour of spontaneously excited low frequency fluctuations in 0.5T H/He H-1NF heliac plasmas is described and compared with compressible ideal-MHD predictions using the CAS3D and CONTI codes. Four dominant types (or clusters) of low frequency modes are identified using datamining techniques. For each of these clusters, mode number and polarisation information is calculated using helical and poloidal magnetic probe arrays. Additionally, detailed radial mode structure is obtained using spectrally filtered synchronous imaging and tomographic inversion techniques and compared with global Alfvén eigenmodes (GAE), beta induced Alfvén eigenmodes (BAE), and beta induced Alfvén -acoustic eigenmodes (BAAE) from CAS3D, to try to better understand the nature of these modes. The radial structure is found to fit better with modes that are localised at outer radii, corresponding more closely with BAEs or BAAEs for two of the clusters. For the other two clusters, the mode resonant surface is not inside the plasma; however, low frequency discrete Alfvén modes that agree well with the experimental data are found among the sound continua, substantially removed from the turning point in the relevant Alfvén continua. The nature of these discrete modes is under investigation. Polarisation information from the magnetic probes show these modes have dominantly shear type motion, although they have a non negligible parallel component pointing towards modes whose existence depends on plasma compressibility. It is hypothesised that the frequency scaling of these modes with H-1NF configuration (rotational transform profile) could be due to configuration related temperature variations. This will be checked in the near future using a diagnostic that is currently being commissioned and will provide temperature measurements using helium line ratios.

I. INTRODUCTION

Basic understanding of the types of waves that can be spontaneously excited in magnetically confined plasmas is important in the wider context of magnetic confinement fusion. As has been observed, MHD instabilities such as Alfvén eigenmodes [1, 2], sawteeth, and tearing modes often limit achievable plasma parameters and can cause detrimental disruptions [3–5], lead to reactor damage, and reduce self-heating efficiency through their interaction with fast particles, such as fusion born alpha-particles.

The frequency of spontaneously excited MHD fluctuations in 0.5T H/He ion cyclotron resonance heated (ICRH) H-1NF heliac [6, 7] plasmas, has been shown to exhibit a systematic dependence on magnetic configuration [8–11]. These initial results motivated the installation of several new diagnostic systems and techniques to try and understand the nature of these modes. These include a helical magnetic probe array [12], a synchronous imaging technique [13] as well as associated analysis techniques such as periodic datamining [14] and tomographic inversion [15]. Additionally, significant progress has been made with the theoretical modelling of these modes [16, 17]. This paper draws together this work by presenting the latest experimental findings and comparing them with recent advances in theoretical mod-

elling of normal modes for H-1NF configurations within the framework of 3D linearised ideal compressible MHD. The aim being to better understand the nature, or taxonomy of these waves, with a broader goal of understanding the relevant drive and damping mechanisms and whether they are a concern for larger machines.

H-1NF is a flexible heliac, which allows fine control of the rotational transform profile. As this profile is changed, by modifying the ratio of the current in the helical winding to the other field coils (quantified by the parameter κ_H), the frequencies and types of modes that are spontaneously excited vary considerably. This paper presents analysis of data from a series of 131 shots, which constitute multiple scans of κ_H from 0.2 to 1 in 0.01 increments (note κ_H is held constant during a shot). Details of the rotational transform profile variation for this type of scan are shown in figure 1 (b).

Datamining techniques were used to extract and group interesting features from this dataset into clusters based on similarity in the magnetic probe signature of the fluctuations [11, 14]. Here each cluster is expected to be a different class of fluctuation based on their different “appearance” to the diagnostic array. A plot of the members of four dominant clusters as a function of κ_H and frequency is shown in figure 1 (a) exhibiting a strong relationship between frequency and rotational transform profile (figure 1 (b)). These features are referred to as whale tails with clusters 1 and 2 forming one whale tail centered at $\kappa_H = 0.4$ and clusters 3 and 4 forming another whale tail centered at $\kappa_H = 0.75$.

The sweeping of the mode frequency as κ_H (or t)

* shaun.haskey@anu.edu.au

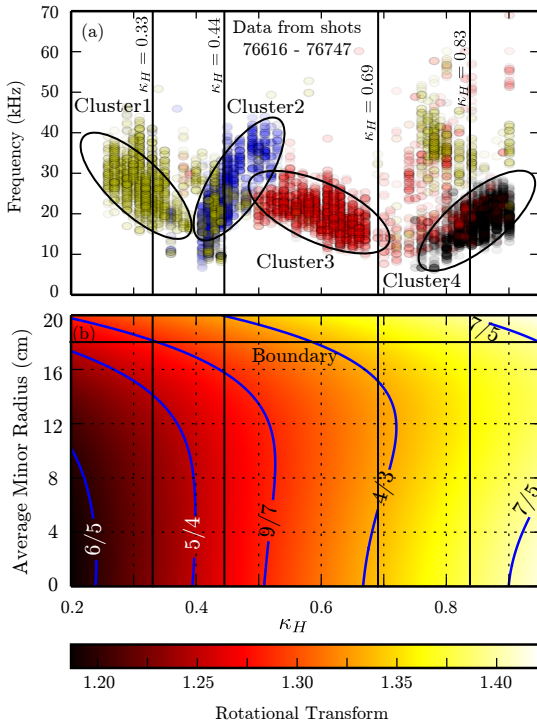


FIG. 1. (a) Clusters of interest and the frequencies of the member instances plotted against κ_H . The κ_H values where radial mode structure is available from the synchronous imaging and tomographic inversions are marked with vertical lines. (b) Vacuum magnetic field rotational transform profile as a function of κ_H . The approximate location of the plasma boundary, as determined using a density interferometer is marked.

changes, is similar to the expected behaviour of conventional and non-conventional global Alfvén eigenmodes (GAE, NGAE). This sweeping is also similar to reversed shear Alfvén eigenmodes (RSAEs) on tokamaks, which follow the evolution of the q profile, although on H-1NF the rotation transform is varied between shots as opposed to during a shot. While there is qualitative agreement with the turning points of the Alfvén continuum, the predicted frequencies are approximately a factor of three higher than the experimental observations [16]. Bertram et al [16] found that by assuming a hollow temperature profile, this frequency sweeping behaviour of clusters 1 and 3 could be attributed to beta induced Alfvén or Alfvén-acoustic eigenmodes (BAEs [18–20], BAAEs [21–23]). It is assumed that the inwardly moving rational surface (as κ_H increases) would cause the temperature at the rational surface to decrease (due to the hollow temperature profile), causing a reduction in the frequency of the BAE gap.

These four clusters (or types of fluctuation) are explored in more detail in this paper. Radial profile infor-

mation is available for a representative fluctuation from each of the clusters using a combination of recently developed tomographic inversion and synchronous imaging techniques [13, 15]. These radial profiles allow in-depth comparisons with theoretical eigenfunctions for GAEs, BAEs and BAAEs.

This paper is organised as follows: The low frequency ideal compressible spectrum for H-1NF is examined in section II using the CAS3D [24] and CONTI [25] codes. Section III provides details of the mode number and polarisation calculations using data from magnetic probe arrays. Details of the radial mode structure, which were obtained using synchronous imaging and tomographic inversion are compared with eigenfunctions from CAS3D in section IV.

II. LINEARIZED IDEAL MHD WAVES ON H-1NF

The ideal-MHD linearized compressible eigenmode spectrum including discrete, quasi-discrete and continua modes was calculated using the established and reliable CAS3D code [24]. Additionally, to provide greater detail of gaps in the continua, the 3D ideal-MHD continuum code CONTI [25] was used. The analysis presented here is an extension of the results that were presented in [16], which also provides more background information, such as the stringent requirements for convergence on H-1NF.

A fixed boundary VMEC [26] equilibrium, where the boundary surface is calculated using DESCUR [27] based on the vacuum magnetic field, is used as the starting point for the calculations. MC3D (part of the CAS3D package) performs the transformation to Boozer coordinates. To improve accuracy, a large number of surfaces (350) is used in the VMEC equilibrium and transformation to Boozer coordinates; however, for the input to CAS3D and CONTI the number of surfaces is reduced to 100 to increase the computation speed.

A special property of heliacs is the large number of Fourier harmonics required to represent the parallel displacement in CAS3D and other codes. Both the first and second sidebands of near resonance helical harmonics are included, leading to a Fourier table that is up to three times larger than for the other components. This is discussed in more detail in [16]. In all cases, CAS3D is run in free boundary mode and linearly decreasing pressure and density profiles that reduce to approximately zero at the plasma edge are used for the spectrum calculations, which implicitly implies that the temperature profile is flat.

Because H-1NF is a three period machine, there are two mode families [16, 24]. These are $N = 0$ with $n \in \{\dots, -6, -3, 0, 3, 6, \dots\}$, and $N = 1$ with $n \in \{\dots, -5, -4, -2, -1, 1, 2, 4, 5, \dots\}$. As will be shown in section III, the modes are dominantly ($n = 4, m = -3$) and (5,-4), which both belong to $N = 1$. Consequently all CAS3D and CONTI analysis shown here is for the

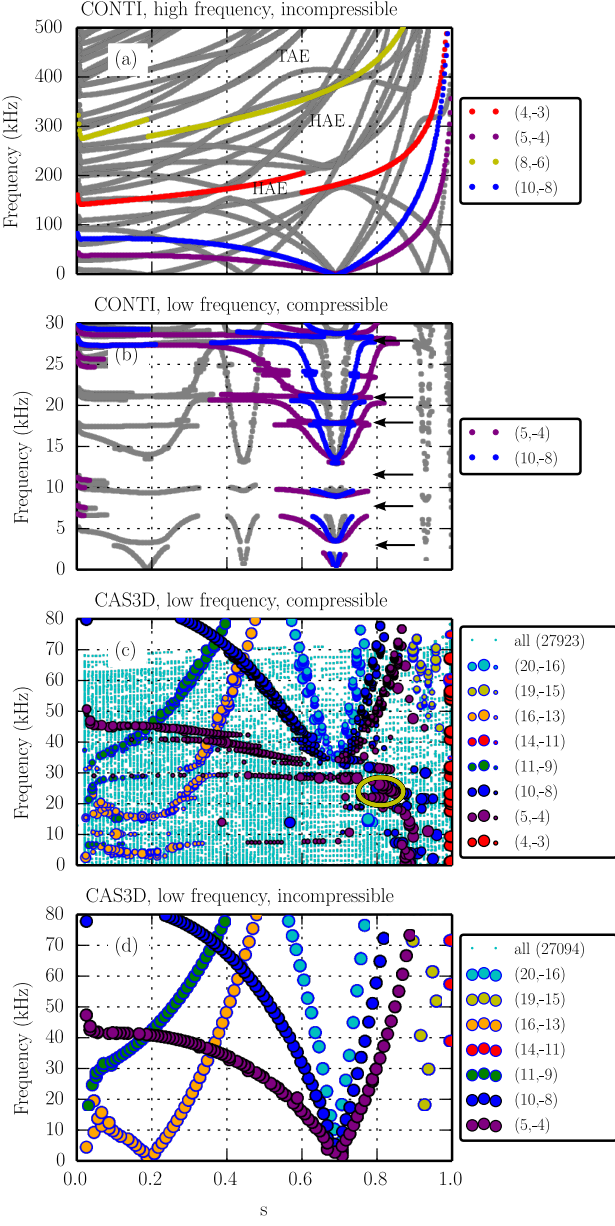


FIG. 2. (a) High frequency incompressible ($\gamma \sim 0$) ideal MHD continuum calculated using CONTI for $\kappa_H = 0.33$, representative of cluster 1. (b) Low frequency compressible ($\gamma \sim 5/3$) continuum showing significant gap structure (marked with arrows). Only modes classified as Shear Alfvénic are plotted. Low frequency discrete modes calculated using CAS3D with (c) and without (d) compressibility. (c) All modes are plotted with a cyan dot, and those that are partly shear Alfvénic are marked with a circle. The larger the circle size, the more shear Alfvénic the mode is based on the potential energy classification (see text for more details). The circled discrete modes in (c) are not present in the incompressible case.

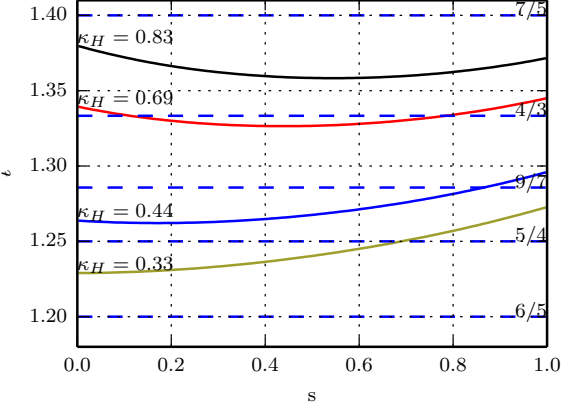


FIG. 3. Rotational transform profiles for several κ_H configurations that are examined in this paper. Low order rational values are marked.

$N = 1$ mode family.

The high frequency spectrum for $\kappa_H = 0.33$ is shown in figure 2 (a). This particular configuration typifies cluster 1. The rotational transform profile for this configuration is shown in figure 3. The first two helical Alfvén eigenmode (HAE) gaps and first toroidal Alfvén eigenmode (TAE) gap are marked. As has been previously noted [16], these gaps are substantially higher than the observed mode frequencies. Before turning to the lower frequencies, which are shown in the other subplots, it is useful to classify the nature of the motion of these modes.

A. Eigenmode classification

In the frequencies of interest there is significant mixing of shear and compressional motion. In order to help classify modes as being dominated by one type of motion, the contributions to the potential energy, δW are used. The size of the circles in figure 2 are given by the shear Alfvén contribution divided by the sum of the contributions by the sound, shear Alfvén and fast components. The relevant quantities are discussed and shown in equations 1 and 26 of [24]. For the CONTI modelling, a discrete classification is used where eigenmodes are considered shear Alfvénic if the largest Fourier harmonic of $\xi_s = \boldsymbol{\xi} \cdot (\mathbf{B} \times \nabla \Psi) / |\nabla \Psi|^2$ is larger than the largest Fourier harmonic for $\nabla \cdot \boldsymbol{\xi}$ in Boozer coordinates (see section IIIB of [25]).

While the classification as sound or shear Alfvénic at these frequencies is somewhat arbitrary, the continuous scale representation of the CAS3D modes in figures 2(c) and 4 is very useful for quantifying the dominant motions. For example, the size of the circles for the (5,-4) shear Alfvén continua in figure 2(c) starts decreasing when the frequencies drop below the frequencies for the

sound continua, and reach a minimum at the frequency turning point which occurs at approximately 40kHz. Below this turning point there are several discrete modes whose motions are strongly dominated by shear motion.

B. Typical low frequency Alfvén-acoustic spectra for each of the clusters

As can be seen in figure 1, the frequency range of interest is below 100kHz for the modes that belong to clusters 1–4 ruling out the possibility that these are HAEs or TAEs. The low frequency continuum for $\kappa_H = 0.33$ including compressibility is shown in figure 2 (b) demonstrating a significant amount of gap structure due to Alfvén -acoustic interactions. Calculations using CAS3D show the beta-induced turning point in the (5,-4) continua, with a large number of discrete modes below this turning point (circled in figure 2(c)). These low frequency discrete modes are not present when compressibility is excluded by setting $\gamma \sim 0$ (figure 2(d)). This demonstrates that the existence of these particular modes, which will be of particular interest in subsequent sections, depends on compressibility.

The low frequency ideal-MHD continuum including compressibility, as calculated using CONTI, for each of the representative κ_H value from each of the different clusters (marked in figure 1) shows a large amount of low frequency gap structure due to Alfvén -acoustic interactions, similar to what is shown in figure 2 (b) for $\kappa_H = 0.33$. Poorly damped global modes could exist within these gaps as is confirmed with CAS3D calculations for each of the four clusters (figure 4). These particular κ_H values were chosen because synchronous imaging and tomographic inversion data are available and will be discussed in more detail in section IV. The rotational transform profiles for each of these configurations is shown in figure 3. The lower κ_H values (for clusters 1 and 2) have monotonically increasing rotational transform profiles and the higher κ_H values (clusters 3 and 4) have reversed shear profiles. For clusters 1 and 3, the low order 5/4 and 4/3 rational surfaces respectively are within the plasma volume, while for clusters 2 and 4, the low order rationals are not within the plasma.

Discrete modes which are in the right frequency range, and have the right mode numbers (see section III A) are circled for each of the configurations (figure 4). For clusters 1 and 3, the mode resonant surface is within the plasma, so the circled low frequency modes towards the plasma edge, near the mode resonant surface are most likely BAEs or BAAEs, while those that are closer to the plasma core where the turning point in the relevant Alfvén continua is located are most likely NGAEs. For clusters 2 and 4, the rational surface is not within the plasma and the circled low frequency modes are quite removed in frequency and radial location from the turning point in the relevant Alfvén continua. The nature of these modes is currently under investigation; however, as

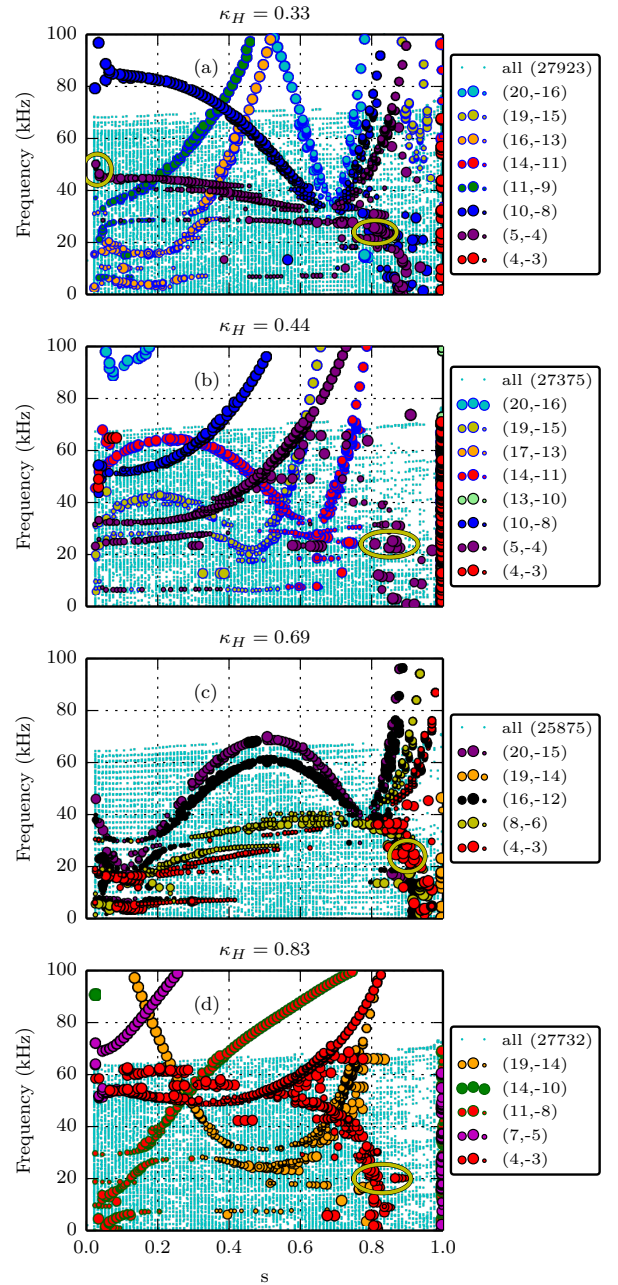


FIG. 4. The low frequency CAS3D spectra using a representative κ_H for each of the four clusters. The circles are modes that have been identified as shear Alfvén waves based on their polarisation and the cyan dots are the sound modes. The size of the circle represents how much larger the shear component is compared to the other components. For each subplot there are discrete shear Alfvén modes in the sound continua. The modes that have been circled are examined in more detail in section IV.

shall be seen in section IV, their radial structure agrees

reasonably well with the experimental observations. For each of the configurations shown in figure 4, the existence of these low frequency discrete modes depends on the inclusion of compressibility in the CAS3D calculations, similar to what was seen by comparing figures 2 (c) and (d).

The CAS3D spectra, and details of the low frequency discrete modes will be discussed in more detail as the experimental observations are described in the following sections, in particular section IV.

III. ANALYSIS OF MAGNETIC PROBE DATA

The location of a poloidal (PMA) and helical Mirnov array (HMA), which are used in this paper, is shown in figure 5. The HMA consists of 16 tri-axis probes, allowing polarisation measurements to be made in addition to mode number identification.

The axial coils of the tri-axis probes provided the raw data for the clustering algorithm, which identified the clusters shown in figure 1 (a). This axis essentially follows the helical winding of H-1NF ($\ell \sim 3$) and was chosen because it has a consistent orientation relative to the equilibrium magnetic field, simplifying the mode number analysis. The nearest neighbour phase differences across the HMA for each of the four clusters of interest are shown in figure 6. Here, all members belonging to a single cluster are plotted on a single subplot along with the mean for their values marked in red, demonstrating that the clustering algorithm is successfully finding common features and grouping them together into clusters. Note that the members of each cluster come from multiple shots as well as different times during the same shot. Including multiple instances of the same fluctuation in a single shot allows the behaviour of the fluctuation, as plasma parameters change, to be examined.

These phase differences are less constant than would be expected for an evenly spaced toroidal array on a tokamak. There are several reasons for this. The helical array is not evenly spaced in magnetic co-ordinates, and when this is taken into account, as described in [12], the agreement with single mode number assignments is improved. The probe signals are quite weak for certain probes such as 5 and 6 for cluster 1 causing these particular phase differences to look more erratic due to noise. Additionally, the presence of non-dominant modes (possibly due to the choice of co-ordinate system) may lead to more complicated phase differences.

A. Mode number identification

Mode number identification is performed using the poloidal Mirnov array and the axial probe of the helical Mirnov array. These mode numbers are crucial for determining the dispersion relation of the mode, comparisons with eigenfunctions from theory, and for providing

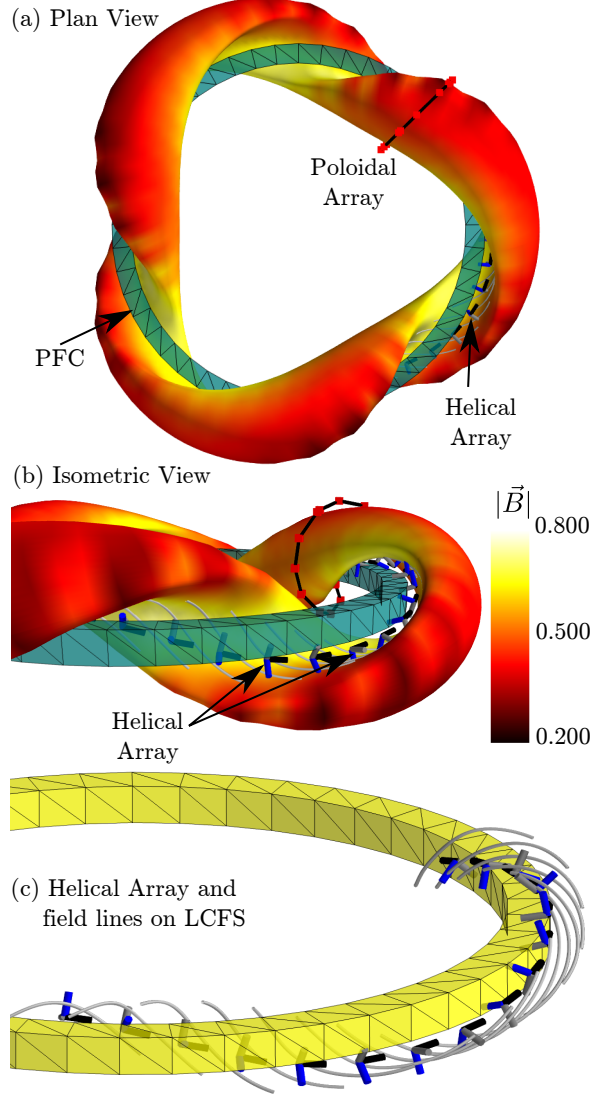


FIG. 5. The location of the poloidal and helical Mirnov arrays. Each of the formers in the HMA is wound with three orthogonal coils, providing polarisation information on the modes. The calculated orientation of each of these coils is shown, along with the poloidal field coil (PFC) and the orientation of some field lines near the probes on the last closed flux surface (LCFS). The probe measurements are decomposed into a component parallel to the magnetic field, perpendicular to the magnetic field and in the surface and perpendicular to the surface for the polarisation measurements.

the basis functions that are required for the tomographic inversions shown in section IV.

The probe locations are mapped to Boozer coordinates based on the nearest point on the last closed flux surface (LCFS) for a typical equilibrium for the cluster in question. A non-uniform discrete Fourier transform (DFT)

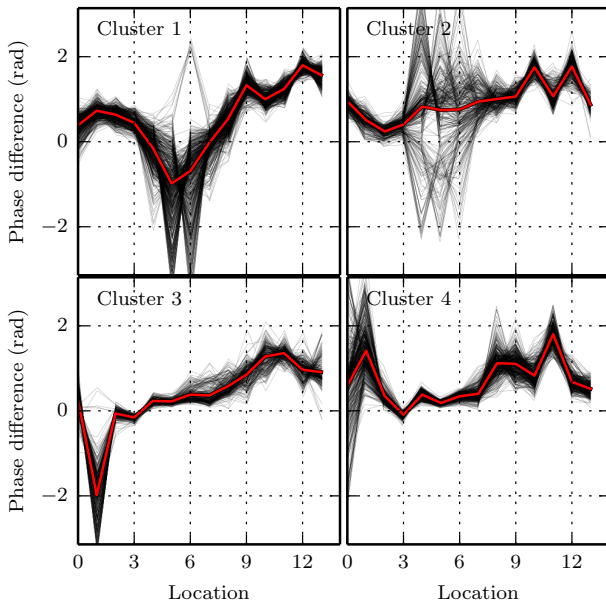


FIG. 6. The phase differences across the HMA for the instances that constitute each of the clusters shown in figure 1 along with the mean values plotted in red. The similarity of the instances belonging to each cluster demonstrates that the clustering algorithm has successfully separated unique types of fluctuations from the raw data. The phase difference measurement between some probes is poorly defined because of weak measurements (for example location 0 for cluster 4).

is then used to fit mode numbers with $-10 < m < 10$ and $-10 < n < 10$ using the magnetic coordinates of the nearest point on the LCFS to the probes.

Mode number identification for clusters 1, 2, 3, and 4 using only the PMA, only the HMA, and the two combined are shown in figure 7. While the PMA is in a single toroidal plane in real space, due to the strong shaping on H-1NF plasmas this is not true in magnetic coordinates. Consequently the array provides a weak degree of toroidal mode number differentiation and a strong degree of poloidal mode number differentiation. The signals from the PMA are difficult to analyse due to the varying distance to the plasma, with some probes being completely unusable. This means that in some cases even the poloidal mode number is not well defined using only this array.

The HMA was designed to be located in the region of strongest signal with relatively constant distance to the plasma. This makes analysis of the signals more straightforward; however this also means that the array essentially measures a helical mode number, which cannot be uniquely decomposed into toroidal and poloidal mode numbers. This is shown clearly in the central column of figure 7 where there is a diagonal stripe of modes that fit the data well.

Using both the PMA and HMA, allows a best fit mode to be uniquely defined with a stronger degree of confidence. Clusters 1 and 2 are both dominantly $n = 5, m = -4$ modes, and clusters 3 and 4 are both most likely to be $n = 4, m = -3$ modes.

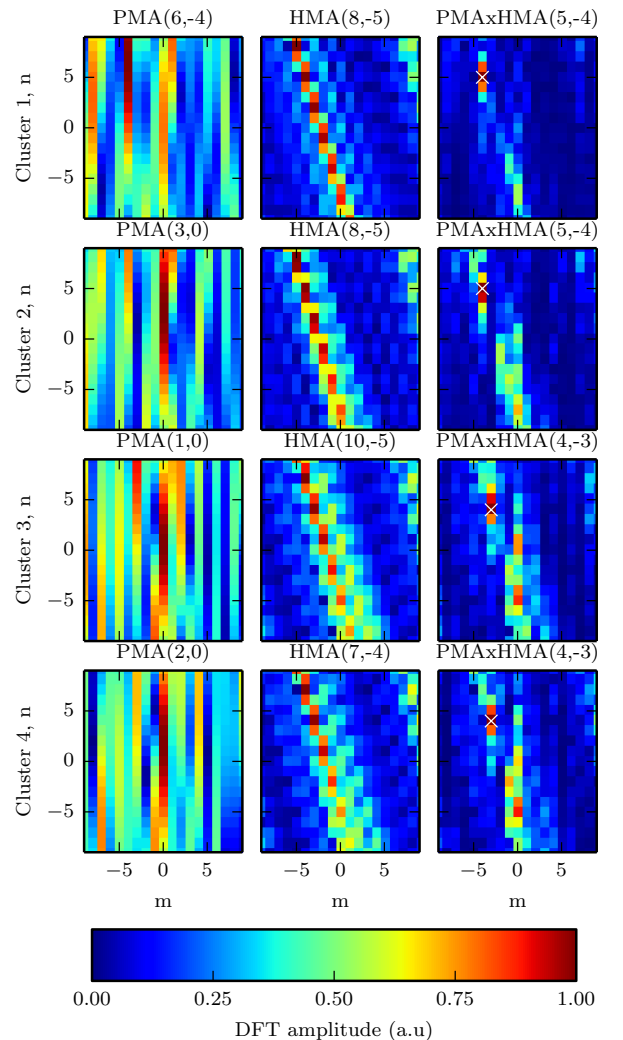


FIG. 7. Mode number identification for clusters 1 (top), 2, 3 and 4 (bottom). Left column is the mode number identification using only the poloidal Mirnov array, center column using the helical Mirnov array, and right column using both arrays. The best fit mode to the data using the individual arrays and the combined arrays are shown in brackets in the title of each subplot, and the best fit mode using both arrays is marked with a white cross.

B. Mode polarisation

The HMA consists of 16 tri-axis formers allowing the polarisation of the magnetic field component of the waves to be determined. Figure 5 shows the location of the formers in the probe array along with the calculated orientation of each of the tri-axis probes. The frequency response for each axis is different due to a preferential shielding direction of the stainless steel bellows that houses the HMA. This frequency response is corrected before performing the polarisation calculations. However, there is still the possibility of attenuation to certain components of the magnetic field due to the other metal structures near the probes, although this is expected to be small.

For each former in the HMA, the nearest point on the LCFS is located and the directions parallel to the magnetic field (parallel, $e_b = \mathbf{B}_0/|\mathbf{B}_0|$), normal to the plasma surface (normal, $e_n = \nabla s/|\nabla s|$), and perpendicular to the magnetic field and in the flux surface (binormal, $e_n \times e_b$), at this point are calculated. This information allows the magnetic probe measurements to be projected onto these directions. To perform these calculations, the VMEC code [26] was used to solve the plasma equilibrium, and the BOOZ_XFORM code (part of the STELLOPT package, which includes VMEC) provides the transformation from Boozer co-ordinates to lab co-ordinates allowing the path of field lines in realspace to be calculated relatively easily. H-1NF plasmas typically have a very low β ($\approx 10^{-4}$) and high rotational transform, so the equilibrium magnetic field is quite similar to the vacuum magnetic field.

The result of decomposing the tri-axis measurements into the parallel, normal and binormal directions for the four clusters that are being investigated for each of the magnetic probe locations is shown in figure 8. Here, the amplitude of the two normal directions have been combined. The component of the wave magnetic field parallel to the equilibrium field is not negligible; however, it is also substantially smaller than the perpendicular component. This indicative of a BAE or BAAE type wave where compressibility is important as opposed to a purely shear Alfvénic mode. The large normal component provides strong evidence that these are not sound modes. The polarisation also changes modestly between probe locations, indicating differences in the polarisation between regions of varying curvature (in the MHD sense). Comparisons with magnetic polarisations calculated using CAS3D are part of future work.

The parallel, binormal, and normal components of a single tri-axis magnetic probe are plotted in the complex plane in figure 9 to further investigate the mode polarisations. For clusters 3 and 4, all components are either in phase, or out of phase with one another indicating that the wave is linearly polarised. Clusters 1 and 2 show a small degree of elliptical polarisation which may be due to inaccuracies in the probe orientation which are known with an accuracy of $\approx 10^\circ$ [12]. It is also worth not-

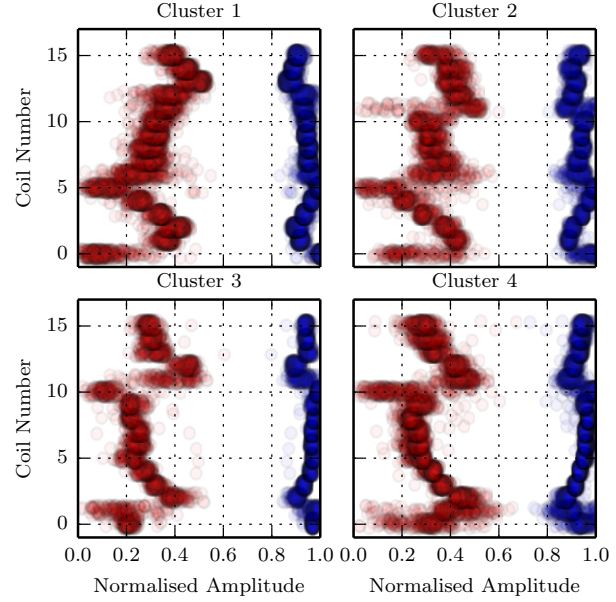


FIG. 8. Projections of the magnetic probe measurements onto the parallel (red) and normal (blue) directions relative to the magnetic field at the nearest location on the LCFS for clusters 1-4. The normal component can be further decomposed into a component normal to the field but in the surface and normal to the field and surface (see figure 9). Results for each of the tri-axis magnetic probes in the HMA are shown, indicating relatively minor variation in polarisation along the array. There are multiple circles for each magnetic probe because the analysis was performed for all instances within each of the clusters.

ing that the polarisation for a given former and cluster is very well defined even though the polarisation is not used in the clustering process.

IV. RADIAL MODE STRUCTURE

A synchronous imaging technique [13] was used to acquire high resolution images of a typical mode for each of the clusters (for configurations $\kappa_H = 0.33, 0.44, 0.63$, and 0.83), using an interference filter to isolate the CII 514nm light emission. Due to the relatively cool electron temperatures in 0.5T H/He plasmas in H-1NF, this particular emission emanates from all regions in the plasma, and consequently, is well suited to revealing the structural details of the modes. Figure 10 illustrates the three camera views which were used to capture images of a wedge shaped section of plasma between two toroidal field coils.

The nature of the synchronous imaging technique means the acquired images can be represented as a Fourier series in time, with the fundamental harmonic revealing the spatial structure of the light emission at the

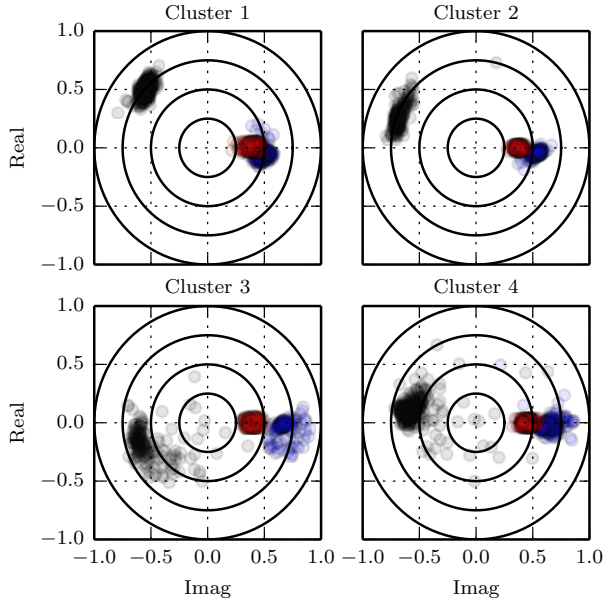


FIG. 9. Mode number polarisation for clusters 1-4 using a single tri-axis probe. Red is the component parallel to the magnetic field, black is binormal (in the surface and normal to the magnetic field), and blue is normal to the surface. The phase is with respect to the parallel component. For each cluster the polarisation only has minor variations and for all cases the normal and binormal components are larger than the parallel components. Clusters 1 and 2 appear to have a slight elliptical polarisation in the plane perpendicular to the field, while clusters 3 and 4 have a more linear polarisation.

frequency of the observed mode in the reference magnetic probe signal. The magnitude and phase of the fundamental harmonic, for the representative mode from each of the four clusters, is shown in figure 11. Images were acquired from three different viewing angles to improve the tomographic inversions; however, only the central viewing location is shown in figure 11. Refer to [13] and [15] for more details of the synchronous imaging technique.

The line of sight measurements show many similarities in the phase and amplitude structure between clusters 1 and 2, and also between clusters 3 and 4. This is to be expected as these clusters appear to have the same dominant poloidal mode numbers from the magnetic probe analysis in the previous section. The phase of the line of sight measurements is shifted 180° between clusters 1 and 2, as well as between clusters 3 and 4. This phase shift is relative to the reference magnetic probe and is discussed in more detail in section IV C.

These images contain information about the radial, poloidal, and toroidal structure of the mode and can be tomographically inverted in magnetic coordinates using all 3 spatial dimensions [15] to provide the radial structure of a set of Fourier basis modes. This inversion requires that the basis modes (for ϕ and θ) be specified, or

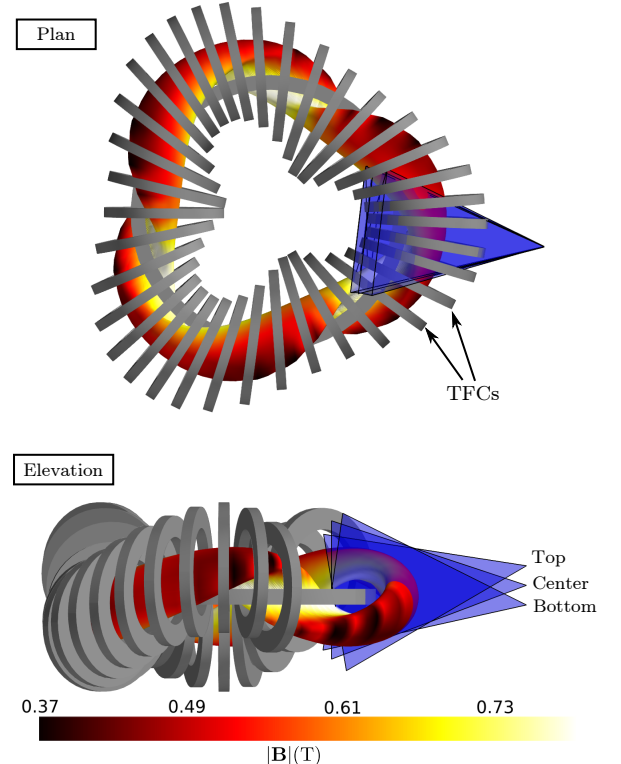


FIG. 10. Details of the three different camera views used to acquire the data on H-1NF. The top plot shows how the toroidal field coils (TFCs) limit the field of view. A typical H-1NF plasma is shown, with the surface colour representing the magnetic field strength. Adapted from Ref. [15].

individual basis modes can be trialed to find the best fit to the data. When modes are trialed, the poloidal mode number agrees well with the magnetic probe data, and a weak minimum in the residual fit is found for toroidal mode numbers within ± 2 of the n from the magnetic probe data. As is discussed in [15], this weak minimum is due to the small amount of toroidal mode number information in these images. The dominant mode numbers that were calculated from the magnetic probes (cluster 1 : (5,-4), cluster 2 : (5,-4), cluster 3 : (4,-3), cluster 4 : (4,-3)) are used as the Fourier basis functions for the tomographic inversions shown in the rest of this paper.

An example of the high quality tomographic inversion using a single Fourier basis mode ($n = 5, m = -4$), which was chosen from analysis of the magnetic probe data, is shown in figure 12, for the representative mode from cluster 2. The mode has a single dominant harmonic (if additional basis functions are included their amplitudes are small), and is localised towards the outer region of the plasma. The Fourier representation of experimental data in magnetic coordinates is the same as that used by CAS3D, allowing a relatively straightforward comparison with theoretical eigenfunctions; however, the relationship

between CII 514nm emission and plasma parameters has to be examined more closely.

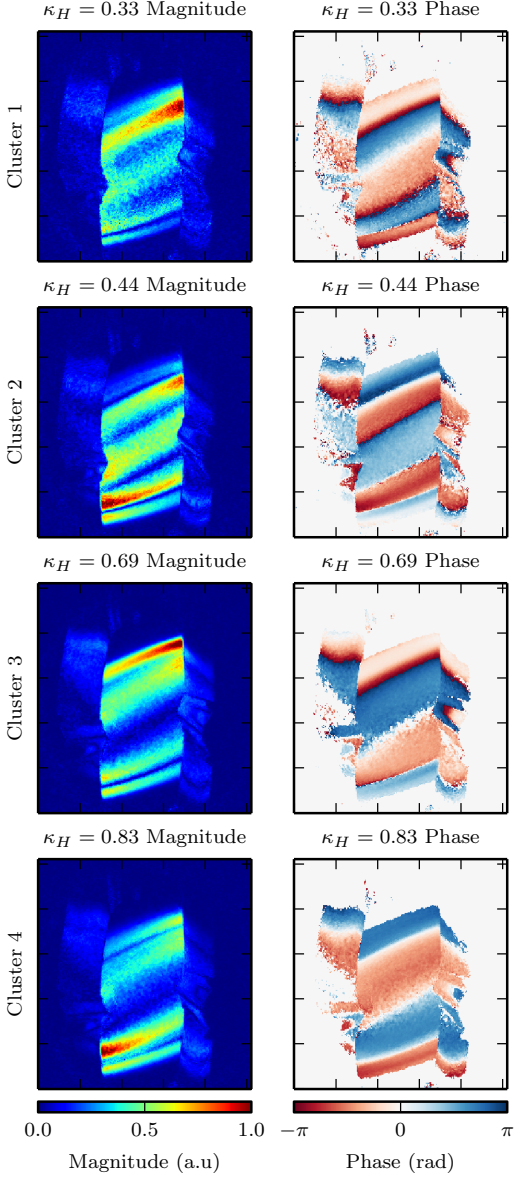


FIG. 11. The magnitude and phase of the first harmonic from the Fourier decomposition of the synchronous imaging data. For each pixel the time varying amplitude is given by $A \cos(\omega t + \phi)$ where ω is the frequency of the mode as observed by the Mirnov pickup coil, and A and ϕ are the magnitude and phase plotted in this figure.

A. CII emission and the perturbed electron density

The CII 514nm light emission is determined by the electron density, electron temperature, and photon emissivity coefficient, which is also a function of electron temperature and density:

$$\epsilon = n_i n_e \zeta(T_e, n_e), \quad (1)$$

where ζ is the photon emissivity coefficient, n_e is the electron density, and $n_i = \alpha n_e$ is the CII impurity density which can be represented as a fraction (α) of n_e . In the absence of experimental measurements of this fraction, we assume that it is constant within the plasma. Details of the photon emissivity coefficient were obtained from ADAS [28]. Changes in the emissivity can be found as follows:

$$\begin{aligned} \delta\epsilon &= \frac{\partial\epsilon}{\partial n_e} \delta n_e + \frac{\partial\epsilon}{\partial T_e} \delta T_e \\ &= 2\zeta \alpha n_e^2 \frac{\delta n_e}{n_e} + \alpha n_e^3 \frac{\partial\zeta}{\partial n_e} \frac{\delta n_e}{n_e} + \alpha n_e^2 T_e \frac{\partial\zeta}{\partial T_e} \frac{\delta T_e}{T_e} \end{aligned} \quad (2)$$

For typical H-1NF plasmas, $n_e < 5 \times 10^{12} \text{ cm}^{-3}$ and $T_e > 20 \text{ eV}$. Using these values and details of the photon emissivity coefficient from ADAS [28], we find that $\zeta \sim 3 \times 10^{-9} \text{ cm}^3/\text{s}$, $\partial\zeta/\partial n_e \sim 1.3 \times 10^{-23} \text{ cm}^6/\text{s}$, and $\partial\zeta/\partial T_e \sim 3 \times 10^{-11} \text{ cm}^3/\text{eVs}$. Assuming $\delta n_e/n_e \sim \delta T_e/T_e$, the first term in equation 2 is approximately 100 times larger than the second, and 10 times larger than the third, allowing us to drop last two terms, and show that the change in CII 514nm emissivity, for H-1NF plasma conditions, is primarily dependent on the density and density fluctuations:

$$\delta\epsilon \propto n_e \delta n_e. \quad (3)$$

The electron density perturbation due to a displacement, $\boldsymbol{\xi}$, in linearized ideal-MHD is [29]:

$$\delta n_e = -\boldsymbol{\xi} \cdot \nabla n_e - n_e \nabla \cdot \boldsymbol{\xi} \quad (4)$$

In this paper, the theoretical predictions of the perturbed emissivities are calculated using the perturbed densities due to the eigenmodes (which are output by CAS3D).

B. Radial structure comparison

Figures 13 (a) and (b) show the normal displacement, calculated using CAS3D, for both the BAE and NGAE type modes (for cluster 1), which are circled in figure 4. The density profile (shown in (c)), which is used to calculate the perturbed density in CAS3D, and the emissivity (using equation 3), is based on a quintic polynomial fit to initial experimental data from a 21 channel imaging density interferometer. This polynomial representation is required by CAS3D. The tomographic inversion and predicted emissivity for both the candidate BAE and NGAE are shown in (d) and (e) respectively. Here, a smaller mode table and a linear density profile were used in CAS3D to reduce the continuum interactions and provide a relatively smooth eigenfunction. The more accurate quintic density profile is then used to calculate the perturbed density and emissivity.

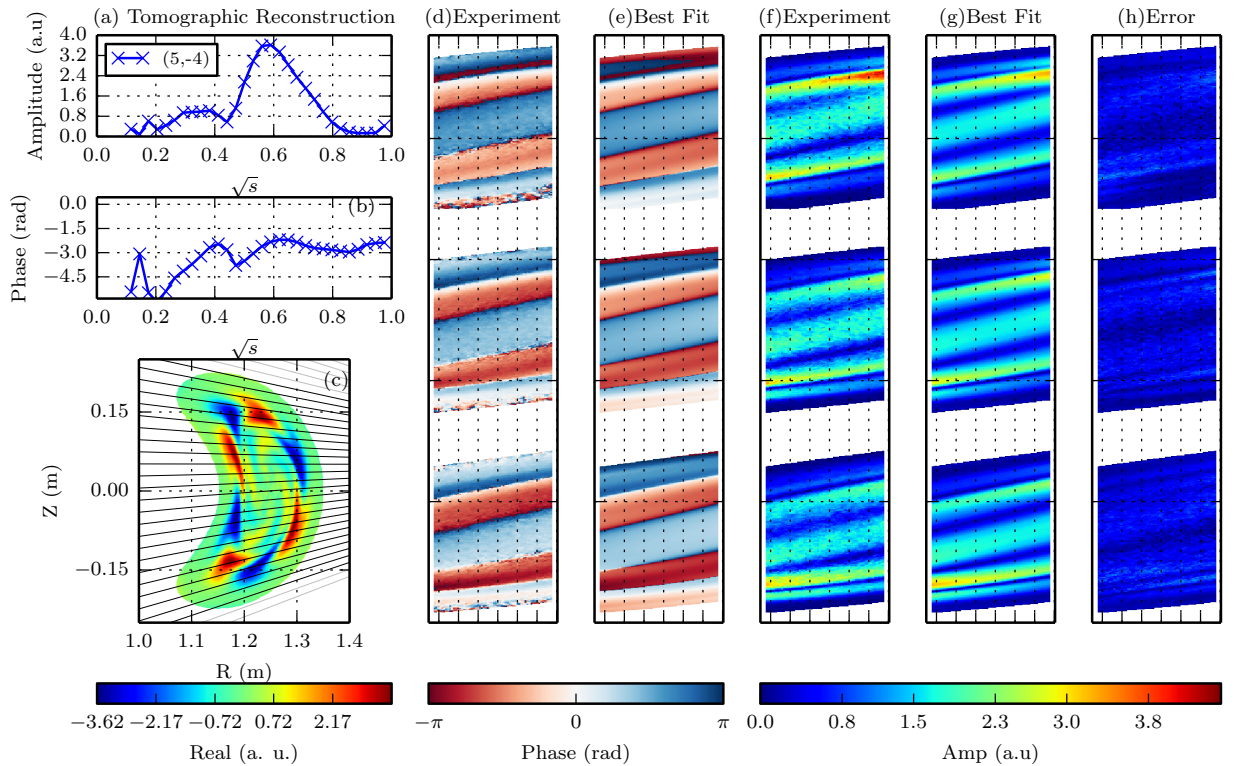


FIG. 12. Details of the tomographic inversion using a (5,-4) mode, and all three camera views, for a fluctuation at $\kappa_H = 0.44$, which is representative of cluster 2. The radial structure of the amplitude and phase are shown in (a) and (b). (c) shows a poloidal cross-section with the real part of the mode and a small subset of the lines of sight from the central camera view. The experimental and best fit phase (d, e) and amplitude (f, g) for all three camera views, and error in the best fit (h) are also shown. The error is the Euclidean distance between the phasors for each pixel in the experimental and best fit reprojection data. The error is generally low demonstrating that the tomographic inversion is extremely good. Note: compared with the reconstructions in [15], the plasma boundary has been expanded to agree more closely with the boundary location, as measured using a density interferometer.

It is important to note that quality of the data from the synchronous imaging allows the internal structure of the emissivity to be tomographically inverted, removing the need to forward model the diagnostic output based on the theoretical eigenfunction. The basis choice, which is provided through analysis of the magnetic probe data and/or selecting the basis modes that minimise the residual error of the tomographic inversions, is very important for achieving an accurate inversion.

The emissivity from the NGAE is more core localised, while the BAE is more edge localised providing a better match with the experimental data. For the H-1NF configurations considered here, the zero shear in the t profile is generally close to the core of the plasma (see figure 3) which explains the core localisation of the GAE/NGAE displacement and emissivity.

Similar comparisons are shown in figure 14 between tomographic inversions, which are representative of each of the four clusters, with the eigenmodes located towards the plasma edge that have been circled in figure 4. In

each case, a good quality tomographic inversion is obtained using a single best fit mode from the analysis of the magnetic probe signals. For all of the clusters, the agreement is very good. The tomographic reconstructions from these four different modes have maximums that are located at similar radial positions ($\sqrt{s} > 0.5$).

For clusters 1 and 3, the BAE or BAAE type modes that are located towards the plasma edge fit the experimental radial structure much better than the more core localised NGAEs. For clusters 2 and 4, the modes that are located towards the plasma edge also provide a good fit to the imaging data. As was discussed in section II, the nature of these discrete modes is currently under investigation as the mode resonant surface is not in the plasma, and they are quite separated in frequency and radial location from the turning point in the relevant Alfvén continua.

The theoretical emissivity is strongly dependent on the density profile. Eigenfunctions whose displacement is strongest at the edge of the plasma will have emissivi-

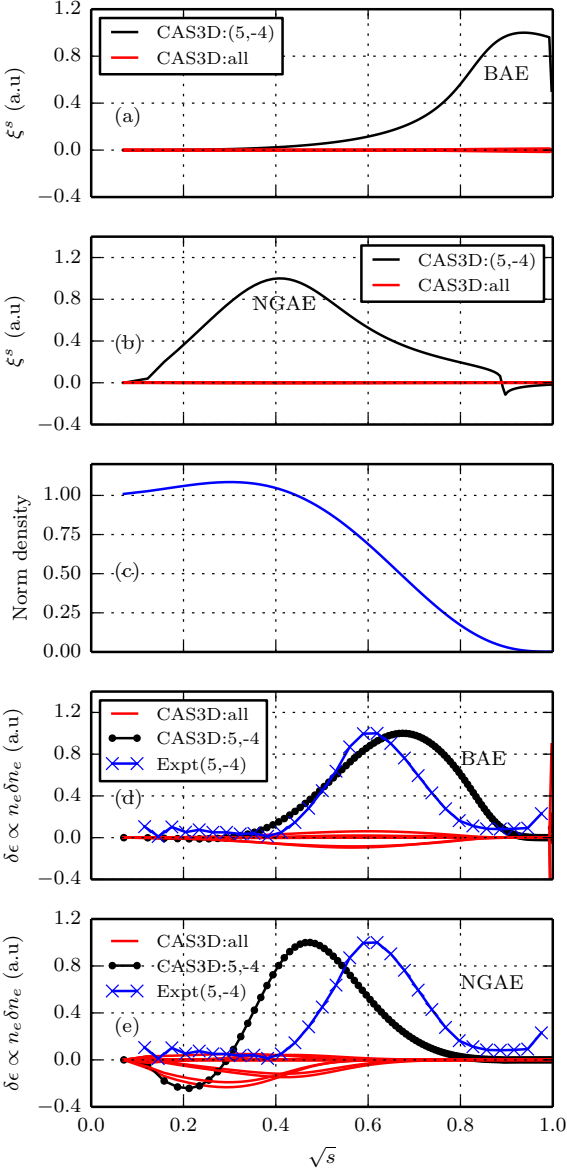


FIG. 13. Experimental comparison with the eigenfunction for a BAE and NGAE for $\kappa_H = 0.33$. (a, b) Normal displacement for the BAE and NGAE calculated using CAS3D. (c) Quintic polynomial fit to the experimental density profile. This profile is used by CAS3D to calculate δn_e and the change in emissivity due to the mode. (d and e) Comparisons between the experimental and the theoretical emissivity for a BAE and NGAE respectively. The experimental measurements for this particular mode show better agreement with the BAE.

ties that are more centrally peaked, while those whose displacement is more centrally localised will have emissivities that are also more centrally localised. While the profile that is used here is the best currently available ex-

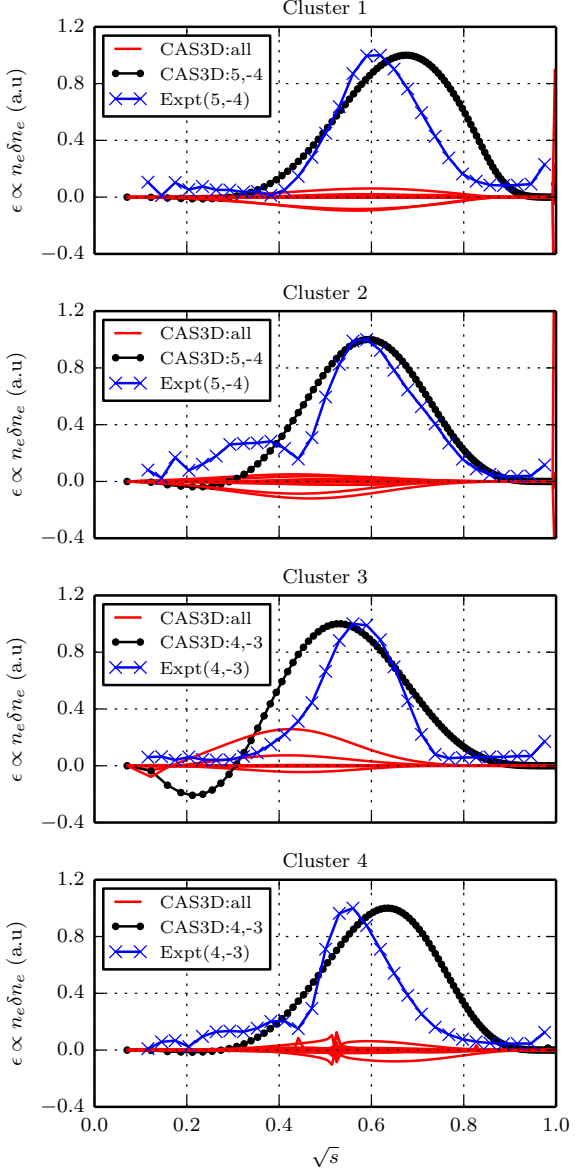


FIG. 14. Comparisons between the tomographic reconstructions and emissivity using the CAS3D eigenfunction for the representative modes for each of the clusters. The eigenmodes that are used are the modes located beyond mid radius that have been circled in figure 4. The dominant basis mode from CAS3D is marked in black and the other non-dominant basis modes are red.

perimental measurement, work is underway to optimise the recently installed 21 channel density interferometer to provide more accurate measurements.

C. Relationship between magnetic, density and emissivity perturbations

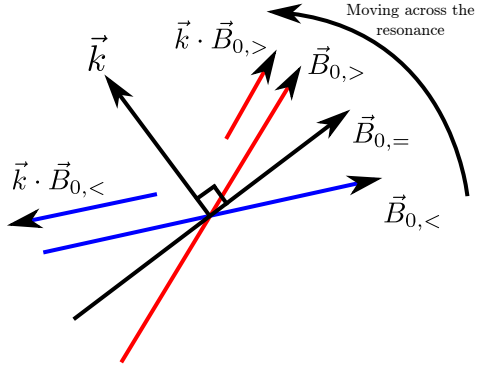


FIG. 15. Moving across the mode resonance with a field line, the rotational transform goes from $t < n/m$, to $t = n/m$ at resonance, to $t > n/m$. The direction of the magnetic field for these three cases is represented by $\mathbf{B}_0,<$, $\mathbf{B}_0,=$ and $\mathbf{B}_0,>$ respectively. Modes that have the same dominant mode numbers for these three different configurations will have the same \mathbf{k} in each case. Consequently $(\mathbf{k} \cdot \mathbf{B}_0,<) < 0$, $(\mathbf{k} \cdot \mathbf{B}_0,=) = 0$, and $(\mathbf{k} \cdot \mathbf{B}_0,>) > 0$. This causes the direction of wave propagation to change from co magnetic field to counter magnetic field. This is a simplified picture of what happens as a result of the rotational transform changes when going from configurations that are typical for the modes in cluster 1 to cluster 2 (both have a (5,-4) dominant mode), or cluster 3 to 4 (both have a (4,-3) dominant mode).

The perturbed magnetic field is given by the following in linearised ideal MHD [29]:

$$\mathbf{B}_1 = \nabla \times (\boldsymbol{\xi} \times \mathbf{B}_0), \quad (5)$$

with all perturbation quantities for normal modes having the form $\exp(i\mathbf{k} \cdot \mathbf{r})$. If for simplicity, we assume \mathbf{B}_0 is not spatially varying, then:

$$\mathbf{B}_1 = i\mathbf{k} \times (\boldsymbol{\xi} \times \mathbf{B}_0) \quad (6)$$

$$= (i\mathbf{k} \cdot \mathbf{B}_0)\boldsymbol{\xi} - (i\mathbf{k} \cdot \boldsymbol{\xi})\mathbf{B}_0. \quad (7)$$

The sign of $\mathbf{k} \cdot \mathbf{B}_0$ changes from negative to positive depending on whether $t < n/m$ or $t > n/m$. This situation is illustrated in figure 15 showing that the direction of mode propagation changes from co to counter-field for these two cases. If $\hat{\mathbf{k}} \cdot \hat{\mathbf{B}}_0 >> \hat{\mathbf{k}} \cdot \hat{\boldsymbol{\xi}}$, as is expected for a transverse wave with some degree of $k_{||}$, then the sign reversal of $\mathbf{k} \cdot \mathbf{B}_0$ will also cause \mathbf{B}_1 to change sign relative to $\boldsymbol{\xi}$. The density perturbation (equation 4) and emissivity perturbation (equation 3), will maintain the same sign because they are not directly dependent on \mathbf{B}_0 . Therefore, in this simplified case, we expect a transverse wave to exhibit a sign reversal between δn_e (or $\delta \epsilon$)

and a magnetic probe signal ($\propto \mathbf{B}_1 \cdot \hat{\mathbf{n}}_{probe}$) when going from a case where $t < n/m$ to $t > n/m$.

Cluster 1 and 2 both have the same dominant mode numbers and the typical rotational transform profiles for a large portion of the plasma is $t < 5/4$ for cluster 1 and $t > 5/4$ for cluster 2 (see figure 3). The same is true for clusters 3 and 4, except now the dominant mode number is (4,-3) and $t < 4/3$ for cluster 3 and $t > 4/3$ for cluster 4. Additionally, the data from synchronous imaging technique relies on a magnetic probe for a reference signal; therefore the phase of the CII 514nm emission is with respect to the phase of the magnetic probe signal allowing us to check for the expected sign reversal between δn_e (or $\delta \epsilon$) and \mathbf{B}_1 as measured at the magnetic probe.

Figure 16 shows that when moving from clusters 1 to 2, and from 3 to 4, the phase of the tomographically reconstructed mode shifts by 180° , which, as we have just shown, is expected for transverse waves with some degree of $k_{||}$. This confirms the polarisation analysis of the magnetic probes in section III B, where it was shown that these waves are dominantly transverse.

V. DISCUSSION AND CONCLUSIONS

Datamining of magnetic probe signals from H-1NF configuration scans uncovers four distinct clusters of low frequency fluctuations whose existence and frequencies exhibit a strong rotational transform dependence. Modelling of the H-1NF low frequency spectrum using CAS3D and CONTI shows the existence of beta induced gaps, Alfvén -acoustic gaps, and low frequency discrete predominantly shear Alfvén eigenmodes for H-1NF configurations that are representative of each of the clusters.

Thorough analysis of poloidal and helical magnetic probe array data using the non uniform discrete Fourier transform provided the best fit toroidal and poloidal mode numbers for these clusters. In all cases, n/m agrees closely with the rotational transform values within the plasma, with the resonant surface being within the plasma for two of the clusters. Additionally, mode polarisation calculations using the tri-axis HMA probes shows that the modes are dominantly transverse with a small but non-negligible parallel component, as expected for BAE or BAAE type modes.

These mode numbers are used to select candidate discrete eigenmodes from the CAS3D simulations for comparison with 3D tomographic reconstruction of CII 514nm emission that was obtained using a high resolution synchronous imaging technique. The Fourier basis modes used in the tomographic inversion are based on the magnetic probe data, although, trialing many different basis modes shows that the best fit poloidal mode number for the imaging data agrees with the magnetic probe analysis.

Comparisons of the experimental data with the radial structure of GAE/NGAE and BAE type modes from CAS3D shows better agreement with the BAE type

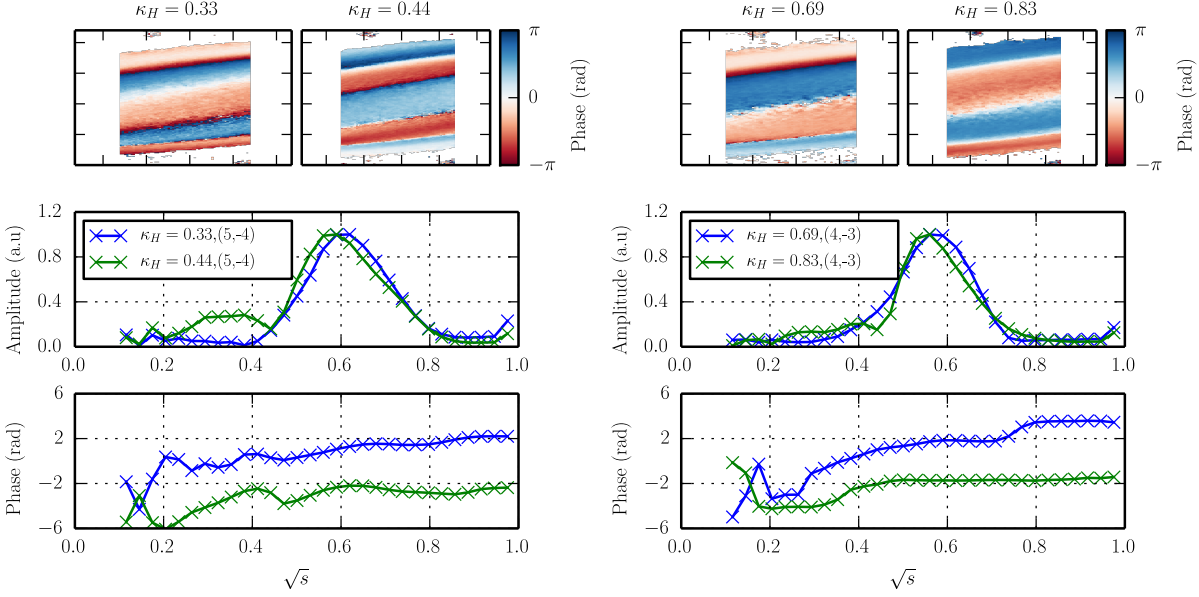


FIG. 16. Phase information and tomographic reconstructions of clusters 1-4. When going from cluster 1 to 2 and cluster 3 to 4, the phase of the signal relative to the reference magnetic probe undergoes a 180° shift. This phase shift is also present in the tomographic inversions in the region of \sqrt{s} where the amplitude is large.

modes as these appear to be more edge localised than the core localised GAE/NGAE type modes (due to the flat t profile near the axis for many H-1NF configurations). For two of the clusters, low frequency, shear dominated discrete modes that agree well with the experimental radial structure are found in the sound continua. The nature of these modes is unclear and is currently under investigation. Their existence depends on including compressibility so they are likely to be some form of Alfvén-acoustic gap mode; however, the mode resonant surface is not within the plasma for these H-1NF configurations and the mode location is quite far from the turning point in the relevant Alfvén continua, differentiating them from what would normally be expected for a GAE, BAE or BAAE type mode.

In previous work, the frequency dependence of these modes on H-1NF configurations (rotational transform profile) was examined in detail [8, 16]. It was found that this dependence can be qualitatively reproduced if the modes are GAEs or NGAEs, through the changes in frequency of the turning points of the Alfvén continuum, due to changes in t ; however, the predicted frequencies are approximately a factor of three higher than the experimental observations [16]. Bertram et al [16] suggested that by assuming a hollow temperature profile, this frequency sweeping behaviour of clusters 1 and 3 could be attributed to BAEs because the inwardly moving mode resonant surface (as κ_H increases) causes the temperature at the rational surface to decrease, leading to a reduction in the frequency of the beta induced turning

point. However, it was noted that this does not reproduce the behaviour for clusters 2 and 4 where the mode resonant surface is not within the plasma. Additionally, for all four clusters, the emissivity-derived density data shows minimal changes in the radial location of the mode (see figure 16), which would require the temperature gradient to be unrealistically large to produce the observed frequency dependence. Here we hypothesize that the frequency dependence can be recovered if there is a dependence of temperature on configuration, which causes the temperature and consequently the beta-induced turning point and Alfvén-acoustic gaps to move to lower frequencies at the minima of the whale tails (at $\kappa_H = 0.4$ and $\kappa_H = 0.72$). Decreased density in the configurations indicates a degradation in confinement. If true, this would allow the frequency dependence for all of the clusters to be reproduced and would be consistent with the similar radial structure for all of the modes. A new diagnostic, which is currently being commissioned, will provide temperature measurements using helium line ratios, allowing this hypothesis to be tested.

Looking forward, data from a recently installed 21 channel density interferometer should provide improved density profiles for input to the theoretical models as well as a more direct measure of the density fluctuations. Additionally, work has begun on the synchronous imaging and tomographic inversion of atomic helium transition-line emission at multiple wavelengths, which in conjunction with collisional radiative models will allow measurements of both the electron density and temperature fluc-

tuations for a more direct comparison with theory.

One outstanding question is the drive mechanism and continuum damping calculations for these modes. The ICRH heating system has the ability to generate a fast ion population, although, ions travelling at the Alfvén speed or a sideband are likely to be poorly confined in H-1NF as their Larmor radius is a significant portion of the plasma radius. Unfortunately, there are currently no fast particle diagnostics on H-1NF to directly measure if these populations exist; however, planned work includes using the LGRO and CAS3DK [30] codes to calculate what types of energetic particle populations are required to destabilise these modes. Additionally, work on contin-

uum damping calculations is also ongoing [31].

VI. ACKNOWLEDGEMENTS

The authors would like to thank the H-1NF team for continued support of experimental operations. This work was supported in part by the Education Investment Fund under the Super Science Initiative of the Australian Government. SRH wishes to thank AINSE Ltd. for providing financial assistance to enable this work on H-1NF to be conducted. JH and BB acknowledge support from the Australian Research Council Discovery, grant numbers DP110104833 and DP0666440 respectively. MH acknowledges ARC support from FT0991899.

-
- [1] W. W. Heidbrink, Physics of Plasmas **15**, 055501 (2008).
 - [2] A. Fasoli *et al.*, Nuclear Fusion **47**, S264 (2007).
 - [3] K. L. Wong, R. J. Fonck, S. F. Paul, D. R. Roberts, E. D. Fredrickson, R. Nazikian, H. K. Park, M. Bell, N. L. Bretz, R. Budny, S. Cohen, G. W. Hammett, F. C. Jobes, D. M. Meade, S. S. Medley, D. Mueller, Y. Nagayama, D. K. Owens, and E. J. Synakowski, Physical Review Letters **66**, 1874 (1991).
 - [4] R. B. White, E. Fredrickson, D. Darrow, M. Zarnstorff, R. Wilson, S. Zweber, K. Hill, Y. Chen, and G. Fu, Physics of Plasmas **2**, 2871 (1995).
 - [5] T. Hender *et al.*, Nuclear Fusion **47**, S128 (2007).
 - [6] S. Hamberger, B. D. Blackwell, L. Sharp, and D. Shenton, Fusion Technology **17**, 123 (1990).
 - [7] R. Jiménez-Gómez, A. Könies, E. Ascasíbar, F. Castejón, T. Estrada, L. Eliseev, A. Melnikov, J. Jiménez, D. G. Pretty, D. Jiménez-Rey, *et al.*, Nuclear Fusion **51**, 033001 (2011).
 - [8] B. D. Blackwell, D. G. Pretty, J. Howard, R. Nazikian, S. T. A. Kumar, D. Oliver, D. Byrne, J. H. Harris, C. A. Nuhrenberg, M. McGann, *et al.*, arXiv preprint arXiv:0902.4728 (2009).
 - [9] J. H. Harris, M. G. Shats, B. D. Blackwell, W. M. Solomon, D. G. Pretty, S. M. Collis, J. Howard, H. Xia, C. A. Michael, and H. Punzmann, Nuclear Fusion **44**, 279 (2004).
 - [10] D. G. Pretty, *A study of MHD activity in the H-1 heliac using data mining techniques*, Ph.D. thesis, The Australian National University (2007).
 - [11] D. G. Pretty and B. D. Blackwell, Computer Physics Communications **180**, 1768 (2009).
 - [12] S. R. Haskey, B. D. Blackwell, B. Seiwald, M. J. Hole, D. G. Pretty, J. Howard, and J. Wach, Review of Scientific Instruments **84**, 093501 (2013).
 - [13] S. R. Haskey, N. Thapar, B. D. Blackwell, and J. Howard, Review of Scientific Instruments **85**, 033505 (2014).
 - [14] S. R. Haskey, , B. D. Blackwell, and D. G. Pretty, Computer Physics Communications **185**, 1669 (2014).
 - [15] S. R. Haskey, B. D. Blackwell, B. Seiwald, and J. Howard, Nuclear Fusion **54**, 083031 (2014).
 - [16] J. Bertram, B. D. Blackwell, and M. J. Hole, Plasma Physics and Controlled Fusion **54**, 055009 (2012).
 - [17] J. Bertram, M. J. Hole, D. G. Pretty, B. D. Blackwell, and R. L. Dewar, Plasma Physics and Controlled Fusion **53**, 085023 (2011).
 - [18] A. D. Turnbull, E. J. Strait, W. W. Heidbrink, M. S. Chu, H. H. Duong, J. M. Greene, L. L. Lao, T. S. Taylor, and S. J. Thompson, Physics of Fluids B: Plasma Physics (1989-1993) **5**, 2546 (1993).
 - [19] W. W. Heidbrink, E. Ruskov, E. M. Carolipio, J. Fang, M. A. van Zeeland, and R. A. James, Physics of Plasmas (1994-present) **6**, 1147 (1999).
 - [20] W. W. Heidbrink, E. J. Strait, M. S. Chu, and A. D. Turnbull, Phys. Rev. Lett. **71**, 855 (1993).
 - [21] N. N. Gorelenkov, H. L. Berk, E. Fredrickson, S. E. Sharapov, and J. E. Contributors, Physics Letters A **370**, 70 (2007).
 - [22] N. N. Gorelenkov, H. L. Berk, N. A. Crocker, E. D. Fredrickson, S. Kaye, S. Kubota, H. Park, W. Peebles, S. A. Sabbagh, S. E. Sharapov, D. Stutmat, K. Tritz, F. M. Levinton, H. Yuh, the NSTX Team, and J. E. Contributors, Plasma Physics and Controlled Fusion **49**, B371 (2007).
 - [23] N. N. Gorelenkov, M. A. Van Zeeland, H. L. Berk, N. A. Crocker, D. Darrow, E. Fredrickson, G.-Y. Fu, W. W. Heidbrink, J. Menard, and R. Nazikian, Physics of Plasmas (1994-present) **16**, 056107 (2009).
 - [24] C. Schwab, Physics of Fluids B: Plasma Physics **5**, 3195 (1993).
 - [25] A. Könies and D. Eremin, Physics of Plasmas **17**, 012107 (2010).
 - [26] S. P. Hirshman and J. C. Whitson, Physics of Fluids **26**, 3553 (1983).
 - [27] S. P. Hirshman and H. K. Meier, Physics of Fluids (1958-1988) **28**, 1387 (1985).
 - [28] H. Summers, Online at <http://adas.phys.strath.ac.uk> (2004).
 - [29] J. P. Freidberg, *Ideal magnetohydrodynamics* (Plenum Press, New York, 1987).
 - [30] A. Könies, Physics of Plasmas (1994-present) **7**, 1139 (2000).
 - [31] G. W. Bowden, A. Könies, M. J. Hole, N. N. Gorelenkov, and G. R. Dennis, Physics of Plasmas (1994-present) **21**, 052508 (2014).

Linear ideal MHD predictions for n=2 non-axisymmetric magnetic perturbations on DIII-D

The previous chapters have dealt with some of the issues that arise in a fully 3D machine such as H-1NF. Tokamaks are an alternative, and currently more advanced approach to magnetic confinement nuclear fusion. They have the significant advantage of being close to axisymmetric, meaning that many problems can be simplified to 2D; however, unlike stellarators, they suffer from problems with steady state operation and current driven instabilities. Recently it has been found that the application of 3D magnetic perturbations has many beneficial outcomes, such as the suppression of edge localised modes (appendix A). Consequently, 3D perturbation coil sets have been installed on all major tokamak experiments and the design of ITER was modified to include a MP coil set.

The publication in this chapter presents an in-depth analysis of the linear ideal plasma response to these 3D magnetic fields. The results demonstrate how to tailor the applied field to meet certain goals such as maximising the vacuum pitch resonant field or driving global modes such as the kink mode more strongly. The effects of safety factor profile, plasma pressure, and phasing between upper and lower MP coil arrays are examined. Recent experiments on DIII-D which explore the effects of upper-lower I-coil phasing are shown in appendix C. Supplementary information which may be useful for future research is included in appendix J. 80% of the research and 80% of the writing presented in this paper are my own work. The paper is also available from <http://dx.doi.org/10.1088/0741-3335/56/3/035005>.

Linear ideal MHD predictions for $n = 2$ non-axisymmetric magnetic perturbations on DIII-D

S R Haskey¹, M J Lanctot², Y Q Liu³, J M Hanson⁴, B D Blackwell¹ and R Nazikian⁵

¹ Plasma Research Laboratory, Research School of Physics and Engineering, The Australian National University, Canberra, ACT 0200, Australia

² General Atomics, PO Box 85806, San Diego, CA 92186-5608, USA

³ Euratom/CCFE Fusion Association, Culham Science Centre, Abingdon, OX14 3DB, UK

⁴ Columbia University, 116th St and Broadway, New York, NY 10027, USA

⁵ Princeton Plasma Physics Laboratory, Princeton, NJ 08543-0451, USA

E-mail: shaun.haskey@anu.edu.au

Received 25 July 2013, revised 20 December 2013

Accepted for publication 14 January 2014

Published 5 February 2014

Abstract

An extensive examination of the plasma response to dominantly $n = 2$ non-axisymmetric magnetic perturbations (MPs) on the DIII-D tokamak shows the potential to control 3D field interactions by varying the poloidal spectrum of the radial magnetic field. The plasma response is calculated as a function of the applied magnetic field structure and plasma parameters, using the linear magnetohydrodynamic code MARS-F (Liu *et al* 2000 *Phys. Plasmas* **7** 3681). The ideal, single fluid plasma response is decomposed into two main components: a local pitch-resonant response occurring at rational magnetic flux surfaces, and a global kink response. The efficiency with which the field couples to the total plasma response is determined by the safety factor and the structure of the applied field. In many cases, control of the applied field has a more significant effect than control of plasma parameters, which is of particular interest since it can be modified at will throughout a shot to achieve a desired effect. The presence of toroidal harmonics, other than the dominant $n = 2$ component, is examined revealing a significant $n = 4$ component in the perturbations applied by the DIII-D MP coils; however, modeling shows the plasma responses to $n = 4$ perturbations are substantially smaller than the dominant $n = 2$ responses in most situations.

Keywords: edge localized modes, resonant magnetic perturbations, magnetohydrodynamics, tokamaks, toroidal plasma confinement

(Some figures may appear in colour only in the online journal)

1. Introduction

Non-axisymmetric magnetic perturbations (MPs) have been used on tokamaks to suppress [1–5], mitigate [6, 7] and destabilize [8] edge-localized modes (ELMs), perform magnetic spectroscopy [9, 10], control resistive wall modes [11, 12] and neoclassical tearing modes [13], and correct error fields [14, 15]. Due to their role in accessing fusion relevant plasma scenarios, perturbation coil sets are now an integral system on many major tokamaks [16, 17]. Recently, ELM suppression using dominantly $n = 2$ perturbations has been

achieved on DIII-D, which was previously only attainable using $n = 3$ fields [18]. The suppression was achieved using the internal coils (I-coils), two rows of six coils each, located above and below the midplane inside the vacuum vessel. ELM suppression was found within different ranges of safety factors depending on the structure of the applied field, with suppression occurring for applied fields found to couple best to marginally stable kink modes. Additionally, the $n = 2$ configuration on DIII-D offers substantially more control over the applied poloidal spectrum of the radial magnetic field than $n = 3$ and as such, has been the focus of recent experiments

[18]. These results have motivated an extensive examination of the $n = 2$ plasma response in DIII-D equilibria over a wide range of plasma parameters and applied fields. The results presented here are useful for guiding future experiments and for correlating the ideal plasma response with observed experimental outcomes.

A single coil produces a magnetic field with a radial component that is normal to the equilibrium magnetic flux surfaces. The radial component of the magnetic field can be Fourier decomposed along the toroidal and poloidal angles of the torus to produce a spectrum of toroidal (n) and poloidal (m) harmonics, hereafter referred to as the toroidal and poloidal spectra. These spectra are controlled by combining fields from multiple coils. The toroidal spectrum is controlled by the relative phase difference of the currents in coils at the same poloidal angle but different toroidal angles. Similarly, the poloidal spectrum is controlled by the relative phase difference of the currents in coils at the same toroidal angle but different poloidal angles. Here, we consider $n = 2$ fields, where the toroidal phase difference between currents in the upper and lower I-coil, $\Delta\phi_{ul}$, is defined through the following relations: $I_{upper} \propto \cos(n\phi_{coil})$ and $I_{lower} \propto \cos(n\phi_{coil} + \Delta\phi_{ul})$, where I_{upper} and I_{lower} are the currents in the MP coils above and below the midplane respectively, and ϕ_{coil} is the DIII-D tokamak toroidal angle location of the center of a MP coil. The DIII-D tokamak toroidal angle is in the opposite direction to the toroidal equilibrium magnetic field.

Previous studies have found that the measured magnetic field is substantially different from that predicted in a pure vacuum case, indicating the need to take into account the plasma response in MP calculations. For example, in [19], the plasma response to an applied MP, as measured by a midplane poloidal pickup coil, normalized to the MP coil current, showed a strong dependence on $\beta_N = \beta(\%)a(m)B_0(T)/I_p(MA)$, with the pickup output due to the plasma response exceeding the output of a radial pickup due to the vacuum field by more than a factor of 10 at high β_N . Here, $\beta = 2\mu_0\langle p \rangle/B_0^2$, $\langle p \rangle$ represents the volume-averaged pressure, μ_0 the magnetic permeability of free space, I_p the plasma current, a the plasma minor radius and B_0 the equilibrium magnetic field strength on axis. This substantial modification of the magnetic field by the plasma indicates the importance of including the plasma response when modeling non-axisymmetric plasma equilibria.

Both screening and amplification can occur in the plasma response to MPs. The screening, at least in the linear (small-island) regime, robustly occurs for the resonant component of the MP, either due to an ideal plasma response or due to fast plasma flow. There is strong experimental evidence of screening, for example smaller lobe sizes than vacuum predictions in MAST, and the absence of strike point splitting in H-mode JET discharges [21]. The amplification, due to excitation of marginally stable modes (such as the kink mode) by the non-resonant components of the MP, depends on the equilibrium configuration, in particular on the plasma pressure. In order to model the plasma response within the framework of magnetohydrodynamic (MHD), one can follow the time-dependent dynamic evolution of the 2D equilibria until a 3D

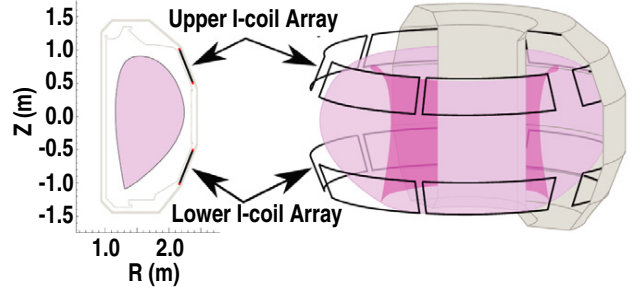


Figure 1. 3D picture showing the radial location of the I-coils with respect to the DIII-D vacuum vessel. Poloidal cross section shows the location of the I-coils above and below the midplane.

steady-state solution is reached, or one can attempt to find a nearby 3D equilibrium. Additionally, the problem can be treated linearly or non-linearly, leading to four different approaches [20].

In this paper, we have used the single fluid linear MHD code MARS-F [22], which treats the 3D MP as a time-dependent, driven problem. This approach does not include non-linear effects, but can include a resistive wall, toroidal rotation, plasma resistivity, and guarantees force balance. In the simulations presented here, we include a resistive wall, but exclude plasma rotation and resistivity.

While there are non-linear codes such as M3D [23, 24], M3D-C¹ [25], NIMROD [26, 27], RMHD [28] or JOREK [29, 30], the linear approach has the significant advantage of being less computationally intensive and has been experimentally validated. For example, previous work looking at the $n = 1$ and 3 perturbations on DIII-D [19, 31] found good qualitative agreement between MARS-F predictions and measurements from the magnetic pickup coils up to 80% of the predicted ideal MHD pressure limit calculated without a conducting wall near the plasma edge (β_N^{NW}). At larger β_N , the MARS-F code predicts a much larger plasma response, indicating the need to include additional physics, or non-linear effects.

This paper is organized as follows. In section 2, we introduce the MP coils on DIII-D and discuss the differences between the MARS-F coil representation and a geometrically accurate representation of the MP coils. Section 3 describes the main components of the ideal plasma response and how we separate and quantify these components. Section 4 presents maps showing the parameter dependence of the components described in section 3. These maps are particularly useful for guiding experiments, and some examples of their use is given. Lastly, section 5 considers the importance of harmonics other than the dominant $n = 2$ component.

2. Validation of the MARS-F MP coil representation

In this study, we consider the plasma response to fields applied with the I-coil. Half of the coils are located above the midplane, and the other half are below, as shown in figure 1. The six toroidal locations allow perturbations with dominant toroidal mode numbers up to 3 to be applied. Higher harmonics are also present due to the geometry of the I-coils as discussed below.

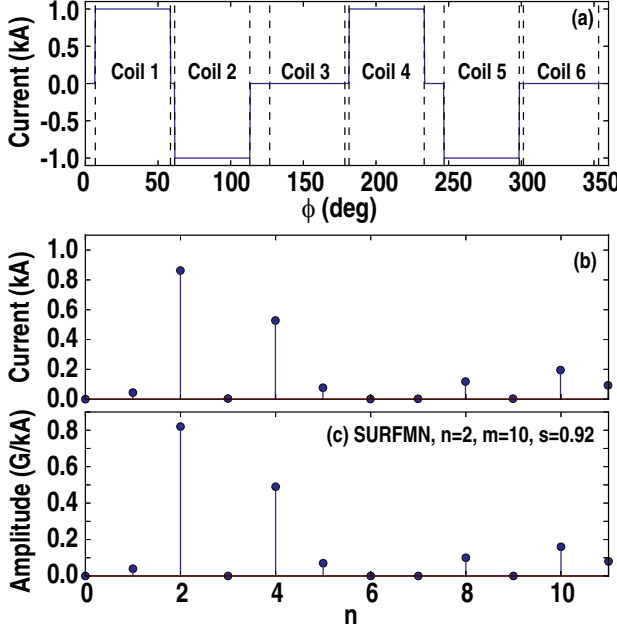


Figure 2. (a) A simplified picture of the magnetic field normal to the midpoint of the upper (or lower) I-coil array as a function of ϕ for a common $n = 2$ configuration on DIII-D (top). The toroidal extent of each of the coils in the array is marked by the dashed vertical lines. (b) Fourier decomposition of this profile in the toroidal direction shows that in addition to the dominant $n = 2$ component, there is a significant $n = 4$ component present. (c) The toroidal harmonic content of the $m = 10$ mode at $s = 0.92$ calculated using SURFMN showing the toroidal harmonics that are present in addition to $n = 2$.

Adjusting $\Delta\phi_{ul}$ allows the poloidal harmonic (m) spectrum of the applied field to be modified. Refer to section 1 for the definition of $\Delta\phi_{ul}$ as it is used in this paper.

As described in [32], MARS-F does not include the full 3D geometry of the MP coils. Instead, the source current, j_{MP} , is represented as a surface current at the radial location of the MP coils. The toroidal component of j_{MP} has a finite width along the poloidal angle, similar to the pointwise MP coil current on the poloidal plane, and varies as $\exp(in\phi)$ along the toroidal angle, ϕ . The poloidal component of j_{MP} is obtained from the divergence-free condition ($\nabla \cdot j_{MP} = 0$) and the MP field generated by j_{MP} is determined by $\nabla \times b = j_{MP}$.

In order to quantitatively compare MARS-F calculations with experiment, it is necessary to calculate the equivalent amplitude of the applied field in the simple coil model. The mapping employed is illustrated in figure 2(a) where the simplified magnetic field normal to the midpoint of the upper (or lower) I-coil array is plotted as a function of toroidal angle ϕ for a common $n = 2$ configuration on DIII-D. Fourier decomposition of this simplified field profile shows that a significant $n = 4$ component is present in addition to the dominant $n = 2$ component (figure 2(b)). While this is a simplistic treatment, it allows us to estimate an approximately equivalent $n = 2$ current for MARS-F in order to compare with experiments and vacuum codes. In this case, using figure 2(b), we set the MARS-F equivalent $n = 2$ current to 0.86 times the maximum current in the I-coils. The presence of harmonics other than $n = 2$ is discussed later in this section.

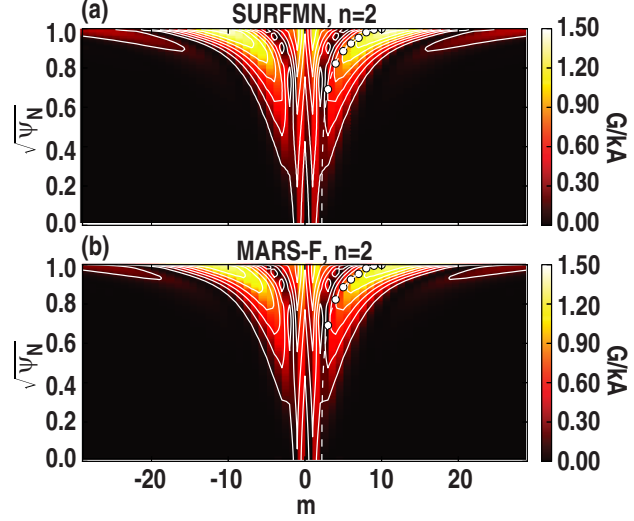


Figure 3. Poloidal harmonic content of the applied field calculated using SURFMN (a) and MARS-F (b) for the $n = 2$ component of the dominantly $n = 2$ MP. The locus of pitch resonance ($m = nq$) for a particular equilibrium with $q_{95} = 3.9$, is overlaid with the location of low order pitch-resonant harmonics marked with a dot. The MARS-F and SURFMN harmonic structures are in good agreement.

To assess the accuracy of the $n = 2$ applied vacuum field from MARS-F, we compare it with the output from the SURFMN vacuum code [33], which includes a realistic geometric model of the I-coils. Here, we Fourier decompose the magnetic field normal to the flux surfaces in the toroidal and poloidal directions in straight field line coordinates, as described in appendix A of [33], to obtain $\delta B_r^{m,n}(s)$, where m and n represent the poloidal and toroidal harmonics respectively, $s = \sqrt{\psi_N}$ is a flux surface label and ψ_N is the normalized poloidal flux. In addition, we can define $\delta B_{r,vac}^{m,n}(s)$, $\delta B_{r,plas}^{m,n}(s)$, and $\delta B_{r,tot}^{m,n}(s) = \delta B_{r,vac}^{m,n}(s) + \delta B_{r,plas}^{m,n}(s)$ where $\delta B_{r,vac}^{m,n}$ is the field generated by the MP coils, $\delta B_{r,plas}^{m,n}$ is the plasma generated field and $\delta B_{r,tot}^{m,n}$ is the sum of the two. Each of these fields is normalized to the MP coil current and is reported in units of G kA^{-1} .

The toroidal spectrum of the applied field calculated with SURFMN shows significant toroidal sidebands. The toroidal harmonic amplitudes for the magnetic field normal to the flux surfaces for the $m = 10$ component at $s = 0.92$ [$|\delta B_{r,vac}^{m=10,n}(s = 0.92)|$] calculated by SURFMN for the $\Delta\phi_{ul} = 0^\circ$ case are shown in figure 2(c). We choose $m = 10$ and $s = 0.92$ for this comparison because these values are in the range of interest in later sections of this paper. As expected, the $n = 2$ component is the largest; however, there are significant contributions from other toroidal harmonics, in particular $n = 4$. Comparing figure 2(c) with figure 2(b), we see that the simplistic model provides a good estimate of the relative amplitude of the different toroidal harmonics.

There is good agreement between SURFMN and MARS-F for the poloidal harmonic structure of the $n = 2$ toroidal harmonic. A comparison between SURFMN and MARS-F for the $|\delta B_{r,vac}^{m,n=2}(s)|$ harmonics for $\Delta\phi_{ul} = 0^\circ$ is shown in figure 3. For clarity, the radial dependence of some individual

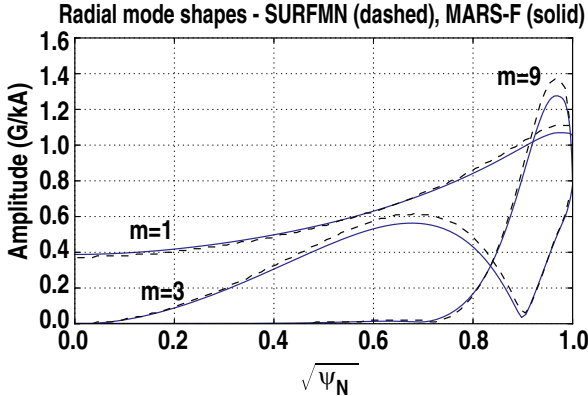


Figure 4. Comparison between the radial structure of selected vacuum poloidal harmonics calculated by SURFMN (dashed) and MARS-F (solid) for $n = 2$, showing good agreement.

poloidal harmonics is shown in figure 4. For this comparison, we set the MARS-F MP current to the $n = 2$ component shown in figure 2(b). In the plasma volume, the MARS-F model is in quantitative agreement with SURFMN to within $\approx 8\%$.

A comparison between SURFMN and MARS-F for the $|\delta B_{r,\text{vac}}^{m,n=4}(s)|$ harmonics for $\Delta\phi_{\text{ul}} = 0^\circ$ is shown in figure 5, with the MARS-F MP current set to the $n = 4$ component shown in figure 2(b). As with the $n = 2$ harmonic, the agreement between the two codes is good suggesting MARS-F can accurately model the individual toroidal harmonics of the I-coil MP.

The presence of toroidal harmonics other than $n = 2$ can be taken into account in MARS-F by performing separate simulations for each harmonic, while accounting for the relative strength of each harmonic in the vacuum field (figure 2(b)). In section 5, we will show that the $n = 4$ plasma response is negligible, except in some special circumstances.

3. Components of the ideal MHD plasma response

The scope of this paper is limited to the ideal MHD plasma response. The effects of resistivity and rotation are the subject of future work. The plasma response, $\delta B_{r,\text{plas}}^{m,n}(s)$, consists of two main components in the ideal MHD case for the low frequency/static, low- n fields, applied by the I-coils. Firstly, there is a screening of the magnetic field normal to the flux surfaces, which occurs for magnetic field line pitch-resonant harmonics $m = nq$ (hereafter referred to as pitch-resonant component of the response). Secondly, there is a coupling to the stable external kink mode, which generally occurs for poloidal harmonics $nq < m < 3nq$ (hereafter referred to as kink-resonant component [34]). The location of these harmonics in the poloidal spectrum of the plasma response to the $n = 2$ component of the MP [$|\delta B_{r,\text{plas}}^{m,n=2}(s)|$] are shown in figure 6, along with $|\delta B_{r,\text{vac}}^{m,n=2}(s)|$ and $|\delta B_{r,\text{tot}}^{m,n=2}(s)|$.

Pitch-resonant fields are of interest due to their role in the creation of stochastic magnetic fields, which may reduce the edge pressure gradient below the ELM instability threshold [35]. In the ideal MHD model, the plasma responds to the pitch-resonant fields by generating currents, which reduce the

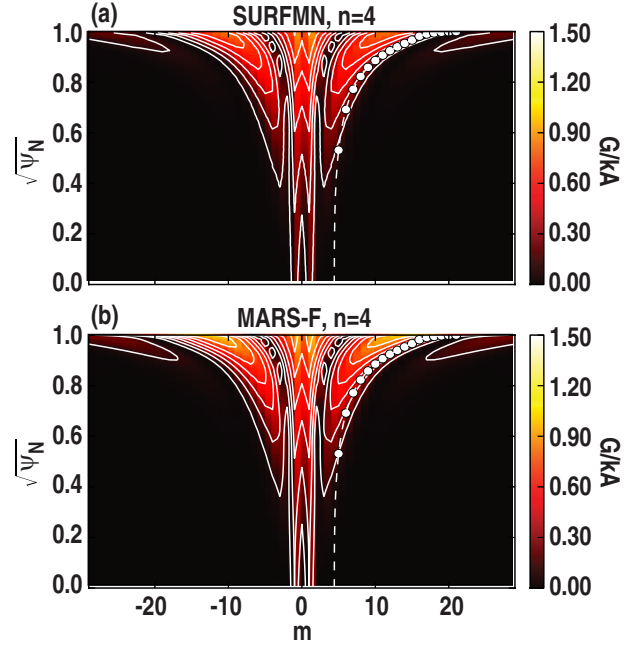


Figure 5. Poloidal harmonic content of the applied field as calculated using SURFMN (a) and MARS-F (b) for the $n = 4$ component of the dominantly $n = 2$ MP. The locus of pitch resonance ($m = nq$) for a particular equilibrium with $q_{95} = 3.9$, is overlaid with the location of low order pitch-resonant harmonics marked with a dot. As with the $n = 2$ harmonic, the MARS-F and SURFMN poloidal harmonic structures are in good agreement.

pitch-resonant components to zero [$\delta B_{r,\text{tot}}^{m=nq,n}(s) = 0$], leaving the magnetic topology unchanged and preventing islands from forming near the rational surfaces. Pitch-resonant fields are also of interest because in the case where the islands are suppressed by plasma rotation, the resulting currents create an electromagnetic torque which acts as a sink in the toroidal momentum balance equation [36]. The cancellation of the fields at the pitch-resonant surfaces can be seen in figure 12. When plasma resistivity and toroidal rotation are taken into account, it is possible to amplify the pitch-resonant components for sufficiently slow rotation leading to larger islands than predicted by vacuum theory alone [32]. More generally, the pitch-resonant harmonics are subject to increased attenuation as the resistivity is decreased or the rotation is increased [32].

To quantify the degree of pitch-resonant drive, we calculate the sum of all the applied pitch-resonant harmonics in the vacuum field, and the average of all the applied pitch-resonant harmonics in the vacuum field (where N_{res}^n is the number of pitch-resonant harmonics satisfying $m = nq$ in the plasma):

$$\delta B_{\text{res}}^n = \sum |\delta B_{r,\text{vac}}^{m=nq,n}(s)|, \quad (1)$$

$$\overline{\delta B}_{\text{res}}^n = \delta B_{\text{res}}^n / N_{\text{res}}^n. \quad (2)$$

It is useful to consider $\overline{\delta B}_{\text{res}}^n$ as well as δB_{res}^n to capture the strength of the individual resonant harmonics in addition to the number of resonant harmonics, which increases

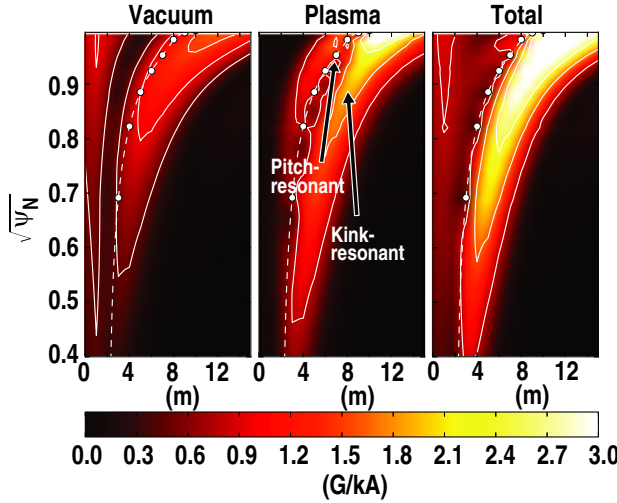


Figure 6. The amplitude of the vacuum, plasma and total $n = 2$ poloidal harmonics ($|\delta B_{r,\text{vac}}^{m,n=2}(s)|$, $|\delta B_{r,\text{plas}}^{m,n=2}(s)|$ and $|\delta B_{r,\text{tot}}^{m,n=2}(s)|$) as calculated by MARS-F. The ideal plasma response has two main components, a pitch-resonant response, which acts to perfectly cancel the applied pitch-resonant field (harmonics $m = nq$) and an amplification of the harmonics that couple to the kink mode (poloidal harmonics satisfying $nq < m < 3nq$). The $m = nq$ line for the equilibrium used ($q_{95} = 3.9$ and $\beta_N/\ell_i = 2.0$) is overlaid with the location of low-order rational surfaces marked with a white dot. These images have been smoothed over the discrete m to make trends easier to see.

with q_{95} . The number of resonant harmonics is bounded for the equilibria used here because MARS-F requires a finite edge q . This is discussed in section 4.

For the pitch-resonant calculations, we do not take the ideal plasma response into account because it is equal and opposite to the applied vacuum field [$\delta B_{r,\text{plas}}^{m=nq,n}(s) = -\delta B_{r,\text{vac}}^{m=nq,n}(s)$]. While the formation of magnetic islands in the ideal plasma response case is not possible, these measures indicate how strongly the vacuum field couples to the pitch-resonant harmonics, and are still useful measures of the possibility of island formation when resistivity and rotation are considered. Including the effects of resistivity and rotation is outside the scope of this paper.

Poloidal harmonics in the range $nq < m < 3nq$ can couple to a stable external global kink mode, resulting in substantial amplification of these harmonics. This is often referred to as resonant field amplification (RFA) [37], and can be clearly seen in figures 6 and 12. The level to which the kink mode is driven is of interest for several reasons. Firstly the experimentally observed $n = 2$ ELM suppression windows in [18] correspond to upper-lower I-coil phasings that maximize the kink-resonant response. Also, a disruption may occur if the mode is driven to sufficiently large amplitude. Finally, the excitation of this mode can give rise to larger plasma displacements which generally apply a braking torque to the plasma through the increased neoclassical toroidal viscosity (NTV) [36]. The responses from other stable global modes (for example Alfvén eigenmodes, internal kink, tearing modes, ballooning modes) are not usually seen because they generally have higher n numbers, and/or high rotation

frequency meaning they cannot be in direct resonance with the low-frequency/static, low- n MPs considered here [38]. These modes can interact non-linearly with the low- n MP, although it is not possible to see this interaction in the linear approach considered here. The effect of resistivity and rotation on the RFA as calculated using MARS-F are described in [38]. It was found that ideal and resistive plasma responses result in similar peak amplitudes for all poloidal harmonics, while decreases in rotation generally increase the RFA although this effect is reduced as plasma resistivity is decreased.

To quantify the extent of the coupling to the external kink mode, we find the strongest harmonic in the plasma response that is in the range $nq + 2 < m < 3nq$ at a particular flux surface near the edge of the plasma. This measure can be represented as follows:

$$\delta B_{\text{kink}}^n = |\delta B_{r,\text{plas}}^{m^*,n}(s = 0.92)|, \quad (3)$$

where m^* is the harmonic that gives the maximum plasma response for any $\Delta\phi_{\text{ul}}$:

$$m^* = \arg \max_{nq+2 < m < 3nq} |\delta B_{r,\text{plas}}^{m,n}(s = 0.92, \Delta\phi_{\text{ul}})|. \quad (4)$$

We set the lower bound for m to be $nq + 2$ so that we avoid accidental selection of harmonics which may be part of the plasma screening response. Low- n peeling modes have also been observed for the low-frequency/static, low- n MPs [38], and as we will show in section 4.2, there is some evidence for excitation of these modes as a new pitch-resonant surface enters the plasma, although the extent to which this is introduced due to smoothing of the x-point (as required by MARS-F) is under investigation. The peeling response is captured as part of the δB_{kink}^n measure but is isolated to narrow q_{95} ranges.

4. Maps of the ideal plasma response sensitivity to upper-lower I-coil phasing and plasma equilibrium parameters

In this section, we explore the amplitudes of the pitch-resonant and kink-resonant responses as a function of $\Delta\phi_{\text{ul}}$ and parameters such as plasma pressure and magnetic topology near the boundary. $\Delta\phi_{\text{ul}}$ represents the toroidal phase difference between currents in the upper and lower I-coil, which determines the poloidal spectrum of the applied radial magnetic field. Kirk *et al* [39] examined ELM mitigation (as measured by the ELM frequency) on MAST as a function of many parameters including $\Delta\phi_{\text{ul}}$ and q_{95} . A strong dependence was found for both of these parameters because they change the alignment of the applied perturbation (affected by $\Delta\phi_{\text{ul}}$) with the pitch of the equilibrium magnetic field (affected by q_{95}). Given the relatively narrow poloidal extent of the coils on MAST and the fine control of $\Delta\Phi_{\text{ul}}$ possible with 12 coils, we speculate that mapping out the parameter dependencies as described here may identify specific coil configurations that could be used to investigate the role of kink- and pitch-resonant harmonics in ELM mitigation on MAST. Unfortunately, on DIII-D, the upper and lower I-coil arrays consist of only six coils, making it impossible to make fine changes in the $n = 3$ poloidal spectrum with the I-coil alone. However,

by including $n = 3$ fields from another coil row such as the C-coil, it may be possible to vary the relative amplitudes of the kink- and pitch-resonant harmonics. This illustrates how mapping out these parameter dependencies is particularly useful for guiding experiments because it helps to identify important regions of parameter space, such as where island creation is more likely, or when coupling to the kink mode is optimized. This type of information can also be used in real-time control applications, such as changing $\Delta\phi_{ul}$ to maximize the resonant drive throughout a shot. We use $\delta B_{res}^{n=2}$ and $\overline{\delta B}_{res}^{n=2}$ to quantify the pitch-resonant response, and $\delta B_{kink}^{n=2}$ to quantify the kink-resonant response. The plasma pressure and magnetic topology are quantified using β_N/ℓ_i and q_{95} respectively (ℓ_i represents the plasma inductance).

Starting with a single experimental equilibrium reconstruction, the plasma pressure profile and safety factor profile were scaled and the equilibria solved by setting current as the free variable, to generate a set of ≈ 1000 equilibria, which form a well-sampled $(\beta_N/\ell_i, q_{95})$ space. The pressure profile is scaled using a single multiplier, while the q profile is scaled so that q near the plasma edge is modified while q near the plasma center remains relatively unchanged. For each q -profile, the maximum pressure is chosen to be marginally below the $n = 2$ no-wall stability limit. We consider H-mode, lower single-null DIII-D scenarios, with ITER similar shape (ISS) as our initial equilibria. As with [31], the magnetic field pitch angle measurements from multiple motional Stark effect (MSE) polarimeters [40], kinetic profile measurements from Thomson scattering [41] and charge exchange recombination spectroscopy (CER) [42], and ONETWO [43] transport calculations of the total pressure, including the contribution from non-thermal beam ions, are used to constrain reconstructions of the axisymmetric magnetic field using the EFIT code [44].

Since the MARS-F calculation is performed in flux coordinates, it cannot treat the exact separatrix geometry. Therefore, the EFIT equilibria were truncated to include 99.7% of the total poloidal flux. Test cases with flux truncation between 99.0% and 99.7% showed the calculated plasma response was not sensitive to this parameter in this range of values. The pressure and q -profiles are then scaled and the equilibria solved by setting current as the free variable, using the Grad-Shafranov solver in the CORSICA code [45]. Examples of the scaled profiles are shown in figure 7, and the location of the equilibria in $(\beta_N/\ell_i, q_{95})$ space is marked by black dots in figure 8. Figure 8 also marks the location of the $n = 2$ no-wall stability limit calculated using the DCON code [46]. The grid for MARS-F is created using the CHEASE code [47] and in the MARS-F calculations, a thin resistive axisymmetric shell is included to model the effect of the DIII-D wall.

4.1. Maps of the pitch-resonant response

The strength of the pitch-resonant drive depends strongly on $\Delta\phi_{ul}$ and the magnetic topology near the boundary (as measured by q_{95}), with a weaker dependence on plasma pressure (as measured by β_N/ℓ_i). Figure 8 shows $\delta B_{res}^{n=2}$ and $\overline{\delta B}_{res}^{n=2}$ (defined in equations (1) and (2)) calculated as

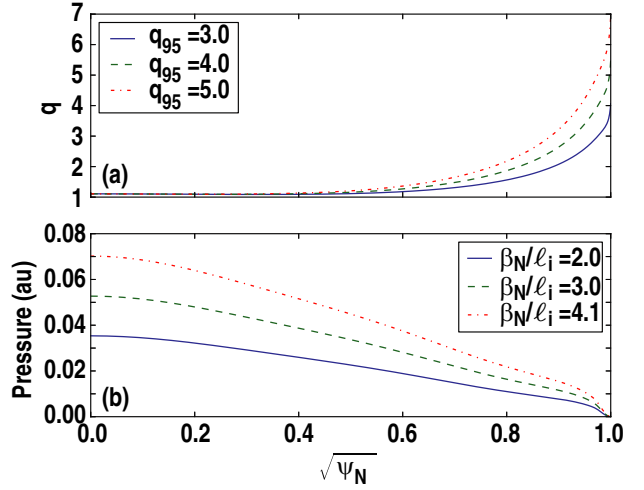


Figure 7. Examples of the scaled pressure (b) and q -profiles (a) that are used in the q_{95} and β_N/ℓ_i scans.

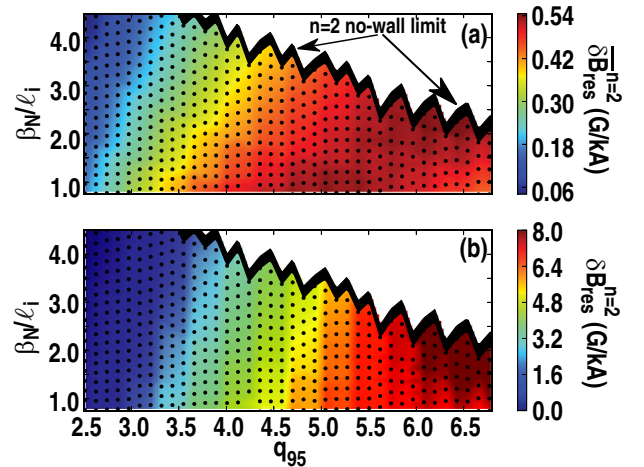


Figure 8. Measures of pitch-resonant drive, $\overline{\delta B}_{res}^{n=2}$ (a) and $\delta B_{res}^{n=2}$ (b) calculated as a function of β_N/ℓ_i and q_{95} , for $\Delta\phi_{ul} = 0^\circ$, exhibiting a strong dependence on q_{95} , and a smaller dependence on β_N/ℓ_i . The β_N/ℓ_i and q_{95} dependence of $\delta B_{res}^{n=2}$ and $\overline{\delta B}_{res}^{n=2}$ are similar. The thick black line marks the $n = 2$ no-wall limit.

a function of these parameters for $\Delta\phi_{ul} = 0^\circ$. The pitch-resonant drive depends predominantly on the location of the pitch-resonant line ($m = nq$) relative to the large amplitude lobes in $\delta B_{r,vac}^{m,n=2}(s)$ (as marked in figure 9). Changes in plasma pressure can modify the location of the flux surfaces relative to the applied field through the Shafranov shift; however, this effect is minimal compared to the dependence on q_{95} and $\Delta\phi_{ul}$. Comparing figures 8(a) and (b), we can see that $\delta B_{res}^{n=2}$ and $\overline{\delta B}_{res}^{n=2}$ produce similar results, although $\overline{\delta B}_{res}^{n=2}$ increases more rapidly at lower q_{95} , and $\delta B_{res}^{n=2}$ increases more rapidly at higher q_{95} . The reason these two measures are alike is because the shape of contours of constant amplitude in $\delta B_{r,vac}^{m,n=2}(s)$, follow a similar path in (s, m) space to the $m = nq$ line as shown in figures 6 and 9.

Varying $\Delta\phi_{ul}$ significantly alters the vacuum poloidal spectrum, which causes large variations in the pitch-resonant

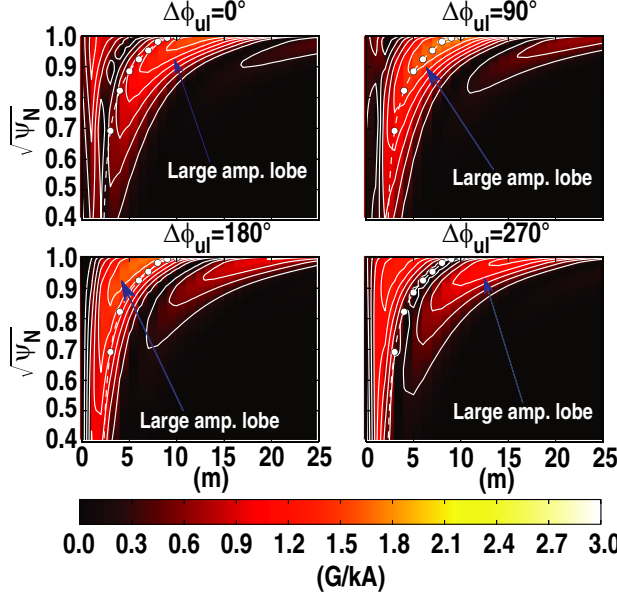


Figure 9. The applied vacuum field ($|\delta B_{r,\text{vac}}^{m,n=2}(s)|$) for four discrete $\Delta\phi_{ul}$ values, where $q_{95} = 3.9$ and $\beta_N/\ell_i = 2.0$. The pitch-resonant strength at the $m = nq$ harmonics (marked by white dots) varies considerably depending on $\Delta\phi_{ul}$. The lobe of strong harmonics sweeps towards lower m as $\Delta\phi_{ul}$ increases from 0° causing the ridge of maximum $|\delta B_{r,\text{vac}}^{m,n=2}(s)|$ to sweep over the pitch-resonant harmonics, with a maximum in $\delta B_{\text{res}}^{n=2}$ occurring near $\Delta\phi_{ul} = 90^\circ$. For $\Delta\phi_{ul} = 270^\circ$, the $m = nq$ line is in a valley and couples very poorly to the pitch-resonant harmonics.

drive. This is demonstrated in figure 9, where $\delta B_{r,\text{vac}}^{m,n=2}(s)$ is shown for four separate $\Delta\phi_{ul}$ values for an equilibrium with $q_{95} = 3.9$ and $\beta_N/\ell_i = 2.0$. As $\Delta\phi_{ul}$ is increased from 0° , the lobe of strong harmonics moves towards the lower poloidal harmonics passing over the $m = nq$ resonances in the process. We can take advantage of the linearity of the MARS-F code to substantially reduce our computation requirements when calculating the dependence on $\Delta\phi_{ul}$. In MARS-F it is possible to calculate the response to the upper array only (δB_U) and the lower array (δB_L) only. $\Delta\phi_{ul}$ can then be taken into account by combining the two responses as follows: $\delta B_{\Delta\phi_{ul}} = \delta B_U + \delta B_L \exp(\Delta\phi_{ul}i)$. This represents a substantial computational saving and allows us to examine the $\delta B_{\text{res}}^{n=2}$ dependence on q_{95} and $\Delta\phi_{ul}$, while setting $\beta_N/\ell_i = 1.15$, without having to perform a new set of calculations for each $\Delta\phi_{ul}$. The result is shown in figure 10. The regions of constant pitch-resonant drive essentially follow a straight line in $(\Delta\phi_{ul}, q_{95})$ space. This result demonstrates how q_{95} and $\Delta\phi_{ul}$ interact with one another to determine the efficiency of the coupling of $\delta B_{r,\text{vac}}^{m,n=2}(s)$ to the pitch-resonant harmonics, with $\Delta\phi_{ul}$ providing a more dominant contribution. There is also a general increase (decrease) in the maximum achievable $\delta B_{\text{res}}^{n=2}$ ($\overline{\delta B}_{\text{res}}^{n=2}$) as q_{95} increases, indicating that while an increase in q_{95} causes more resonant harmonics to be present in the plasma, the average amplitude of these harmonics decreases as q_{95} increases. This is ultimately due to the geometry of the MP coils, which restrict the range of accessible poloidal harmonics.

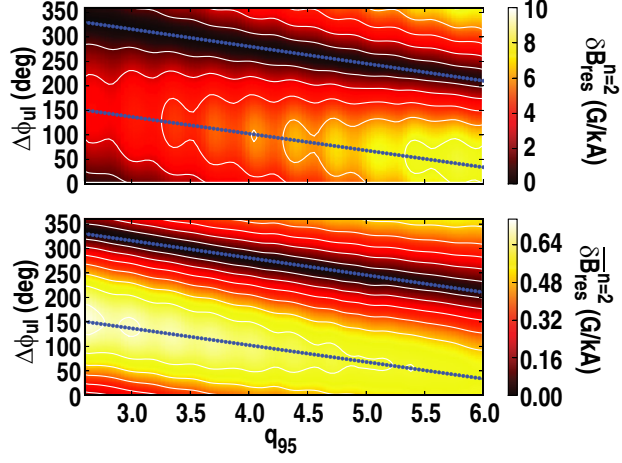


Figure 10. Measures of the pitch-resonant drive ($\delta B_{\text{res}}^{n=2}$ and $\overline{\delta B}_{\text{res}}^{n=2}$) plotted as a function of $\Delta\phi_{ul}$ and q_{95} . The regions of maximum and minimum pitch-resonant drive follow nearly straight lines. Linear best fits to the maxima and minima are overlaid in blue. For any given q_{95} value, it is possible to achieve a large range in $\delta B_{\text{res}}^{n=2}$ and $\overline{\delta B}_{\text{res}}^{n=2}$ by varying $\Delta\phi_{ul}$.

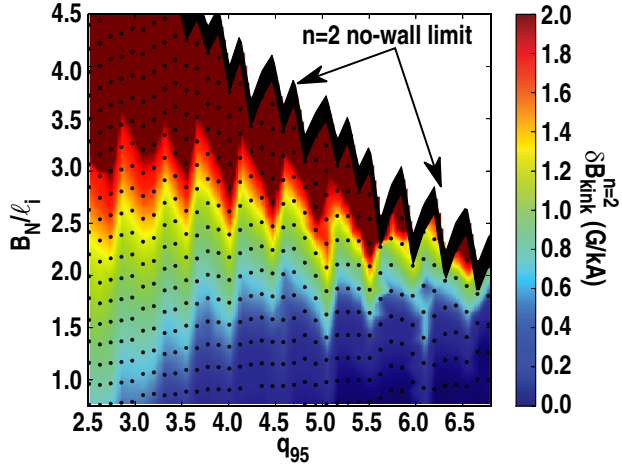


Figure 11. A measure of the kink-resonance, $\delta B_{\text{kink}}^{n=2}$, calculated as a function of β_N/ℓ_i and q_{95} for $\Delta\phi_{ul} = 0^\circ$. There is a strong dependence on β_N/ℓ_i and a smaller periodic dependence on q_{95} due to low- n peeling modes. The thick black line marks the $n = 2$ no-wall limit.

4.2. Maps of kink resonance

The strength of the kink resonance depends strongly on $\Delta\phi_{ul}$ and the plasma pressure (as measured by β_N/ℓ_i) with a weaker dependence on the magnetic topology near the boundary (as measured by q_{95}). Figure 11 shows $\delta B_{\text{kink}}^{n=2}$ calculated as a function of these parameters for $\Delta\phi_{ul} = 0^\circ$. The strong dependence on plasma pressure is expected because as the pressure is increased, the kink mode approaches instability causing a larger RFA. The dependence on q_{95} is more complicated, with periodic maxima occurring twice every half integer increase in q_{95} . This is due to the response from low- n peeling modes, which can also couple to the low-frequency/static, low- n MPs [38]. An important question, which is currently being investigated, is whether this instability

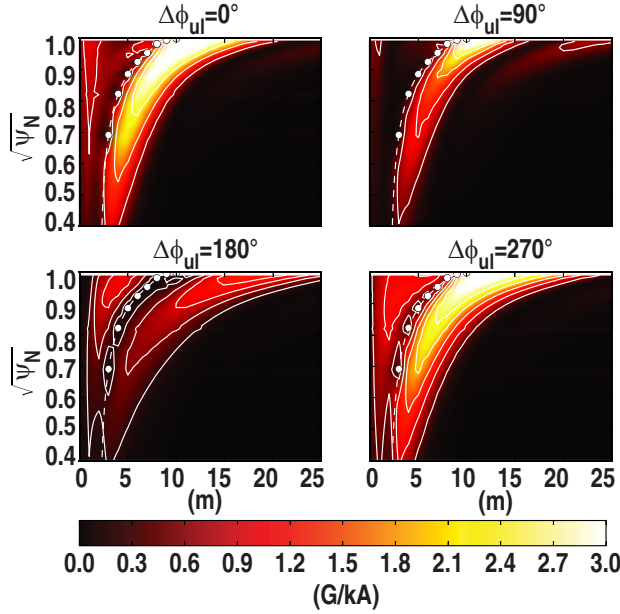


Figure 12. The vacuum field plus the plasma response ($|\delta B_{r,\text{tot}}^{m,n=2}(s)|$) for the same equilibrium and $\Delta\phi_{ul}$ values as figure 9. The amplitude of the harmonics $nq < m < 3nq$ vary considerably depending on $\Delta\phi_{ul}$ with the strongest amplification occurring for 0° and 270° which are the cases where $|\delta B_{r,\text{vac}}^{nq < m < 3nq, n=2}(s)|$ is greatest. These images also show the nulls in the pitch-resonant harmonics (white dots) which are due to the ideal plasma response. These images have been smoothed over the discrete m to make trends easier to see.

is artificially induced by the finite edge q due to the flux truncation required by MARS-F (described in section 4), or if this is a physical result that would still occur if the x-point were included in the calculation.

As with the pitch-resonant component, varying $\Delta\phi_{ul}$ significantly alters the vacuum poloidal spectrum causing large variations in the kink-resonant response. This is demonstrated in figure 12, where the same four $\Delta\phi_{ul}$ values from figure 9 are used, except here $|\delta B_{r,\text{tot}}^{m=nq,n}(s)|$ is shown to illustrate the contribution from the plasma response. Strong amplification occurs for $\Delta\phi_{ul} = 0^\circ$ and 270° , which are also the cases where $|\delta B_{r,\text{vac}}^{nq < m < 3nq, n=2}(s)|$ is greatest.

A harmonic in the edge vacuum magnetic field that satisfies $nq < m < 3nq$ can be used to provide a good first-order estimate of the kink response. This is shown in figure 13 where $|\delta B_{\text{kink}}^{n=2}(s=0.92)|$ (a) and $|\delta B_{\text{vac}}^{m=nq+3,n=2}(s=0.92)|$ (b) are plotted as a function of q_{95} and $\Delta\phi_{ul}$, with $\beta_N/\ell_i = 1.15$. The trends in the two plots are similar, suggesting $|\delta B_{\text{vac}}^{m=nq+3,n=2}(s=0.92)|$ can be used as a first-order estimate of the kink resonance without calculating the plasma response.

The periodic maxima occurring twice every integer due to low- n peeling modes are a prominent feature in the measure of the kink response (figures 13(a) and 17). Here, substantially more artificial equilibria were used to more densely sample q_{95} to capture the periodic maxima (q_{95} is sampled in increments of ≈ 0.02). The maxima occur over a narrow q_{95} range of ≈ 0.1 and could be associated with the narrow q_{95} ELM suppression windows that have been observed [18, 48]. These

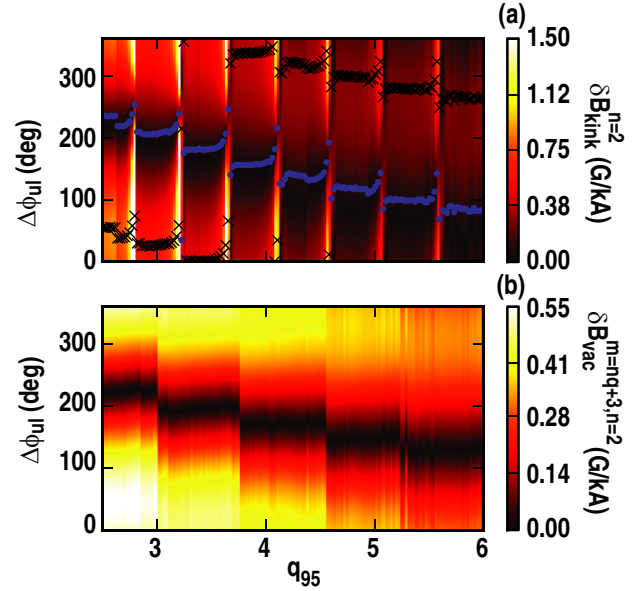


Figure 13. Plots of (a) $|\delta B_{\text{kink}}^{n=2}|$ and (b) $|\delta B_{\text{vac}}^{m=nq+3,n=2}(s=0.92)|$ as a function of $\Delta\phi_{ul}$ and q_{95} , with $\beta_N/\ell_i = 1.15$. The maxima and minima are marked by crosses and dots respectively. The location of the dots also marks the q_{95} values of the equilibria used for the calculations showing a dense sampling of q_{95} to capture the maxima.

periodic maxima are not captured in the vacuum calculation (figure 13(b)) and illustrate the importance of including the plasma response.

As with the pitch-resonant drive, the $\Delta\phi_{ul}$ that gives the maximum kink-resonant response decreases slowly as q_{95} is increased, following an almost linear trend. Varying $\Delta\phi_{ul}$ can change the kink resonance by more than an order of magnitude for the same q_{95} value, illustrating the utility of multi-row perturbation coils and the importance of including the plasma response.

4.3. Example uses of the pitch-resonant drive and kink-resonance maps

In this section, some examples are given that demonstrate how maps, like those shown in figures 10, 11 and 13, can be used to guide machine operations. It is possible to estimate the value of $\Delta\phi_{ul}$, which maximizes the possibility of generating islands, or minimizes the excitation of the stable kink mode, for example. Additionally, these types of maps can be used for real-time control of $\Delta\phi_{ul}$, and suggest that varying $\Delta\phi_{ul}$ provides an effective method of testing the dependence of outcomes, such as ELM suppression, on pitch-resonant and kink-resonant drive. The experimentally observed $n = 2$ ELM suppression windows in [18] correspond to upper-lower I-coil phasings that maximize the kink-resonant response as opposed to the pitch-resonant response. This suggests that if one is looking for ELM suppression windows, the maps should be used to locate regions of strong kink-resonant forcing.

The maps allow $\Delta\phi_{ul}$ to be optimized to achieve certain goals prior to an experiment. For example, if a shot is constrained such that $q_{95} = 3.5$, $\beta_N/\ell_i = 1.15$, and one wants to maximize (minimize) the possibility of generating islands,

then one could look for a maximum (minimum) in the applied pitch-resonant drive. The optimum $\Delta\phi_{ul} \approx 130^\circ(310^\circ)$ can be easily determined using figure 10. Alternatively, for the same shot, if a maximum (minimum) is required in the kink-resonant component, the optimum value of $\Delta\phi_{ul} \approx 10^\circ(190^\circ)$ can be calculated using figure 13. For the kink-resonant calculations, it is important to take β_N/ℓ_i into account, as this will play a critical role in the extent of the RFA; however, q_{95} and $\Delta\phi_{ul}$ determine the efficiency of the coupling of the MP to the kink-mode.

It is possible to achieve a substantial range of pitch-resonant drive and kink resonance for any given q_{95} by varying $\Delta\phi_{ul}$ (figures 10 and 13). This suggests that changing $\Delta\phi_{ul}$ throughout a shot provides an effective way of checking the effect of pitch-resonant drive, and kink resonance on experimental outcomes, such as ELM suppression. In [48], a q_{95} ramp-down was performed, which swept q_{95} across a resonant ridge in the poloidal mode number spectrum of the MP, to check for correlation with regions of ELM suppression. An alternative, is to sweep $\Delta\phi_{ul}$ and keep q_{95} fixed. This sweeps the poloidal mode number spectrum of the MP across the pitch-resonant harmonics (similar to what is shown in figure 12), allowing a larger range of pitch-resonant drive to be accessed. Additionally, this can be tried for any q_{95} value. Experimentally, sweeping the poloidal mode number spectrum of the MP across the pitch-resonant harmonics can be achieved by having a slight frequency difference between the upper MP array and the lower. If the frequency difference was 0.5 Hz, this would allow a rate of change in $\Delta\phi_{ul}$ of 180° s^{-1} . The rate of change in the phasing can be increased or decreased depending on the time available and the extent of the phasing window that one wants to examine. This idea is illustrated in figure 14 where, for $q_{95} = 3.5$ and $\beta_N/\ell_i = 1.15$, the normalized amplitudes of δB_{res} and $\delta B_{kink}^{n=2}$ are plotted as a function of $\Delta\phi_{ul}$, or time, if the perturbation in the lower array is slowly rotated as described above. Figure 14 clearly illustrates how effective $\Delta\phi_{ul}$ is at controlling the pitch-resonant (δB_{res}) and kink-resonant (δB_{kink}) components of the response.

The maps can also be used for real-time control of $\Delta\phi_{ul}$ to achieve a particular goal, such as maximizing the possibility of generating islands by maximizing the pitch-resonant drive throughout a shot. For example, as q_{95} varies throughout a shot, a real-time calculation of q_{95} can be used together with the relevant maps to change $\Delta\phi_{ul}$ to optimally align the ridge in the poloidal mode number spectrum of the MP with the pitch-resonant harmonics.

4.4. Relationship between pitch- and kink-resonant measures, and $n = 2$ ELM suppression

The narrow q_{95} ELM suppression windows (0.02, 0.06 and 0.2) that have been observed [18] are more consistent with the kink-resonant measure than the pitch-resonant measure. The pitch-resonant measure is quite smooth, and for any given q_{95} value, it is possible to achieve roughly the same level of pitch resonance by varying $\Delta\phi_{ul}$ (figure 10). On the other hand, the kink-resonant measure (figure 13) shows significant localized maxima in q_{95} due to a low- n peeling response.

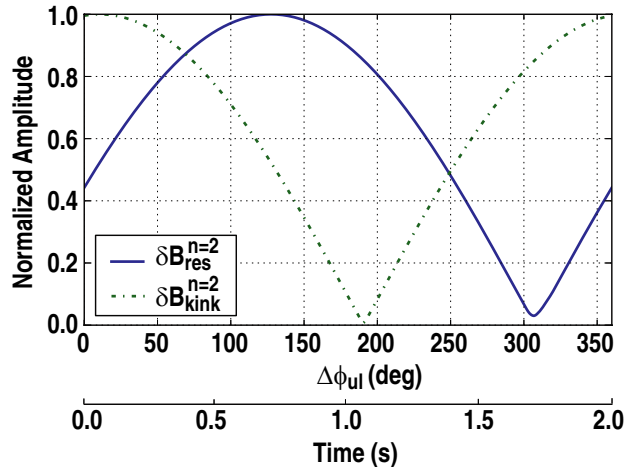


Figure 14. The $n = 2$ kink and pitch-resonant components ($\delta B_{kink}^{n=2}$ and $\delta B_{res}^{n=2}$) normalized to their maximum values plotted as a function of $\Delta\phi_{ul}$, or time, in a simulated experiment where the upper array has a $n = 2$ static MP, and the bottom array has a rotating 0.5 Hz $n = 2$ perturbation. Here, $q_{95} = 3.5$ and $\beta_N/\ell_i = 1.15$.

The width of these maxima is approximately 0.1 which is similar to the experimentally observed $n = 2$ ELM suppression windows. This suggests that the suppression of ELMs may be more closely related to the modified stability of global modes than with the creation of stochastic magnetic fields. However, it is important to point out that while the pitch-resonant measure is a good metric for how well the applied MP aligns with the resonant surfaces, it does not capture where the resonant surfaces are, or how they interact with one another, both of which will show a q_{95} dependence. Including these dependencies is the subject of future work. Additionally, because we are using the ideal MHD approximation, we are only looking at the vacuum field for the pitch-resonant measure. This does not capture the interplay between the stability of the global modes, and the pitch-resonant fields. A full two-fluid plasma response calculations with rotation and resistivity is necessary to more accurately calculate the pitch-resonant fields and confirm these results.

5. The importance of the $n = 4$ component in the dominantly $n = 2$ MP

In this section, we examine the importance of the $n = 4$ harmonic in the dominantly $n = 2$ MP. As was discussed in section 2, the $n \neq 2$ vacuum field harmonics are small, except for the $n = 4$ component. We show that the $n = 4$ pitch-resonant and kink-resonant components are substantially smaller than their $n = 2$ counterparts. Therefore, only considering the $n = 2$ component in the dominantly $n = 2$ MP provides a good approximation in most cases.

The $n = 2$ component of the pitch-resonant drive is substantially larger than the $n = 4$ component in most regions of parameter space. To measure the relative importance of $\overline{\delta B}_{res}^{n=2}$, figure 15 shows the proportion of the total drive caused by the $n = 2$ component ($\overline{\delta B}_{res}^{n=2}/(\overline{\delta B}_{res}^{n=2} + \overline{\delta B}_{res}^{n=4})$). This plot shows that $\overline{\delta B}_{res}^{n=2} \gg \overline{\delta B}_{res}^{n=4}$ in most regions of parameter

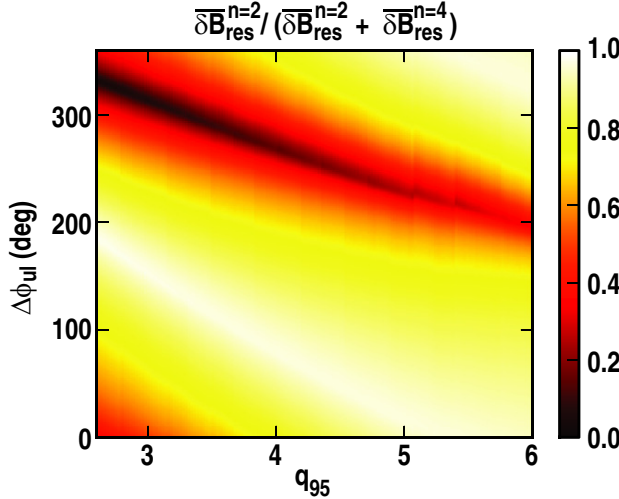


Figure 15. Proportion of the total pitch-resonant component caused by the dominant $n = 2$ harmonic as a function of $\Delta\phi_{ul}$ and q_{95} , showing the regions of parameter space where the $n = 4$ pitch-resonant component becomes significant.

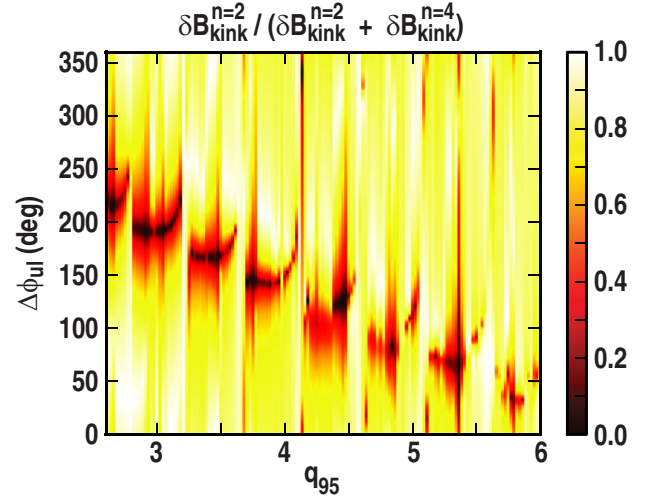


Figure 16. Proportion of the total kink-resonant component caused by the dominant $n = 2$ harmonic as a function of $\Delta\phi_{ul}$ and q_{95} , showing the regions of parameter space where the $n = 4$ kink-resonant component becomes significant.

space demonstrating that for the pitch-resonant response, the $n = 4$ component of the dominantly $n = 2$ MP can usually be ignored. In certain regions of parameter space where $\overline{\delta B}_{res}^{n=2}$ is small, $\overline{\delta B}_{res}^{n=4} > \overline{\delta B}_{res}^{n=2}$ indicating that the $n = 4$ component needs to be considered; however, the total pitch-resonant drive in these regions is still small. Another situation where the $n = 4$ component may be important is if one is considering island overlap between $n = 2$ and $n = 4$ islands. Note that the pitch-resonant drive calculation does not include the plasma response. If the resonant fields are amplified (for example due to an unstable tearing mode) for a particular equilibrium, this is not captured in these calculations.

As with pitch-resonant drive, the $n = 2$ component of the kink-resonant response is significantly larger than the $n = 4$ component. The proportion of the kink-resonant drive caused by the $n = 2$ component is shown in figure 16. This figure clearly illustrate that $\delta B_{kink}^{n=2} \gg \delta B_{kink}^{n=4}$ in most regions of parameter space. Additionally, $\delta B_{kink}^{n=2}$ and $\delta B_{kink}^{n=4}$, plotted as a function of q_{95} for $\Delta\phi_{ul} = 0^\circ$, are shown in figure 17 further demonstrating $\delta B_{kink}^{n=2} \gg \delta B_{kink}^{n=4}$ and highlighting the periodic maxima due to the low- n peeling modes. Therefore, we conclude that in most regions of parameter space, $\delta B_{kink}^{n=4}$ is substantially smaller than $\delta B_{kink}^{n=2}$ in the dominantly $n = 2$ MP.

6. Summary

An extensive examination of the $n = 2$ non-axisymmetric magnetic perturbation, as a function of $\Delta\phi_{ul}$ and plasma parameters on the DIII-D tokamak, using the linear MHD code MARS-F, has been presented. Pitch- and kink-resonant measures have been introduced and used to characterize the magnetic perturbations. These measures, while imperfect, represent an improvement on previous work on $n = 3$ perturbations [31] where a simulated magnetic probe response, and visual identification was used to separate out the responses.

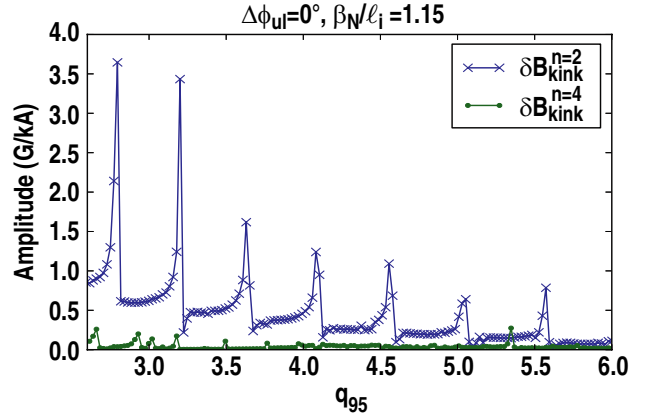


Figure 17. The $n = 2$ and $n = 4$ kink-resonant component ($\delta B_{kink}^{n=2}$ and $\delta B_{kink}^{n=4}$) as a function of q_{95} , with $\beta_N/\ell_i = 1.15$. The periodic maxima are due to the peeling response, and occur over narrow q_{95} ranges, which may be related to the narrow q_{95} ELM suppression regions.

Revisiting the $n = 3$ and other toroidal mode number perturbations on DIII-D, and the impact of the plasma response on $n = 3$ ELM suppression is the subject of future work. The $\Delta\phi_{ul}$ and plasma parameter dependence of pitch-resonant fields and the plasma kink-resonant response, have been mapped out, showing that $\Delta\phi_{ul}$ has a substantial influence on both of these responses. In many cases, $\Delta\phi_{ul}$ can have a larger effect than plasma parameters such as q_{95} and β_N/ℓ_i . This is of particular interest because $\Delta\phi_{ul}$ can be modified at will throughout a shot to achieve a desired effect provided sufficient power supplies are available.

The maxima and minima in the kink-resonant and pitch-resonant responses were found to follow an almost linear path in $(\Delta\phi_{ul}, q_{95})$ space, demonstrating how these two parameters interact to determine how efficiently the MP drives a pitch-resonant or kink-resonant response. Additionally, β_N/ℓ_i mainly determines the extent of the kink-resonant response.

Periodic increases in δB_{kink} are found twice for every integer increase in q_{95} due to low- n peeling modes. These periodic increases occur over small ranges in q_{95} suggesting that they could be related to the narrow, q_{95} ELM suppression windows that have been observed.

The separation of the plasma response into pitch-resonant and kink-resonant components is also useful for toroidal momentum confinement studies as these measures are related to the electromagnetic and NTV torque respectively. It should therefore be possible to use these measures to help determine under what plasma conditions and MP fields the electromagnetic or NTV torque will dominate. During such studies, it is critical to keep in mind the potential to indirectly increase the pitch-resonant harmonics by driving the kink mode, a key physics result observed in error field correction studies [15]. This will be the subject of future work.

The presence of other toroidal harmonics in the applied magnetic field was examined showing a substantial $n = 4$ component is present in the perturbations applied by the DIII-D I-coils. Examination of the plasma response to $n = 4$ perturbations shows that they are substantially smaller than the dominant $n = 2$ responses. This demonstrates that a good approximation to the dominantly $n = 2$ MP on DIII-D can be achieved using MARS-F and an idealized $n = 2$ MP.

The work presented here shows that a linear MHD code such as MARS-F can be used to effectively map out the plasma response dependence on plasma parameters and MP coil parameters such as dominant n and $\Delta\phi_{\text{ul}}$. These maps can then be used to guide real-time control of $\Delta\phi_{\text{ul}}$ to achieve specified outcomes, or alternatively decide on an optimum $\Delta\phi_{\text{ul}}$ in advance. Additionally, this type of approach can be used to optimize the design of MP coil sets.

Acknowledgments

This work was supported in part by the US Department of Energy under DE-FC02-04ER54698, DE-FG02-04ER54541 and DE-AC02-09CH11466. The authors wish to thank Drs A D Turnbull and M J Schaffer for several insightful discussions and the referee's for comments that helped clarify the ideas in this paper. SRH wishes to thank AINSE Ltd for providing financial assistance to enable this work to be conducted.

References

- [1] Evans T E *et al* 2006 *Nature Phys.* **2** 419
- [2] Evans T E *et al* 2008 *Nucl. Fusion* **48** 024002
- [3] Evans T E *et al* 2004 *Phys. Rev. Lett.* **92** 235003
- [4] Jeon Y M *et al* 2012 *Phys. Rev. Lett.* **109** 035004
- [5] Suttrop W *et al* 2011 *Phys. Rev. Lett.* **106** 225004
- [6] Liang Y *et al* 2007 *Phys. Rev. Lett.* **98** 265004
- [7] Kirk A *et al* 2010 *Nucl. Fusion* **50** 034008
- [8] Canik J M *et al* 2010 *Nucl. Fusion* **50** 034012
- [9] Reimerdes H, Chu M S, Garofalo A M, Jackson G L, La Haye R J, Navratil G A, Okabayashi M, Scoville J T and Strait E J 2004 *Phys. Rev. Lett.* **93** 135002
- [10] Shilov M *et al* 2004 *Phys. Plasmas* **11** 2573
- [11] Okabayashi M *et al* 2005 *Nucl. Fusion* **45** 1715
- [12] Cates C, Shilov M, Mauel M, Navratil G, Maurer D, Mukherjee S, Nadle D, Bialek J and Boozer A 2000 *Phys. Plasmas* **7** 3133
- [13] La Haye R J *et al* 2002 *Phys. Plasmas* **9** 2051
- [14] Garofalo A M, La Haye R J and Scoville J T 2002 *Nucl. Fusion* **42** 1335
- [15] Park J-K, Schaffer M J, Menard J E, and Boozer A H 2007 *Phys. Rev. Lett.* **99** 195003
- [16] Suttrop W *et al* 2009 *Fusion Eng. Des.* **84** 290
- [17] Barlow I *et al* 2001 *Fusion Eng. Des.* **58** 189
- [18] Lanctot M J *et al* 2013 *Nucl. Fusion* **53** 083019
- [19] Lanctot M J *et al* 2010 *Phys. Plasmas* **17** 030701
- [20] Turnbull A D 2012 *Nucl. Fusion* **52** 054016
- [21] Nardon E *et al* 2011 *J. Nucl. Mater.* **415** S915–17
- [22] Liu Y, Bondeson A, Fransson C, Lennartson B and Breitholtz C 2000 *Phys. Plasmas* **7** 3681
- [23] Park W, Belova E V, Fu G Y, Tang X Z, Strauss H R and Sugiyama L E 1999 *Phys. Plasmas* **6** 1796
- [24] Strauss H R *et al* 2009 *Nucl. Fusion* **49** 055025
- [25] Ferraro N M and Jardin S 2009 *J. Comput. Phys.* **228** 7742
- [26] Glasser A H, Sovinec C R, Nebel R A, Gianakon T A, Plimpton S J, Chu M S, Schnack D D and the NIMROD Team 1999 *Plasma Phys. Control. Fusion* **41** A747
- [27] Izzo V A *et al* 2008 *Nucl. Fusion* **48** 115004
- [28] Bécoulet M *et al* 2012 *Nucl. Fusion* **52** 054003
- [29] Huysmans G and Czarny O 2007 *Nucl. Fusion* **47** 659
- [30] Orain F *et al* 2013 *Phys. Plasmas* **20** 2510
- [31] Lanctot M J *et al* 2011 *Phys. Plasmas* **18** 056121
- [32] Liu Y, Kirk A, and Nardon E 2010 *Phys. Plasmas* **17** 122502
- [33] Schaffer M J, Menard J, Aldan M, Bialek J, Evans T E and Moyer R A 2008 *Nucl. Fusion* **48** 024004
- [34] Reimerdes H *et al* 2009 *Nucl. Fusion* **49** 115001
- [35] Snyder P B *et al* 2012 *Phys. Plasmas* **19** 056115
- [36] Liu Y *et al* 2012 *Plasma Phys. Control. Fusion* **54** 124013
- [37] Garofalo A M, Jensen T H and Strait E J 2003 *Phys. Plasmas* **10** 4776
- [38] Liu Y *et al* 2010 *Plasma Phys. Control. Fusion* **52** 045011
- [39] Kirk A *et al* 2013 *Nucl. Fusion* **53** 043007
- [40] Holcomb C *et al* 2006 *Rev. Sci. Instrum.* **77** 10E506
- [41] Carlstrom T N *et al* 1992 *Rev. Sci. Instrum.* **63** 4901
- [42] Burrell K H, Kaplan D, Gohil P, Nilson D, Groebner R J and Thomas D M 2001 *Rev. Sci. Instrum.* **72** 1028
- [43] St John H E, Ferron J R, Lao L L, Osborne T H, Thompson S J and Wroblewski D 1994 *Proc. 15th Int. Conf. on Plasma Physics and Controlled Nuclear Fusion Research (Seville, Spain, 1994)* vol 3, p 603
- [44] Lao L L, St John H E, Peng Q, Ferron J R, Strait E J, Taylor T S, Meyer W H, Zhang C and You K 2005 *Fusion Sci. Technol.* **48** 968
- [45] Crottinger J, LoDestro L, Pearlstein L, Tarditi A, Casper T and Hooper E 1997 ‘Corsica: a comprehensive simulation of toroidal magnetic-fusion devices, Final Report to the LDRB Program Technical Report Lawrence Livermore National Laboratory, Livermore, CA
- [46] Glasser A and Chance M S 1997 *Bull. Am. Phys. Soc.* **42** 1848
- [47] Lutjens H, Bondeson A and Sauter O 1996 *Comput. Phys. Commun.* **97** 219
- [48] Schmitz O *et al* 2009 *Phys. Rev. Lett.* **103** 165005

Effects of resistivity and rotation on the linear plasma response to non-axisymmetric magnetic perturbations on DIII-D

The work in this chapter is an extension of the research shown in chapter 7. Here, the ideal MHD assumption is relaxed and the effects of plasma resistivity and rotation on the plasma response to the 3D magnetic fields are examined. The regions of parameter space where the plasma response transitions from ideal to resistive/rotation dependent are clearly demonstrated. These results are particularly important for guiding experiments and providing interpretation of observations in ELM suppression experiments. Additionally, comparisons with experimental data are presented which show good agreement, although an event that leads to a significant drop in the magnetic probe output is not reproduced, motivating further investigation with two-fluid and non-linear models. Supplementary information which may be useful for future research is included in appendix J. 90% of the research and 85% of the writing presented in this paper are my own work. The paper is also available from <http://dx.doi.org/10.1088/0741-3335/57/2/025015>.

Effects of resistivity and rotation on the linear plasma response to non-axisymmetric magnetic perturbations on DIII-D

S R Haskey¹, M J Lanctot², Y Q Liu³, C Paz-Soldan², J D King⁴,
B D Blackwell¹ and O Schmitz⁵

¹ Plasma Research Laboratory, Research School of Physics and Engineering, The Australian National University, Canberra, ACT 0200, Australia

² General Atomics, PO Box 85806, San Diego, CA 92186-5608, USA

³ Culham Centre for Fusion Energy (CCFE), Culham Science Centre, Abingdon, OX14 3DB, UK

⁴ Oak Ridge Institute for Science and Education, Oak Ridge, TN 378300-8050, USA

⁵ Department of Engineering Physics, University of Wisconsin-Madison, Madison, WI 53706, USA

E-mail: shaun.haskey@anu.edu.au

Received 19 August 2014, revised 5 November 2014

Accepted for publication 3 December 2014

Published 5 January 2015



Abstract

Parameter scans show the strong dependence of the plasma response on the poloidal structure of the applied field highlighting the importance of being able to control this parameter using non-axisymmetric coil sets. An extensive examination of the linear single fluid plasma response to $n = 3$ magnetic perturbations in L-mode DIII-D lower single null plasmas is presented. The effects of plasma resistivity, toroidal rotation and applied field structure are calculated using the linear single fluid MHD code, MARS-F (Liu *et al* 2000 *Phys. Plasmas* **7** 3681). Measures which separate the response into a pitch-resonant and resonant field amplification (RFA) component are used to demonstrate the extent to which resonant screening and RFA occurs. The ability to control the ratio of pitch-resonant fields to RFA by varying the phasing between upper and lower resonant magnetic perturbations coils sets is shown. The predicted magnetic probe outputs and displacement at the x-point are also calculated for comparison with experiments. Additionally, modelling of the linear plasma response using experimental toroidal rotation profiles and Spitzer like resistivity profiles are compared with results which provide experimental evidence of a direct link between the decay of the resonant screening response and the formation of a 3D boundary (Schmitz *et al* 2014 *Nucl. Fusion* **54** 012001). Good agreement is found during the initial application of the MP, however, later in the shot a sudden drop in the poloidal magnetic probe output occurs which is not captured in the linear single fluid modelling.

Keywords: non-axisymmetric coil, plasma response, magnetic perturbation, toroidal rotation, plasma resistivity

(Some figures may appear in colour only in the online journal)

1. Introduction

The subject of type-I edge localised mode (ELM) suppression is of considerable importance for future experiments such as ITER as well as future nuclear fusion power plants because the anticipated heat loads will severely limit the lifetime of plasma

facing components. Non-axisymmetric magnetic perturbation (MP) coils have been used to suppress [1–6], mitigate [7–9], pace [10], and destabilise [11] ELMs. The underlying mechanism for this behaviour is an active area of research with one current working hypothesis suggesting that the MP forms a stochastic layer which enhances radial transport, limiting the

expansion of the pedestal width and height, and consequently stabilising the ballooning part of the peeling-balloonning type-I ELM [12].

MPs have also been used to control resistive wall modes [13, 14] and neoclassical tearing modes [15], perform magnetic spectroscopy [16, 17], and correct error fields [18, 19]. Consequently thorough studies of the plasma response dependence on MP coil toroidal and poloidal geometry and plasma parameters are important.

The plasma response to the MP has the ability to significantly modify the total fields (vacuum plus plasma), highlighting the importance of taking the plasma response into consideration in MP calculations [19–22]. Here, the perturbations are referred to as non-axisymmetric MPs as opposed to the more common resonant magnetic perturbations (RMPs) because the spectra of the applied fields contain both resonant and non-resonant components with respect to the q -profile of the equilibrium magnetic field.

In previous work [22] the MPs and the ideal linear plasma response to them were characterised as being either pitch-resonant or kink-resonant depending on whether the field coupled more strongly to pitch-resonant harmonics, or a kink-type mode respectively. This characterisation allowed significant scans to be performed to determine the effects of q -profile, pressure and applied field structure on the plasma response.

The work presented here is a significant extension of the parameter scans in [22]. As before, the MARS-F code [23] is used to calculate the linear plasma response to the external MP fields. However, here, the effects of plasma resistivity, toroidal rotation, and applied field structure are examined using extensive parameter scans in L-mode lower single null DIII-D discharges. The simulations have been used to calculate external probe measurements to correlate with changes in the pitch-resonant or resonant field amplification (RFA) plasma responses.

The linear approach used here is less computationally intensive than nonlinear codes and good qualitative agreement has been found between MARS-F predictions and measurements from the magnetic pickup coils up to 80% of the predicted ideal MHD pressure limit calculated without a conducting wall near the plasma edge on DIII-D plasmas [20, 21]. For larger pressures, the MARS-F code overestimates the plasma response, indicating that in these regimes it is necessary to include additional physics. The linear response model does not include the effect the MP has on the plasma flow. For the comparison with experiment in this paper, this effect is considered by artificially scaling the rotation to match the measured value at each discrete time interval. Models which include the nonlinear MP penetration dynamics are discussed in [24–29].

Examples of nonlinear and two fluid effects include experiments on the penetration of MPs on TEXTOR, which showed a dependence on the relative frequency between MPs and the electron fluid [30], as opposed to just the plasma rotation frequency. These results were confirmed using nonlinear two-fluid calculations [31, 32]. Further calculations showed that depending on the frequency, direction, and amplitude, a MP can lead to either increases or decreases in the density gradient

at the relevant rational surface [33]. For a thorough examination of the differences between the various models and comparisons on a DIII-D equilibrium, the reader is referred to [34, 35].

Experimental evidence of the formation of a 3D boundary following the decay of the plasma screening response to a $n = 3$ MP was recently reported for a lower single null (LSN) L-mode DIII-D discharge [36]. In this paper, MARS-F has been used to simulate the plasma response in 40 ms increments throughout this shot using the experimental main ion toroidal rotation profiles and Spitzer like resistivity profiles. The simulations agree with the experimental values for the outboard midplane poloidal probe [37] output to within 20% in the initial phase of the MP. However, the simulations do not reproduce a sudden drop in the probe output which was observed in this shot. This drop may be further explained using two-fluid, nonlinear, or kinetic physics, which are not included in the MARS-F model. The drop is accompanied by a significant rise in the $n = 1$ component of the plasma response which may be related to static island formation due to $n = 1$ error field penetration. This may be a case where the applied $n = 2$ field creates the conditions that allow another toroidal mode number such as the residual $n = 1$ error field to penetrate. The generation of toroidal harmonics other than the applied $n = 3$ indicates that a nonlinear process may be occurring.

This paper is organised as follows: section 2 describes the MARS-F model, then in section 3, the MP coils, MARS-F calculations and various measures used to quantify the plasma response are introduced. Section 4 compares the experimental observations in [36] with MARS-F simulations. Lastly, section 5 presents extensive scans of plasma response dependence on plasma resistivity, toroidal rotation and applied field structure.

2. MARS-F formulation

The MARS-F formulation is described in detail in [23, 49]. For convenience a brief overview is given here. As has already been stated, MARS-F uses the single-fluid, resistive MHD framework with a given toroidal rotation, $V_0 = R\Omega\hat{\phi}$. The plasma response to the MP is treated as a forced oscillation problem with the plasma model described as follows:

$$i(\Omega_{MP} + n\Omega)\xi = \mathbf{v} + (\xi \cdot \nabla \Omega)R\hat{\phi}, \quad (1)$$

$$\begin{aligned} i\rho(\Omega_{MP} + n\Omega)\mathbf{v} &= -\nabla p + \mathbf{j} \times \mathbf{B} + \mathbf{J} \times \mathbf{b} \\ &\quad - \rho[2\Omega\hat{\mathbf{Z}} \times \mathbf{v} + (\mathbf{v} \cdot \nabla \Omega)R\hat{\phi}] \\ &\quad - \rho\kappa_{||}|k_{||}v_{th,i}|[\mathbf{v} + (\xi \cdot \nabla) V_0]_{||}, \end{aligned} \quad (2)$$

$$i(\Omega_{MP} + n\Omega)\mathbf{b} = \nabla \times (\mathbf{v} \times \mathbf{B}) + (\mathbf{b} \cdot \nabla \Omega)R\hat{\phi} - \nabla \times (\eta\mathbf{j}), \quad (3)$$

$$i(\Omega_{MP} + n\Omega)p = -\mathbf{v} \cdot \nabla P - \Gamma P \nabla \cdot \mathbf{v}, \quad (4)$$

$$\mathbf{j} = \nabla \times \mathbf{b}, \quad (5)$$

with the following definitions, R : plasma major radius, ϕ : geometric toroidal angle, $\hat{\phi}$: unit vector along ϕ , $\hat{\mathbf{Z}}$: unit vector

in the vertical direction, Ω_{MP} : excitation frequency of the MP field, n : toroidal harmonic number, and η : plasma resistivity. The perturbed displacement, velocity, magnetic field, current, and pressure are represented by ξ , v , b , j , and p respectively, and the equilibrium plasma density, magnetic field, current, and pressure are represented by ρ , B , J , and P respectively. The last term in equation (2) describes parallel sound wave damping, with the coefficient κ determining the damping strength. In this work, we set $\kappa = 1$, which represents reasonably strong sound damping. k_{\parallel} is the parallel wave number, $v_{th,i}$ is the thermal ion velocity, and the parallel component of the perturbed velocity is taken along the equilibrium field line.

The magnetic field due to the MP current is given as follows:

$$\nabla \times b = j_{MP} , \quad \nabla \cdot j_{MP} = 0, \quad (6)$$

with j_{MP} representing the (surface) current density of the MP coils, varying as $\exp(i n \phi)$ along the toroidal angle ϕ . The vacuum vessel is also included and is modelled as a thin shell. At the plasma-vacuum interface, there is a continuity of the normal component of b and the (total) perturbed pressure balance condition. The boundary conditions are set by a perfectly conducting wall beyond the vacuum vessel.

3. Components of the plasma response

This section describes some simple scalar metrics for the components of the plasma response allowing a simplified representation of the full 3D data. Spatial Fourier decomposition of the magnetic field component normal to the flux surfaces in a toroidal coordinate system produces a spectrum of toroidal (n) and poloidal harmonics (m). Phase differences in the currents in the upper and lower MP coil arrays at the same toroidal location significantly alter the poloidal harmonics of the applied spectra, and consequently the plasma response to it. $\Delta\phi_{ul}$ is used to identify this phase difference and is defined through the following relations: $I_{upper} \propto \cos(n\phi_{coil})$ and $I_{lower} \propto \cos(n\phi_{coil} + \Delta\phi_{ul})$ where I_{upper} and I_{lower} are the currents in the MP coils above and below the midplane respectively and ϕ_{coil} is the DIII-D tokamak toroidal angle location of the center of a MP coil (ϕ is in the same direction as the plasma current). On DIII-D there are arrays of 6 MP coils above and below the midplane inside the vacuum vessel. These coils are known as the Internal coils (I-coils) and their location in a poloidal cross-section is shown in figure 1. For $n = 3$ fields, the limited number of coils in the toroidal direction means only $\Delta\phi_{ul} = 0^\circ$ (even) and 180° (odd) phase differences between the upper and lower arrays is possible. The even configuration is up-down symmetric while the odd configuration is up-down anti-symmetric.

This paper focuses on the effects of plasma resistivity, toroidal rotation and $\Delta\phi_{ul}$ on the various types of plasma responses such as resonant-screening, RFA and the formation of a 3D boundary. To allow a compact representation of this complex information several metrics are used, which while imperfect, are particularly useful for highlighting general trends and regions of parameter space that are interesting. The remainder of this section discusses these components

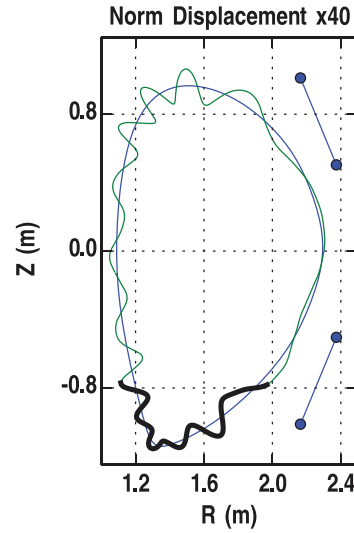


Figure 1. The real part of the normal plasma displacement on the LCFS multiplied by 40 to make it clearer. The region around the x-point where the displacement amplitude is integrated to provide the 3D boundary measure ($\int |\xi^r| dl / \int dl$) is marked with a thicker black line. Also shown are the locations of the upper and lower DIII-D MP coils (I-coils).

of the plasma response as well as the measures used to quantify them.

3.1. Pitch-resonant fields

Harmonics of the total magnetic field normal to the flux surfaces which are pitch-resonant with the equilibrium field ($m = nq$) are particularly interesting due to their role in the creation of magnetic islands. If magnetic islands overlap, a region with a stochastic magnetic field is formed, which enhances radial transport. One current working hypothesis for type-I ELM suppression using MPs is that this limits the expansion of the pedestal width and height, stabilising the ballooning part of the peeling-balloon mode [12].

The plasma response is extremely important when considering the effects of pitch-resonant components of the magnetic fields because plasma currents are generated which reduce the strength of the pitch-resonant field. This effect is illustrated in figure 2. The extent to which this screening occurs depends on the plasma toroidal rotation and resistivity. In the limit of ideal MHD, the pitch resonant fields are shielded completely. Therefore, attempts to model the pitch-resonant fields should include the plasma response as well as the resistivity and toroidal rotation of the plasma.

To leading order, the radial component of the magnetic field (normal to the flux surfaces) is responsible for magnetic island formation. This field can be Fourier decomposed into toroidal (n) and poloidal (m) harmonics in straight field line co-ordinates (see appendix A of [38]) to obtain $\delta B_r^{m,n}(s)$ where $s = \sqrt{\psi_N}$ is a flux surface label and ψ_N is the normalized poloidal flux. Whether the magnetic field is the vacuum field (MP coils only), field due to the plasma, or combined (plasma + vacuum) is signified with a plas, vac or tot superscript or subscript (i.e. $B_r^{m,n}_{plas,vac,tot}(s)$).

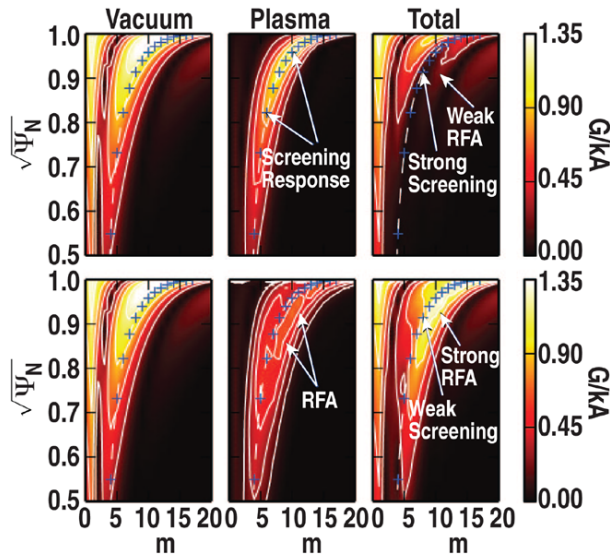


Figure 2. Amplitudes of the vacuum, plasma and total $n = 3$ poloidal harmonics of the magnetic field normal to the flux surfaces as calculated by MARS-F for a high (top row) and low (bottom row) toroidal rotation. The pitch-resonant screening and RFA components in the plasma and total fields are marked. The pitch-resonant $m = nq$ line is overlayed and the location of low order rational surfaces is marked with blue + symbols.

As in [22] the strength of the pitch-resonant field is quantified using all pitch-resonant harmonics:

$$\delta B_{\text{res}} = \langle |\delta B_r^{m=nq,n}(s)| \rangle, \quad (7)$$

where $\langle \cdot \rangle$ means the average. Because plasma resistivity and toroidal rotation are included in the work presented here, the vacuum component ($\delta B_{\text{res}}^{\text{vac}}$), plasma component ($\delta B_{\text{res}}^{\text{plas}}$), and total pitch-resonant field ($\delta B_{\text{res}}^{\text{tot}}$) can be calculated using the appropriate magnetic field component. Previously, only $\delta B_{\text{res}}^{\text{vac}}$ was calculated because in the ideal MHD limit, the vacuum and plasma components are equivalent in magnitude but opposite in sign so the total pitch-resonant field is zero.

The ability to calculate the pitch-resonant field including the screening response from the plasma ($\delta B_{\text{res}}^{\text{tot}}$) is a significant extension of previous work [22], providing a more accurate measure of the opportunity for magnetic island and stochastic region formation. Accurate estimates of the island size and/or stochasticity are needed for understanding the associated electromagnetic torque, which acts as a sink in the toroidal momentum balance equation for the single fluid case [39]. The situation is substantially more complicated in nonlinear two-fluid theory where, for example, the poloidal plasma frequency can increase or decrease depending on the frequency and direction of the original rotation [32].

3.2. Coupling to global modes

The applied MP can also couple to global modes such as the external kink mode resulting in substantial amplification of poloidal harmonics in the range $nq < m < 3nq$. This effect is often referred to as RFA [40] and is clearly shown in figure 2. The strength of the RFA response is important because it has

been correlated with $n = 2$ ELM suppression windows [6], can amplify pitch resonant harmonics, and if driven to large enough amplitude can lead to a disruption.

The extent of the coupling to global modes such as the external kink-mode is quantified using a similar approach as in [22] where the strongest harmonic in the plasma response that is in the range $nq + 4 < m < 3nq$ at a particular flux surface near the edge of the plasma is used:

$$\delta B_{\text{RFA}}^n = |\delta B_{r,\text{plas}}^{m^*,n}(s = 0.92)|, \quad (8)$$

where m^* is the harmonic that gives the maximum plasma response for any $\Delta\phi_{\text{ul}}$:

$$m^* = \arg \max_{nq+4 < m < 3nq} |\delta B_{r,\text{plas}}^{m,n}(s = 0.92, \Delta\phi_{\text{ul}})|. \quad (9)$$

The lower bound for m is offset from nq by four to minimise contamination of this measure by the pitch-resonant screening response. This offset works well for the $n = 3$ cases shown in this paper; however, when applied to different cases and different n , its value should be selected by careful examination of the plasma response spectrums.

3.3. Formation of a 3D boundary: displacement near the x-point

The density pump out which is commonly observed preceding ELM suppression has been strongly correlated with the formation of a 3D boundary. Striation of the divertor footprint has been observed in several experiments [41–43] and has been linked with the decay of the screening plasma response [36] which presumably leads to the formation of stochastic regions within the plasma.

To quantify the distortion to the boundary, the average magnitude of the plasma displacement normal to the last closed flux surface (LCFS) around the x-point is calculated: $\int |\xi^n| dl / \int dl$, where the integrals are along the LCFS near the x-point (shown in figure 1). The average displacement provides a proxy for the extent to which a 3D boundary is formed so that its dependence on plasma resistivity, rotation and applied field structure can be shown.

Because MARS-F is a finite element (in s)—Fourier (in θ) code, it cannot treat the exact geometry at the x-point. Consequently, the poloidal flux is truncated to 99.5% of its original value and the equilibrium is re-solved using the Grad–Shafranov solver in the CORSICA code [44]. The CHEASE code [45] then re-solves the Grad–Shafranov equation and based on that solution, creates the flux based grid for MARS-F.

4. Comparison with experimental results

In this section MARS-F simulations that include the resistivity and toroidal rotation are compared with experimental results that were originally presented in [36] for DIII-D shot #142614. This shot is a L-mode LSN discharge with the following parameters: $I_P = 1.4$ MA, $B_T = -2.0$ T, $P_H = 2.51$ MW, mean-averaged triangularity $\bar{\delta} = 0.52$, $\beta_N = 0.5$ and central electron density $n_{\text{ec}} = 4.0 \times 10^{19}$ m⁻³. Reconstructions of the

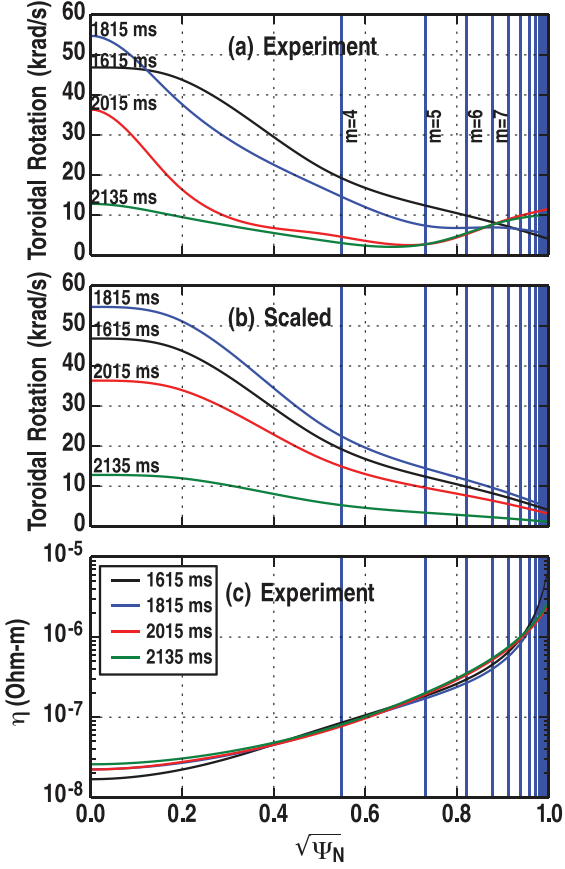


Figure 3. (a) Main ion toroidal rotation profiles at certain times during shot 142614. (b) Scaled profiles using the original rotation profile at 1615 ms before the MP is applied. The location of the $n = 3$ rational surfaces is marked with vertical lines. (c) Resistivity profiles assuming a Spitzer resistivity.

axisymmetric magnetic field were performed using the EFIT code [46] constrained by the magnetics and multiple motional Stark effect (MSE) polarimeters [47].

The effect of the reduction in toroidal rotation on the linear plasma response for this shot is calculated using MARS-F. Time varying EFIT equilibrium are used along with the time varying (in 40 ms intervals) main ion toroidal rotation profiles. The density and q profiles for the equilibrium at $t = 1615$ ms are shown in figure 6. Spitzer resistivity is assumed and the time varying electron temperature profiles are included in the analysis.

A separate MARS-F run is performed for each individual rotation and resistivity profile throughout the shot. The main ion rotation profiles at selected times are shown in figure 3(a). These profiles were calculated by NCLASS [48] using measurements of the carbon impurity profile from charge exchange recombination spectroscopy (CER). A significant drop in central toroidal rotation is observed following the application of the MP; meanwhile, the edge rotation is increasing (also shown in figure 4(b)). To isolate the effects of the changes in the edge rotation profile, the MARS-F analysis was also performed using the rotation profile from 1615 ms (before the MP was applied) scaled by the central rotation speed at

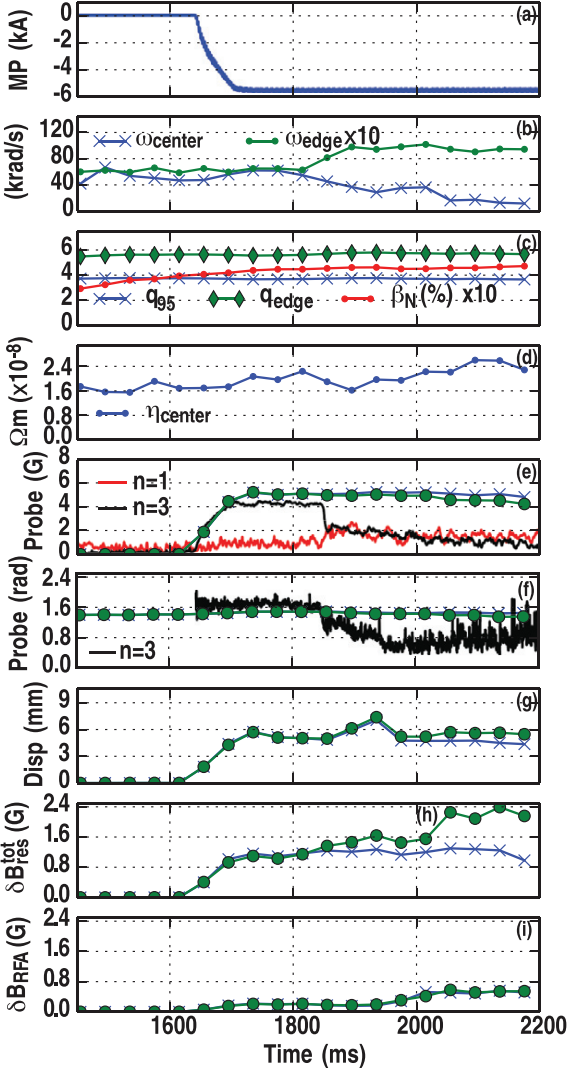


Figure 4. Details of shot #142614: (a) I-coil current, (b) central and edge main ion toroidal rotation, (c) plasma parameters, and (d) normalised central resistivity. (e)–(i) Results of the MARS-F modelling using the time varying rotation profiles (crosses), and the scaled profiles (circles) for the $n = 3$ perturbation. (e) The amplitude of the $n = 1$ and 3 components of the experimental poloidal probe output are also shown in red and black respectively, (f) phase of the $n = 3$ component of the experimental probe output is shown in black, (g)–(i) values of the x-point displacement, residual pitch resonant field, and RFA metrics introduced in section 3.

different times (figure 3(b)). These two cases are referred to as the experimentally-derived and scaled profiles in the rest of this paper. The resistivity profiles and location of the rational surfaces are also shown in figure 3.

The following key observations were made in [36] regarding the probe array output and toroidal rotation: following the application of the MP, the bulk rotation starts to decrease and the plasma response as measured by an outboard midplane poloidal probe array increases until the MP current reaches its flat top value. Two-hundred milliseconds later, the poloidal probe array output decreases abruptly, and then continues to decrease slowly as the bulk rotation continues to decrease.

The $n = 3$ and $n = 1$ components of the probe array output are shown in figure 4(e) along with the simulated $n = 3$ probe output from the MARS-F simulations using the experimentally-derived rotation profiles and scaled profiles. The MARS-F simulations using the experimentally-derived rotation profiles and scaled profiles accurately predict the poloidal probe array output to within $\approx 20\%$ as the MP increases to its flat top value at 1700 ms. However, the abrupt decrease at 1830 ms is not replicated using either of the rotation profiles. From 1850 ms onwards, the response using the scaled profiles decreases, following the experimental trend, while the response using the experimentally-derived profiles stays relatively constant. This indicates that for the single fluid linear model, ‘uniform’ reductions in main ion toroidal rotation in this type of equilibrium lead to decreases in the probe output; however, changes in the rotation profile are also important and can offset the reduction in bulk rotation.

The inability to reproduce the sudden drop in probe output at 1830 ms indicates nonlinear, two-fluid, or kinetic physics, which are not included in the MARS-F model may be responsible, motivating further investigation. As the $n = 3$ component of the probe output abruptly decreases, the $n = 1$ component increases until it is of comparable size, or even larger than the $n = 3$ component indicating that nonlinear processes are likely to be occurring. The increase in the $n = 1$ component may be related to the formation of a static island due to residual $n = 1$ error field penetration which results from the reduced toroidal rotation.

Additionally, [36] presented camera images of CII emission near the separatrix showing the development of a 3D boundary following the decay of the magnetic probe output. The metric for the displacement near the x-point (shown in figure 4(g)) increases slightly towards the end of the shot; however, there is no clear increasing trend. The spike in the displacement around 1950 ms is due to the q profile at the plasma edge approaching the integer 6 (note: the flux is truncated to remove the x-point for MARS-F as described in section 3.3). This poor qualitative comparison between the camera images in [36] and the x-point displacement metric may be further explained using two-fluid, nonlinear, or kinetic physics.

As the central toroidal rotation decreases, the total pitch-resonant field metric (which includes the plasma screening response) increases for the scaled profiles, but stays relatively constant for the experimentally-derived rotation profiles (figure 4(h)) highlighting the importance that changes in the edge rotation have on the plasma screening response within the single fluid linear model. For both the scaled and experimentally-derived profile rotation cases, the RFA metric increases as the central rotation decreases; however, the amplitude is still very small compared with the amplitude of other harmonics (0.5 G compared to ~ 8 G for some harmonics in the vacuum field). The hypothesis in [36]: that the reduced rotation causes a reduction in the plasma screening which allows the MP to penetrate further into the plasma leading to the formation of a 3D boundary appears to be only partly shown in the modelling for this shot. However, in section 5, controlled parameter scans are conducted which show that large changes in toroidal rotation lead to changes that agree with the hypothesis.

Because the plasma screening response cancels the applied field and the RFA amplifies the applied field, these two responses are expected to be 180° out of phase with one another. Figure 4(f) shows the measured and simulated phase of the $n = 3$ component of the probe signal. There is good agreement before 1830 ms when the $n = 3$ component of the probe array halves in value over a short period of approximately 12 ms. The change in the phase of the probe signal which accompanies the drop in the probe signal is not seen in the simulations. This change in phase could indicate a change in the RFA and plasma screening components of the experiment plasma response as measured at the probe.

To shed some light on the difference between the results of the MARS-F simulations using the experimentally-derived rotation profiles and the scaled profiles, the island width (in units of normalised poloidal flux) and Chirikov overlap parameter (sum of island half widths divided by island separation) for the resonant harmonics are plotted for both cases in figure 5 at different times throughout this shot. The effects of plasma screening are clear in this figure, with the island width decreasing substantially when the plasma response is included. Consequently the region where the Chirikov overlap parameter is greater than 1 moves significantly further outward. The scaled profiles case shows the decrease in plasma screening as the central rotation decreases while the experimentally-derived profiles case shows minimal change. The modifications to the rotation profile, in particular the increase in the edge rotation clearly have a significant effect on the plasma screening because a large portion of the resonant harmonics are near the plasma boundary (figure 3). This demonstrates that the plasma response is very sensitive to changes in the edge rotation, and this should be carefully considered when calculating the plasma response to the MP.

5. Plasma response dependence on resistivity, rotation and applied field structure

5.1. Overview of the parameter scans

In this section, MARS-F is used to perform rotation, resistivity, and applied field structure scans to further understand their effects on the linear plasma response. The equilibrium that is used is from $t = 1615$ ms in the same LSN L-mode shot that was used in section 4. Details of this shot are given in the first paragraph of section 4. The effects of resistivity and rotation on the linear plasma response in H-mode MAST plasmas has been described in [49, 50], and a comparisons with those results is made throughout this section showing the significant effect resistivity, rotation and applied field structure have on the plasma response.

The normalised density, resistivity, toroidal rotation and q -profiles for this base equilibrium are shown in figure 6. A Spitzer like resistivity is assumed where the resistivity scales as a function of electron temperature, $T_e^{-3/2}$. For the parameter scans presented here, the entire resistivity profile is scaled, and this scaling is represented by the value of the MARS-F normalised resistivity at the plasma center $\eta_0 = 1/S_0$ where S_0 is the Lundquist number at the plasma center. The main ion

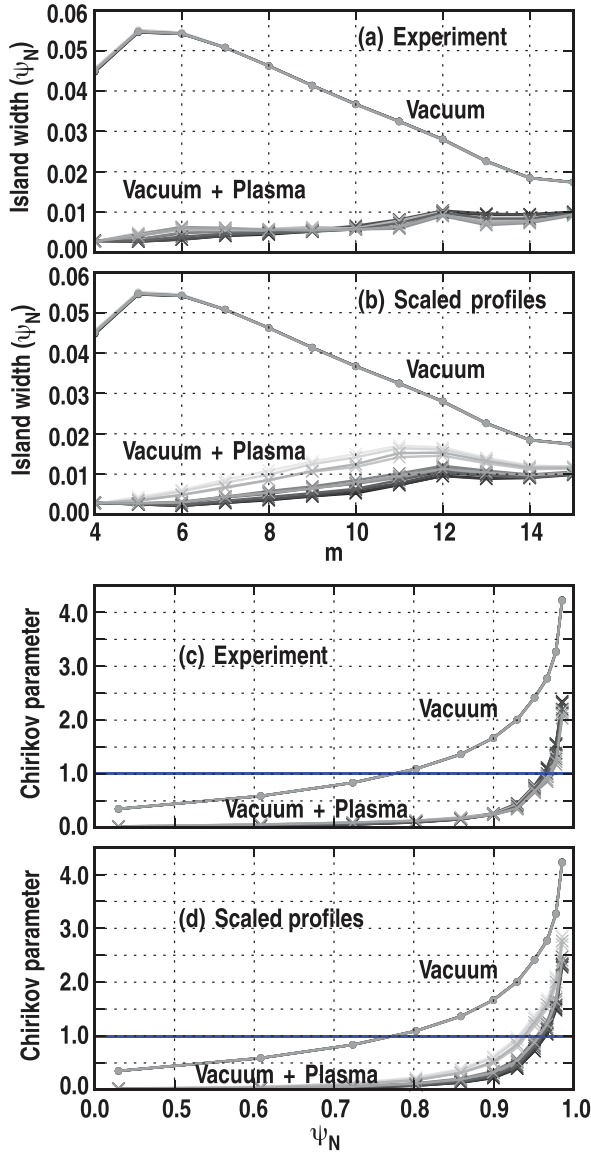


Figure 5. Calculated $n = 3$ island width (a, b) in units of normalised poloidal flux and Chirikov overlap parameter (c, d) for the vacuum pitch-resonant harmonics (dots), and total pitch-resonant harmonics which includes the plasma screening (crosses), for an I-coil current of 5.5 kA. The total pitch-resonant harmonics are plotted for times between 1735 ms and 2175 ms in 40 ms increments. The darkness of the shade of gray decreases as time increases. The analysis was performed using the main ion toroidal rotation profile (a, c) and the scaled profiles (b, d) as shown in figure 3.

toroidal rotation profiles are also scaled, and this scaling is represented by the value of the toroidal rotation at the plasma center normalised to the Alfvén time, ($\omega_0 = \omega_i \tau_A$).

A total of 400 separate MARS-F simulations were performed with scaled rotation and resistivity profiles on a logarithmic grid in (η_0, ω_0) space. The normalised toroidal rotation at the plasma center, ω_0 , varied between 10^{-3} and 10^{-1} , and the normalised resistivity at the plasma center η_0 , varied between 5×10^{-9} and 5×10^{-7} . For each of these simulations, the pitch-resonant metric, RFA metric, x-point displacement metric, and poloidal outboard midplane magnetic probe responses, which

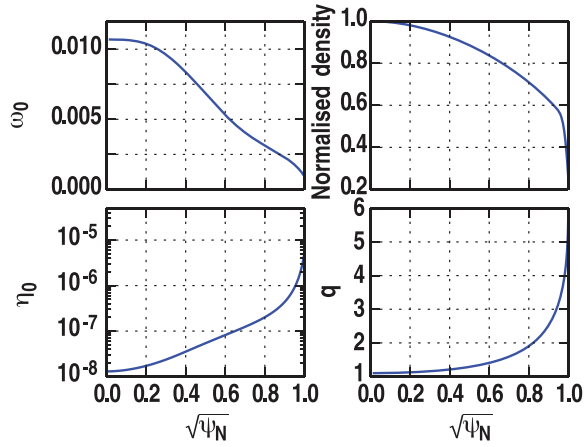


Figure 6. Profiles for the base equilibrium (DIII-D shot #142614 1615 ms). The normalised toroidal rotation and normalised resistivity profiles are scaled in the parameter scans.

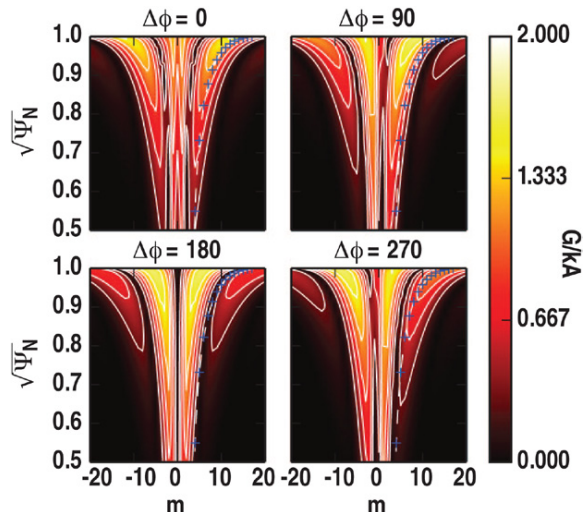


Figure 7. The harmonics in the applied $n = 3$ vacuum magnetic field normal to the flux surfaces for four different upper-lower I-coil phasings. The location of the $m = nq$ pitch-resonant harmonics is marked with a blue + symbols.

were described in section 3, were calculated. Additionally, for each of these simulations, the plasma response using different applied field structures (controlled by the upper-lower I-coil array phasing, $\Delta\phi_{ul}$) was also calculated.

While only odd ($\Delta\phi = 180^\circ$) and even ($\Delta\phi = 0^\circ$) phasings are currently possible for $n = 3$ MPs on DIII-D, the effects of resistivity and rotation for several phasings ($0^\circ, 90^\circ, 180^\circ, 270^\circ$) were simulated to demonstrate the range of plasma responses that can be obtained if the perturbation coil set on DIII-D is improved as part of future upgrades. The applied vacuum harmonics for these different phasings are shown in figure 7 demonstrating the large effect the phasing has on the applied field. For example, the pitch resonant harmonics are substantially larger for $\Delta\phi = 0^\circ$ compared with 270° . Interestingly, the 90° and 270° applied field structures are reflections of one another across $m = 0$. Therefore, either

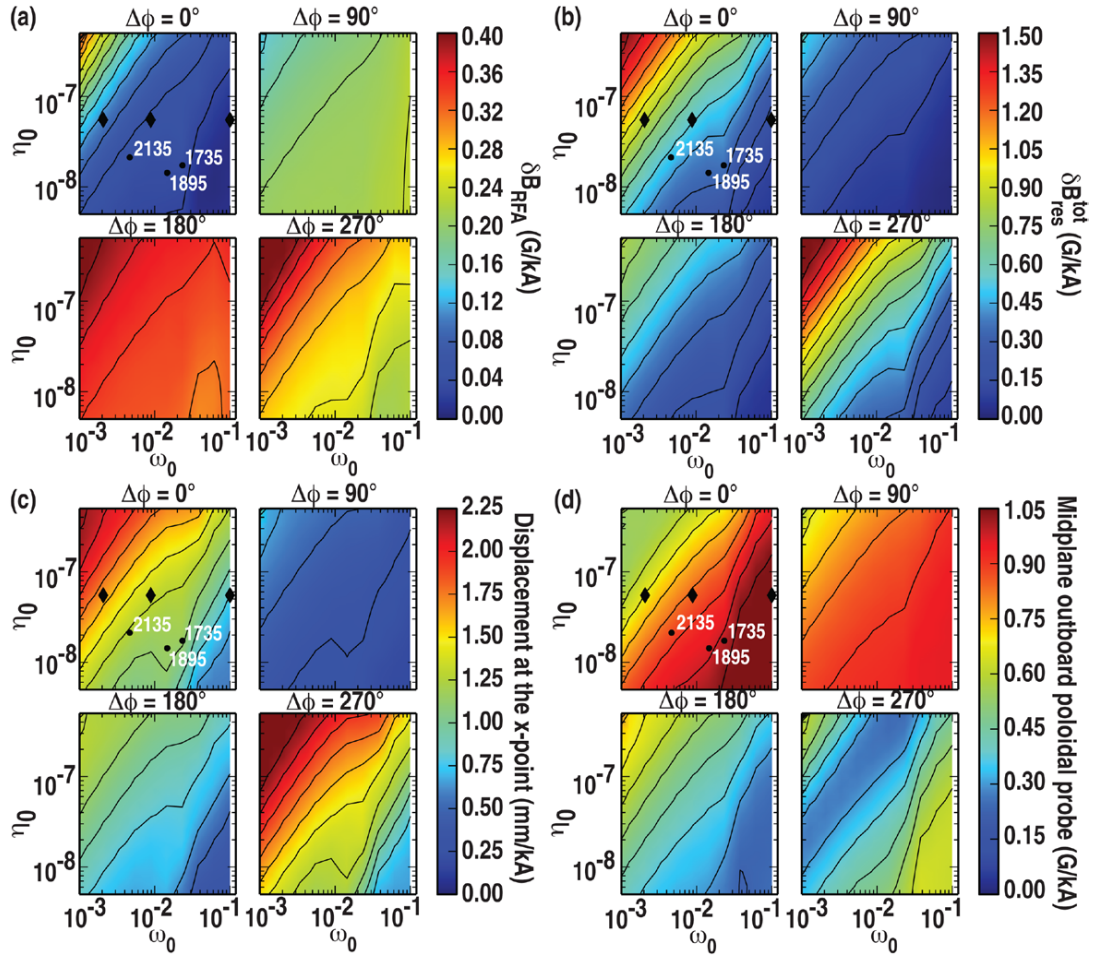


Figure 8. Various metrics and simulated outputs as a function of resistivity, toroidal rotation and four distinct upper-lower MP array phasing values. (a) The plasma RFA response which gives an indication of where global modes such as the kink-mode are driven most strongly by the MP. (b) The total pitch-resonant measure which describes the residual pitch-resonant field including the plasma screening response and is a proxy for the formation of magnetic islands. (c) The plasma displacement near the x-point which is a proxy for the formation of a 3D boundary, and the associated density pumpout effects that have been observed. (d) The simulated outboard midplane poloidal magnetic probe output due to the plasma response only. The simulations marked with diamonds are examined in more detail in figure 9 and the location of some of the simulations used in the experimental comparison (scaled profiles) in section 4 are marked with dots and a label indicating the relevant time in the shot.

configuration can also be accessed by reversing the sign of the toroidal magnetic field or the plasma current, but not both.

5.2. Effects of rotation and resistivity

The integrated normal plasma displacement around the x-point on the LCFS (section 3.3), midplane outboard poloidal magnetic probe output, total pitch-resonant (section 3.1) metric, and RFA (section 3.2) metric calculated as a function of resistivity and toroidal rotation for four different upper-lower I-coil phasings are shown in figure 8. Focusing on the even I-coil phasing ($\Delta\phi = 0^\circ$), there is a clear transition from an ideal to resistive-inertial response for all of the measures as the toroidal rotation decreases and resistivity increases. This type of transition is also described in [49, 50]. The transition is clearly seen in the δB_{res}^{tot} metric which approaches zero for low enough resistivity or high enough toroidal rotation speed indicating a perfect screening of the pitch-resonant harmonics which is also the case for ideal MHD. This transition occurs

over an order of magnitude change the rotation and resistivity parameters. Additionally the parameters at which the transition occurs follow an almost linear relation between the values of $\log(\eta_0)$ and $\log(\omega_0)$.

As can be seen in figure 8, the ideal response is characterised by a small displacement at the x-point, a large output from the midplane outboard poloidal probe and a small RFA (small δB_{RFA}). The outboard midplane poloidal probe output is negatively correlated with the total pitch-resonant field indicating that its output increases with the plasma screening response. In the regions of parameter space where the plasma screening response is smallest (regions where δB_{res}^{tot} is maximised in figure 8(b)), the probe output is reduced. RFA does not appear to have a strong impact on the poloidal probe output. This is because the fields from the resonant screening and RFA plasma responses have opposite signs (or are 180° out of phase with one another) so that in one case the vacuum field harmonics are attenuated and in the other they are amplified. In this low beta L-mode case, the decrease in the probe

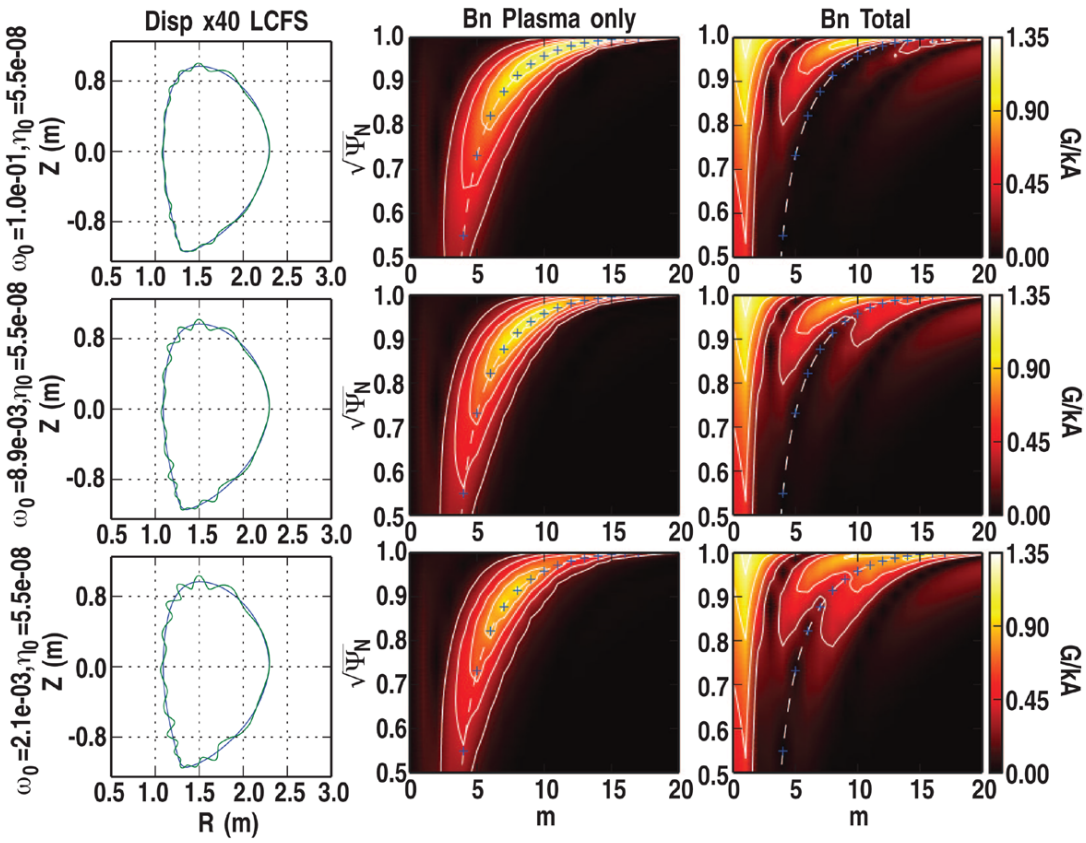


Figure 9. Plasma response as the rotation is decreased with the resistivity kept constant ($\eta_0 = 5.5 \times 10^{-8}$). Top row: $\omega_0 = 10^{-1}$, center row: $\omega_0 = 8.9 \times 10^{-3}$, bottom row: $\omega_0 = 2.1 \times 10^{-3}$. The plots show the plasma displacement normal to the LCFS (left column), plasma only component of the radial magnetic field structure (center column) and total radial magnetic field structure (right column).

output from the plasma generated magnetic field screening overwhelms changes due to increased excitation of the global modes. For the $\Delta\phi = 270^\circ$, which gives the strongest RFA response, the phase of the probe signal changes by 110° going from the high toroidal rotation and low resistivity to low toroidal rotation and higher resistivity. For the other $\Delta\phi$ values, the change in the phase of the probe signal is small indicating that for these cases, the RFA is not a strong effect compared to the plasma screening response.

To provide a more in-depth analysis of what is happening as the rotation decreases, the plasma and total magnetic field structure as well as the plasma displacement normal to the LCFS for three different rotations are shown in figure 9. The location of these simulations in parameter space is marked with diamonds in figure 8. As the rotation decreases (from the top row to the bottom of the figure), the resonant-screening component of the response from the plasma decreases, and harmonics associated with the kink-mode ($m > nq$) increase in amplitude. The reduced screening causes the total magnetic field at resonant surfaces to increase considerably which increases the possibility of stochastic region formation. Additionally, the plasma displacement at the x-point increases as the rotation slows. This confirms the results shown in the resistivity and rotation scans in figures 8, demonstrating that the measures used to quantify these effects are good proxies for what is occurring within the plasma.

The reduction in plasma screening and increase in x-point displacement shown in figure 9 as the toroidal rotation decreases agrees with the hypothesis for what was occurring in shot #142614, as described in section 4 and [36]: The reduction in toroidal rotation reduces the plasma screening allowing the field to penetrate further into the plasma (this can be clearly seen in the right column of figure 9). This reduction in plasma screening causes the poloidal probe response to fall and is accompanied by an increase in the displacement at the x-point which leads to the formation of a 3D boundary which is also seen in figure 9.

While there is qualitative agreement with this hypothesis, the quantitative agreement is not so good. The location of some data points that were used in the scaled profile analysis from section 4 are shown in figure 8. The reduction in toroidal rotation observed in the experiment was substantially smaller than what is shown in figure 9. Additionally, based on the parameter scans in figure 8, in order for the poloidal probe output to decrease by a factor of two (which occurred over a time of ≈ 12 ms), the toroidal rotation must decrease by a factor of ≈ 50 which is clearly not seen in the experimental toroidal main ion rotation profiles. Therefore, the sudden drop in probe output is not captured in the modelling presented here using the linear single-fluid plasma response. As was discussed in section 4, following the drop in the probe response the $n = 1$ component of the probe output increases

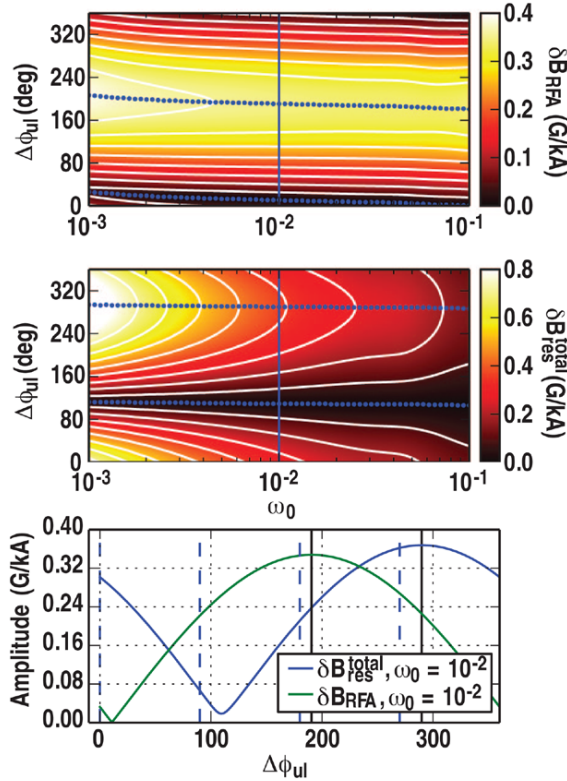


Figure 10. The effect of toroidal rotation and upper–lower I-coil array phasing on the RFA (top) and pitch-resonant (center) metrics for $\eta_0 = 1.3 \times 10^{-8}$. The maxima and minima are marked with blue dots. Each dot represents a simulation showing the dense sampling in the rotation parameter. Bottom: RFA and pitch-resonant metrics as a function of upper–lower I-coil array phasing for $\omega_0 = 10^{-2}$. The maximum phasing is marked with a solid vertical line. Dashed vertical lines mark the phasings shown in figure 8.

significantly, and at some times exceeds the $n = 3$ component providing evidence that nonlinear processes may be occurring.

5.3. Effect of the applied field structure

The poloidal spectra of the applied vacuum magnetic field normal to the LCFS for 0° , 90° , 180° , and 270° phasings are shown in figure 7 demonstrating the large effect the phasing has on the applied field. The effect that these different spectra have on the plasma response is clearly demonstrated in figure 8. For example, the x-point displacement for the even parity field is greater than the odd parity field by a factor of 2–3 for the wide range of central toroidal rotation and resistivity values shown. Detailed calculations using four different phasing values are shown even though DIII-D can only achieve 0° and 180° configurations with its 2×6 coil configuration to demonstrate the additional plasma responses that can be achieved with a MP coil set that has more than 6 toroidal coils.

As described in [22], using a linear code like MARS-F it is possible to calculate the response to the upper array only (δB_U) and the lower array (δB_L) only. $\Delta\phi_{ul}$ can then be taken into account by combining the two responses as follows: $\delta B_{\Delta\phi_{ul}} = \delta B_U + \delta B_L \exp(\Delta\phi_{ul}i)$. This represents a substantial

computational saving and allows us to examine the effect phasing has on the pitch-resonant and RFA components of the plasma response.

Using this technique, the toroidal rotation and detailed upper–lower I-coil array phasing dependence of the pitch-resonant and RFA components of the plasma response are shown in figure 10 for $\eta_0 = 1.3 \times 10^{-8}$. This resistivity is similar to the one in shot #142614. Both measures show a strong dependence on the applied field structure, similar to the results presented in [22] where the upper–lower I-coil phasing played a dominant role in determining the plasma response to the perturbation. For a given toroidal rotation (see bottom plot figure 10), the strength of the pitch resonant field including the plasma screening response can vary by a factor of 20 based on the upper–lower I-coil array phasing. This is very significant if the aim is to maximise the pitch-resonant field. Additionally, by varying the upper–lower I-coil phasing, it is possible to modify the ratio of the total pitch resonant field to the RFA. While this is partly due to the low β_N and relatively high $n = 3$ value considered here it contrasts with the $n = 1$ H-mode case on DIII-D where the plasma's sensitivity to the poloidal spectrum is strongly related to the RFA [51].

The phasing that maximises the RFA ($\approx 190^\circ$ for $\omega_0 = 10^{-2}$) and pitch-resonant ($\approx 290^\circ$ for $\omega_0 = 10^{-2}$) responses are offset from one another by approximately 100° (figure 10 lower) for the $q_{95} = 3.8$ equilibrium considered here, indicating that it is possible to obtain a dominantly RFA response or pitch-resonant response from the plasma. However, in order to access a phasing close to $\approx 290^\circ$ an upgrade to the perturbation coil set on DIII-D is required. These findings highlight the importance of being able to modify the phasing between the upper and lower MP coil arrays to achieve the maximum range of plasma responses. It is important to note that the optimal phasings are dependent on the q -profile.

6. Summary

The MARS-F code has been used to perform an extensive scan of the dependence of the linear single fluid plasma response on resistivity, rotation, and applied field structure for $n = 3$ MPs in DIII-D L-mode lower single null discharges. Two metrics which characterise the response as either pitch-resonant or RFA have been used to effectively illustrate the regions of parameter space where the ideal or resistive-inertial type responses dominate. Additionally, the displacement near the x-point and the output from an outboard midplane poloidal probe were calculated for comparison with experiment.

The plasma response was shown to be strongly dependent on the applied field structure. This is particularly important because this is a parameter that is relatively easy to change experimentally to achieve a desired outcome. The upper–lower I-coil array phasings (controls the applied field structure) which maximise either the RFA or pitch-resonant responses are offset from one another by 100° (for a $q_{95} = 3.8$ equilibrium), allowing either to be targeted more strongly. However, in order to achieve the optimum phasing for the strongest RFA response, the MP coils on DIII-D need to be upgraded to have more coils in the toroidal direction.

Modelling of the linear plasma response using experimental toroidal rotation profiles and Spitzer like resistivity profiles were compared with results which provide experimental evidence of a direct link between the decay of the resonant screening response and the formation of a 3D boundary [36] following a reduction in the toroidal rotation. The parameter scans support the link between the reduction in toroidal rotation, decay of the resonant screening and formation of a 3D boundary; however, the required change in rotation is substantially greater than what is observed during the experiment. Additionally, while good agreement with the simulated poloidal probe output is found during the initial application of the MP, later in the shot a sudden drop in the probe output is not captured in the modelling. This drop may be further explained using two-fluid, non linear, or kinetic physics, which are not included in the MARS-F model. Additionally, the drop in the $n = 3$ probe output is accompanied by an increase in the $n = 1$ component indicating that nonlinear processes such as the formation of a static $n = 1$ island may be occurring, motivating further investigations of this experiment. For example, as a first step, the effects the evolution of the perpendicular electron rotation has on the plasma response using a two fluid model should be explored.

Acknowledgments

This material is based upon work supported in part by the US Department of Energy, Office of Science, Office of Fusion Energy Sciences, using the DIII-D National Fusion Facility, a DOE Office of Science user facility, under Award DE-FC02-04ER54698. SRH wishes to thank AINSE Ltd. for providing financial assistance to enable this work to be conducted. DIII-D data shown in this paper can be obtained in digital format by following the links at https://fusion.gat.com/global/D3D_DMP. This paper has benefited greatly from input from the referees, R J Buttery and W M Solomon.

References

- [1] Evans T E et al 2006 *Nat. Phys.* **2** 419
- [2] Evans T E et al 2008 *Nucl. Fusion* **48** 024002
- [3] Evans T E et al 2004 *Phys. Rev. Lett.* **92** 235003
- [4] Jeon Y M et al 2012 *Phys. Rev. Lett.* **109** 035004
- [5] Suttrop W et al 2011 *Phys. Rev. Lett.* **106** 225004
- [6] Lanctot M J et al 2013 *Nucl. Fusion* **53** 083019
- [7] Liang Y et al 2007 *Phys. Rev. Lett.* **98** 265004
- [8] Kirk A et al 2010 *Nucl. Fusion* **50** 034008
- [9] Nardon E et al 2009 *Nucl. Fusion* **51** 124010
- [10] Solomon W M et al 2012 *Nucl. Fusion* **52** 033007
- [11] Canik J M et al 2010 *Nucl. Fusion* **50** 034012
- [12] Snyder P B et al 2012 *Phys. Plasmas* **19** 056115
- [13] Okabayashi M et al 2005 *Nucl. Fusion* **45** 1715
- [14] Cates C, Shilov M, Mauel M, Navratil G, Maurer D, Mukherjee S, Nadle D, Bialek J and Boozer A 2000 *Phys. Plasmas* **7** 3133
- [15] La Haye R J et al 2002 *Phys. Plasmas* **9** 2051
- [16] Reimerdes H, Chu M S, Garofalo A M, Jackson G L, La Haye R J, Navratil G A, Okabayashi M, Scoville J T and Strait E J 2004 *Phys. Rev. Lett.* **93** 135002
- [17] Shilov M et al 2004 *Phys. Plasmas* **11** 2573
- [18] Garofalo A M, La Haye R J and Scoville J T 2002 *Nucl. Fusion* **42** 1335
- [19] Park J-K, Schaffer M J, Menard J E and Boozer A H 2007 *Phys. Rev. Lett.* **99** 195003
- [20] Lanctot M J et al 2011 *Phys. Plasmas* **18** 056121
- [21] Lanctot M J et al 2010 *Phys. Plasmas* **17** 030701
- [22] Haskey S R, Lanctot M J, Liu Y Q, Hanson J M, Blackwell B D and Nazikian R 2014 *Plasma Phys. Control. Fusion* **56** 035005
- [23] Liu Y, Bondeson A, Fransson C, Lennartson B and Breitholtz C 2000 *Phys. Plasmas* **7** 3681
- [24] Strauss H R et al 2009 *Nucl. Fusion* **49** 055025
- [25] Izzo V A et al 2008 *Nucl. Fusion* **48** 115004
- [26] Ferraro N M and Jardin S 2009 *J. Comput. Phys.* **228** 7742
- [27] Bécoulet M et al 2012 *Nucl. Fusion* **52** 054003
- [28] Huysmans G and Czarny O 2007 *Nucl. Fusion* **47** 659
- [29] Orain F et al 2013 *Phys. Plasmas* **20** 2510
- [30] Koslowski H R et al 2006 *Nucl. Fusion* **46** L1
- [31] Yu Q et al 2008 *Nucl. Fusion* **48** 024007
- [32] Yu Q et al 2009 *Phys. Plasmas* **16** 042301
- [33] Yu Q et al 2009 *Nucl. Fusion* **49** 062001
- [34] Turnbull A D et al 2013 *Phys. Plasmas* **20** 056114
- [35] Turnbull A D et al 2012 *Nucl. Fusion* **52** 054016
- [36] Schmitz O et al 2014 *Nucl. Fusion* **54** 012001
- [37] King J D et al 2014 *Rev. Sci. Instrum.* **85** 083503
- [38] Schaffer M J, Menard J, Aldan M, Bialek J, Evans T E and Moyer R A 2008 *Nucl. Fusion* **48** 024004
- [39] Liu Y et al 2012 *Plasma Phys. Control. Fusion* **54** 124013
- [40] Garofalo A M, Jensen T H and Strait E J 2003 *Phys. Plasmas* **10** 4776
- [41] Kirk A et al 2013 *Nucl. Fusion* **53** 043007
- [42] Harting D et al 2012 *Nucl. Fusion* **52** 054009
- [43] Nardon E et al 2011 *J. Nucl. Mater.* **415** S915
- [44] Crotninger J, LoDestro L, Pearlstein L, Tarditi A, Casper T and Hooper E 1997 *Corsica: a Comprehensive Simulation of Toroidal Magnetic-Fusion Devices, Final Report to the LDRB Program* (Livermore, CA: Lawrence Livermore National Laboratory)
- [45] Lutjens H, Bondeson A and Sauter O 1996 *Comput. Phys. Commun.* **97** 219
- [46] Lao L L, John H E St, Peng Q, Ferron J R, Strait E J, Taylor T S, Meyer W H, Zhang C and You K 2005 *Fusion Sci. Technol.* **48** 968
- [47] Holcomb C et al 2006 *Rev. Sci. Instrum.* **77** 10E506
- [48] Houlberg W A, Shaing K C, Hirshman S P and Zarnstorff M C 1997 *Phys. Plasmas* **4** 3230
- [49] Liu Y, Kirk A and Nardon E 2010 *Phys. Plasmas* **17** 122502
- [50] Liu Y, Kirk A, Gribov Ym Gryaznevich M, Hender T and Nardon E 2011 *Nucl. Fusion* **51** 083002
- [51] Paz-Soldan C et al 2014 *Phys. Plasmas* **21** 072503

Conclusions and future work

Several advances in the modelling, analysis, and measurement of 3D fields have been presented, which have significantly improved the diagnosis and understanding of Alfvén waves in H-1NF stellarator plasmas and the role of non-axisymmetric magnetic perturbations (MPs) in ELM suppression on the DIII-D tokamak. Details of the design and results from two newly implemented diagnostic systems on H-1NF are presented: a helical Mirnov array and a synchronous imaging system.

The helical Mirnov array consists of 16 tri-axis probes (48 coils in total) which can detect magnetic fluctuations in the hundreds of kHz range and provide details of the toroidal and poloidal mode numbers, as well as mode polarisation. The placement of the array means the probes are similar distances from the plasma and are located in regions where the magnetic fluctuations are relatively strong. Consequently, the signals are substantially easier to analyse than the existing poloidal Mirnov arrays. When used in conjunction with a poloidal Mirnov array, both the toroidal and poloidal mode numbers can be obtained with a relatively high level of confidence - a difficult task on a stellarator. In addition to the array itself, a system of programmable pre-amplifiers was designed and built, allowing amplifier settings to be digitally controlled as part of the MDSplus shot initialisation cycle and recorded along with the digitised signals. This high level of usefulness means that the helical array is now one of the ‘always on’ diagnostics on H-1NF and is crucial for providing information on magnetic fluctuations.

In order to analyse the large quantity of data generated by the helical Mirnov array and other similar multi-channel broadband diagnostics, a new datamining algorithm and feature extraction technique was developed. The EM-VMM periodic datamining algorithm naturally accommodates the periodic phase differences between probes in an array, overcoming the limitations of existing datamining techniques when applied to this periodic data. The algorithm was shown to be superior to non-periodic alternatives using several artificial datasets without imposing a significant additional computational cost. This

datamining algorithm was then used to identify interesting clusters within several magnetic configuration scans on H-1NF. This information formed the basis of further analysis of the behaviour of modes on that device.

For detailed comparisons with theory, the radial structure of the mode is required in addition to the mode number and polarisation information already supplied by the magnetic diagnostics. In this work, a synchronous imaging technique which was originally developed by Professor John Howard, was improved and used to provide the line of sight measurements required to obtain the radial mode structure, when combined with the tomographic inversion technique described below. A phase locked loop, which uses a magnetic probe as a reference, generates gating pulses for an intensified charge coupled device (ICCD) camera. The technique overcomes readout noise and frame rate limitations of cameras, allowing MHD fluctuations in the kHz - MHz range to be imaged in high resolution for the first time. These images can be used for comparisons with theory, which helps improve the understanding of these modes which play an important role in stability and particle transport on both tokamaks and stellarators. This imaging technique was used to obtain high resolution images in 514nm CII light of a sample of modes that belong to the four main clusters of low frequency mode activity on H-1NF. These sequences of images are among the highest quality images of high frequency MHD fluctuations to date.

To take advantage of these images which provide both toroidal, poloidal, and radial structure information, a tomographic reconstruction technique, which is based on a 3D representation of the mode in magnetic coordinates, was developed. The inversion technique can be used to determine poloidal and toroidal mode number information, in addition to providing crucial radial structure information, without the need for representation in the form of radial basis functions. The inversion technique was applied to the data obtained from the synchronous imaging to obtain highly detailed radial structure information of the modes on H-1NF. All of the modes are localised to the outer region of the plasma and can be well represented using a single helical Fourier harmonic in Boozer coordinates, indicating that this co-ordinate system is well suited to a compact representation of these modes.

Extensive modelling of normal modes for H-1NF configurations within the framework of linearised ideal compressible MHD, using the CONTI and CAS3D codes, showed considerable low frequency gap structure in the Alfvén continua as well as the existence of a significant number of low frequency discrete modes. The new diagnostic systems and anal-

ysis techniques developed in this work showed that the low frequency modes on H-1NF are localised outside of mid-radius, have polarisations that are dominantly shear-like with non-negligible parallel components, and have mode numbers that are near resonance. These observations correspond most closely with discrete modes where compressibility (beta induced Alfvén eigenmodes) or interaction with sound modes (beta-induced Alfvén-acoustic eigenmodes) are important. The frequency dependence on H-1NF configurations (rotational transform profile) can be recovered for these modes if the temperature decreases for configurations where the modes have lower frequencies. A new diagnostic, which is currently being commissioned, will provide temperature measurements using helium line ratios, allowing this hypothesis to be tested.

A large part of this research has focused on the effects of 3D magnetic perturbations (MPs) on the linear resistive and ideal MHD plasma response in the DIII-D tokamak. These fields are of great interest due their role in edge localised mode (ELM) suppression, which is critical for the operation of future devices. Extensive parameter scans using the MARS-F code have shown the importance of the applied magnetic field structure in achieving one of two dominant types of response from the plasma. The applied vacuum field can strongly couple to pitch-resonant harmonics, or it can couple more strongly to a stable global mode such as the kink mode. In many situations, it has been demonstrated that it is possible to target a specific type of response. This is significant because the structure of the applied magnetic field is largely under our control through the design of MP coil sets, or the careful use of flexible coil sets.

Recent and ongoing experiments on DIII-D in which the phasing between the upper and lower perturbation coil sets is varied, have provided experimental validation of several of the predictions of the modelling that was undertaken as part of this research. These experiments highlight the importance of targeting the kink type response as opposed to directly coupling to pitch-resonant harmonics when trying to achieve ELM suppression. Interestingly, targeting the kink mode appears to lead to a larger residual pitch-resonant field because these harmonics also form part of the kink mode structure, and as such, are amplified when the kink mode is driven. These greater pitch-resonant fields increase the possibility that the plasma will be unable to fully screen them out. This in turn may lead to island and stochastic region formation, which modifies the pedestal, resulting in ELM suppression.

9.1 Future work

The work presented in this thesis has covered many topics, and while providing solutions to a variety of problems, it has also uncovered several avenues of research that can be pursued. In particular, the methods and techniques that have been developed can easily be adapted for use on other machines around the world. In each of the following subsections, some ideas for future work are explored.

9.1.1 Further analysis of modes on H-1NF

One significant outstanding question about the modes on H-1NF is the drive mechanism. Using the candidate eigenmodes that were identified in chapter 6, this question can be examined by calculating the drive and damping for these modes. The drive can be calculated using the LGRO and/or CAS3DK codes. Clearly, these codes require descriptions of the fast ion populations. This information is not currently experimentally diagnosed on H-1NF; however, by calculating the drive using trial energetic particle populations, it should be possible to estimate what is required and then to determine if these populations sound reasonable.

The dependence of the mode frequency on various plasma parameters, such as electron density, temperature, and magnetic field strength, has not been completely uncovered. This information is crucial for determining the dispersion relation of these modes. Some initial progress has been made; however, these quantities are coupled together because the source of the mode drive is the same ion cyclotron resonant heating (ICRH) system that is responsible for plasma heating. This makes it difficult to determine what is causing the frequency variations of the modes. Magnetic field strength scans have recently become possible with the upgraded ICRH transmitters and it is substantially easier to modulate the input power from the transmitters, allowing more detailed experiments to be conducted. Additionally, the upgraded 21 channel interferometer should provide a density profile as well as show the density variations at the surface, where the mode amplitude is greatest, to be calculated, providing great improvement over comparisons using single channel integrated line of sight measurements.

The radial structure of the mode was calculated using synchronous imaging of the 514nm CII light. This emission is dependent on both the electron density and temperature fluctuations. Analysis of the photon emissivity coefficient showed that in the relevant parameter range, the emissivity is primarily dependent on the electron density fluctuation

as well as the equilibrium electron density (chapter 6). A more direct approach to this problem is to use helium line ratios and a collisional radiative model to obtain the electron density and electron temperature fluctuations. Tomographic inversion of the data from the new 21 channel interferometer would also allow a more direct measurement of the electron density variations.

Finally, time was spent trying to actively excite modes using a specially designed broadband amplifier and the old ICRH antenna (see appendix I for more details). The initial results from these experiments looked promising; however, this was not fully explored due to a lack of time. If it is possible to successfully target gap modes, this provides a method of decoupling the mode excitation method from the ICRH heating system, allowing a great deal of progress to be made.

9.1.2 Application of datamining to other machines and diagnostics

The datamining techniques discussed here have been applied to magnetic diagnostics on other machines such as TJ-II and LHD. However, generally speaking, it should be possible to apply these techniques to any type of multi-channel broadband diagnostic such as soft x-ray arrays, photo multiplier tube (PMT) arrays, and multi-channel interferometers. Many of these diagnostics take line of sight measurements where the amplitude as well as the phase of the signal is critical.

The development of a datamining algorithm which uses both the amplitude and phase of the signal between channels is almost complete and ready to apply to these types of diagnostics. This application is likely to be even more beneficial than the magnetic probe measurements, due to their substantially larger channel counts and the likelihood that amplitude data will be more consistent than for magnetic probe arrays (see chapter 2 section IIIA). Additionally, for line of sight diagnostics, operations such as tomographic inversion are computationally expensive. Using datamining to identify interesting features reduces the size of the dataset and allows these computationally intensive tasks to be performed a minimal number of times on the average values for each of the clusters. This has the additional benefit of boosting the signal to noise ratio of the measurements by finding the same feature in the signals at multiple times over multiple shots.

Additionally, there are several outstanding technical questions with the datamining, such as the effect of neglecting covariances between dimensions when using model based datamining algorithms. Covariance, at least between neighbouring channels, is unavoid-

able when using the phase difference between channels as the clustering quantity. The effect of ignoring this covariance should be more fully investigated, and some initial analysis for this is shown in appendix G.

Looking further into the future, the model that is developed using model based clustering can be improved on a shot-by-shot basis using the new data, and can be used to quickly classify modes, either in real-time or in near real-time post-processing. Real-time identification would enable the possibility of real-time mode control. This also allows interesting features that do not fit any of the existing clusters to be flagged for further investigation, improving the chances of noticing a mode that has not previously been investigated.

9.1.3 Future work using synchronous imaging

There are several avenues for improving the synchronous imaging technique. Currently, the main limitation is the ICCD camera readout time. By using a separate fast framing camera and intensifier, it is possible to greatly reduce the time required to acquire a sequence of images. Other ways to decrease the readout time include using multiple intensifiers, each of which are combined into different areas on the image. By locking each intensifier to a different phase of the wave, multiple phases can be obtained in a single image, removing the need to take multiple images. Alternatively, a split fibre bundle can be used to image multiple poloidal views onto a single image increasing the amount of information available for the tomographic inversion.

It may be possible to improve the phase locked loop portion of the system by digitising the reference signal and using the field programmable gate array (FPGA) and digital signal processing techniques to lock to the signal. This would simplify the system, allowing more flexibility, easy implementation of filter banks, and the option for different frequency ranges.

The current system requires knowledge of the approximate frequency of the mode being imaged before the shot. This prevents the imaging of unexpected modes which may be even more interesting. To overcome this limitation, a bank of digitally switchable filters could be used, allowing different frequency ranges to be targeted throughout a shot. On long pulse machines, modes can be intelligently targeted when they are detected in the probe signal, or the filter bank could constantly loop through the various frequency bands, and image anything that is in that frequency range at any given time. Using this technique in conjunction with a separate intensifier and fast framing camera would allow

many different modes to be imaged as they appear during a shot.

There is a great deal of flexibility in the optical system that is placed in front of the camera. In addition to interference filters, one can image bremsstrahlung, soft x-rays (using a scintillation plate), or even use coherence imaging techniques to look at the changes in flow and temperature caused by the fluctuations. Some of these options are currently being investigated.

9.1.4 Future work with magnetic perturbations on tokamaks

There is significant room for improving the metrics that quantify the extent to which the applied field is coupling directly to the pitch-resonant or kink-resonant type response (see chapters 7, and 8). For example, the kink-resonant optimisation metric can be improved to be the inner product of the applied field or plasma response with the least stable kink mode.

Several different effects contribute to the amplitude of the pitch-resonant harmonics. These include the applied vacuum magnetic field perturbation, kink mode based amplification, and plasma screening. Developing a robust technique for separating these three components, in particular the plasma screening and kink mode amplification would improve the understanding of how to maximise the residual pitch resonant harmonics. For example, it may be possible to achieve the largest residual pitch resonant field by choosing a vacuum field perturbation that partially couples the kink mode, as well as partially coupling to the pitch-resonant harmonics.

Additionally, there are opportunities for significant model validation by comparing synthetic diagnostic outputs with those that are measured in experiments. To date the comparisons have mainly concentrated on magnetic measurements with substantial progress being made possible due to the recent upgrade of the magnetic probes on DIII-D (appendix B). Another possibility is to compare the modelled plasma displacement with measurements from the reflectometer.

Looking forward, the type of modelling presented in chapters 7 and 8 could form the basis of realtime control of the applied field structure to most accurately target a specific objective, such as ELM suppression.

Appendices

Contents of Appendices

Appendix A (Published) Sustained suppression of ELMs in DIII-D ($n=2$)	117
Appendix B (Published) An upgrade of the DIII-D magnetic diagnostics	119
Appendix C (Accepted) Observation of multi-component plasma response	121
Appendix D Code repositories	123
D.1 Obtaining copies of the code repositories	123
D.2 Details of the H1 module	124
Appendix E Supplementary HMA details	127
E.1 Location of the HMA probes	127
E.2 Orientation of the HMA probes	129
E.3 HMA polarisation calculations	131
E.4 Digital control of the amplifier settings	136
Appendix F Supplementary imaging and tomography details	143
F.1 Location of the camera	143
F.2 Shot numbers for the important modes	144
F.3 Details of the PLL and FPGA	146
F.4 Running the tomographic routines	151
Appendix G Supplementary details for the datamining chapter	153
G.1 Using the feature extraction and clustering algorithms	153
G.2 Covariance between phase difference measurements	156
Appendix H Supplementary details for the H-1NF mode analysis chapter	161
H.1 Plotting the spectra from CAS3D and CONTI	161
H.2 Running the polarisation and mode number analysis	162
H.3 Code compilation notes	163

Appendix I Attempts to actively drive modes in H-1NF	169
I.1 Active excitation experiments	169
I.2 Details of the broadband power amplifier design	171
Appendix J Supplementary details for the MP chapters	173
J.1 The pyMARS module	174
J.2 The pyMARS input file	177
J.3 Examples	184

Sustained suppression of type-1 edge-localized modes with dominantly $n=2$ magnetic fields in DIII-D

This paper is the first to document ELM suppression on DIII-D using $n = 2$ non-axisymmetric magnetic perturbations. The dependence of the suppression on the applied field structure, as well as plasma parameters, motivated the extensive modelling shown in chapters 7 and 8, as well as the further experiments shown in appendix C. My contribution to this paper is the MP coil phasing dependence simulations which are included in section 3. This analysis showed that ELM suppression occurs for applied fields that couple more strongly to the kink mode than those that directly apply a pitch-resonant field. This amounts to approximately 15% of the research and 5% of the writing. Only the first page of this paper is shown here, the full version is available here: <http://dx.doi.org/10.1088/0029-5515/53/8/083019>.

Sustained suppression of type-I edge-localized modes with dominantly $n = 2$ magnetic fields in DIII-D

**M.J. Lanctot^{1,a}, R.J. Buttery², J.S. de Grassie², T.E. Evans²,
N.M. Ferraro², J.M. Hanson³, S.R. Haskey⁴, R.A. Moyer⁵,
R. Nazikian⁶, T.H. Osborne², D.M. Orlov⁵, P.B. Snyder²,
M.R. Wade² and the DIII-D Team**

¹ Lawrence Livermore National Laboratory, 7000 East Ave, Livermore, CA 94550, USA

² General Atomics, PO Box 85608, San Diego, CA 92186-5608, USA

³ Department of Applied Physics and Applied Mathematics, Columbia University, 116th St and Broadway, New York, NY 10027, USA

⁴ Plasma Research Laboratory, Research School of Physical Sciences and Engineering, The Australian National University, Canberra, ACT 0200, Australia

⁵ Center for Energy Research, University of California San Diego, 9500 Gilman Drive, La Jolla, CA 92093-0417, USA

⁶ Princeton Plasma Physics Laboratory, Princeton, NJ 08543-0451, USA

Received 12 March 2013, accepted for publication 24 June 2013

Published 16 July 2013

Online at stacks.iop.org/NF/53/083019

Abstract

Type-I edge-localized modes (ELMs) have been suppressed in DIII-D (Luxon *et al* 2003 *Nucl. Fusion* **43** 1813) H-mode discharges with a H_{98Y_2} confinement factor near 1.0 using magnetic perturbations (MPs) with dominant toroidal mode number $n = 2$. This expands access to the ELM-suppressed regime, which was previously attainable in DIII-D only with $n = 3$ fields. ELM suppression is obtained with two rows of internal coils for 1.8 s with normalized beta of 1.9 and average triangularity of 0.53, corresponding to a scaled version of ITER scenario 2 at an ITER relevant electron collisionality of 0.2. The applied field reduces the pedestal pressure and edge current via the density without degrading the edge thermal transport barrier. ELITE calculations find that the resulting profiles are stable to intermediate- n peeling–ballooning modes. ELM suppression is found within different ranges of q_{95} depending on the coil configuration used to generate the MP. The edge safety factors associated with suppression do not correspond to those that maximize the pitch-resonant components of the applied vacuum field. Instead, ELM suppression is correlated with an increase in the amplification of kink-resonant components of the calculated ideal MHD plasma response field.

(Some figures may appear in colour only in the online journal)

1. Introduction

Controlling the stability of large type-I edge-localized modes (ELMs) in high-confinement (H-mode) tokamak discharges remains a major challenge for near-term magnetic confinement fusion experiments, such as ITER, and for future nuclear fusion power plants. In H-mode, the stored energy and density become stationary due to intermittent losses of particles and energy during ELM events occurring with frequencies of 10–200 Hz [2, 3]. Inductive scenarios in ITER will operate in the type-I ELM regime, which has the enhanced energy confinement required to achieve fusion burn. Unfortunately, the impulsive heat loads associated with ELM events limit the lifetime of plasma facing components, especially the

divertor, and therefore set the limit on the maximum allowable ELM energy loss in ITER [4]. Without a validated model for the nonlinear ELM evolution and resulting energy transport, extrapolations to ITER from present experimental measurements of particle and power fluxes onto the divertor targets are uncertain, with estimates of the ELM energy loss spanning a range from a level of 5–11 MJ to 22 MJ. The upper end of this range is expected to be $\sim 20\%$ of the energy in the H-mode pedestal, and unacceptable for present divertor lifetime requirements [5, 6]. Therefore, there is a present need for control techniques that can reduce ELM energy loss, or suppress ELMs entirely. To be viable for future reactors, it is critical that the ELM stabilizing mechanism not significantly degrade plasma performance, or worse increase the frequency of tokamak disruptions.

^a Current address: General Atomics, USA.

An upgrade of the magnetic diagnostic system of the DIII-D tokamak for non-axisymmetric measurements

The $n = 2$ ELM suppression results, shown in appendix A, motivated an upgrade to the magnetic diagnostics on DIII-D to better diagnose the non-axisymmetric plasma response to magnetic perturbations. These upgraded diagnostics are used for the measurements shown in appendix C and demonstrate that the low field side midplane magnetic probes are substantially more sensitive to the kink type plasma response than the midplane high field side probes. My contribution to this paper is towards the MARS-F modelling which helped inform the design decisions for the new magnetic diagnostics. This amounts to approximately 5% of the research presented in the paper. The new magnetic diagnostic system described here will be very useful for testing some of the results shown in chapters 7 and 8. Only the first page of this paper is shown, the full version is available from : <http://dx.doi.org/10.1063/1.4891817>.



An upgrade of the magnetic diagnostic system of the DIII-D tokamak for non-axisymmetric measurements

J. D. King,¹ E. J. Strait,² R. L. Boivin,² D. Taussig,² M. G. Watkins,² J. M. Hanson,³ N. C. Logan,⁴ C. Paz-Soldan,¹ D. C. Pace,² D. Shiraki,³ M. J. Lanctot,² R. J. La Haye,² L. L. Lao,² D. J. Battaglia,⁴ A. C. Sontag,⁵ S. R. Haskey,⁶ and J. G. Bak⁷

¹Oak Ridge Institute for Science and Education, Oak Ridge, Tennessee 378300-8050, USA

²General Atomics, P.O. Box 85608, San Diego, California 92186-5608, USA

³Department of Applied Physics and Applied Mathematics, Columbia University, 116th and Broadway, New York, New York 10027, USA

⁴Princeton Plasma Physics Laboratory, P.O. Box 451, Princeton, New Jersey 08543-0451, USA

⁵Oak Ridge National Laboratory, P.O. Box 2008, Oak Ridge, Tennessee 37831, USA

⁶Plasma Research Laboratory, Research School of Physical Sciences and Engineering,

The Australia National University, Canberra, ACT 0200, Australia

⁷Research and Development Division, National Fusion Research Center, Daejeon, South Korea

(Received 7 March 2014; accepted 21 July 2014; published online 7 August 2014)

The DIII-D tokamak magnetic diagnostic system [E. J. Strait, Rev. Sci. Instrum. **77**, 023502 (2006)] has been upgraded to significantly expand the measurement of the plasma response to intrinsic and applied non-axisymmetric “3D” fields. The placement and design of 101 additional sensors allow resolution of toroidal mode numbers $1 \leq n \leq 3$, and poloidal wavelengths smaller than MARS-F, IPEC, and VMEC magnetohydrodynamic model predictions. Small 3D perturbations, relative to the equilibrium field ($10^{-5} < \delta B/B_0 < 10^{-4}$), require sub-millimeter fabrication and installation tolerances. This high precision is achieved using electrical discharge machined components, and alignment techniques employing rotary laser levels and a coordinate measurement machine. A 16-bit data acquisition system is used in conjunction with analog signal-processing to recover non-axisymmetric perturbations. Co-located radial and poloidal field measurements allow up to 14.2 cm spatial resolution of poloidal structures (plasma poloidal circumference is ~ 500 cm). The function of the new system is verified by comparing the rotating tearing mode structure, measured by 14 B_p fluctuation sensors, with that measured by the upgraded B_R saddle loop sensors after the mode locks to the vessel wall. The result is a nearly identical 2/1 helical eigenstructure in both cases. © 2014 AIP Publishing LLC. [<http://dx.doi.org/10.1063/1.4891817>]

I. INTRODUCTION

Inductive loop and coil magnetic field measurement is the bedrock diagnostic for studying magnetically confined plasmas. These sensors provide a simple, robust measurement of static and fluctuating magnetic properties spanning the full range of operational space. The foundation of magnetic measurements dates back to the 19th century with the discovery of electromagnetic induction by Michael Faraday and, while not discussed in this paper, further application to laboratory plasma measurements has been thoroughly reviewed in previous works.^{1,2} Here we have taken the step to explore subtle changes to the tokamak magnetic field topology associated with small distortions in toroidal symmetry. A large disparity between Tesla equilibrium field and sub-Gauss asymmetries ($10^{-5} < \delta B/B_0 < 10^{-4}$) exists in tokamaks, requiring great care in sensor positioning, alignment and electronic instrumentation.

The tokamak is nominally an axisymmetric device and the full suite of axisymmetric magnetic field measurements on DIII-D is detailed in Ref. 20. Recently, small non-axisymmetric, or “3D,” fields have been found to be beneficial in fusion energy relevant plasma studies. Some examples of these results include resonant magnetic perturbations

(RMP) causing edge localized mode (ELM) suppression,³ non-resonant magnetic field (NRMF) induced torque increasing toroidal plasma rotation,^{4,5} and active feedback control of resistive wall modes (RWM).^{6,7}

This article will discuss a large diagnostic upgrade that extends the non-axisymmetric magnetic field measurement capability of DIII-D. The physics objectives of this upgrade are diverse. The primary goal is measurement of the plasma response^{8,9} to applied 3D fields. This measurement may prove critical to understanding how $n = 3$ RMPs suppress ELMs. Furthermore, the validation of 3D perturbed or equilibrium model predictions will be possible, allowing for accurate extrapolation to ITER. A second objective is a more complete measurement of the toroidal and poloidal structure of non-rotating magnetohydrodynamic (MHD) modes such as locked tearing modes¹⁰ and resistive wall modes. Furthermore, local electromagnetic torque between the plasma and applied fields may be directly measured,¹¹ which can further elucidate error field braking effects and enable the optimization of necessary corrections. The eventual full reconstruction of non-axisymmetric equilibria will be possible. This upgrade is intended to improve axisymmetric equilibrium EFIT¹² reconstructions, as well. Finally, a small subset of 6 high frequency response sensors was added to improve the detection of ELM

Observation of multi-component plasma response and its relationship to density pumpout and edge-localized mode suppression

This paper continues the work shown in appendix A and investigates the role of the kink mode in ELM suppression for $n=2$ non-axisymmetric fields on DIII-D. By rotating the field in one of the I-coil arrays and leaving the other fixed, a continuous phase sweep is applied. This is similar to the simulated experiment shown in figure 14 of chapter 7. During this phase sweep, ELM suppression was observed for specific upper-lower phasings. My contribution to this work is the linear resistive MHD modelling using the MARS-F code, which allows the regions of ELM suppression to be compared with metrics that quantify the extent to which the field couples to the kink-mode or directly to the pitch resonant harmonics. Additionally, the output from synthetic diagnostics has been calculated for comparison with experiments. This amounts to approximately 20% of the research and 10% of the writing. This paper was accepted for publication with the physical review letters journal in February 2015. Only the first page of this paper is shown here.

Observation of multi-component plasma response and its relationship to density pumpout and edge-localized mode suppression

C. Paz-Soldan,¹ R. Nazikian,² S.R. Haskey,³ N.C. Logan,² E.J. Strait,¹ N. Ferraro,¹ J.M. Hanson,⁴ J.D. King,⁵ M.J. Lanctot,¹ R. Moyer,⁶ M. Okabayashi,² J.-K. Park,² and M. Shafer⁷

¹*General Atomics, San Diego, California 92121, USA**

²*Princeton Plasma Physics Laboratory, Princeton, New Jersey 08543, USA*

³*Plasma Research Laboratory, Australian National University, Canberra, ACT 0200, Australia*

⁴*Columbia University, New York, New York 10027, USA*

⁵*Oak Ridge Institute for Science and Education, Oak Ridge, Tennessee 37831, USA*

⁶*University of California San Diego, 9500 Gilman Dr., La Jolla, CA 92093-0417, USA*

⁷*Oak Ridge National Laboratory, PO Box 2008, Oak Ridge, Tennessee 37831-6169, USA*

(Dated: September 8, 2014)

Density pumpout and edge-localized mode (ELM) suppression by applied $n=2$ magnetic fields in low collisionality DIII-D plasmas are shown to be correlated with the magnitude of the plasma response driven on the high field side (HFS) of the magnetic axis, but not the low-field side (LFS) midplane. These distinct responses yield the first evidence that two separate components of the magnetic response exist, each of which is preferentially excited by a different $n=2$ poloidal spectrum and preferentially detected on the LFS or HFS. Ideal and resistive MHD calculations find that the LFS measurement is primarily sensitive to excitation of stable kink modes, while the HFS measurement is primarily sensitive to resonant currents. The resonant currents are themselves strongly modified by kink excitation, with the optimal applied field pitch for pumpout and ELM suppression found to significantly differ from equilibrium field-alignment. The kink mode is found to drive pumpout and ELM suppression primarily through its impact on the resonant components.

Introduction and Motivation The simultaneous control of transiently large heat loads while maintaining high thermal confinement is essential in future fusion reactors. However, instabilities such as edge localized modes (ELMs) can lead to unacceptable levels of wall erosion in a burning plasma experiment such as ITER unless these loads can be substantially mitigated [1]. One approach for ELM mitigation and suppression is the use of non-axisymmetric magnetic fields, a technique which has been demonstrated on several facilities [2–5].

Beyond the effect on ELMs, non-axisymmetric fields also excite weakly stable resistive wall modes (here termed ‘kink’ modes) [6–10]. Kink excitation has been critical to understanding $n=1$ error field correction [11–13] (where n is toroidal mode number). In contrast, its function in $n>1$ pumpout and ELM suppression has remained unclear. As kink excitation is sensitive to particular equilibrium properties, basic understanding of its role in pumpout and ELM suppression is an essential element of a predictive model for either phenomenon.

On the DIII-D tokamak $n=2$ fields are uniquely suited to understand this connection. Recent work has shown that $n=2$ fields can suppress ELMs [14], yet unlike $n=3$, the $n=2$ poloidal spectrum can be finely controlled with existing in-vessel coils [15]. Recent upgrades to the magnetic probe suite on DIII-D also allow constrained measurement of $n=2$ responses both on the tokamak low-field side (LFS) and high-field side (HFS) [16].

In this Letter we employ fine control of the applied $n=2$ poloidal spectrum to show that pumpout and ELM suppression is correlated with the amplitude of the mag-

netic plasma response measured near the HFS midplane. The LFS midplane response is found to be best excited by a different poloidal spectrum than that which best excites the HFS, directly demonstrating the presence of multiple components in the response. Linear MHD simulations indicate that the LFS measurement is primarily sensitive to the excitation of stable kink modes, while the HFS measurement is primarily sensitive to the resonant currents on rational surfaces. The resonant currents are themselves strongly modified by kink mode excitation, with the optimal applied spectrum for pumpout and ELM suppression found to significantly differ from equilibrium field-alignment. The role of the kink is thus found to be limited to amplification of the resonant components which in turn drive pumpout and ELM suppression.

The remainder of this letter is structured as follows. The experimental setup is first described, with emphasis on the non-axisymmetric coil configuration used. The global plasma ($n=0$) response is then described and compared to ideal-MHD modeling of global plasma response metrics. The connection to the measured $n=2$ magnetic plasma response follows, where experimental data combined with ideal and resistive MHD modeling allow separation of the response due to resonant (shielding) currents and kink mode excitation.

Experimental Setup These discharges are configured as ITER-similar shape plasmas, with normalized current (I_N) of 1.2, internal inductance (l_i) of 1.0, neutral beam injected power of 6 MW, modest electron resonance heating of 1 MW, yielding a normalized pedestal electron collisionality (ν_*) of 0.23. The value of the edge safety factor

Code repositories

Code repositories have been maintained using the git source control management system. All the code that has been developed and used in this thesis, including all history of modifications is openly available on github, or locally on the h1svr computer at RSPE.

Outline

D.1	Obtaining copies of the code repositories	123
D.2	Details of the H1 module	124

D.1 Obtaining copies of the code repositories

The source code for the work presented in this thesis is kept in three main git repositories. The first one covers all the work related to MARS-F analysis of RMPs on DIII-D and can be obtained as follows:

```
$ git clone https://github.com/shaunhaskey/pyMARS.git
$ git clone h1svr:/home/srh112/code/pyMARS.git
```

The second repository is my branch of the pyfusion module which was originally written by David Pretty. My branch of this module (SH_branch) has been updated to include the clustering algorithms that were developed as part of this research:

```
$ git clone https://github.com/shaunhaskey/pyfusion.git
$ git clone h1svr:/home/srh112/code/pyfusion.git
$ git checkout SH_branch
```

The h1 module includes much of the work on H-1NF including diagnostic details:

```
$ git clone https://github.com/shaunhaskey/python-h1.git
$ git clone h1svr:/home/srh112/code/python-h1.git
```

This module is quite large and its various parts are described in the next section.

A repository of the source code for the micro controller which controls the helical Mirnov array amplifier settings is available from here:

```
$ git clone https://github.com/shaunhaskey/hma_micro_program.git
```

The Verilog source code for the Spartan 3E FPGA that controls the PLL for the synchronous imaging work is available from here:

```
$ git clone https://github.com/shaunhaskey/PLL_dig_freq_range.git
```

Additionally repositories are available for some MDSplus devices that were developed as part of this project:

```
$ git clone https://github.com/shaunhaskey/AnuDevices.git
```

Each of these modules is described in the relevant appendix. The h1 module contains many useful scripts for work on H-1NF and is briefly described below.

D.2 Details of the H1 module

The h1 module was created to bring together the Python code that has been written for various projects on H-1NF. The majority of the module was developed as part of this thesis. The various parts can be imported individually as follows:

```
import h1.tomography as tomo
import h1.h1model as h1model
import h1.helper as helper
import h1.mhd_eq as mhd_eq
import h1.diagnostics as diag
import h1.h1_operations as h1_ops
```

These individual parts are described below:

- **tomography:** Scripts and algorithms for the tomographic inversion described in chapter 5.
- **h1model:** Mayavi based plotting functions for various parts of H-1NF which are useful for generating publication ready plots, or for trying to calculate the orientation of a diagnostic. Surfaces based on a VMEC equilibrium can also be plotted.
- **helper:** Functions that are useful to all the other parts of the module.
- **mhd_eq:** The VMEC and BOOZER scripts written by Bernhard Seiwald to interpret the output of VMEC and the output of various VMEC to BOOZER coordinate

transformation codes. The versions included here have been modified slightly. Additionally, there are scripts which are useful for interpreting the output from the HELIAC, DESCUR, CAS3D, and CONTI codes.

- **diagnostics:** Interferometer demodulation routines, PiMAX image analysis routines, and scripts that are useful for analysing the magnetic probe data. The magnetics section contains everything for the HMA along with several other useful functions.
- **h1_operations :** Contains the scripts for programming the arbitrary waveform generator which controls the RF power modulation. The pulse_blasters folder contains the scripts for programming the pulse trigger timer system, and h1data_run contains the MDSplus shot looper script for H-1NF.

Supplementary details for the helical Mirnov array and amplifiers

This appendix provides detailed information about the helical Mirnov array probes (HMA), digitisers, amplifiers, and digital control of the amplifier settings. The information provided here supplements what was already shown in chapter 2. Additionally, a large amount of information is available on the HMA part of the H-1NF wiki: <http://h1svr.anu.edu.au/wiki/HMA/>, or by searching for “Mirnov”.

Outline

E.1	Location of the HMA probes	127
E.2	Orientation of the HMA probes	129
E.3	HMA polarisation calculations	131
E.4	Digital control of the amplifier settings	136
E.4.1	Micro controller program	137
E.4.2	Modifications to the backplane and MCU code	139
E.4.3	Additional information	139

E.1 Location of the HMA probes

The coils were placed inside a stainless steel bellows which makes calculating their orientation and location difficult. Their location was determined using a test probe that output a $\approx 100\text{kHz}$ magnetic field. By moving the test probe along the bellows, the location of the individual formers was identified by looking for a maximum in the coil signals. This

Table E.1: Probe locations in cylindrical and Cartesian co-ordinates. Refer to figure E.1 for the definition of the relevant directions.

Former	R (m)	phi (rad)	Z (m)	X (m)	Y (m)	Z (m)
1	0.912	0.711	0.029	0.691	0.595	0.029
2	0.936	0.550	0.069	0.798	0.489	0.069
3	0.975	0.393	0.093	0.900	0.373	0.093
4	1.018	0.242	0.097	0.988	0.244	0.097
5	1.058	0.098	0.082	1.052	0.103	0.082
6	1.087	-0.043	0.053	1.086	-0.046	0.053
7	1.101	-0.179	0.017	1.084	-0.196	0.017
8	1.100	-0.317	-0.023	1.045	-0.343	-0.023
9	1.082	-0.455	-0.059	0.972	-0.476	-0.059
10	1.051	-0.596	-0.086	0.870	-0.590	-0.086
11	1.011	-0.740	-0.097	0.746	-0.682	-0.097
12	0.967	-0.893	-0.090	0.607	-0.753	-0.090
13	0.930	-1.050	-0.063	0.463	-0.807	-0.063
14	0.910	-1.211	-0.021	0.320	-0.852	-0.021
15	0.911	-1.375	0.026	0.178	-0.894	0.026
16	0.934	-1.536	0.067	0.033	-0.934	0.067

allowed their position to be described relative to the H-1NF structure. With the additional information that the coils follow a helical path next to the HFC with an inter-coil spacing of 15.6cm allows the probe locations to be described relatively accurately.

The location of the probes is included in the Python h1 module and can be obtained as follows:

```
import h1.diagnostics.magnetics as mag
hma = mag.HMA()
hma.cart #probe locations in Cartesian co-ordinates
hma.cyl #probe locations in cylindrical co-ordinates
```

For convenience the values are also included in table E.1. The definition of the R, Z, ϕ and x, y, z directions that are used in this appendix are shown in figure E.1 along with a 3D rendering of the location of the probes and their orientation.

Because each coil on the tri-axis formers is wound on top of the previous one, their sensitivities are slightly different. The probe outputs for the same magnetic field are listed in table E.2. These values can also be obtained from the h1 module as follows:

```
import h1.diagnostics.magnetics as mag
hma = mag.HMA()
hma.probe_sensitivities #probe sensitivities
```

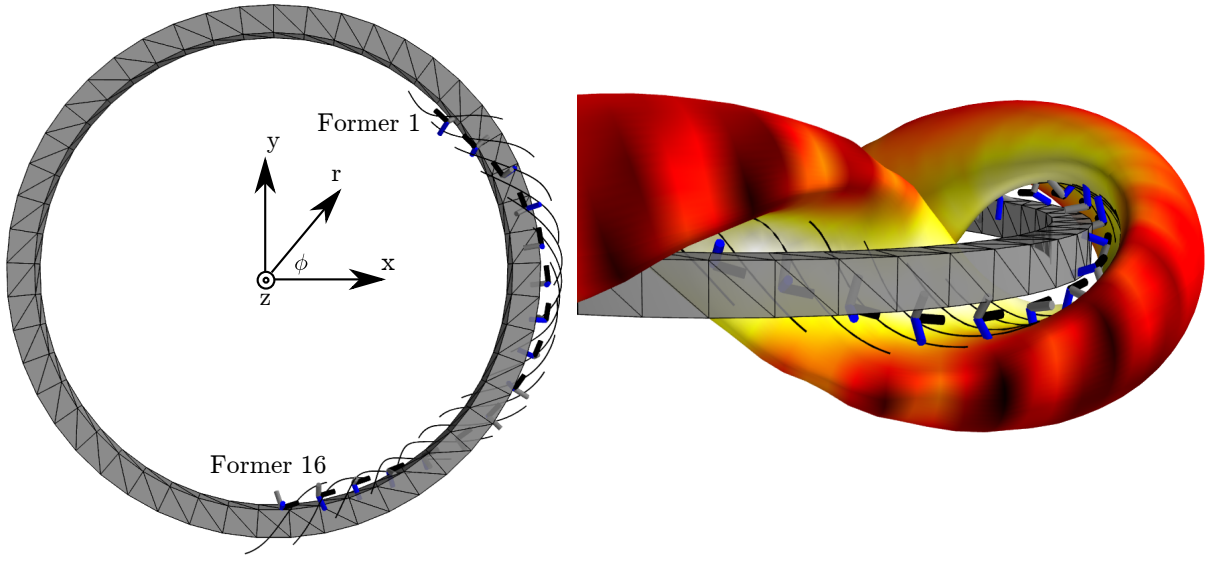


Figure E.1: The location of HMA probes and the orientation of the different axes for each tri-axis probe. The axes are coloured blue, black and gray because these are the colours that were used to mark the respective twisted pair wires (see figure E.2). The axes form a right handed coordinate system (blue, black, gray). Field lines near the probes are also shown for a typical H-1NF configuration.

The three twisted pairs that connect each former to the amplifiers are separated from the twisted pairs for the other formers using heatshrink. The individual twisted pairs are marked with either blue, black or gray to differentiate the axes on the probe as well as the polarity. The orientation of these axes is shown in figure E.2, and a diagram showing how the probes were wound is shown in figure E.3. The coloured wire on each coil has a positive voltage for the directions marked $\hat{n}_1, \hat{n}_2, \hat{n}_3$ in figure E.2. The normals to the blue, black and gray coils form a right handed coordinate system and correspond to the x, y, and z markings on amplifier housing. The “axial” coils are within $\pm 10^\circ$ of the helical field coil direction (3,1) but at a significant angle to the local magnetic field. The termination of the twisted pairs onto the amplifier backplane is shown in figure E.5.

E.2 Orientation of the HMA probes

To calculate the orientation of the coils, various field coil sets were turned on individually using a $\approx 50\text{A}$ 4Hz current which has a sufficiently low frequency that eddy currents could be ignored. The outputs of the coils were integrated and recorded. The measurements using the TFC, OVC, PFC and HFC are shown in tables E.3, E.4, E.5 and E.6. Note that

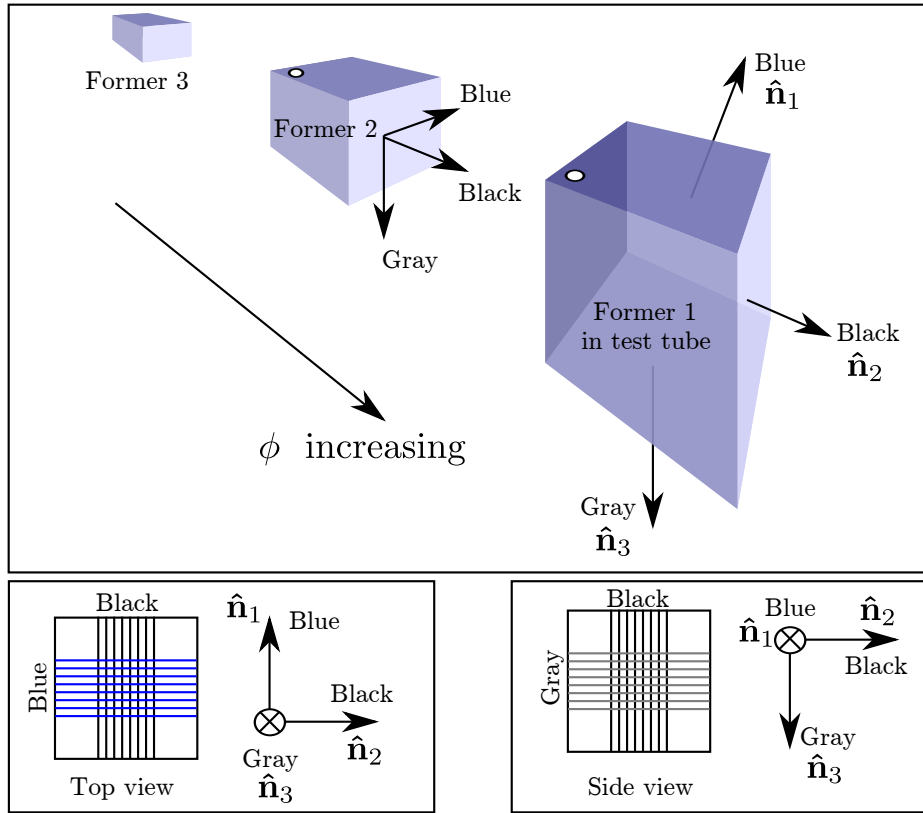


Figure E.2: The orientation of the different axes on the tri-axis helical Mirnov array probes. The axes are labelled blue, black and gray because these colours were used to mark the respective twisted pair wires. As can be seen, the axes form a right handed coordinate system (blue, black, gray). The first former is located inside the pyrex test tube and as the former number increases, their toroidal location decreases.

the applied field for the HFC is in the opposite direction to the standard field from the HFC due to polarity limitations of the helical shunt. These values can be obtained from the h1 module as follows:

```
import h1.diagnostics.magnetics as mag
hma = mag.HMA()
hma.tfc_sens
hma.ovc_sens
hma.pfc_sens
hma.hfc_sens
```

Each of these field coils generates a unique magnetic field allowing the orientation of each probe to be calculated. The HELIAC code is used to calculate the direction of the applied vacuum magnetic field at the probe locations. Additionally, we know that the coil faces are orthogonal to each other. The methods for calculating the orientations is described in chapter 2B. The orientations are recorded table E.7 and can be obtained from

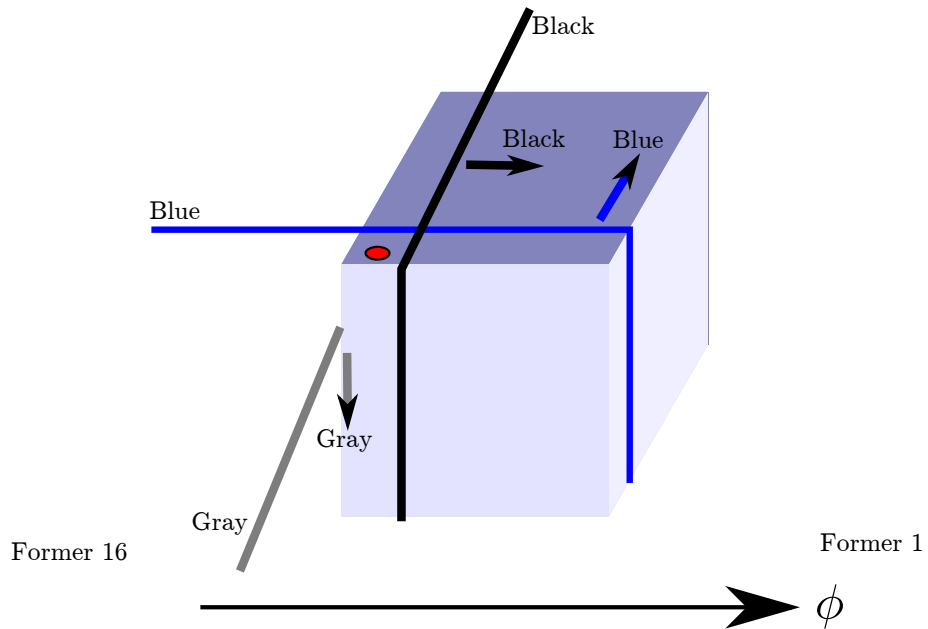


Figure E.3: Details of how each probe was wound showing the coloured wire and the first loop. Subsequent loops on the first layer continue in the direction shown by the arrows. The coloured wire is connected to the positive input on the instrumentation amplifiers. This is also the wire that will have a positive voltage for δB fields in the direction of the arrows. Note the pre-amplifiers have two inverting stages which cancel each other out.

the h1 module as follows:

```
import h1.diagnostics.magnetics as mag
hma = mag.HMA()
hma.orientations
```

E.3 HMA polarisation calculations

This section provides additional information about the polarisation calculations that were performed for the HMA probes in chapter 6. The three directions of the faces of the pickup coil can be represented by the following unit vectors (see table E.7 for the components):

$$\begin{aligned}\hat{\mathbf{n}}_1 &= n_{1x}\hat{\mathbf{x}} + n_{1y}\hat{\mathbf{y}} + n_{1z}\hat{\mathbf{z}}, \\ \hat{\mathbf{n}}_2 &= n_{2x}\hat{\mathbf{x}} + n_{2y}\hat{\mathbf{y}} + n_{2z}\hat{\mathbf{z}}, \\ \hat{\mathbf{n}}_3 &= n_{3x}\hat{\mathbf{x}} + n_{3y}\hat{\mathbf{y}} + n_{3z}\hat{\mathbf{z}},\end{aligned}\tag{E.1}$$

Table E.2: Probe outputs for the same dB/dt. The differences are due to construction tolerances and the fact that the three coils on each former are wound on top of each other.

Former	Blue (x)	Black (y)	Gray (z)
1	1.127	1.066	1.001
2	1.143	1.024	1.060
3	1.129	1.013	1.054
4	1.125	1.017	1.051
5	1.111	1.004	1.038
6	1.121	1.008	1.048
7	1.124	1.011	1.051
8	1.125	1.011	1.045
9	1.128	1.014	1.047
10	1.122	1.060	1.003
11	1.124	1.062	1.018
12	1.125	1.063	1.000
13	1.130	1.074	1.004
14	1.123	1.069	1.017
15	1.124	1.063	1.014
16	1.120	1.060	1.009

Table E.3: Measured probe outputs for the TFC field only.

Former	Blue (x)	Black (y)	Gray (z)
1	0.651	-7.492	1.625
2	1.640	-7.998	-0.245
3	-0.427	-8.412	-1.504
4	-1.098	-9.006	0.137
5	-0.421	-9.238	0.803
6	0.123	-8.889	2.161
7	1.489	-8.567	-0.307
8	-0.116	-8.001	-1.484
9	-1.269	-7.480	0.159
10	-1.106	-6.999	0.729
11	0.090	-6.785	1.325
12	1.101	-6.795	0.994
13	1.786	-6.848	-0.421
14	1.011	-7.216	-0.972
15	-0.555	-7.526	-1.709
16	-1.157	-8.026	1.293

Table E.4: Measured probe outputs for the OVC field only.

Former	Blue (x)	Black (y)	Gray (z)
1	0.321	0.146	0.333
2	0.477	0.101	0.128
3	0.197	0.041	-0.450
4	-0.379	-0.024	-0.318
5	-0.480	-0.053	0.119
6	-0.467	-0.043	0.185
7	-0.105	-0.105	0.471
8	0.201	-0.133	0.434
9	0.474	-0.097	0.124
10	0.481	-0.073	-0.100
11	0.336	-0.029	-0.374
12	0.281	0.056	-0.402
13	0.082	0.136	-0.468
14	-0.177	0.115	-0.454
15	-0.371	0.145	-0.307
16	-0.419	0.118	0.242

Table E.5: Measured probe outputs for the PFC field only.

Former	Blue (x)	Black (y)	Gray (z)
1	-7.997	-3.059	-4.565
2	-8.654	-3.332	3.816
3	5.981	-2.955	6.635
4	6.189	-1.942	-6.184
5	-4.857	-1.600	-7.156
6	-7.218	-1.694	-2.489
7	-3.338	-1.626	5.929
8	3.601	-1.911	5.926
9	7.285	-2.081	-2.919
10	1.032	-2.261	-8.187
11	-6.733	-2.153	-4.885
12	-9.008	-2.894	-1.710
13	-7.626	-4.064	6.878
14	1.794	-2.746	10.059
15	8.100	-3.087	5.333
16	5.499	-3.421	-8.376

Table E.6: Measured probe outputs for the HFC field only. Note the applied field is in the opposite direction for this particular coil set due to polarity limitations of the helical shunt.

Former	Blue (x)	Black (y)	Gray (z)
1	0.247	0.387	1.994
2	1.816	0.314	1.110
3	0.775	0.347	-2.057
4	-1.987	0.274	-0.636
5	-0.989	0.248	1.577
6	0.075	0.437	1.642
7	1.485	0.286	0.209
8	0.965	0.226	-1.015
9	-0.842	0.178	-1.271
10	-1.620	0.282	-0.154
11	-0.642	0.304	1.427
12	0.142	0.274	1.422
13	1.407	0.362	0.982
14	1.670	0.410	-0.995
15	-0.096	0.385	-1.587
16	-1.605	0.308	0.070

Table E.7: Orientation of the unit vectors for each coil on each former in Cartesian coordinates.

#	$\hat{\mathbf{n}}_1$			$\hat{\mathbf{n}}_2$			$\hat{\mathbf{n}}_3$		
	n_{1x} Bu-x	n_{1y} Bu-y	n_{1z} Bu-z	n_{2x} Ba-x	n_{2y} Ba-y	n_{2z} Ba-z	n_{3x} Gr-x	n_{3y} Gr-y	n_{3z} Gr-z
1	-0.380	-0.634	-0.674	-0.671	0.690	-0.271	0.637	0.349	-0.687
2	-0.090	-0.323	-0.942	-0.695	0.697	-0.173	0.713	0.640	-0.287
3	0.752	0.508	-0.421	-0.583	0.810	-0.063	0.309	0.293	0.905
4	0.647	0.218	0.730	-0.373	0.926	0.055	-0.664	-0.308	0.681
5	-0.159	-0.119	0.980	-0.179	0.980	0.090	-0.971	-0.161	-0.177
6	-0.295	-0.098	0.951	-0.134	0.989	0.061	-0.946	-0.109	-0.305
7	-0.957	0.073	0.281	0.119	0.981	0.152	-0.264	0.179	-0.948
8	-0.857	0.389	-0.339	0.342	0.920	0.192	0.386	0.049	-0.921
9	-0.170	0.271	-0.948	0.550	0.824	0.136	0.818	-0.497	-0.289
10	0.248	-0.054	-0.967	0.669	0.731	0.131	0.700	-0.680	0.217
11	0.477	-0.591	-0.650	0.805	0.591	0.054	0.352	-0.549	0.758
12	0.285	-0.766	-0.576	0.904	0.415	-0.104	0.319	-0.491	0.811
13	0.275	-0.950	-0.147	0.917	0.306	-0.257	0.289	-0.064	0.955
14	0.342	-0.869	0.358	0.937	0.285	-0.202	0.074	0.405	0.912
15	0.346	-0.618	0.706	0.938	0.226	-0.262	0.002	0.753	0.658
16	0.058	0.417	0.907	0.946	0.268	-0.184	-0.320	0.868	-0.379

and the field due to the wave is:

$$\begin{aligned}\delta\mathbf{B}(t) &= \mathbb{R}[\delta\tilde{\mathbf{B}} \exp(i\omega t)] \\ &= \delta\tilde{B}_{n1}\hat{\mathbf{n}}_1 + \delta\tilde{B}_{n2}\hat{\mathbf{n}}_2 + \delta\tilde{B}_{n3}\hat{\mathbf{n}}_3.\end{aligned}\quad (\text{E.2})$$

Here $\hat{\mathbf{n}}_1$, $\hat{\mathbf{n}}_2$, and $\hat{\mathbf{n}}_3$ are the unit vectors for each of the probes on a single former (see equation E.1 and figure E.2) and the experimental measurement provides the complex values $\delta\tilde{B}_{n1}, \delta\tilde{B}_{n2}, \delta\tilde{B}_{n3}$. We want to decompose this vector into components that are along field lines (parallel), perpendicular to field lines but in the surface of the plasma (perpendicular), and perpendicular to the surface (binormal) : $\hat{\mathbf{B}}_{||}, \hat{\mathbf{B}}_{\perp}$, and $\hat{\mathbf{B}}_{\perp,\perp}$ respectively. The components in each of these directions can be found by calculating the dot product with these unit vectors, i.e:

$$\begin{aligned}\delta\tilde{B}_{||} &= \delta\tilde{\mathbf{B}} \cdot \hat{\mathbf{B}}_{||}, \\ \delta\tilde{B}_{\perp} &= \delta\tilde{\mathbf{B}} \cdot \hat{\mathbf{B}}_{\perp}, \\ \delta\tilde{B}_{\perp,\perp} &= \delta\tilde{\mathbf{B}} \cdot \hat{\mathbf{B}}_{\perp,\perp}.\end{aligned}\quad (\text{E.3})$$

Before performing this dot product, the measurement vectors are transformed to Cartesian co-ordinates:

$$\begin{aligned}\delta\tilde{\mathbf{B}} &= \delta\tilde{B}_{n1}\hat{\mathbf{n}}_1 + \delta\tilde{B}_{n2}\hat{\mathbf{n}}_2 + \delta\tilde{B}_{n3}\hat{\mathbf{n}}_3, \\ \delta\tilde{B}_x &= \delta\tilde{B}_{n1}n_{1x} + \delta\tilde{B}_{n2}n_{2x} + \delta\tilde{B}_{n3}n_{3x}, \\ \delta\tilde{B}_y &= \delta\tilde{B}_{n1}n_{1y} + \delta\tilde{B}_{n2}n_{2y} + \delta\tilde{B}_{n3}n_{3y}, \\ \delta\tilde{B}_z &= \delta\tilde{B}_{n1}n_{1z} + \delta\tilde{B}_{n2}n_{2z} + \delta\tilde{B}_{n3}n_{3z}.\end{aligned}\quad (\text{E.4})$$

The parallel, perpendicular and binormal directions are found at the nearest point on the LCFS for each former. Using a VMEC equilibrium that has been transformed to Boozer coordinates, the parallel basis unit vector is calculated by moving a small distance along a field line that has been transformed to Cartesian co-ordinates. The field line must pass through the nearest point to the probe on the LCFS. The perpendicular unit basis vector is found using the closest point, evaluated in Cartesian co-ordinates, on a nearby field line on the same surface. The binormal is the cross product of the other two vectors.

E.4 Digital control of the amplifier settings

The gain and filter settings of all 48 amplifiers are controlled using ADG714 SPST CMOS switches that control the routing of the signal. The ADG714 switch states are determined by an internal shift register that is controlled through a SPI interface. Each preamplifier has two ADG714s with all of the ADG714s in the entire array daisy chained together (96 chips in total). This essentially makes one large shift register that controls all of the amplifier filter and gain settings. The amplifiers are plugged into backplanes allowing the ADG714s to be daisy chained together (see figure 9 in chapter 2 and figure E.5).

An Adapt9S12C32 Micro controller (MCU) manufactured by <http://www.technologicalarts.com/> is the master on the SPI bus. The MCU is connected to a host computer via an RS232 serial connection allowing the amplifier settings to be downloaded to the MCU (usually from the MDSplus database) before the MCU programs the switch chips. Documentation for this MCU is available from <http://support.technologicalarts.ca/docs/Adapt9S12C/>.

Each ADG714 is programmed with an 8 bit word. The meanings of each bit for the two switch chips on each board are shown in table E.8. Generally the amplifier settings are added to the model shot in the h1data tree using the following widget which is available in the python-h1 code repository:

```
$ cd /usr/local/prl/python/python-h1/h1/diagnostics/
$ python HMA_amplifier_settings
```

As part of the MDSplus initialisation sequence for each shot, these settings are read out of the tree, and transferred to the MCU over the RS232 interface. The MCU then sends the necessary signals down the SPI interface to program all the switch chips. During the MDSplus store sequence, the same settings are programmed into the amplifiers which, by the nature of shift registers, causes the values that were held in the shift registers during the shot to be recovered. This provides a check to ensure that the amplifier settings during the shot were correct.

The MCU is housed in a copper box (figure E.4) above the amplifiers. The SPI bus consists of a clock (SCK), synchronise (SYNC), master output slave input (MOSI), and master input slave output (MISO). These signals communicate with the amplifiers via feedthroughs which can be seen in figure E.4. The data is clocked into the shift registers on a falling SCK and out of the shift register on a rising SCK. When SYNC is low the SCK in and DIN buffers are enabled, taking SYNC high updates the switches. The pinouts that

Table E.8: Bit assignments for the two ADG714 switch chips on each amplifier board.

Switch Chip 1 Bits	Values	Decimal	Effect
0,1	10	1	Filter 1 off
0,1	01	2	Filter 1 on (2 pole 1.45MHz LP Bessel)
2,3	10	4	Filter 2 off
2,3	01	8	Filter 2 on (2 pole 1.66MHz LP Bessel)
4,5	10	16	Filter 3 off
4,5	01	32	Filter 3 on (2 pole 927Hz HP Bessel)
6,7	10	64	Filter 4 off
6,7	01	128	Filter 4 on (2 pole 380kHz LP Bessel)
Switch Chip 2 Bits	Values	Decimal	Effect
0	1	1	Not used
1	1	2	Not used
2	1	4	Anti alias on (4 pole 1MHz LP Bessel)
3	1	8	Anti alias off
4	1	16	Not used
5	1	32	Not used
6, 7	10	64	Gain 1 (125x)
6, 7	11	64+128	Gain 2 (350x)
6, 7	00	0+0	Gain 3 (625x)
6, 7	01	128	Gain 4 (1500x)

Table E.9: Pinouts and MCU program variable names for the SPI signals.

Signal	Pin	Name	Description
SCK	H1 pin 3	PTM[5] (0x20)	Serial clock
SYNC	H1 pin 6	PTT[7] (0x80)	SYNC - L read in data, H update switches
MOSI	H1 pin 2	PTM[4] (0x10)	Data from Micro to switch chips
MISO	H1 pin 1	PTM[2] (0x04)	Data from switch chips to Micro

are used for these signals are shown in table E.9.

E.4.1 Micro controller program

The source code for the micro controller program can be obtained from the following repository:

```
$ git clone https://github.com/shaunhaskey/hma_micro_program.git
```

The Codewarrior program, which is available in limited form without a license was used to program the micro controller.

Transferring the amplifier settings to the MCU and programming the amplifiers happens as part of the H-1NF shot initialisation sequence. The sh_amp.py script, which is part of the AnuDevices module (see appendix D for details on how to obtain this module)

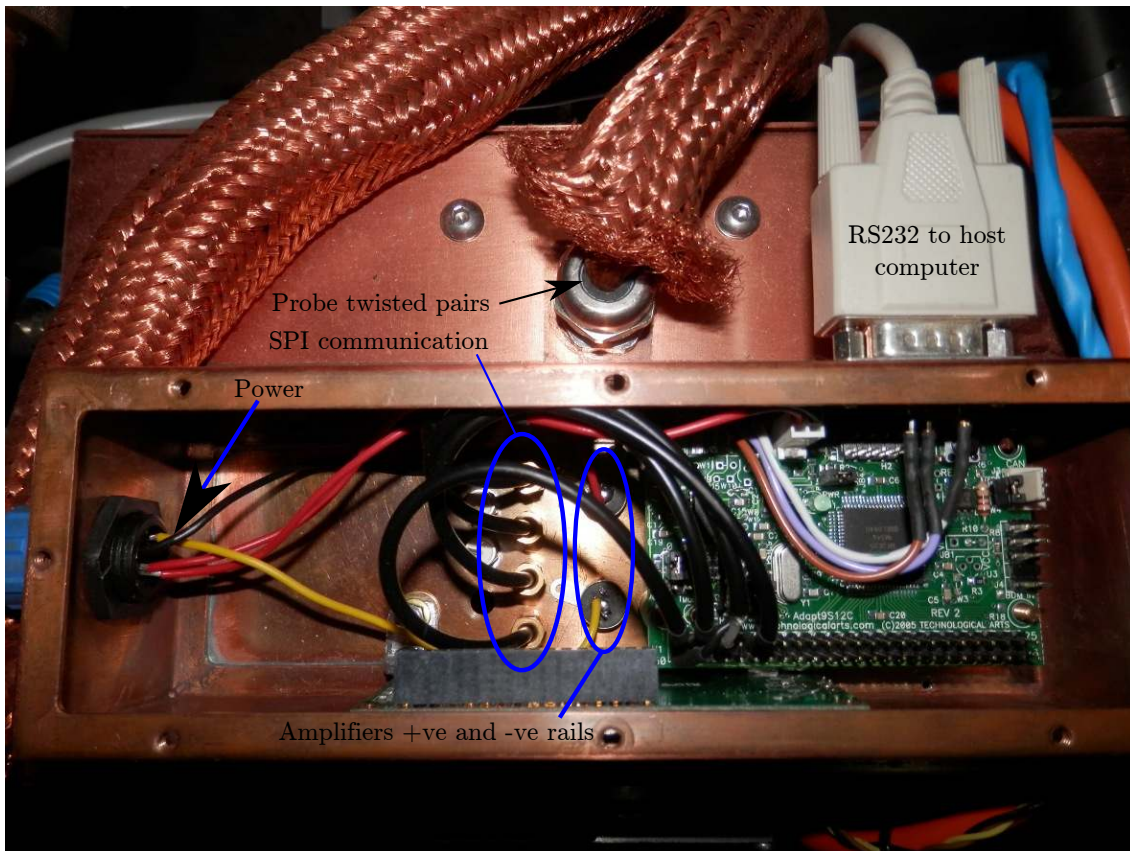


Figure E.4: The micro controller is housed in a separate copper box that is attached to the main amplifier enclosure. Details of the power cabling, RS232, and SPI interfaces are shown.

performs this task. The serial port is opened with a baud rate of 19200 and the settings are transferred as follows:

```

ser=serial.Serial(0, 19200, timeout = 1)
self.sendMicroCommand(ser, '7')
#'7' tells the micro that it is about to receive the input settings

#Then each of the settings for each switch chip are sent
for i in range(0,16):
    for j in range(0,6):
        data[i][j]
        ser.write(chr(data[i][j]))

#obtain the echoed values
self.waitForData(ser, 96)
returnedData=map(ord,ser.read(96))

#check validity of the returned values
if returnedData==data2:
    print ' ReturnedValuesCorrect::',

```

```
#Tell the micro controller to program the amplifiers
#'3' means go to transmit menu
self.sendMicroCommand(ser, '3')
#'6' means program all the amplifiers
self.sendMicroCommand(ser, '6')
```

E.4.2 Modifications to the backplane and MCU code

The SPI communication with the ADG714s was unreliable at first because the clock was not buffered and had difficulty driving all 96 ADG714 chips. To fix this, the SCK tracks on the two backplanes were cut half way along the backplanes (see figure E.5). A buffer board using 74AC245 chips generates four separate but simultaneous clocks, and two sync signals to drive each segment of the backplanes. The input connectors for driving two of the backplane segments are shown in figure E.6. Also shown are the data outputs (MISO) which connect the first backplane to the second, and the second back to the MCU. Additionally, the micro-controller was programmed to offset the clock and data edges to give the signals more time to settle as follows:

```
SCK high
wait 10us,
repeat for each bit:
    put data bit on MOSI,
    wait 10us,
    SCK low,
    wait 2us,
    read MISO,
    wait 10 us,
    SCK high ,
    wait 2us
```

A debugging card and a smaller version of the backplane were made to deal with issues with the digitally controlled switches and to check the performance of the amplifiers. These are shown in figure E.7. The debugging card has on board LEDs which display the state of the switches making it easy to check if the chips are being programmed correctly.

E.4.3 Additional information

The HMA signals are digitised using DTACQ ACQ-132 digitisers running at 2MHz. The node names for each of the coils are listed in table E.10. Two PT100 temperature sensors were also included in the HMA. Their breakout headers are shown in figure E.6.

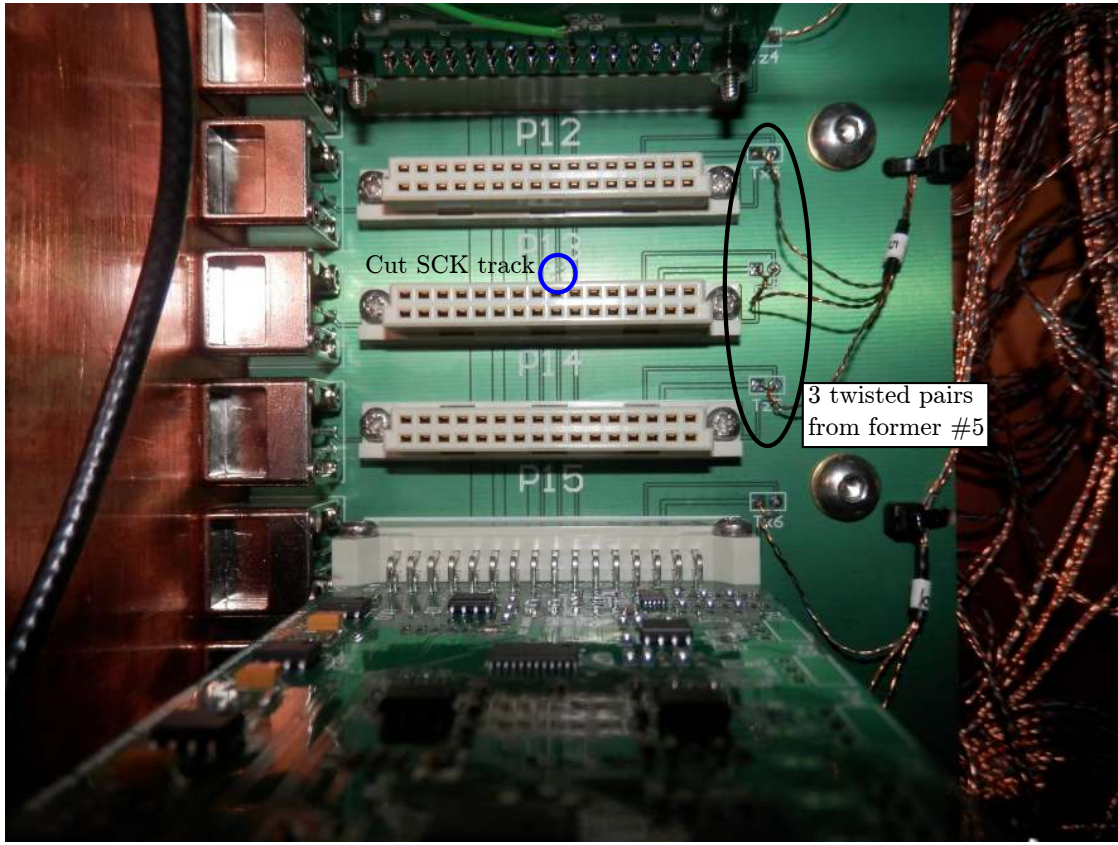


Figure E.5: The three twisted pairs from each magnetic probe former are terminated on the backplane. The cabling from each former are bundled together and labelled with the former number. The three separate twisted pairs can be separated by the colouring of one of the wires in the twisted pair, which will be blue, black or gray depending on the axis it belongs to. Also shown is the cut SCK track which splits each backplane into two separate sections with clocks that are driven independently. This significantly improved the reliability of the programming of the switches.



Figure E.6: Two PT100 temperature sensors were included in the array. The wiring for these are terminated onto two three pin headers on the backplane (left image). Right image: small breakout boards for supplying the clock, and outputting the MISO signal.

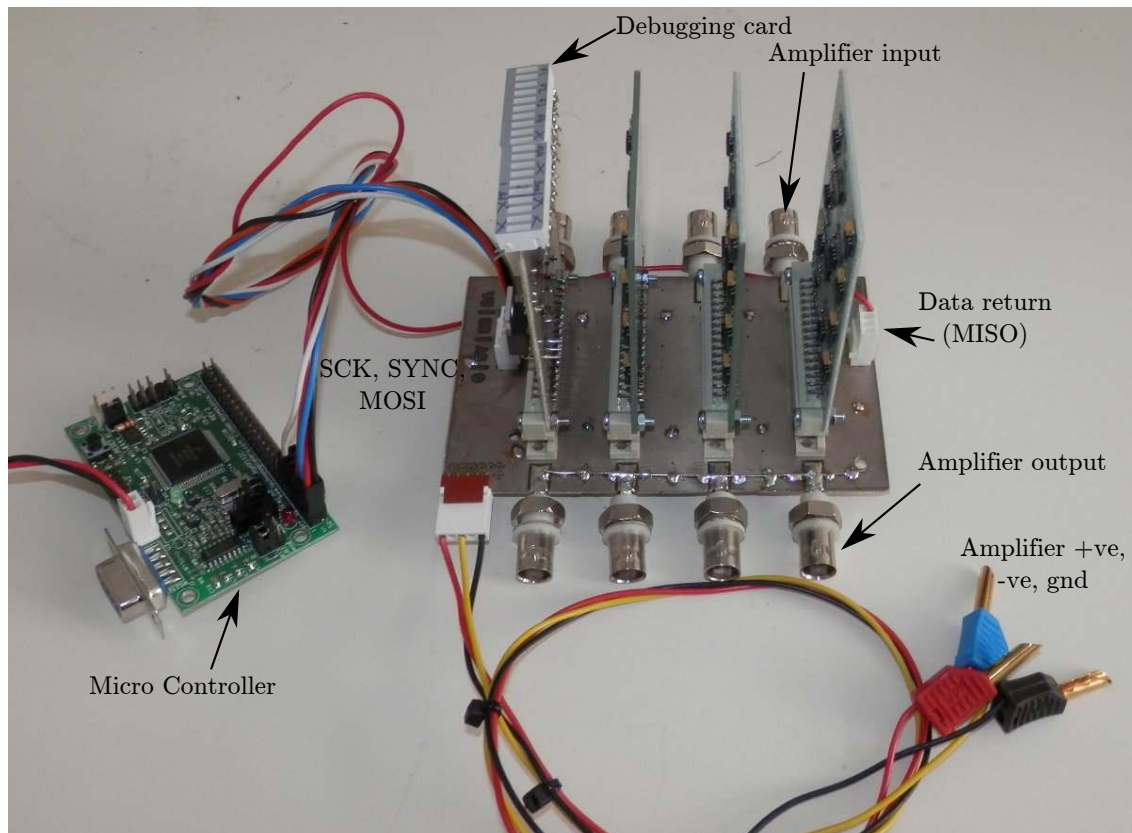


Figure E.7: To help with debugging, a small version of the backplane was made which allows the amplifiers and switch chips settings to be tested. Two separate debugging cards were made that have LEDs on them allowing the state of the switches to be determined.

Table E.10: Digitiser channels for each probe and axis. All locations are within the mirnov MDSplus tree which is at the top level in the h1data tree. These nodes are valid for shot #70000 onwards.

#	Blue (x) channel	Black (y) channel	Gray (z) channel
1	ACQ132_8:input_01	ACQ132_8:input_02	ACQ132_8:input_03
2	ACQ132_8:input_04	ACQ132_8:input_05	ACQ132_8:input_06
3	ACQ132_8:input_07	ACQ132_8:input_08	ACQ132_8:input_09
4	ACQ132_8:input_10	ACQ132_8:input_11	ACQ132_8:input_12
5	ACQ132_8:input_13	ACQ132_8:input_14	ACQ132_8:input_15
6	ACQ132_8:input_16	ACQ132_8:input_17	ACQ132_8:input_18
7	ACQ132_8:input_19	ACQ132_8:input_20	ACQ132_8:input_21
8	ACQ132_8:input_22	ACQ132_8:input_23	ACQ132_8:input_24
9	ACQ132_8:input_25	ACQ132_8:input_26	ACQ132_8:input_27
10	ACQ132_8:input_28	ACQ132_8:input_29	ACQ132_8:input_30
11	ACQ132_8:input_31	ACQ132_7:input_01	ACQ132_7:input_02
12	ACQ132_7:input_03	ACQ132_7:input_04	ACQ132_7:input_05
13	ACQ132_7:input_06	ACQ132_7:input_07	ACQ132_7:input_08
14	ACQ132_7:input_09	ACQ132_7:input_10	ACQ132_7:input_11
15	ACQ132_7:input_12	ACQ132_7:input_13	ACQ132_7:input_14
16	ACQ132_7:input_15	ACQ132_7:input_16	ACQ132_7:input_17

Supplementary details for the synchronous imaging and tomography chapters

This appendix provides detailed information about the synchronous imaging and tomographic inversion techniques, such as, how to run the tomographic inversion, important shot numbers, and details of the camera setup, field programmable gate array and phase locked loop. The information provided here supplements what was already shown in chapters 3 and 5.

Outline

F.1	Location of the camera	143
F.2	Shot numbers for the important modes	144
F.3	Details of the PLL and FPGA	146
F.3.1	Python control of the FPGA	146
F.4	Running the tomographic routines	151

F.1 Location of the camera

Measurements of the camera location and lens setup for the synchronous imaging described in chapters 3 and 5 are shown in figure F.1. The camera is setup at the Thompson scattering port on H-1NF, which is located at $\phi = 120^\circ$. The lens system consists of a C-mount $f = 17\text{mm}$ lens with an aperture of $f/0.95$, which is placed very close to the port window and 2 F-mount $f = 50\text{mm}$ lenses with apertures of $f/1.2$ and $f/1.4$. The first and second lenses act as a relay system. Figure F.2 (a) shows the location of the lenses as

well as a ray trace. Note the camera system is elevated by 5cm from the midplane.

The line of sight for each pixel is calculated by setting the CCD at a radius of 1973mm which is the radial location of the first lens, and then tracing rays from a pixel through the focal point of L1 (note the image inversion by the relay system must also be taken into account). The camera was mounted on a stage that can be tilted vertically about the first lens allowing three different viewing angles which were used for the tomographic reconstructions. These are labelled top, center and bottom in figure F.2 (b). The mount for the camera rotates vertically with the angle offsets limited to $\approx \pm 10^\circ$ due to the size of the port window.

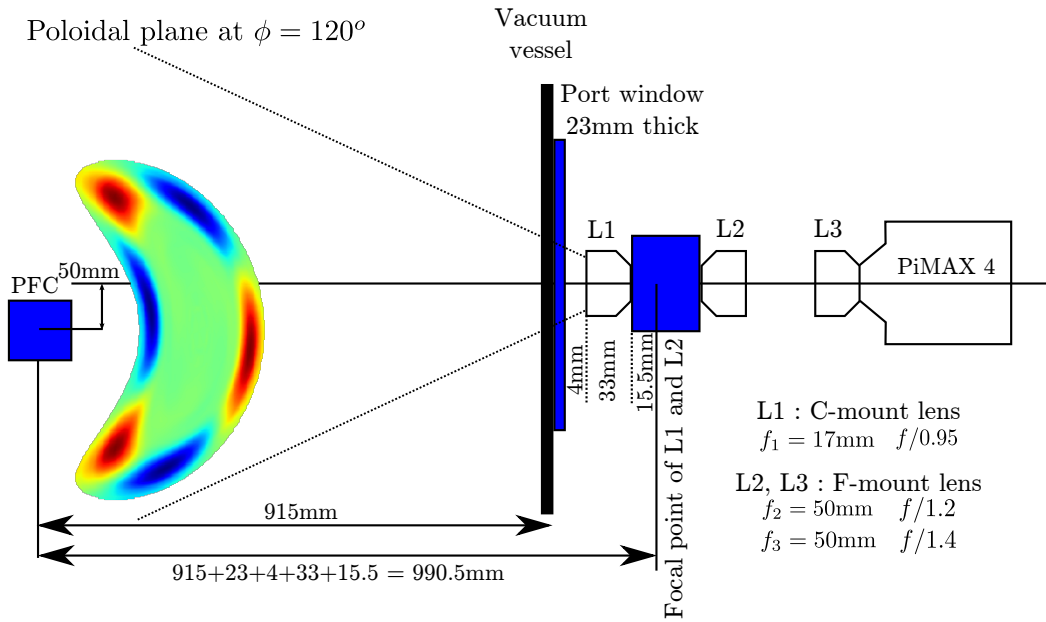


Figure F.1: Measured dimensions for the synchronous imaging camera setup. L1 and L2 act as a relay system, so the spacing between L2 and L3 is not important. The interference filter is usually attached to L3. The center of the PFC is at a radius of 1m from the center of H-1NF.

F.2 Shot numbers for the important modes

Details of the important shots are included in the h1 module and can be obtained as follows (see appendix D for details on how to obtain the h1 module):

```
import h1.diagnostics.imax as imax
dict_shots = imax.database_of_shots()

#Obtain shot numbers for the top view in 514nm light at kh=0.83
```

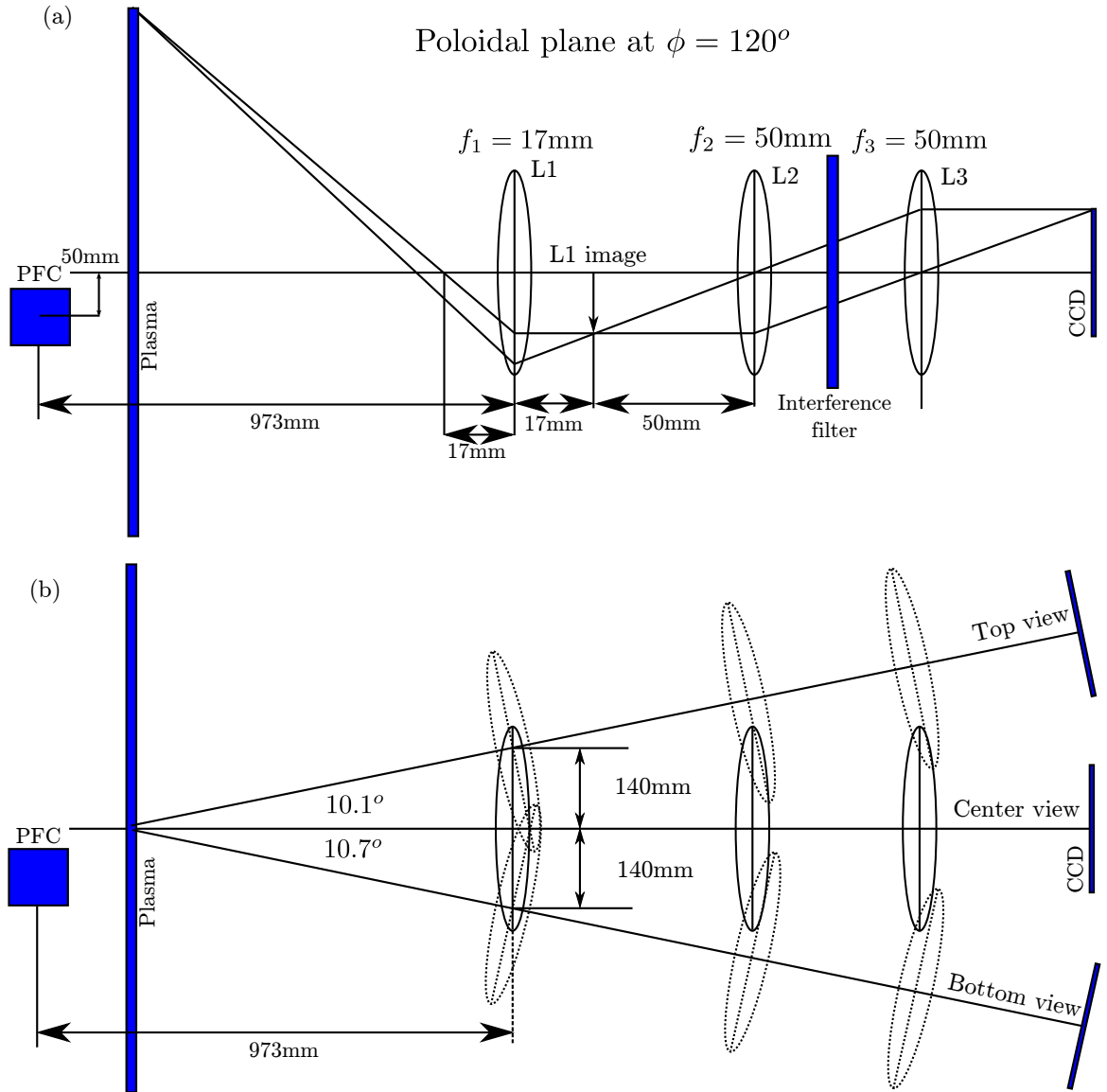


Figure F.2: (a) Location of the three lenses, camera and a ray trace. The plasma is located a significant distance from the first lens which is focused at infinity as are the other two lenses. L1 forms an image at its focal point, L2 forms an image at infinity, and L3 forms an image onto the CCD. The spacing between L2 and L3 does not affect the formation of an image on the CCD. The lines of sight for each pixel can be calculated by placing the CCD at L1 and tracing a ray from the relevant pixel through the focal point of L1 on the plasma side. (b) Details of the three different viewing angles. The camera and lens mount moves vertically at the location of the first lens (this is where the rotation is locked) and tilts the mount to point towards the center of the plasma as it moves up or down.

```

shots = dict_shots['514nm']['0.83']['top']['shot_list']

#various other useful information is available
info = dict_shots['514nm']['0.83']

```

```

info['top']['white_SPE']
# output : '/home/srh112/code/python/imax/imax_calibrations/white_514_1x.spe'

info['top']['dark_SPE']
# output : '/home/srh112/code/python/imax/imax_calibrations/dark_514_x1_400.spe'

info['top']['mdsplus_tree_path']
# output : 'h1data::/data/h1/recent;h1data::/data/h1/sorted/~f~e~d~c'

info['top']['mdsplus_tree']
# output : 'h1data'

info['top']['mdsplus_node']
# output : '.mirnov.pimax.pimax.images'

```

The shot numbers are also listed in tables F.1 and F.2.

F.3 Details of the PLL and FPGA

The synchronous imaging technique relies on a phase locked loop as described in chapter 3. Figure F.3 shows the detailed operation of the PLL and FPGA during a shot where multiple images are acquired. A circuit diagram of the PLL is shown in figure F.4. A field programmable gate array (FPGA) was used to divide the clock and select the appropriate phasing for the camera gating pulses as described in chapter 3. The Verilog source code and project files for Xilinx Design Suite 13.2 are available in the following git repository:

```
$ git clone https://github.com/shaunhaskey/PLL_dig_freq_range.git
```

The design was implemented on the Spartan 3E starter board from Digilent although a much simpler board could also be used. The FPGA was also used to stretch the camera gating signal allowing it to be captured on digitisers running at 2MHz. Details of the relevant pins which are defined in the constraints file are also listed in table F.3.

A host computer communicates with the FPGA over a RS232 interface allowing the sequence of phase offsets to be chosen, as well as the number of different phase offsets to implement for each shot. This also allows the FPGA to be armed and software triggered.

F.3.1 Python control of the FPGA

A Python script is used to communicate with the FPGA over the RS232 serial link. The Python script is included in the python-h1 module and can be run as follows:

Table F.1: Shot numbers for the different phasings for the synchronous imaging data.

κ_H	Light	View	Shots
0.28	514nm	top	80620, 80612, 80605, 80621, 80613, 80614, 80607, 80608, 80615, 80616, 80609, 80617, 80610, 80618, 80611, 80619
0.28	514nm	center	80637, 80622, 80630, 80623, 80631, 80624, 80632, 80625, 80633, 80626, 80634, 80627, 80635, 80628, 80636, 80629
0.28	514nm	bottom	80640, 80649, 80641, 80650, 80642, 80643, 80651, 80652, 80644, 80653, 80645, 80654, 80646, 80655, 80656, 80647
0.33	514nm	top	80028, 80036, 80029, 80037, 80030, 80038, 80031, 80039, 80032, 80040, 80033, 80041, 80034, 80042, 80035, 80043
0.33	514nm	center	79996, 80004, 79997, 80005, 79998, 80006, 79999, 80007, 80000, 80008, 80001, 80009, 80002, 80010, 80003, 80011
0.33	514nm	bottom	80012, 80020, 80013, 80021, 80014, 80022, 80015, 80023, 80016, 80024, 80017, 80025, 80018, 80026, 80019, 80027
0.37	514nm	top	80590, 80583, 80591, 80584, 80592, 80585, 80593, 80586, 80594, 80587, 80595, 80588, 80596, 80589, 80597, 80582
0.37	514nm	center	80574, 80567, 80575, 80568, 80576, 80569, 80577, 80570, 80578, 80571, 80579, 80572, 80580, 80573, 80581, 80566
0.37	514nm	bottom	80557, 80565, 80558, 80551, 80559, 80552, 80560, 80553, 80561, 80554, 80562, 80555, 80563, 80556, 80564, 80549
0.44	514nm	top	79887, 79888, 79880, 79889, 79881, 79890, 79882, 79891, 79883, 79892, 79884, 79893, 79885, 79894, 79886, 79895
0.44	514nm	center	79927, 79912, 79920, 79913, 79921, 79914, 79922, 79915, 79923, 79916, 79924, 79917, 79925, 79918, 79926, 79919
0.44	514nm	bottom	79911, 79896, 79904, 79897, 79905, 79898, 79906, 79899, 79907, 79900, 79908, 79901, 79909, 79902, 79910, 79903
0.56	514nm	top	80166, 80176, 80159, 80167, 80160, 80168, 80161, 80169, 80162, 80170, 80163, 80171, 80164, 80172, 80165, 80173
0.56	514nm	center	80150, 80158, 80143, 80151, 80144, 80152, 80145, 80153, 80146, 80154, 80147, 80155, 80148, 80156, 80149, 80157
0.56	514nm	bottom	80134, 80142, 80118, 80135, 80119, 80136, 80120, 80137, 80121, 80138, 80122, 80139, 80123, 80140, 80133, 80141

Table F.2: Shot numbers for the different phasings for the synchronous imaging data.

κ_H	Light	View	Shots
0.58	514nm	top	80490, 80475, 80483, 80476, 80484, 80477, 80485, 80478, 80486, 80479, 80487, 80480, 80488, 80481, 80489, 80482
0.58	514nm	center	80491, 80499, 80492, 80500, 80493, 80501, 80494, 80502, 80495, 80503, 80496, 80504, 80497, 80505, 80498, 80506
0.58	514nm	bottom	80522, 80507, 80515, 80508, 80516, 80509, 80517, 80510, 80518, 80511, 80523, 80512, 80520, 80513, 80521, 80514
0.63	514nm	top	80056, 80064, 80057, 80065, 80058, 80066, 80059, 80067, 80060, 80068, 80061, 80069, 80062, 80070, 80063, 80071
0.63	514nm	center	80072, 80080, 80073, 80081, 80074, 80082, 80075, 80083, 80076, 80084, 80077, 80085, 80078, 80086, 80079, 80087
0.63	514nm	bottom	80088, 80096, 80089, 80097, 80090, 80098, 80091, 80099, 80092, 80100, 80093, 80101, 80094, 80102, 80095, 80103
0.69	514nm	top	80461, 80454, 80462, 80455, 80463, 80456, 80464, 80457, 80465, 80458, 80466, 80459, 80467, 80452, 80460, 80453
0.69	514nm	center	80428, 80421, 80429, 80422, 80430, 80423, 80431, 80424, 80432, 80425, 80433, 80426, 80434, 80419, 80427, 80420
0.69	514nm	bottom	80444, 80437, 80445, 80438, 80446, 80439, 80447, 80440, 80448, 80441, 80449, 80442, 80450, 80435, 80443, 80436
0.83	514nm	top	79680, 79712, 79681, 79713, 79682, 79714, 79683, 79715, 79684, 79716, 79685, 79717, 79686, 79718, 79687, 79719
0.83	514nm	center	79677, 79704, 79678, 79705, 79671, 79706, 79672, 79707, 79673, 79708, 79674, 79709, 79675, 79710, 79676, 79711
0.83	514nm	bottom	79688, 79696, 79689, 79697, 79690, 79698, 79691, 79699, 79692, 79700, 79693, 79701, 79694, 79702, 79695, 79703

Table F.3: FPGA inputs and outputs

Name	Pin out	Description
FPGA inputs		
VCO_clock	B4	VCO clock from the PLL
change_phase_pin	D18	Manual change of phasing
trigger_pin	E8	Data system trigger to begin sequence
camera_monitor_in	B11	Camera readout monitor signal
FPGA outputs		
clock_out	A4	
PLL_out	F8	For the Camera gate input
PLL_out2	G9	For the digitisers
change_phase_out	A8	
camera_monitor_out	A11	Stretched version for digitising
PLL_cap 3	A6	Controls the frequency range of the PLL
PLL_cap 2	B6	Controls the frequency range of the PLL
PLL_cap 1	F7	Controls the frequency range of the PLL
PLL_cap 0	E7	Controls the frequency range of the PLL

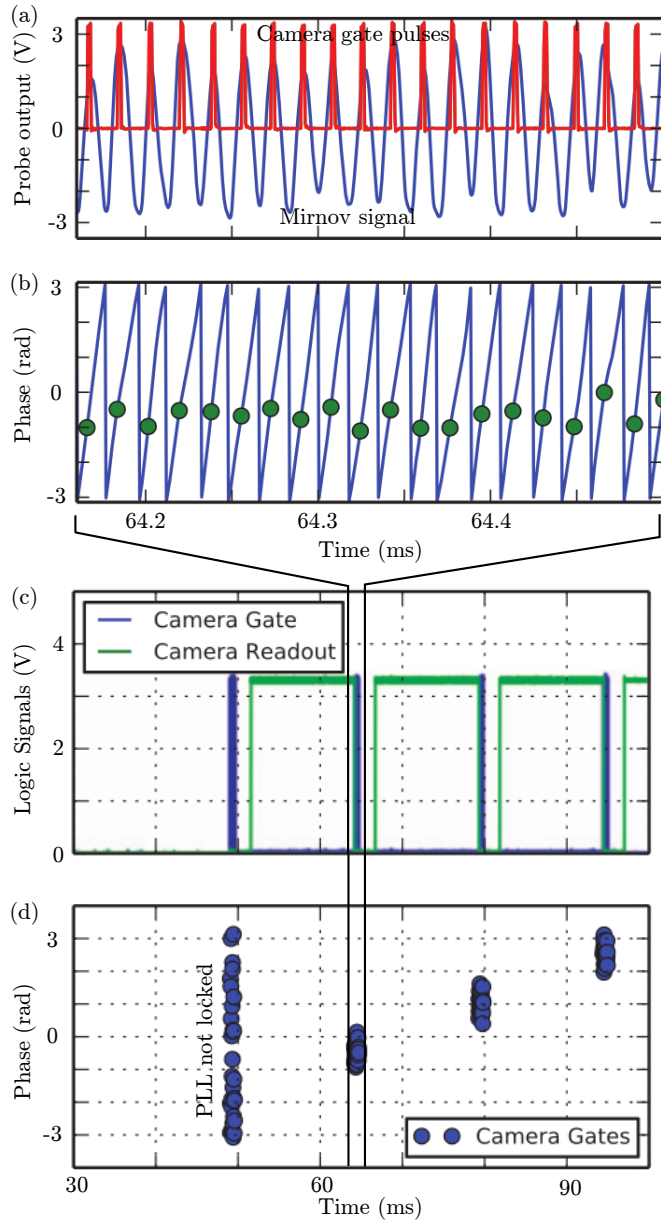


Figure F.3: Operation of the phase locked loop. (a) Camera gating pulses are generated by the FPGA based on the up shifted frequency generated by the phase locked loop using the shown Mirnov signal. (b) Argument of the Hilbert transform of the Mirnov signal shows the instantaneous phase of the reference signal. The times that the gating pulses are generated are marked, showing that the PLL is well locked to the Mirnov signal. (c) Behaviour of the PLL when acquiring multiple images during a shot. Gating pulses are generated at a particular phasing, then the camera phosphor is allowed to decay for 3ms before reading out the CCD. Once the readout is complete a different phase in the wave is acquired. (d) The phase of each camera gating signal showing that different phasings are being acquired at different times. In this case the PLL is not correctly locked for the first image due to insufficient signal.

```
$ cd /usr/local/prl/python/python-h1/h1/iagnostics/
$ python fpga_talk_w_gui.py
```

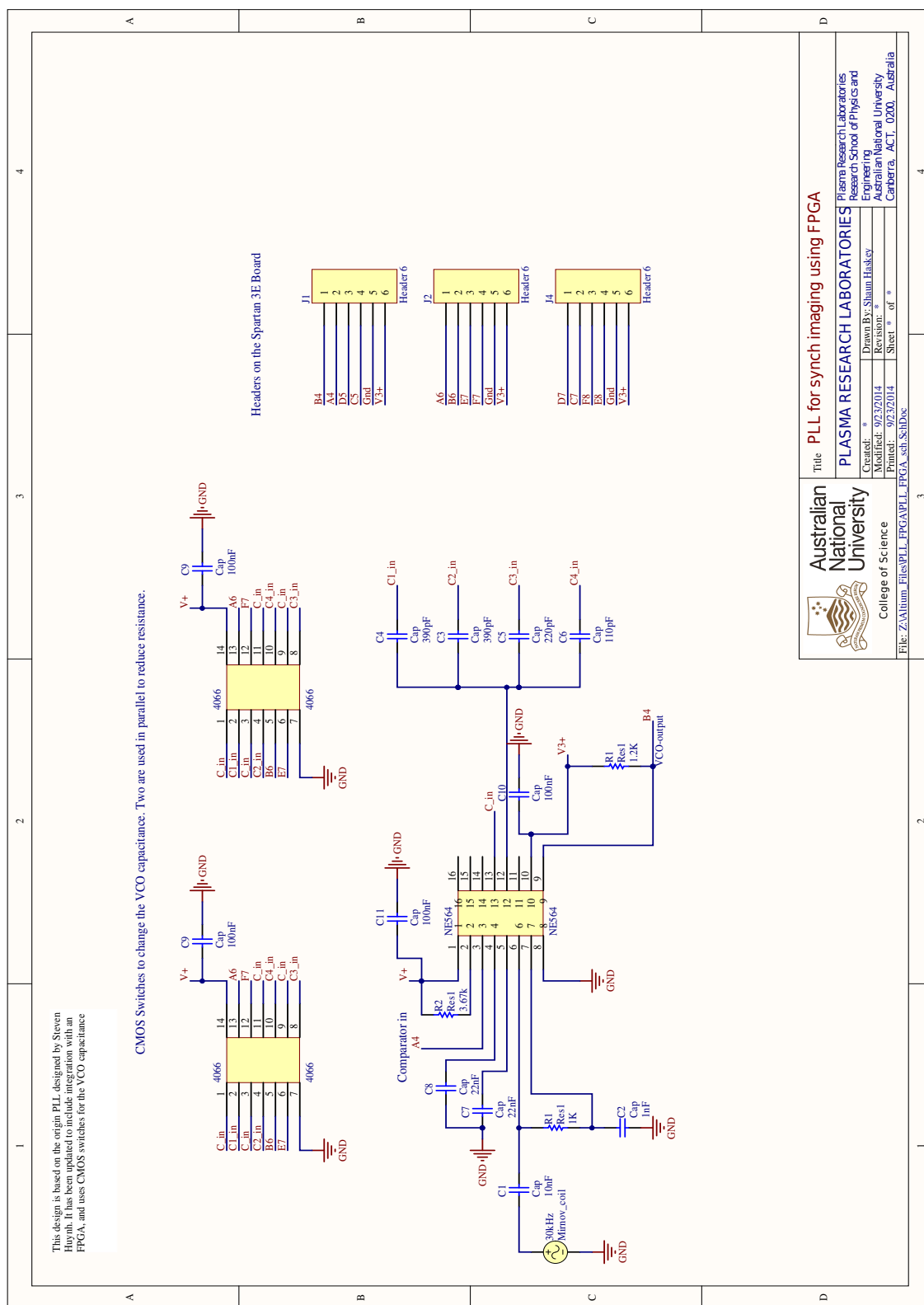


Figure F.4: Circuit diagram for the phase locked loop. Headers J1, J2, and J4 correspond to the PMOD connectors on the Spartan 3E development board. The net names (i.e A4, B4, etc...) also correspond to the relevant FPGA pins.

This allows the phase setting to be changed along with the frequency lock range. This script also integrates with the shot looper and the MDSplus data system. It leaves semaphores for an add-in for the Lightfield software which takes care of auto re-arming the camera, and making sure the shot number is correct. Lightfield is the software which controls the PiMAX cameras. During the store cycle of each shot it writes the SPE data to the tree based on the information about the node provided by the looper.

F.4 Running the tomographic routines

The tomographic inversion routines that were developed for this research are included in the h1 module. Refer to the documentation with the code for details on how to use it. Below is a simple example:

```

import h1.diagnostics.imax as imax
import h1.tomography.tomography as tomo
import h1.tomography.LOS_diagnostics as LOS_diag

#Obtain the experimental data
#Refer to function documentation for details of the arguments
tmp = imax.extract_data(light_type, kh, orientations, shot_database,
                       decimate_pixel, cal_sum = False,
                       norm_orient_relative = True, clip = clip)
fourier_data, n_pixels_y, n_pixels_x, camera_data_list = tmp

#The phasing information for each image can be checked
for i in camera_data_list: i.get_phase_std(plot=True, ax = ax)

#Get the camera geometry
#Refer to function documentation for details of the arguments
answer = LOS_diag.LOS_geometry(kh, use_pickled_data, light_type,
                                orientations, shot_database, phi_range, n_phi,
                                decimate_pixel, measurements, n_pixels_x,
                                n_pixels_y, min_valid_pixel, max_valid_pixel,
                                fourier_data, cut_values,
                                TFC_intersection = TFC_intersection,
                                save_patch_grid = save_patch_grid,
                                boozer_filename = boozer_filename)

#Perform the transformation to Boozer coordinates
#for the points on each LOS
answer.create_interpolation_points(n_interp_pts)
answer.perform_interpolation(no_theta = 180, s_increment = 2,
                             sin_cos_theta=False)

#Details of the LOS can be plotted

```

Supplementary details for the datamining chapter

This appendix provides extra information about the datamining algorithms that was not already shown in chapter 4. It includes information for obtaining and using the algorithms as well as some initial analysis of the covariance between the phase difference measurements. Further development of this analysis is the subject of future work.

Outline

G.1	Using the feature extraction and clustering algorithms	153
G.2	Covariance between phase difference measurements	156
G.2.1	Covariance properties	156
G.2.2	Modeling the phase differences between probes	156
G.2.3	Purely electrical noise	157
G.2.4	Noisy mode number	158
G.2.5	Plasma position changes, and κ_h variations	158

G.1 Using the feature extraction and clustering algorithms

All of the clustering and feature extraction algorithms are contained in my fork of David Pretty’s pyfusion Python module, which can be obtained as follows:

```
$ git clone git@github.com:shaunhaskey/pyfusion.git  
$ git checkout SH_branch
```

Make sure the path to pyfusion is included in the PYTHONPATH environment variable so that it can be imported.

The feature extraction algorithms can be run over sequences of shots that are defined in `pyfusion.H1_scan_list`. The following is an example of how to run the SVD and STFT feature extraction algorithms:

```
import pyfusion.clustering as clust
import pyfusion.clustering.extract_features_scans as ext

#This dataset must be defined in pyfusion.H1_scan_list
#The array name must be defined in the pyfusion.cfg file
dataset = ['June16_2014_21inter']; array = ['H1ToroidalAxial']

#List of other arrays whose data at the right frequency will be recorded
#as meta data
other_arrays = ['H1ToroidalNakedCoil']

#Labels for the additional data in the dictionary, note that the
#None item in the list means don't get the DC data, if it had a
#name, the DC data would be recorded in addition to the data at
#the fluctuation frequency
other_array_labels = [[None, 'naked_coil']]

#List of meta data to get – pyfusion must know how to get these
#if you want to add additional items
meta_data = ['kh', 'heating_freq', 'main_current', 'sec_current', 'shot']

#Settings for the SVD extraction routine
ext_settings_svd = {'min_svs': 2, 'power_cutoff': 0.006,
                     'lower_freq': 4000, 'upper_freq': 200000}

#Perform the SVD based extraction using 8 CPUs to speed up the process
svd_data = ext.multi_extract(dataset, array,
                             other_arrays=other_arrays,
                             other_array_labels=other_array_labels,
                             meta_data=meta_data, n_cpus=8, NFFT=1024,
                             overlap=4, extraction_settings=ext_settings_svd,
                             method='svd')

#Settings for the datamining filter part of the STFT extraction
datamining_settings = {'n_clusters': 16, 'n_iterations': 20,
                       'start': 'k_means', 'verbose': 0, 'method': 'EM_VMM'}

#Settings for the STFT based extraction
extraction_settings = {'n_pts': 5, 'lower_freq': 1500, 'filter_cutoff': 0.18,
                       'cutoff_by': 'sigma_bar',
                       'datamining_settings': datamining_settings,
                       'upper_freq': 100000}

#Perform the STFT based extraction using 8 CPUs to speed up the process
stft_data = ext.multi_extract(dataset, array, other_arrays=other_arrays,
```

```

        other_array_labels = other_array_labels,
        meta_data = meta_data, n_cpus=8, NFFT = 1024,
        overlap = 4, extraction_settings = extraction_settings,
        method = 'stft')

#Combine the SVD and STFT datasets removing duplicates
comb_data = ext.combine_feature_sets(svd_data, stft_data)

#The data can now be saved for later
svd_data.dump_data("svd_{0}_{1}.pickle".format(dataset[0],array[0]))
stft_data.dump_data("stft_{0}_{1}.pickle".format(dataset[0],array[0]))
comb_data.dump_data("comb_{0}_{1}.pickle".format(dataset[0],array[0]))

```

The instance phase differences and meta data such as electron density can be accessed as follows:

```

svd_data.instance_array
svd_data.misc_data_dict['ne']

```

Saved data can be loaded as follows:

```

import pyfusion.clustering as clust
feat_obj = clust.feature_object(filename="June15_LL.pickle")

```

Clustering is performed as follows:

```

#The data can be clustered as follows
svd_cluster = svd_data.cluster(method="EM_VMM", start='k_means',
                                n_clusters = 16, n_iterations=50,
                                number_of_starts = 4, n_cpus = 4)

```

Each time the clustering is run, the cluster object is appended to the `svd_data.clustered_objects` list. If the data is saved again, all of the items in `svd_data.clustered_objects` are also saved for future reference.

Accessing one of the clustered objects and finding out details about it:

```

clust_obj = svd_data.clustered_objects[0]
clust_obj.cluster_assignments
clust_obj.cluster_details

```

There are also many plotting methods attached to the cluster object allowing the clusters to be visualised better. The relevant figure number in chapter 4 is also listed where appropriate.

```

svd_cluster.plot_phase_vs_phase() #Fig 13, 14 in CPC paper
svd_cluster.plot_clusters_phase_lines()
svd_cluster.plot_clusters_polarisations()
svd_cluster.plot_clusters_amp_lines()
svd_cluster.plot_clusters_re_im_lines()
svd_cluster.plot_single_kh() #Fig 15 in CPC paper
svd_cluster.plot_cumulative_phases()
svd_cluster.plot_kh_freq_all_clusters()
svd_cluster.mode_num_analysis()
svd_cluster.plot_VM_distributions() #Fig 10 and 11 in CPC paper
svd_cluster.plot_dimension_histograms()

```

See the function definitions for more details about these plotting functions.

G.2 Covariance between phase difference measurements

For some of the clustering algorithms such as EM using von Mises distributions (described in chapter 4) assume that the phase differences between measurements in a magnetic probe array are independent of one another. The consequences of this are briefly discussed in section 4.1 of chapter 4. This issue should be investigated further. As a starting point, this section describes the effects of various types of noise on the covariances.

G.2.1 Covariance properties

The following are direct consequences of the covariance formula where x , y , w , and v are random variables and a , b , c , and d are constants:

$$\sigma(ax + by, cw + dv) = ac \sigma(x, w) + ad \sigma(x, v) + bc \sigma(y, w) + bd \sigma(y, v) , \quad (\text{G.1})$$

$$\sigma(x, y) = \sigma(y, x) , \quad (\text{G.2})$$

$$\sigma(a + x, b + y) = \sigma(x, y) , \quad (\text{G.3})$$

$$\sigma(ax, by) = ab \sigma(x, y) . \quad (\text{G.4})$$

G.2.2 Modeling the phase differences between probes

The phase at a coil (i) due to a mode with toroidal mode number n is given as follows (ignoring the poloidal mode number for simplicity), where φ_i is the toroidal location of the probe, and E_i is noise in the phase measurement which may be due to electrical noise or phase fluctuations:

$$\phi_i = n\varphi_i + E_i + \omega t . \quad (\text{G.5})$$

The quantity that is used in the clustering is the phase differences between coils:

$$\phi_i - \phi_{i-1} = n(\varphi_i - \varphi_{i-1}) + E_i - E_{i-1}, \quad (\text{G.6})$$

which gives the following covariance between two phase differences:

$$\sigma(\phi_i - \phi_{i-1}, \phi_j - \phi_{j-1}) = \sigma[n(\varphi_i - \varphi_{i-1}) + E_i - E_{i-1}, n(\varphi_j - \varphi_{j-1}) + E_j - E_{j-1}] \quad (\text{G.7})$$

G.2.3 Purely electrical noise

If the only variation in the signals is due to phase noise (which may be due to electrical noise or phase fluctuations local to each channel) then $n(\varphi_i - \varphi_{i-1})$ is a constant. Assuming random Gaussian phase noise, we can simplify the covariance as follows using the covariance properties:

$$\sigma(\phi_i - \phi_{i-1}, \phi_j - \phi_{j-1}) = \sigma(E_i - E_{i-1}, E_j - E_{j-1}) \quad (\text{G.8})$$

$$= \sigma(E_i, E_j) - \sigma(E_i, E_{j-1}) - \sigma(E_{i-1}, E_j) + \sigma(E_{i-1}, E_{j-1}) \quad (\text{G.9})$$

If we model the electrical noise as Gaussian noise with no correlation between channels then $\sigma(E_i, E_j) = 0$, where $i \neq j$, which allows us to simplify further. There are three interesting cases: the variance, the covariance between adjacent measurements, and the covariance for all other measurements.

Variance

For variance, $i = j$, therefore:

$$\sigma(\phi_i - \phi_{i-1}, \phi_i - \phi_{i-1}) = \sigma(E_i, E_i) + \sigma(E_{i-1}, E_{i-1}) \quad (\text{G.10})$$

Covariance between adjacent phase differences

For adjacent channels $j = i + 1$:

$$\begin{aligned} \sigma(\phi_i - \phi_{i-1}, \phi_{i+1} - \phi_i) &= \sigma(E_i - E_{i-1}, E_{i+1} - E_i), \\ &= \sigma(E_i, E_{i+1}) - \sigma(E_i, E_i) - \sigma(E_{i-1}, E_{i+1}) + \sigma(E_{i-1}, E_i), \\ &= -\sigma(E_i, E_i). \end{aligned} \quad (\text{G.11})$$

This is $-1/2$ the value of the variance for the case if $\sigma(E_i, E_i)$ is the same for all channels.

Covariance between non-adjacent phase differences

This covers all other possibilities:

$$\sigma(\phi_i - \phi_{i-1}, \phi_j - \phi_{j-1}) = \sigma(E_i - E_{i-1}, E_j - E_{j-1}) \quad (\text{G.12})$$

$$= \sigma(E_i, E_j) - \sigma(E_i, E_{j-1}) - \sigma(E_{i-1}, E_j) + \sigma(E_{i-1}, E_{j-1}) \quad (\text{G.13})$$

$$= 0 \quad (\text{G.14})$$

G.2.4 Noisy mode number

We can model a noisy mode number by setting n to a random variable. Although the mode number is fixed to integer values ideally, this ansatz is intended to approximate a situation in which the local propagation speed varies, for example due to density fluctuations. Everything else is set as constants:

$$\sigma(\phi_i - \phi_{i-1}, \phi_j - \phi_{j-1}) = \sigma[n(\varphi_i - \varphi_{i-1}), n(\varphi_j - \varphi_{j-1})] \quad (\text{G.15})$$

$$= (\varphi_i - \varphi_{i-1})(\varphi_j - \varphi_{j-1})\sigma(n, n) \quad (\text{G.16})$$

This is nonzero for all variances and covariances. If the probe spacing is approximately constant, then the value is the same for all covariances and variances.

G.2.5 Plasma position changes, and κ_h variations

As κ_h changes or the plasma moves, the location of the probes in magnetic coordinates changes. Therefore, we model φ_i as a random variable and set everything else to a constant:

$$\sigma(\phi_i - \phi_{i-1}, \phi_j - \phi_{j-1}) = \sigma(n\varphi_i - n\varphi_{i-1}, n\varphi_j - n\varphi_{j-1}) \quad (\text{G.17})$$

$$= n^2\sigma(\varphi_i, \varphi_j) - n^2\sigma(\varphi_i, \varphi_{j-1}) - n^2\sigma(\varphi_{i-1}, \varphi_j) + n^2\sigma(\varphi_{i-1}, \varphi_{j-1}) \quad (\text{G.18})$$

If the position changes of one probe are not correlated with another $\sigma(\varphi_{i-1}, \varphi_j) = 0$ for $i \neq j$ allowing us to simplify further.

Variance

For variance $i = j$:

$$\begin{aligned}\sigma(\phi_i - \phi_{i-1}, \phi_i - \phi_{i-1}) &= n^2\sigma(\varphi_i, \varphi_i) - n^2\sigma(\varphi_i, \varphi_{i-1}) - n^2\sigma(\varphi_{i-1}, \varphi_i) + n^2\sigma(\varphi_{i-1}, \varphi_{i-1}) \\ &\quad (G.19)\end{aligned}$$

$$= n^2[\sigma(\varphi_i, \varphi_i) + \sigma(\varphi_{i-1}, \varphi_{i-1})] \quad (G.20)$$

Covariance between adjacent phase differences

For adjacent channels $j = i + 1$:

$$\sigma(\phi_i - \phi_{i-1}, \phi_{i+1} - \phi_i) = \sigma(n\varphi_i - n\varphi_{i-1}, n\varphi_{i+1} - n\varphi_i) \quad (G.21)$$

$$\begin{aligned}&= n^2\sigma(\varphi_i, \varphi_{i+1}) - n^2\sigma(\varphi_i, \varphi_i) - n^2\sigma(\varphi_{i-1}, \varphi_{i+1}) + n^2\sigma(\varphi_{i-1}, \varphi_i) \\ &\quad (G.22)\end{aligned}$$

$$= -n^2\sigma(\varphi_i, \varphi_i) \quad (G.23)$$

This is $-1/2$ the value of the variance for the case where $\sigma(\varphi_i, \varphi_i)$ is the same for all channels.

Covariance between non-adjacent phase differences

This covers all other possibilities:

$$\sigma(\phi_i - \phi_{i-1}, \phi_j - \phi_{j-1}) = \sigma(n\varphi_i - n\varphi_{i-1}, n\varphi_j - n\varphi_{j-1}) \quad (G.24)$$

$$\begin{aligned}&= n^2\sigma(\varphi_i, \varphi_j) - n^2\sigma(\varphi_i, \varphi_{j-1}) - n^2\sigma(\varphi_{i-1}, \varphi_j) + n^2\sigma(\varphi_{i-1}, \varphi_{j-1}) \\ &\quad (G.25)\end{aligned}$$

$$= 0 \quad (G.26)$$

Supplementary details for the H-1NF mode analysis chapter

This appendix provides additional information for the experiment-theory comparison of modes on H-1NF, which was not included in chapter 6. Details of the post processing of CONTI and CAS3D data, as well as compilation instructions for several codes on the raijin supercomputer are included. This information is provided to help with future work. The post processing requires the h1 and pyfusion modules. Instructions for obtaining these is included in appendix D.

Outline

H.1	Plotting the spectra from CAS3D and CONTI	161
H.2	Running the polarisation and mode number analysis	162
H.3	Code compilation notes	163
H.3.1	CAS3D	163
H.3.2	LGRO	165
H.3.3	CAS3DK	165
H.3.4	VMEC	166
H.3.5	CONTI	166

H.1 Plotting the spectra from CAS3D and CONTI

To produce the continua plots such as those shown in chapter 6:

```
import h1.mhd_eq.cas3d as cas3d
directory = '/data/input.kh0.440-kv1.000fixed_dir/cas3d_r_n1_fixed/'

#Create the object with the data
```

```

continua = cas3d.cas3d_continua_data(path = directory, maxscan = 32,
                                       output_log='out_cas3d_r')

#This widget allows you to click the dots in the spectra, and the
#eigenmode structure is plotted in a subplot
continua_picker_widget(path = directory, maxscan = 32, output_log='out_cas3d_r')

#The publication ready image can be plotted as follows:
#Note that the pub_plot function would need to be modified to know where to look
#for the correct directories

inc_legend = [False, True]
ylims = [[0,500],[0,100]]
size_scale = [10, 20]
line_width = [0.3,0.5]
kh_list = [33,33]
file_name = ''.join(['{}-'.format(i) for i in kh_list]) + 'continua'
cas3d.pub_plot(size_scale = size_scale, kh_list = kh_list, fname = file_name,
                ylims = ylims, inc_legend = inc_legend, linewidths = line_width)

```

The following achieves the same outcome using the output from CONTI:

```

import h1.mhd_eq.conti as conti
kh_vals_list = [33, 44, 69, 83]
ylims = [[0,50],[0,50],[0,50],[0,50]]
alf_plot_props = {'markersize':1,'marker':'.', 'linestyle':'None',
                  'rasterized':True, 'zorder':100}
conti.pub_plot(kh_list = kh_vals_list, figname = fig_name, ylims = ylims,
               inc_sound = False, alf_plot_props = alf_plot_props)

```

H.2 Running the polarisation and mode number analysis

Several types of plots were made using the magnetic probes, such as the mode number and polarisation analysis. These rely on the output from a clustering run such as the ones described in appendix G. Details of the calculations are shown in appendix E. This demonstrates how to perform the polarisation calculations:

```

#Must have the output from a clustering run
import pyfusion.clustering.clustering as clust
cluster_data = clust.feature_object(filename = 'polarisation_tests2.pickle')

#Plot the polarisation of the clusters on a polar plot using
#all 16 probe locations, and the binormal direction as the reference phase
cluster_data.plot_clusters_polarisations(coil_numbers = range(0,16),
                                          decimate = 3, polar_plot = True, y_axis = None,
                                          reference_phase = 'b_perp_perp')

```

```
#In this case just look at the amplitude and vector sum the two perpendicular
#components
cluster_data.plot_clusters_polarisations(coil_numbers = range(0,16), decimate = 3,
                                           polar_plot = False, y_axis = None, add_perp = False)

#Make another plot to see what the polarisation is doing for a cluster
#as another parameter changes – in this case, polarisation vs frequency
cluster_data.plot_clusters_polarisations(coil_numbers = [2], decimate = 3,
                                           polar_plot = False, y_axis = 'freq', add_perp=False)
```

This demonstrates how to perform the mode number calculations.

```
cluster_data.mode_num_analysis(array = 'HMA')
HMA_dict = copy.deepcopy(cluster_data.cluster_mode_fits)
HMA_dict['m'] = cluster_data.arr.m_rec
HMA_dict['n'] = cluster_data.arr.n_rec

#if other_array is True then the data is obtained from
#self.feature_obj.misc_data_dict[other_array_name] instead of the
#main instance array. Make sure this data exists and is
#included using 'other_arrays' when extracting the data
cluster_data.mode_num_analysis(array = 'HMA', other_array = True,
                                other_array_name = 'H1ToroidalAxial')
cluster_data.mode_num_analysis(array = 'PMA1_reduced', other_array = True,
                                other_array_name = 'H1Poloidal1.Reduced1')
PMA_dict = copy.deepcopy(cluster_data.cluster_mode_fits)
PMA_dict['m'] = cluster_data.arr.m_rec
PMA_dict['n'] = cluster_data.arr.n_rec
```

H.3 Code compilation notes

Several codes which require substantial computational resources were used in this thesis. These codes were run on the raijin cluster at ANU. Compiling them is not trivial, and this section includes some notes to help with future issues compiling them.

H.3.1 CAS3D

Our copy of the CAS3D code has been modified with the help of Carolin Nührenberg to include calculations of the density, temperature, and pressure components of the eigenmode perturbation. Additionally, it outputs several extra files that contain more information on the eigenmodes that allow various things to be plotted more easily, and global eigenmodes to be identified more easily.

The `configure.in` file generally asks the user the relevant questions; however, the version of autoconf on raijin does not wait for answers to the questions, therefore, the answers have been hard wired in. Modify these in `configure.in` if they need to be changed.

```
DEBUG="no"
PARAL="yes"
CLEAN="clean"
symmetry_mode="stelsym"
normalization="wkin"
phasefactor="no"
modeparity="even"
v_in="all"
```

A raijin entry has also been added to `configure.in`:

```
raijin *)
COMPILER=INTEL
FC="ifort"
FC_MPI="mpif90"
FCFLAGS="-cpp -r8 -O3 -ip -I \$(OBJ_DIR) -module \$(OBJ_DIR)"
FCFLAGS_FIX=$FCFLAGS" -fixed"
FCFLAGS=$FCFLAGS" -free"
FPPFLAGS="-fpp"
FPPFLAGS_FIX=-fpp"
DPREF=
BITS=
LD=$FC
LDFLAGS=
PLPLOT_DIR=
PLPLOT=
LIB_DIR=
LIB="-lnag_mkl -lmkl_intel_lp64 -lmkl_intel_thread -lmkl_core -liomp5 \
-lpthread -lpplotf95d -lpplotf77d -lpplotd"
IRAM="no"
```

Run autoconf at the top of the cas3d directory. This creates the configure file based on `configure.in`. Next run `./configure` to create the makefiles and `os.mk`. Then everything should be ready for compilation:

Check that the `/cas3d_2007_10_12/source/src/os.mk` and the equivalent in the mc3d directory have the following library entries:

```
LIB      ==-lnag_mkl -lmkl_intel_lp64 -lmkl_intel_thread \
           -lmkl_core -liomp5 -lpthread -lpplotf95d \
           -lpplotf77d -lpplotd
PLPLOT   =
PLPLOT_DIR =
```

Make sure the following modules are loaded using module load
\$ module list

-
- | | |
|--------------------|---------------------------|
| 1) pbs | 3) intel-cc / 12.1.9.293 |
| 5) openmpi / 1.6.3 | 7) nag/f116i23dcl |
| 2) dot | 4) intel-fc / 12.1.9.293 |
| 6) plplot / 5.9.9 | 8) intel-mkl / 12.1.9.293 |

Clean and compile
\$ make clean
\$ make cas3d

H.3.2 LGRO

Below are the important details for compiling LGRO.

Important modules:

```
$ module load nag/fn16i04dcl fftw2/2.1.5 intel-cc intel-fc
```

LGRO is compiled as a serial code on raijin.
Make the following changes to the makefile:

```
ifeq ($(PARS),SERIAL)
CC=icpc
C_OPT = -c $(INCPATH) -D $(SYSTEM) -O2 -fomit-frame-pointer
LINK_OPT= -Wl,-rpath=$(LIBVERSION)
FC=ifort
F_OPT= -c $(FINCPATH) -I$(EIS_DIR) --dbl -O
LIBRARIES= -lrf fftw -lfft w -lnagfl90_nag \
           -lc -lstdc++ \
           -lif core -lcrypt
```

On raijin fouriercII.h needs to be edited because there isn't a symlink from rfft w.h to drfft w.h in the fftw2 include directory.
include <rfft w.h> -> <drfft w.h>

Clean and compile:
\$ make cleanall
\$ make lgro

H.3.3 CAS3DK

Below are the important details for compiling CAS3DK.

Load the following modules

```
$ module list
```

Currently Loaded Modulefiles:

- | | |
|--------------------------|---------------------------|
| 1) pbs | 3) dot |
| 5) intel-cc / 12.1.9.293 | 7) intel-mkl / 10.1.3.027 |
| 2) openmpi / 1.6.3 | 4) intel-fc / 12.1.9.293 |
| 6) nag/f116i23dcl | 8) plplot / 5.9.9 |

Make the following changes to the makefile

(note need to include the `-L /apps/nag/fnl6idcl/lib/`):

```
LIBRARIES= -L /apps/nag/fnl6i23dcl/lib/ -lnag_nag \
            -lmkl_intel_lp64 -lmkl_intel_thread -lmkl_core \
            -lmkl_em64t -lguide -lpthread \
            -lc -lmpi_f77 -lmpi_f90 -lifcore

PLOT_LIBS= -lplplotf77d -lplplotf77cd -lplplotd \
            -lpng -ljpeg -lfreetype \
            -lz -lX11 -lm
```

Clean and compile:

```
$ make clean
$ make wkin
```

H.3.4 VMEC

Below are the important details for compiling VMEC. Add the following entry to the setup script:

```
elif [[ $MACHINE_ID == raijin* ]]
then
    module load netcdf
    module load intel-fc
    module load intel-cc
    module load intel-mkl
    module load pgplot
    LOCALMAKE="gmake"
    COMPILE="ifort"
    LINK="ifort"
    FREEFORM="-free"
    FLAGS_D="-g"
    PREPROC="cpp -E -P -C "
    # -r8" IMPORTANT TO REMOVE -r8 this was causing problems
    FLAGS_R="-O3 -vec-report0"
    LIBNETCDF="-lncdff -lncdf"
    NETCDF_DIREC=$NETCDF
    NETCDF_LIB="-L$NETCDF_DIREC $LIBNETCDF"
    NETCDF_INC=$NETCDF/include
    COMPRESS="gzip"
    ZIP="zip"
    UNCOMPRESS="gunzip"
    UNZIP="unzip"
    LIB="-lmkl_intel_lp64 -lmkl_intel_thread -lmkl_core -liomp5 -lpthread"
```

H.3.5 CONTI

Below are the important details for compiling CONTI.

```
$ module load dot intel-cc/12.0.084 intel-fc/12.0.084 openmpi
$ module load intel-mkl/12.1.13.367 fftw2/2.1.5 nag/fnl6i04dcl
```

On Raijin fouriercII.h needs to be edited because there isn't a symlink from rfftw.h to drfftw.h in the fftw2 include directory.
include <rfftw.h> -> <drfftw.h>

Change the makefile so the following are the settings
for the Linux64 part:

```
LIBRARIES= $(EIS_DIR)/eislib.a -lrfftw -lfftw -lc -lstdc++ \  
-lnagfl90_mkl -lmkl_intel_lp64 -lmkl_intel_thread \  
-lmkl_core -liomp5 -lpthread -lifcore -lcrypt
```

```
LIBVERSION=
```

```
LIB_PATH =
```

```
FINC PATH =
```

```
INCPATH =
```

```
Clean and compile:
```

```
$ make cleanall
```

```
$ make conti
```

Attempts to actively drive modes in H-1NF

This appendix includes details of experiments to actively drive modes in H-1NF using an existing ICRH antenna and two pulsed broadband amplifiers that were designed and built specifically for this purpose. The data from these experiments was not included in the thesis as it has not been properly analysed. However, this work could easily form the basis of a new project.

Outline

I.1	Active excitation experiments	169
I.2	Details of the broadband power amplifier design	171

I.1 Active excitation experiments

The final set of experiments were performed from the 29th of August 2012 to the 4th September 2012, with the aim of actively exciting modes on H-1NF. Refer to the log files for these days for details of the experiments and shot numbers. Below are some examples of what was attempted:

- Shots 75281-75287 are examples of frequency ramps with the two antennas 180deg out of phase.
- Shots 75288-75291 are examples of frequency ramps with the two antennas in phase with each other
- Shots 75296-75330 are examples of fixed frequency excitation in the 35kHz - 500kHz range. The minimum frequency that is still detectable in the magnetic probes was found to be 40kHz. These shots include a continuous phasing sweep between the

lower and upper antennas. This was achieved by running for 30ms and offsetting the frequency in the two antennas by 33Hz.

For these shots, antenna 1 current, antenna 2 current, and drive from the signal generator were recorded in : `.mirnov.ACQ132_8:input_32`, `.mirnov.ACQ132_9:input_32`, and `.mirnov.ACQ132_7:input_32` respectively.

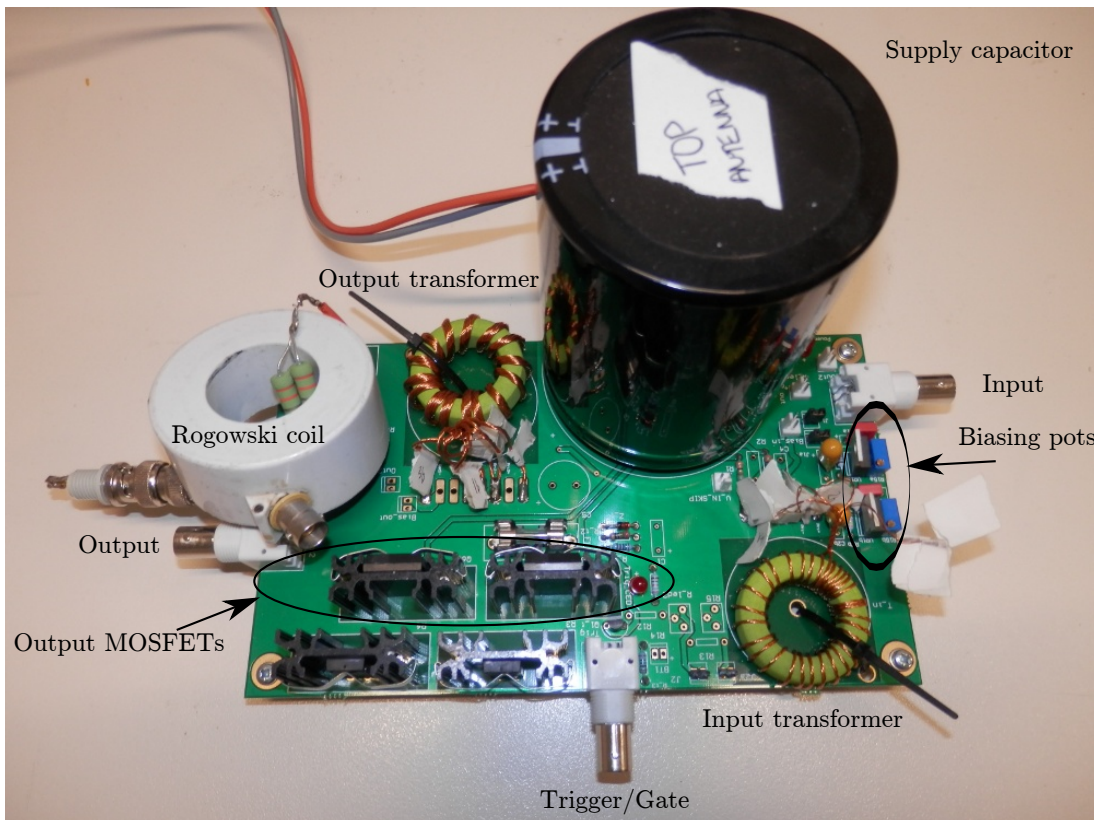


Figure I.1: Image of the top of a broadband amplifier with several important components labeled.

The initial results from these experiments showed that the magnetic probe output was strongly dependent on the phasing between the upper and lower antennas, and was substantially larger when a plasma is present. Additionally, across the HMA, the phasing showed a standing wave pattern indicating the interference of two counter propagating waves. No signal was detected by the density interferometer even when using sensitive synchronous detection methods. Ideas for future experiments include more targeted attempts at hitting high frequency gap modes and intelligent frequency sweeping to target frequencies where the launching antenna impedance has been identified to be markedly different due to the interaction with global modes.

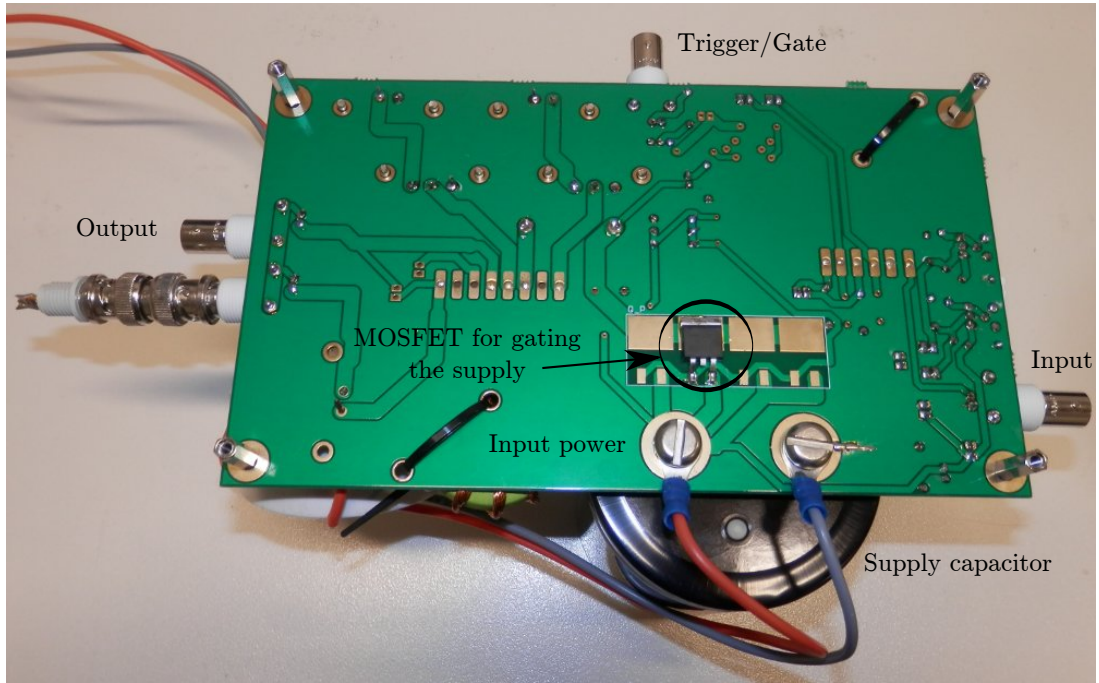


Figure I.2: Image of the bottom of a broadband amplifier with several important components labeled.

I.2 Details of the broadband power amplifier design

A schematic of the broadband power amplifiers that were designed and built for this project is shown in figure I.3. Images of the top and bottom of the amplifier are shown in figure I.1 and I.2. These amplifiers are only supposed to be on for brief periods of time, but can supply approximately 50A at frequencies between 30kHz and 1MHz. A fuse is included to protect the amplifier from being on for too long. A trigger/gate signal determines when power is supplied to the amplifier, and a large capacitor ensures that the high current output can be maintained throughout a shot. The trigger/gate signal should only be on for a minimal period of time to prevent the amplifier from destroying itself. Two methods of biasing the MOSFETs were included - a variable voltage using high voltage rated LM317 variable voltage regulators, and a 9V battery with a variable voltage divider.

All of the Altium design files including the PCB design are in the `Shaun_Haskey_Files` folder on the Electronics Unit projects network drive.

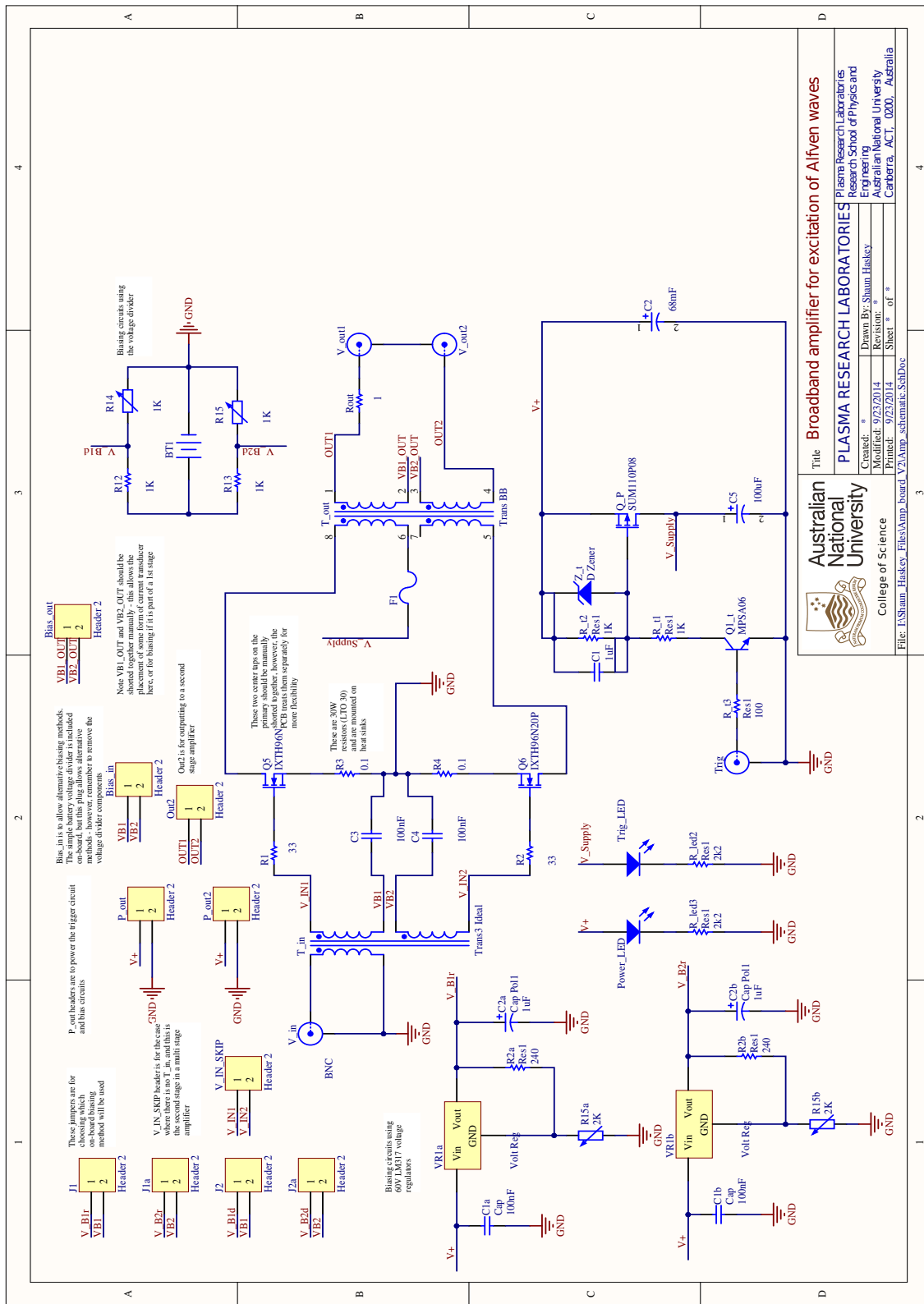


Figure I.3: Circuit diagram for the pulsed broadband excitation amplifiers.

Supplementary details for the MP chapters

This section provides details of how to use the pyMARS module to perform many MARS-F runs on the DIII-D clusters.

Outline

J.1	The pyMARS module	174
J.1.1	Setting up CHEASE, CORSICA and MARS-F	175
J.1.2	Setting up pyMARS	176
J.1.3	Running pyMARS	176
J.2	The pyMARS input file	177
J.2.1	Process control	177
J.2.2	Directory details	178
J.2.3	Execution scripts	179
J.2.4	Template names	179
J.2.5	Cluster details	180
J.2.6	RMZM	180
J.2.7	Scan filter details	181
J.2.8	RMP coil details	181
J.2.9	Pickup coil details	181
J.2.10	CORSICA settings	182
J.2.11	CHEASE settings	183
J.2.12	MARS settings	183
J.2.13	Cleaning up details	184
J.3	Examples	184

J.3.1	Single run through	184
J.3.2	Resistivity and rotation scan	185
J.3.3	β_N scan	185
J.3.4	Multiple EFITs	185

J.1 The pyMARS module

The pyMARS module was created to perform all of the steps required for a MARS-F simulation, starting with an EFIT equilibrium. This allows extensive MARS-F scans like those shown in chapters 7 and 8 to be run using a cluster to substantially speed up the process. There are four main modes that the scripts can currently be run in:

- Single EFIT equilibrium, no scaling.
- Single EFIT equilibrium, scale q_{95} and/or β_N .
- Single EFIT equilibrium, scale toroidal rotation and/or resistivity.
- Multiple EFIT equilibria, run a single MARS-F simulation for each equilibrium without scaling any of the values. This is for comparing the evolution of an experiment with MARS-F simulations at discrete times throughout the shot.

An example of each of these is given at the end of this appendix.

The scripts essentially take an EFIT equilibrium and use the Grad-Shafranov solver in CORSICA (stability calculations can be performed with DCON at this stage) to generate a set of artificial equilibria with scaled pressure and q-profiles. CHEASE and Fourier.x use these equilibria to generate the required input files for MARS-F. The pyMARS module also includes a great deal of post processing options that are essentially based on the RZplot Matlab routines that come with the MARS-F code.

The process consists of the following steps. All of the information about the simulations is output in a Python pickle file at the end of each step allowing the process to be stopped and resumed:

1. Copy the EFIT equilibrium files and run CORSICA to generate the artificial scaled equilibria
2. Generate the directory structure
3. Run CHEASE and Fourier.x to prepare the equilibria for MARS-F
4. Find the location of the I-coils on the CHEASE grid
5. Generate the MARS-F RUN files

6. Run MARS-F
7. Post processing part1 - simulated probe output calculations
8. Post processing part2 - pitch resonant and RFA metric calculations

pyMARS essentially follows the steps that are described in the MARS-F user guide by Matthew Lanctot.

J.1.1 Setting up CHEASE, CORSICA and MARS-F

Login to one of the DIII-D computers such as venus or benten. Copy `/u/haskeysr/bin/runchease` and `/u/haskeysr/bin/runmarsf` to your `~/bin` directory. These are wrappers that run the CHEASE and MARS-F executables on the DIII-D computers. Note that you will have to change the relevant settings in `[execution_scripts]` in the `input.cfg` file (described in section J.2 to point to these files).

Put the following aliases in your `~/.bashrc`:

```
alias 'caltrans'='d/caltrans/vcaltrans/bin/caltrans'
alias 'fourier.x'='u/reimerde/mars/MarsF20060714/FourierRF/FourierRF.x'
alias 'fxrun'='fourier.x < fxin'
```

pyMARS has not been tried in shells other than bash.

Create a `~/.caltrans` file that contains the following line (with username set appropriately), or copy and edit my version:

```
pathadd("u/username/caltrans")
```

Copy the CORSICA scripts in `/u/haskeysr/caltrans/` to `~/caltrans`:

```
$ cd /u/haskeysr/caltrans
$ cp *.bas ~/caltrans/
```

Make a template directory and copy across some relevant templates:

```
$ mkdir -p ~/mars/templates
$ cd /u/haskeysr/mars/templates
#Copy MARS and CHEASE templates
$ cp datain_template RUN_template ~/mars/templates/
#Copy CORSICA templates
$ cp sspqi_sh3 equal_spacing_pt1.bas equal_spacing_pt2.bas \
~/mars/templates/
```

Note you must correctly set `template_directory` in the `[directory_details]` section of the `input.cfg` file to point to your template directory.

J.1.2 Setting up pyMARS

Create a directory for pyMARS and make a git clone of it:

```
$ mkdir ~/code
$ cd ~/code
$ git clone https://github.com/shaunhaskey/pyMARS.git
```

Add the following to your `~/.bashrc`:

```
export PYTHONPATH="/u/username/code/pyMARS/python/pyMARS/:${PYTHONPATH}
export PYTHONPATH="/u/username/code/pyMARS/python/:${PYTHONPATH}
```

Make the following symbolic link and make it executable:

```
$ cd ~/bin
$ ln -sf /u/username/code/pyMARS/python/pyMARS/read_cfg.py run_pyMARS
$ chmod +x ~/bin/run_pyMARS
```

Log out and log back in to the DIII-D computers for the changes to take effect (or source `.bashrc`). Make sure you can start Python and import pyMARS without any errors. Note the capital P in Python is important as this points to an installation that is setup with numpy and scipy:

```
$ Python
>>> import pyMARS
```

J.1.3 Running pyMARS

The behaviour of pyMARS is completely controlled by an input file which is located in the same directory into which the simulation files will be written. The various sections of the input file are described in the next section. Copying one of the input files from the examples section is probably the simplest starting point, making sure to modify the `[directory_details]` and `[execution_scripts]` sections of the input file to point to your directories.

Login to the venus head node computer, which will allow you to submit jobs to the venus cluster. Make sure you are using a bash shell:

```
$ ssh -Y venus
$ cd ~/mars
$ mkdir test_run
$ cd test_run
$ cp /u/haskeysr/mars/shot158115_04780/input.cfg .
# edit [directory_details] and [execution_scripts] part of input.cfg
```

```
# In particular change project_name to test_run , and base_directory
# to /u/username/mars/
# Also set start_from_step to 1, and end_at_step to 9 to make sure it
# does all of the steps
# Run pyMARS
$ nohup unbuffer run-pyMARS input.cfg &> log &
# Watch what it is doing
$ tail -f log
```

Also monitor the following to see how busy the cluster is and what jobs you have running on it. Note at the moment CORSICA/CALTRANS runs on the head node and not on the cluster except for the q_{95} and β_N scans.

```
$ qhost # to see how busy the cluster is
$ qstat # to see how many jobs you have running
```

Be very careful to only run large pyMARS jobs when the cluster is not busy and experiments aren't being run. If you are running 40+ simultaneous jobs it can seriously slow the system down.

J.2 The pyMARS input file

J.2.1 Process control

This controls the general type of run you are going to do. Typical settings:

```
[process_control]
start_from_step = 1
end_at_step = 10
include_chease_PEST_run = 1
multiple_efits = 0
rotation_scan = 0
rotation_scan_start = -4
rotation_scan_end = -0.8
rotation_scan_number = 30
rotation_spacing = log
resistivity_scan = 0
resistivity_scan_start = -9
resistivity_scan_end = -6
resistivity_scan_number = 30
resistivity_spacing = log
```

Setting explanation:

- **start_from_step [1-8]** : Which step in the process to begin from. After each step pyMARS outputs a pickle file that contains all of the work that has been done so far, allowing the simulations to be restarted at a later time from the same step. See the step descriptions in the section J.1.

- `end_at_step [2-8 (or a number >8)]` : Which step to stop at.
- `include_chease_PEST_run [0,1]` : Include the CHEASE run in PEST coordinates.
Generally leave as 1, this allows co-ordinate transformations to be performed later on.
- `multiple_efits [0,1]` : Whether there are multiple EFIT equilibria to use - this is meant to simplify a comparison between MARS-F and experiment at many times throughout the shot.
- `rotation_scan [0,1]` : Whether to perform a toroidal rotation scan or not.
- `rotation_scan_start = -4` : Start value for the scan.
- `rotation_scan_end = -0.8` : End value for the scan.
- `rotation_scan_number = 30` : Number of simulations to run.
- `rotation_spacing = log ['log', 'linear']` : Type of spacing.
This is how the spacing occurs for log spacing - $10^{**(\text{linspace}(\text{start}, \text{end}, \text{num}, \text{endpoint=True}))}$ and for linear spacing - $\text{linspace}(\text{start}, \text{end}, \text{num}, \text{endpoint=True})$.
- `resistivity_scan = 0` : Whether to perform a resistivity scan or not
- `resistivity_scan_start = -9` : Start value for the scan
- `resistivity_scan_end = -6` : End value for the scan
- `resistivity_scan_number = 30` : Number of simulations to run
- `resistivity_spacing = log ['log', 'linear']` : Type of spacing. Spacing behaviour is the same as for rotation.

Note that you can only choose `multiple_efits`, `rotation_scan` and/or `resistivity_scan`, or the pressure and q95 scans which are implemented in the CORSICA settings section. Selecting more than one of these options will lead to strange results.

J.2.2 Directory details

Typical settings:

```
[directory_details]
project_name = shot158115_04780_scan_ideal
base_directory = /u/haskeysr/mars/
efit_file_location = /u/haskeysr/efit/shot158115_04780/
profile_file_location = /u/haskeysr/efit/shot158115_04780/
template_directory = /u/haskeysr/mars/templates/
post_proc_script=
```

```
/u/haskeysr/code/NAMP_analysis/python/pyMARS/post_proc_script.py
post_proc_script_PEST=
/u/haskeysr/code/NAMP_analysis/python/pyMARS/post_proc_script_PEST.py
```

Setting explanation:

- `project_name [string]` : Name of the project within `base_directory`. This is where the `.cfg` file should live.
- `base_directory [string]` : Base directory where the projects are stored.
- `efit_file_location [string]` : Location directory of the EFIT input files.
- `profile_file_location [string]` : Location directory of the profile input files.
- `template_directory [string]` : Location of the input templates for the various codes.
- `post_proc_script [string]` : Location of the script that is used in post processing step 7.
- `post_proc_script_PEST [string]` : Location of the script that is used in post processing step 8.

J.2.3 Execution scripts

This lists where to find the CHEASE and MARS-F executable wrappers. Should point to the files in your bin dir.

```
[execution_scripts]
MARS_execution_script = /u/haskeysr/bin/runmarsf
CHEASE_execution_script = /u/haskeysr/bin/runchease
```

J.2.4 Template names

Typical settings:

```
[template_names]
CORSICA_template_name = sspqi_sh3.bas
CORSICA_template_name2 = equal_spacing_pt2.bas
CHEASE_template_name = datain_template
MARS_template_name = RUN_template
```

Setting explanation:

- `CORSICA_template_name [sspqi_sh3,equal_spacing_pt1.bas]` : The CORSICA input template (`sspqi_sh3.bas`). If a β_N or q_{95} scan is being performed, this is a two stage process to find the β_N limit. In this case set this to `equal_spacing_pt1.bas`.

Values that have the form <<NAME>> will be replaced by the relevant NAME in the settings section.

- **CORSICA_template_name2 [equal_spacing_pt2.bas]** : The second stage input template if a β_N or q_{95} scan is being performed. Comment this item out if this is not the case. Values that have the form <<NAME>> will be replaced by the relevant NAME in the settings section.
- **CHEASE_template_name [datain_template]** : The CHEASE input file template. <<NAME>> will be replaced by the relevant NAME in the settings section.
- **MARS_template_name [RUN_template]** : The MARS-F input file template - items with the form <<NAME>> will be replaced by the relevant NAME in the settings section.

J.2.5 Cluster details

This controls how many simultaneous jobs will be run. Be very careful with these settings!

```
[cluster_details]
cluster_job = 1
CHEASE_simultaneous_jobs = 10
MARS_simultaneous_jobs = 10
post_proc_simultaneous_jobs = 10
CORSICA_workers = 1
```

- **cluster_job [1,0]** : Leave this set to 1.
- **CHEASE_simultaneous_jobs [int]** : Maximum number of simultaneous CHEASE jobs on the cluster.
- **MARS_simultaneous_jobs [int]** : Maximum number of simultaneous MARS jobs on the cluster.
- **post_proc_simultaneous_jobs [int]** : Maximum number of simultaneous post processing jobs on the cluster.
- **CORSICA_workers [int]** : Number of simultaneous CORSICA jobs for stage 2 of a β_N or q_{95} scan.

J.2.6 RMZM

```
[RMZM_python_details]
RMZM_python = 1
```

Leave this set to 1. It used to be used as a switch to use the RZplot routines; however, that functionality is not still included properly.

J.2.7 Scan filter details

Used to filter out the equilibria from the CORSICA step based on DCON stability (if you chose to include this), and q_{95} and β_N/L_i ranges.

```
#filter out equilibria that DCON finds unstable (1=filter , 0=don't filter)
#also set allowable q95 and Beta_N/Li range , must have set <<calldcon>>=1
#in corsica settings for the DCON filters to be meaningful
[filters]
filter_WTOTN1 = 0
filter_WTOTN2 = 0
filter_WTOTN3 = 0
filter_WWTOTN1 = 0
q95_range = 0.,10.
Bn_Div_Li_range = 0.,10.
```

J.2.8 RMP coil details

```
[i_coil_details]
coilN1 = 2.164, 1.012, 2.374, 0.504
coilN2 = 2.164, -1.012, 2.374, -0.504
I_coil_frequency = 5.
N_Icoils = 6
I_coil_current = 1., -0.5, -0.5, 1, -0.5, -0.5
```

- `coilN1` and `coilN2` : Geometrical details of the upper and lower RMP coils.
- `I_coil_frequency [float]` : Frequency of the current in the RMP coils in Hz.
- `N_Icoils` : Number of discrete RMP coils, set to 6 for DIII-D. This is used to calculate I0EXP in post processing, a conversion factor from the MARS representation of the coils to real life.
- `I_coil_current [list]` : Relative currents in the coils at a given time. Also used to calculate I0EXP in the post processing.

J.2.9 Pickup coil details

This lists the pickup coils whose output will be calculated as part of the post processing. For each probe, the name, type (radial or poloidal), R, Z, length and poloidal inclination must be specified.

```
# #instead of using the defaults which are stored in PythonMARS_funcs.py
# # probe type 1: poloidal field , 2: radial field
```

```
[pickup_probe_details]
probe = 67A,66M,67B,ESL,ISL,UISL,LISL,Inner-pol,Inner-rad
probe-type = 1, 1, 1, 0, 0, 0, 0, 1,0
Rprobe = 2.265, 2.413, 2.265, 2.477, 2.431, 2.300, 2.300,1.,1.
Zprobe = 0.755, 0.0,-0.755, 0.000, 0.000, 0.714,-0.714,0.,0.
# poloidal inclination
tprobe = -67.5, -90.0,-112.5, 0.000, 0.000, 22.6, -22.6,-90.,0.
# Length of probe
lprobe = 0.155, 0.140, 0.155, 1.194, 0.800, 0.680, 0.680, 0.05,0.05,
```

J.2.10 CORSICA settings

```
# Corsica settings , note , each <<XXX>> must exist in the template as a
# placeholder to be replaced. You can add other values to this list if
# you want, just include the new placeholder
[corsica_settings]
single_runthrough = 0
p_mult_min = 0.01
p_mult_max = 2.5
p_mult_number = 20
q_mult_min = 1
q_mult_max = 1
q_mult_number = 1
```

- **single_runthrough [0,1]** : Set to 1 if no pressure or q95 scaling is required
- **p_mult_min [float]** : Min value of pressure multiplier
- **p_mult_max [float]** : Max value of pressure multiplier
- **p_mult_number [int]** : Number of pressure values between min and max
- **q_mult_min [float]** : Min value of q profile multiplier
- **q_mult_max [float]** : Max value of q profile multiplier
- **q_mult_number [int]** : Number of q profile values between min and max

```
[corsica_settings2]
<<npsi>> : 270
<<calldcon>> : 0
<<thetac>> : 0.003
<<stab_mode>> : 2
<<pmult_max>> : 4.5
<<q95_max>> : 7
<<q95_min>> : 2.5
<<min_bn_li>> : 0.5
<<bn_li_limit>> : 0.1
```

Some important items:

- **<<calldcon>> [1,0]** : Whether or not to check the stability. Need to set **<<stab_mode>>** to select the mode to test for stability with.

- `<<thetac>>` [float] : Proportion of flux to truncate to remove the x-point.
- `<<stab_mode>>` [int] : Mode to check for stability with DCON.

J.2.11 CHEASE settings

Settings related to the CHEASE run:

```
# CHEASE settings , note , each <<XXX>> must exist in the template as a
# placeholder to be replaced. You can add other values to this list if
# you want, just include the new placeholder in the template
[CHEASE_settings]
<<NCHI>> : 240
<<NPSI>> : 180
<<NT>> : 60
<<NS>> : 60
<<NV>> : 200
<<NVEXP>> : 4
<<REXT>> : 4.0
```

Refer to the Lutjens paper [46] on CHEASE or the source code for more details about these settings. Note that `<<NVEXP>>` and `<<REXT>>` are important for determining the radial packing in vacuum. Setting these to 4 and 4.0 respectively gave good results because we wanted decent mesh resolution where the I-coils were.

J.2.12 MARS settings

```
# MARS settings
[MARS_settings]
MARS_phasing = 0
upper_and_lower = 1
```

For the I-coils on DIII-D it is possible to run the simulations with just the upper I-coil array and just the lower I-coil array. An arbitrary upper-lower phasing can then be applied using these two separate simulations. This option is used if `upper_and_lower = 1`, otherwise, the phasing in `MARS_phasing` is used.

```
[MARS_settings2]
<<M1>>: -29
<<M2>>: 29
<<RNTOR>> : -2
<<ROTE>>: 0.0
<<NPROFT>>: 3
<<NPROFIE>>: 4
<<ETA>>: 0
<<PVISC>>:1.
```

- `<<M1>>` : Minimum poloidal mode number.

- <<M2>> : Maximum poloidal mode number.
- <<RNTOR>> : Toroidal mode number of the perturbation.
- <<ROTE>> : Normalised toroidal rotation. If it is set to -1, then the calculated value using the data in PROFROT is used, otherwise whatever value is put here is used.
- <<NPROFT>> : Index for input temperature profile - see MARS-F RUN.exp
- <<NPROFIE>> : Density and pressure profiles - see MARS-F RUN.exp
- <<ETA>> : Normalised resistivity (inverse of Lundquist number). If it is set to -1, then the calculated value using the data in PROFTE is used, otherwise whatever value is put here is used. Set to 0 for ideal MHD.
- <<PVISC>> : Coefficient for the sound wave damping model.

J.2.13 Cleaning up details

```
# # Cleaning up to save space , these files will be removed
[clean_up_settings]
MARS_rm_files = OUTDATA JPLASMA PPLASMA JACOBIAN
MARS_rm_files2 = OUTRMAR OUTVMAR
CHEASE_rm_files = NUPLO INP1 FORMATTED
CHEASE_PEST_rm_files = OUTRMAR OUTVMAR INP1_FORMATTED NUPLO
CORSICA_rm_files = *_int_te*q*
```

This lists the files that are supposed to be deleted at the end of each step of the process. Some of these files, in particular OUTDATA and OUTRMAR and OUTVMAR take up considerable amounts of space.

- **MARS-rm_files2** are removed after all of the MARS-F runs are complete. This is when the large CHEASE files are removed.
- **MARS-rm_files** are removed after all the MARS-F run

J.3 Examples

J.3.1 Single run through

The `/u/haskeysr/mars/example_single_run_through/` directory contains an example of a single run through using the experimental toroidal rotation profile and resistivity profile. The EFIT and profile directories in `input.cfg` contain the EFIT files and the density, ion temperature, and electron temperature profiles : `dne158115.04780.dat`, `dte158115.04780.dat`, and `dti158115.04780.dat`. Note that there are files from only a single shot in this directory. `rotation_scan` and `resistivity_scan` are both set to zero

and `single_run_through` is set to one.

J.3.2 Resistivity and rotation scan

The `/u/haskeysr/mars/example_res_rot_scan/` directory contains an example of a rotation and resistivity scan on a single equilibrium. The EFIT and profile directories in `input.cfg` contain the EFIT files and the density, ion temperature and electron temperature profiles. `rotation_scan`, `resistivity_scan`, and `single_run_through` are all set to one.

J.3.3 β_N scan

The `/u/haskeysr/mars/example_betaN_scan/` directory contains an example of β_N scan up to the no wall limit, with fixed rotation and resistivity using a single equilibrium. The EFIT and profile directories in `input.cfg` contain the EFIT files, and the density, ion temperature and electron temperature profiles. `rotation_scan`, `resistivity_scan` and `single_run_through` are all set to zero.

J.3.4 Multiple EFITs

`/u/haskeysr/mars/example_multiple_efit/` contains an example using multiple EFITs throughout a shot. The EFIT and profile directories in the `input.cfg` contain multiple EFIT files, and the density, ion temperature and electron temperature profiles for various times throughout this shot. `rotation_scan`, and `resistivity_scan` are set to zero and `single_run_through` is set to one.

Bibliography

Each of the papers in this thesis has its own bibliography. This bibliography is for the introduction, conclusion, and appendices.

- [1] A. D. Pasternak. Global energy futures and human development: a framework for analysis. *US Department of Energy Report UCRL-ID-140773, Lawrence Livermore National Laboratory, Livermore, CA*, 2000.
- [2] IEA. World energy outlook 2012.
- [3] World Health Organisation. *Global health risks*. World Health Organisation, 2009.
- [4] World health organisation. 7 million premature deaths annually linked to air pollution, March 2014.
- [5] Intergovernmental Panel on Climate Change. *Contribution of Working Group I to the Fourth Assessment Report of the Intergovernmental Panel on Climate Change*. 2007.
- [6] J. D. Lawson. Some criteria for a power producing thermonuclear reactor. *Proceedings of the Physical Society. Section B*, 70(1):6, 1957.
- [7] F. F. Chen. *Introduction to plasma physics and controlled fusion*. Plenum Press, New York, 1984.
- [8] R. O. Dendy. *Plasma physics: an introductory course*. Cambridge University Press, 1995.
- [9] S. P. Hirshman and J. C. Whitson. Steepest-descent moment method for three-dimensional magnetohydrodynamic equilibria. *Physics of Fluids*, 26:3553, 1983.
- [10] W. W. Heidbrink. Basic physics of Alfvén instabilities driven by energetic particles in toroidally confined plasmas. *Physics of Plasmas*, 15(5):055501, 2008.
- [11] K. L. Wong, R. J. Fonck, S. F. Paul, D. R. Roberts, E. D. Fredrickson, R. Nazikian, H. K. Park, M. Bell, N. L. Bretz, R. Budny, S. Cohen, G. W. Hammett, F. C. Jobes,

- D. M. Meade, S. S. Medley, D. Mueller, Y. Nagayama, D. K. Owens, and E. J. Synakowski. Excitation of toroidal Alfvén eigenmodes in TFTR. *Physical Review Letters*, 66:1874–1877, Apr 1991.
- [12] R. B. White, E. Fredrickson, D. Darrow, M. Zarnstorff, R. Wilson, S. Zweben, K. Hill, Y. Chen, and G. Fu. Toroidal Alfvén eigenmode-induced ripple trapping. *Physics of Plasmas*, 2(8):2871–2873, 1995.
- [13] T.C. Hender et al. Progress in the ITER physics basis chapter 3: MHD stability, operational limits and disruptions. *Nuclear Fusion*, 47(6):S128–S202 (beginning of chapter), 2007.
- [14] S. E. Sharapov, D. Testa, B. Alper, D. N. Borba, A. Fasoli, N. C. Hawkes, R. F. Heeter, M. Mantsinen, M. G. Von Hellermann, et al. MHD spectroscopy through detecting toroidal Alfvén eigenmodes and Alfvén wave cascades. *Physics Letters A*, 289(3):127–134, 2001.
- [15] B. N. Breizman and S. E. Sharapov. Major minority: energetic particles in fusion plasmas. *Plasma Physics and Controlled Fusion*, 53:054001, 2011.
- [16] A. Könies and D. Eremin. Coupling of Alfvén and sound waves in stellarator plasmas. *Physics of Plasmas*, 17(1):012107, 2010.
- [17] C. Schwab. Ideal magnetohydrodynamics: Global mode analysis of three-dimensional plasma configurations. *Physics of Fluids B: Plasma Physics*, 5:3195, 1993.
- [18] C. Nührenberg. Compressional ideal magnetohydrodynamics: Unstable global modes, stable spectra, and Alfvén eigenmodes in Wendelstein 7-X-type equilibria. *Physics of Plasmas*, 6(1):137–147, 1999.
- [19] J. H. Harris, M. G. Shats, B. D. Blackwell, W. M. Solomon, D. G. Pretty, S. M. Collis, J Howard, H Xia, C. A. Michael, and H. Punzmann. Fluctuations and stability of plasmas in the H-1NF heliac. *Nuclear Fusion*, 44(2):279, 2004.
- [20] D. G. Pretty. *A study of MHD activity in the H-1 heliac using data mining techniques*. PhD thesis, The Australian National University, 2007.
- [21] D. G. Pretty and B. D. Blackwell. A data mining algorithm for automated characterisation of fluctuations in multichannel timeseries. *Computer Physics Communications*, 180(10):1768–1776, 2009.

- [22] B. D. Blackwell, D. G. Pretty, J. Howard, R. Nazikian, S. T. A. Kumar, D. Oliver, D. Byrne, J. H. Harris, C. A. Nuhrenberg, M. McGann, et al. Configurational effects on Alfvénic modes and confinement in the H-1NF heliac. *arXiv preprint arXiv:0902.4728*, 2009.
- [23] J. Bertram, B. D. Blackwell, and M. J. Hole. Ideal-magnetohydrodynamic theory of low-frequency Alfvén waves in the H-1 heliac. *Plasma Physics and Controlled Fusion*, 54(5):055009, 2012.
- [24] J. Bertram, M. J. Hole, D. G. Pretty, B. D. Blackwell, and R. L. Dewar. A reduced global Alfvén eigenmodes model for mirnov array data on the H-1NF heliac. *Plasma Physics and Controlled Fusion*, 53:085023, 2011.
- [25] T. E. Evans, R. A. Moyer, K. H. Burrell, M. E. Fenstermacher, I. Joseph, A. W. Leonard, T. H. Osborne, G. D. Porter, M. J. Schaffer, P. B. Snyder, et al. Edge stability and transport control with resonant magnetic perturbations in collisionless tokamak plasmas. *Nature Physics*, 2(6):419–423, 2006.
- [26] T. E. Evans, M. E. Fenstermacher, R. A. Moyer, T. H. Osborne, J. G. Watkins, P. Gohil, I. Joseph, M. J. Schaffer, L. R. Baylor, M. Bécoulet, et al. RMP ELM suppression in DIII-D plasmas with ITER similar shapes and collisionalities. *Nuclear Fusion*, 48:024002, 2008.
- [27] T. E. Evans, R. A. Moyer, P. R. Thomas, J. G. Watkins, T. H. Osborne, J. A. Boedo, E. J. Doyle, M. E. Fenstermacher, K. H. Finken, R. J. Groebner, et al. Suppression of large edge-localized modes in high-confinement DIII-D plasmas with a stochastic magnetic boundary. *Physical Review Letters*, 92(23):235003, 2004.
- [28] Y. M. Jeon, J. K. Park, S. W. Yoon, W. H. Ko, S. G. Lee, K. D. Lee, G. S. Yun, Y. U. Nam, W. C. Kim, Jong-Gu Kwak, et al. Suppression of edge localized modes in high-confinement KSTAR plasmas by nonaxisymmetric magnetic perturbations. *Physical Review Letters*, 109(3):035004, 2012.
- [29] W. Suttrop, T. Eich, J. C. Fuchs, S. Günter, A. Janzer, A. Herrmann, A. Kallenbach, P. T. Lang, T. Lunt, M. Maraschek, et al. First observation of edge localized modes mitigation with resonant and nonresonant magnetic perturbations in ASDEX upgrade. *Physical Review Letters*, 106(22):225004, 2011.

- [30] M. J. Lanctot, R. J. Buttery, J. S. de Grassie, T. E. Evans, N. M. Ferraro, J. M. Hanson, S. R. Haskey, R. A. Moyer, R. Nazikian, T. H. Osborne, et al. Sustained suppression of type-I edge-localized modes with dominantly $n = 2$ magnetic fields in DIII-D. *Nuclear Fusion*, 53(8):083019, 2013.
- [31] Y. Liang, H. R. Koslowski, P. R. Thomas, E. Nardon, B. Alper, P. Andrew, Y. Andrew, G. Arnoux, Y. Baranov, M. Bécoulet, et al. Active control of type-I edge-localized modes with $n = 1$ perturbation fields in the JET tokamak. *Physical Review Letters*, 98(26):265004, 2007.
- [32] A. Kirk, E. Nardon, R. Akers, M. Bécoulet, G. De Temmerman, B. Dudson, B. Hnat, Y. Q. Liu, R. Martin, P. Tamain, et al. Resonant magnetic perturbation experiments on MAST using external and internal coils for ELM control. *Nuclear Fusion*, 50(3):034008, 2010.
- [33] E. Nardon, A. Kirk, R. Akers, M. Bécoulet, P. Cahyna, G. De Temmerman, B. Dudson, B. Hnat, Y. Q. Liu, R. Martin, et al. Edge localized mode control experiments on MAST using resonant magnetic perturbations from in-vessel coils. *Plasma Physics and Controlled Fusion*, 51(12):124010, 2009.
- [34] W. M. Solomon, K. H. Burrell, A. M. Garofalo, R. J. Groebner, C. J. Lasnier, M. A. Makowski, T. H. Osborne, H. Reimerdes, E. J. Doyle, T. E. Evans, et al. ELM pacing using modulated non-axisymmetric magnetic fields on DIII-D. *Nuclear Fusion*, 52(3):033007, 2012.
- [35] J. M. Canik, R. Maingi, T. E. Evans, R. E. Bell, S. P. Gerhardt, H. W. Kugel, B. P. LeBlanc, J. Manickam, J. E. Menard, T. H. Osborne, et al. ELM destabilization by externally applied non-axisymmetric magnetic perturbations in NSTX. *Nuclear Fusion*, 50(3):034012, 2010.
- [36] P. B. Snyder, T. H. Osborne, K. H. Burrell, R. J. Groebner, A. W. Leonard, R. Nazikian, D. M. Orlov, O. Schmitz, M. R. Wade, and H. R. Wilson. The EPED pedestal model and edge localized mode-suppressed regimes: Studies of quiescent h-mode and development of a model for edge localized mode suppression via resonant magnetic perturbations. *Physics of Plasmas*, 19(5):056115, 2012.
- [37] M. Okabayashi, J. Bialek, A. Bondeson, M. S. Chance, M. S. Chu, A. M. Garofalo,

- R. Hatcher, Y. In, G. L. Jackson, R. J. Jayakumar, et al. Control of the resistive wall mode with internal coils in the DIII-D tokamak. *Nuclear Fusion*, 45:1715, 2005.
- [38] C. Cates, M. Shilov, M. E. Mauel, G. A. Navratil, D. Maurer, S. Mukherjee, D. Nadle, J. Bialek, and A. Boozer. Suppression of resistive wall instabilities with distributed, independently controlled, active feedback coils. *Physics of Plasmas*, 7:3133, 2000.
- [39] R. J. La Haye, S. Günter, D. A. Humphreys, J. Lohr, T. C. Luce, M. E. Maraschek, C. C. Petty, R. Prater, J. T. Scoville, and E. J. Strait. Control of neoclassical tearing modes in DIII-D. *Physics of Plasmas*, 9:2051, 2002.
- [40] H. Reimerdes, M. S. Chu, A. M. Garofalo, G. L. Jackson, R. J. La Haye, G. A. Navratil, M. Okabayashi, J. T. Scoville, and E. J. Strait. Measurement of the resistive-wall-mode stability in a rotating plasma using active MHD spectroscopy. *Physical Review Letters*, 93(13):135002, 2004.
- [41] M. Shilov, C. Cates, R. James, A. Klein, O. Katsuro-Hopkins, Y. Liu, M. E. Mauel, D. A. Maurer, G. A. Navratil, T. S. Pedersen, et al. Dynamical plasma response of resistive wall modes to changing external magnetic perturbations. *Physics of Plasmas*, 11:2573, 2004.
- [42] A. M. Garofalo, R. J. La Haye, and J. T. Scoville. Analysis and correction of intrinsic non-axisymmetric magnetic fields in high-beta DIII-D plasmas. *Nuclear Fusion*, 42(11):1335, 2002.
- [43] Jong-Kyu Park, M. J. Schaffer, J. E. Menard, and A. H. Boozer. Control of asymmetric magnetic perturbations in tokamaks. *Physical Review Letters*, 99:195003, Nov 2007.
- [44] E. J. Strait. Magnetic diagnostic system of the DIII-D tokamak. *Review of Scientific Instruments*, 77:023502, 2006.
- [45] J. D. King, E. J. Strait, R. L. Boivin, D. Taussig, M. G. Watkins, J. M. Hanson, N. C. Logan, C. Paz-Soldan, D. C. Pace, D. Shiraki, M. J. Lanctot, R. J. La Haye, L. L. Lao, D. J. Battaglia, A. C. Sontag, S. R. Haskey, and J. G. Bak. An upgrade of the magnetic diagnostic system of the DIII-D tokamak for non-axisymmetric measurements. *Review of Scientific Instruments*, 85(8):083503, 2014.

- [46] H. Lütjens, A. Bondeson, and O. Sauter. The CHEASE code for toroidal MHD equilibria. *Computer physics communications*, 97(3):219–260, 1996.